Technische Universität München

TUM School of Engineering and Design

Model-Based Fast Charging Control of Lithium-Ion Batteries in Electric Vehicles

Nikolaos Wassiliadis, M.Sc.

Vollständiger Abdruck der von der TUM School of Engineering and Design der Technischen Universität München zur Erlangung des akademischen Grades eines

Doktors der Ingenieurwissenschaften

genehmigten Dissertation.

Vorsitz:	Prof. Dr.-Ing. Rüdiger Daub
Prüfende der Dissertation:	1. Prof. Dr.-Ing. Markus Lienkamp
	2. Prof. Dr.-Ing. Andreas Jossen
	3. Prof. Dr.-Ing. Kai Peter Birke

Die Dissertation wurde am 27.10.2023 bei der Technischen Universität München eingereicht und durch die TUM School of Engineering and Design am 16.04.2024 angenommen.

Abstract

Fast charging of lithium-ion cells marks one of the most demanding and critical use cases in electric vehicle applications, which is still a significant and interdisciplinary challenge from a battery management perspective. In recent years, many different approaches to determining fast charging current control strategies have been proposed, levering the charging algorithm to operate at the physical limits, trading-off charging time and cycle life without compromising the safety of lithium-ion battery cells in high-voltage systems.

In this work, remaining challenges in the research field of fast charging current control are extracted in a literature review and a comprehensive method is proposed to determine a model-based health-aware fast charging strategy for lithium-ion batteries. Starting with a commercial lithium-ion cell without any information about the properties, the process to collect key data for electrochemical-thermal modeling during a cell teardown and electrode characterization is outlined. The extracted information is used as a baseline for a systematic parameter identification approach of an electrochemical-thermal model, which successfully distinguishes the individual contributions of both electrodes to the overall cell behavior. The model is validated against various charging currents and ambient temperatures to highlight its strength and weaknesses. Subsequently, the model is used for fast charging current control based on real-time anode potential predictions sensitive to the three most relevant states of lithium-ion cells, i.e., the state of charge, the temperature, and the state of health to mitigate the risk of non-linear aging due to lithium plating at varying operating conditions. Special attention is given to outlining the required steps for model deployment in a laboratory environment. The model-based health-aware fast charging strategy is applied in extensive cycle life tests with non-destructive and *post-mortem* investigations of the dominant aging mechanisms, and the onset of nonlinear aging is mitigated. As lithium-ion cells are usually connected in parallel and serial by laser-welded joints in automotive applications, a comparison between the laboratory environment and laser-welded lithium-ion cells during fast charging is made. It is shown that a major contribution to the heat-up phase of the lithium-ion cell is originating from high electrical contact resistances and tab-to-core heat conduction in laboratory environments, which may lead to an overestimation of the cell's self-heating capability during fast charging.

In general, the findings contribute to a successful end-to-end development of model-based fast-charging current control strategies starting from a lithium-ion cell with unknown characteristics, to ensure safety and good cycle life during operation, to ultimately improve ultra-fast charging and combat range anxiety associated with battery electric vehicles.

Acknowledgment

This work was carried out during my time as a research associate at the Institute of Automotive Technology at the Technical University of Munich under a publicly funded position by the Free State of Bavaria. My sincere thanks go to Prof. Dr.-Ing. Markus Lienkamp. He not only gave me paramount freedom in pursuing my research interest but also entrusted me with the leadership and development of one of his research fields. He has created a unique environment of self-determination, empowerment, and camaraderie that enables scientific work under the best conditions, which should be a blueprint for academic research worldwide. I am very grateful to Prof. Dr.-Ing. Andreas Jossen and Prof. Dr.-Ing. Kai Peter Birke for taking over the co-evaluation and supporting this work. Furthermore, I would like to thank Prof. Dr.-Ing. Rüdiger Daub for chairing the final examination.

As one of the research associates spending almost all of my academic life at the Technical University of Munich, I had the opportunity to meet many inspiring and talented people working in the interdisciplinary fields of automotive technology. First and foremost, I want to thank the “older generation” of research associates, especially Dr.-Ing. Christoph Reiter, Dr.-Ing. Jörn Adermann, Dr.-Ing. Michael Wittmann, and Prof. Dr.-Ing. Johannes Betz, who accompanied me with advice, endorsed me in my first years, and were good friends throughout. Special thanks also go to all the associates who shared the different stages of this journey and for the unforgettable times from the start, Julian Kreibich, Leo Wildfeuer, Dr.-Ing. Lorenzo Nicoletti, Sebastian Krapf, Dr.-Ing. Ferdinand Schockenhoff, Lennart Adenaw, and Dr.-Ing. Matthias Steinsträter. Finally, I also want to thank the “younger generation” in my former team for providing me with lots of challenging discussions and exciting ideas. Beyond, I want to thank my colleagues at the Institute for Machine Tools and Industrial Management, especially Dr.-Ing. Florian Günter, Johannes Kriegler, Michael Kick, Sandro Stock, and Alessandro Sommer for their cooperation and support. I further acknowledge the dedication spent by my proofreaders, especially Ilse New, refining this work to the present version. Without all of you, this work would not have been possible.

I also like to thank all the students who enriched this work with tremendous commitment and engagement. But most of all, I want to thank those running the extra mile.

Finally, I thank my family, who gave me every freedom in choosing my career path and, at the same time, also encouraged me in my desire to pursue and obtain a doctorate without coming from an academic background or a privileged financial situation, if you genuinely believe in yourself, follow your ambitions, and buckle down. I am incredibly grateful to my wife, Marlene, who stayed by my side throughout the complete journey—with all the ups and downs.

Nikolaos Wassiliadis
Ingolstadt, October 2023

Contents

List of Abbreviations

BEV	battery electric vehicle
BMS	battery management system
CA	constant anode potential
CAN	controlled area network
CC	constant current
CP	constant power
C-rate	current rate
CT	computed tomography
DC	direct current
DMC	dimethyl carbonate
DOD	depth of discharge
DVA	differential voltage analysis
EC	ethylene carbonate
ECR	electrical contact resistance
EDX	energy-dispersive X-ray analysis
EIS	electrochemical impedance spectroscopy
EOL	end of life
GITT	galvanic intermediate titration technique
HPPC	high pulse power characterization
ICA	incremental capacity analysis
ICEV	internal-combustion engine vehicle
LFP	lithium iron phosphate
NCA	nickel cobalt aluminum oxide
NMC	nickel manganese cobalt oxide
OCP	open-circuit potential
OCV	open-circuit voltage
ODE	ordinary differential equation
P2D	pseudo-two-dimensional
PDE	partial differential equation
pECM	physics-enhanced equivalent circuit model

pOCV	pseudo-open-circuit voltage
R&D	research and development
RMSE	root mean square error
SEI	solid electrolyte interphase
SEM	scanning electron microscopy
SOC	state of charge
SOH	state of health
SPM	single particle model
SR	Standard Range
UI-SOC	state of charge displayed in the user interface

Please note that the listed abbreviations correspond to the underlying and overarching work. The attached publications' abbreviations may differ.

Formula Symbols

Formula Symbols	Unit	Description
C-rate	1/h	Current rate
Q_{N}	Ah	Nominal capacity
Q	Ah	Capacity
Q_{initial}	Ah	Initial capacity
I	A	Current
t	h	Time
R	mΩ	Resistance
R_{initial}	mΩ	Initial resistance
SOC	%	State of charge
$\mathrm{SOC}_{\mathrm{initial}}$	%	Initial state of charge
$\mathrm{SOH}_{\mathrm{C}}$	%	State of health (Capacity)
$\mathrm{SOH}_{\mathrm{R}}$	%	State of health (Resistance)
U	V	Voltage
U_{cell}	V	Cell voltage
U_{OCV}	V	Open-circuit voltage
U_{pack}	V	Pack voltage
T	°C	Temperature
T_{min}	°C	Minimal cell temperature within a pack
T_{max}	°C	Maximum cell temperature within a pack
P	kW	Power
T_{amb}	°C	Ambient temperature
T_{c}	°C	Cell core temperature
T_{s}	°C	Cell surface temperature

ϕ^{-}	V	Anode potential
ϕ^{+}	V	Cathode potential
ϕ^{-}_{OCP}	V	Anode open-circuit potential
ϕ^{+}_{OCP}	V	Cathode open-circuit potential
η^{-}	V	Anode overpotential
η^{+}	V	Cathode overpotential
η^{-}_{Ohm}	V	Ohmic overpotential at the anode
η^{+}_{Ohm}	V	Ohmic overpotential at the cathode
η^{-}_{CT}	V	Charge transfer overpotential at the anode
η^{+}_{CT}	V	Charge transfer overpotential at the cathode
$\eta^{-}_{\mathrm{Diffusion}}$	V	Diffusion overpotential at the anode
$\eta^{+}_{\mathrm{Diffusion}}$	V	Diffusion overpotential at the cathode
$\eta_{\mathrm{Electrolyte}}$	V	Diffusion overpotential of the electrolyte
L^{-}	μm	Anode thickness
L^{sep}	μm	Separator thickness
L^{+}	μm	Cathode thickness
c^{-}_{s}	μm	Lithium concentration in the anode
c^{e}	μm	Lithium concentration in the electrolyte
c^{+}_{s}	μm	Lithium concentration in the cathode
n_{r}	-	Radial electrode discretization
n^{-}_{x}	-	Axial anode discretization
n^{+}_{x}	-	Axial cathode discretization

Please note that the listed formula symbols correspond to the underlying and overarching work. The attached publications' formula symbols may differ.

1 Introduction and problem statement

An increasing scarcity of resources, growing public environmental awareness, and governmental regulations led to the establishment of lithium-ion battery packs as the dominant power-delivering component in battery electric vehicles (BEVs). It has been shown that electrified transport can eliminate the increasing economic and political dependence on fossil fuels by omitting the use of carbon-based fuels, thereby improving the overall energy efficiency and reducing the severe impact of carbon dioxides on the world climate [1, 2]. Beyond that, BEVs provide further advantages compared to combustion-power vehicles, such as the less frequent need for maintenance and repairs due to fewer mechanical parts [3], reduced urban noise pollution [4], and the potential for grid-stabilizing services [5].

The major technological limitation hampering the worldwide adaptation of BEVs in all possible applications remains in the limited driving range compared to combustion-powered vehicles. With the start of mass-series electric vehicle development, most vehicle manufacturers followed the design paradigm of steadily increasing the lithium-ion battery pack's volumetric and gravimetric energy density to improve the overall range of BEVs [6]. Likewise, considerable research effort is put into maximizing the electric range at all costs [7]. While the energy density increased, the power density decreased, as both design trends are known to be contradictory [8].

However, many applications and usage situations of BEVs also require a high-power capability of the lithium-ion battery pack and short charging times. For example, long-distance trips are impossible to realize with charging times beyond 8 h by using commonly available three-phase charging power. BEVs may be started with a depleted battery pack that does not cover the intended trip distance, even if this distance may be short. Moreover, densely-populated metropolitan areas are difficult to supply with overnight charging access points, so that not all BEVs can be charged during their idle time [9], and communities contemplate how to meet the growing charging demand [10]. Beyond that, commercial vehicles are intended to keep the idle time at a minimum to maximize profitability, and long charging times render this specific scenario a bad business case [11]. Combustion-powered vehicles created a user expectation of similar fast refueling times of BEVs [12].

To counter these issues, a great deal of political interest has been generated to promote and subsidize charging infrastructure over the past decade [13]. On the other hand, governmental institutions have defined research and development (R&D) goals to promote technological improvements to enable fast charging of BEVs. For example, the United States Department of Energy (DOE) defined a fast charging time target of less than 15 min between 10–80 % until 2028 [14], while the European Council for Automotive Research and Development (EUCAR) defined a similarly challenging fast charging target of 3.5 C between 0–80 % until 2030 at cell level [15].

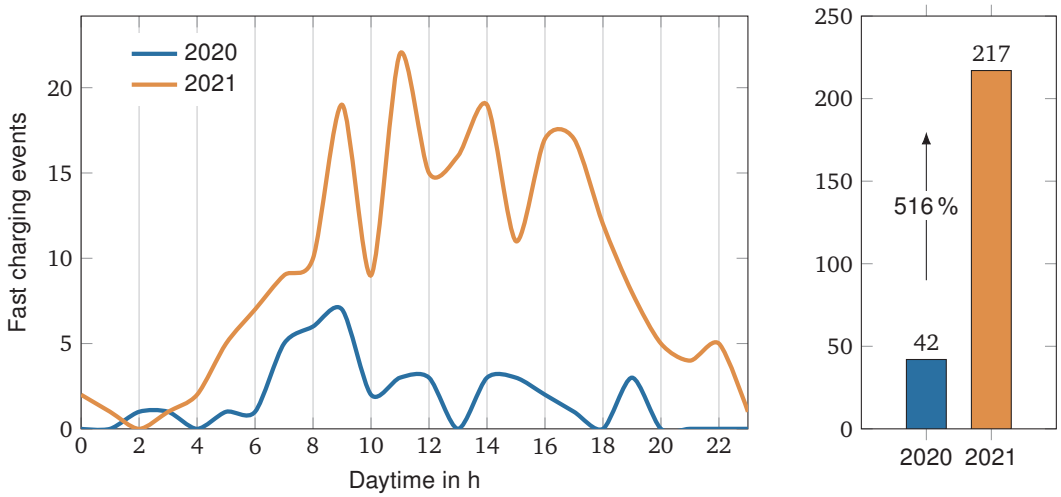

Figure 1.1: Fast charging demand of the fast charger pool with four 350 kW chargers in Bad Honnef, Germany [18]. The charging demand is compared for calendar week 42 in the years 2020 and 2021 due to limited data availability.

Following these targets, significant progress has been made in increasing the fast-charging capability of BEVs. Due to the steady improvement of the fast-charging power, BEVs have already been fast-charged more frequently. Both increased fast charging events and more BEVs capable of fast charging can be measured indirectly if the corresponding infrastructure usage is monitored. For example, as shown in Figure 1.1, the 350 kW fast charger pool in Bad Honnef, Germany, has seen an increase of 516 % between the years 2020 and 2021 if all fast charging events in a specific week of the year are compared. While this data sample is limited, an increased usage of public fast charging points was revealed in other studies with broader datasets [16]. With the increasing usage of and demand for fast charging, the relevance in the design decision-making during the early development phases of new BEVs can be expected to increase even further.

Beyond that, fast charging already marks the most significant challenge for automotive engineers. The required high charging power may lead to accelerated aging of the lithium-ion cells due to the complex mechanisms inherited by the electrochemical nature of the lithium-ion cells [17]. If the lithium-ion battery pack is aging rapidly, the capacity is fading and the resistance is rising, perceivable as a decrease in range and power by the user. Aging mechanisms may amplify and self-reinforce once they occur, leading to a rapid failure and replacement of the overall lithium-ion battery pack.

At the same time, the lithium-ion battery pack remains the most expensive component of the electric powertrain, as shown in Figure 1.2, compared to an internal-combustion engine vehicle (ICEV). Engineers must ensure that the lithium-ion battery pack achieves a long lifetime to meet warranty but also future sustainability or circular economy targets. Consequently, the lithium-ion battery's fast and unpredictable aging must be strictly avoided. Therefore, the fast charging functionality of lithium-ion battery packs requires thorough management by in-depth knowledge of the lithium-ion cells' behavior and their system interactions to hedge against unintended operational or safety-critical hazards during usage. Hereby, the issues arising with enhanced fast charging utilization are complex and multidisciplinary at various levels [19].

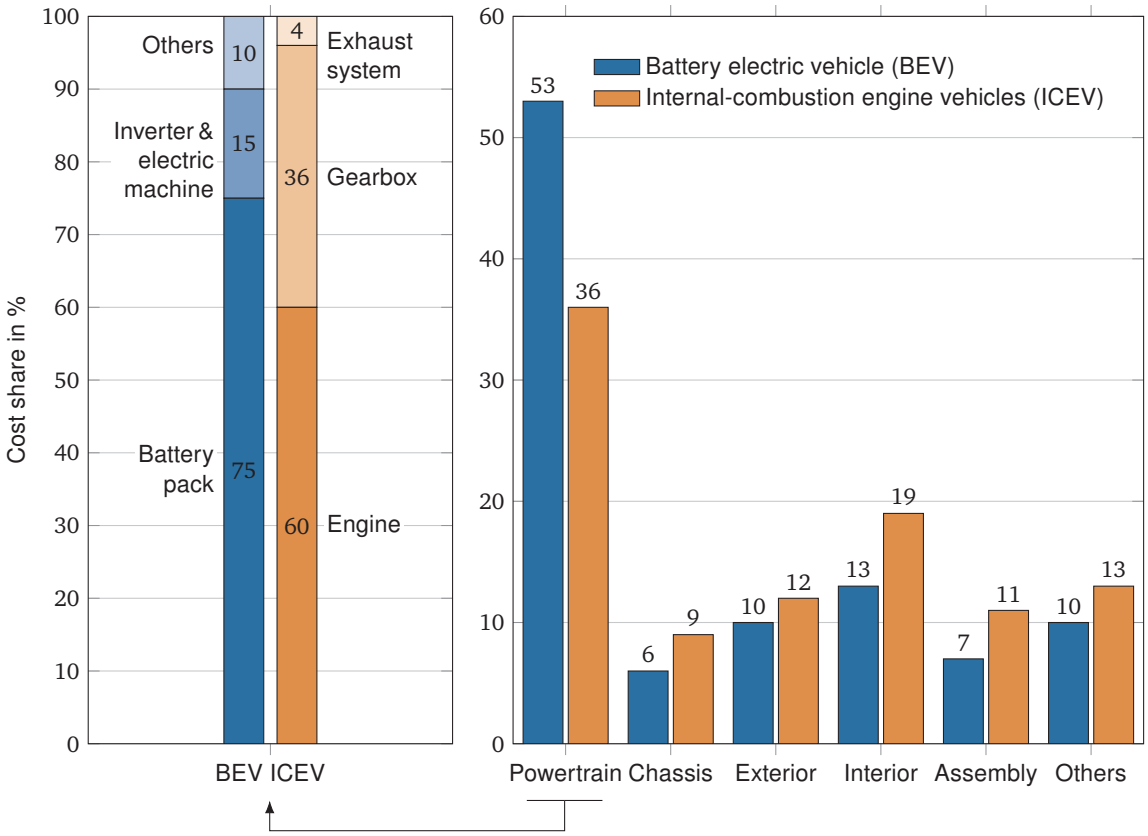

Figure 1.2: Cost structure of the key powertrain components in combustion and electrified powertrains [18]. The presented data is based on aggregated data from studies covering electric powertrain cost shares [32], combustion-powered powertrain cost shares [33], and lithium-ion battery pack cost shares [34].

In recent years, R&D efforts of industry and academia have been heading towards technological improvements of fast charging at multiple levels along the system integration path of lithium-ion cells into electrified powertrains. Advanced manufacturing and optimal material composition of lithium-ion cells have been identified as a significant field to improve the charging performance [20, 21]. For example, research groups enhanced the lithium-ion cell performance by laser structuring graphite anodes [22–24] or building optimized electrolyte compositions [25] at the material level. Beyond this, advanced control algorithms have been proposed to prolong the life of lithium-ion cells [26]. Further, it was shown that elevated temperatures were beneficial for achieving a longer cycle life under high charging currents [27–29]. At a system level, optimized thermal management [30] and lithium-ion cell-to-pack integration [31] were also identified as potential fields to further optimize the fast charging speed under the tight design constraints in the automotive development.

To date, one of the major questions remains on how to develop fast charging strategies for lithium-ion cells with unknown properties that control the charging current to minimize charging time while avoiding any early failure. To gain a deeper understanding of the origins of the charging current limitations and the need for advanced algorithms, the fundamentals and state of the art of lithium-ion cells, systems, and their aging mechanisms during fast charging must first be introduced.

1.1 Lithium-ion cells, high-voltage systems, and fast charging strategies

Lithium-ion cells are typically composed of different electrode materials predefining the lithium-ion cell's performance and cost. To understand the barriers of enabling faster charging times, the following sections provide a brief overview of the fundamental principles of lithium-ion cells (Subsection 1.1.1) and summarize the commonly used materials, formats, system configurations (Subsection 1.1.2) and fast charging strategies (Subsection 1.1.3) used in modern BEVs.

1.1.1 Fundamental principles and definitions

Lithium-ion cells are composed of two individual electrodes and an ion-permeable separator, as shown in Figure 1.3. The voids and cavities within the cell are filled with an ion conductor, the electrolyte, which connects both electrodes ionically but isolates them electrically. From an electrochemical perspective, the oxidation occurs at the anode and the reduction at the cathode, leading to changing spatial definitions of the negative and positive electrode, depending on whether the lithium-ion cell is charged or discharged. Here we define the negative electrode as the commonly carbon-based anode coated to a copper current collector. The positive electrode consists of transition metal oxides coated to an aluminum current collector.

When charging, lithium ions move from the cathode through the separator structure to the anode. During this procedure, dynamics are driven by charge transfer, double-layer, and mass transport effects, as described by Jossen [36]. Starting at the cathode side, lithium ions move through the electrolyte to the anode side, overcoming an ohmic resistance. At the anode surface, lithium ions intercalate into the host lattice, known as the charge transfer reaction associated with the charge transfer overvoltage. In the second step, the lithium diffuses from the surface to the interior of the active material, stimulated by a concentration gradient in the active material and an associated

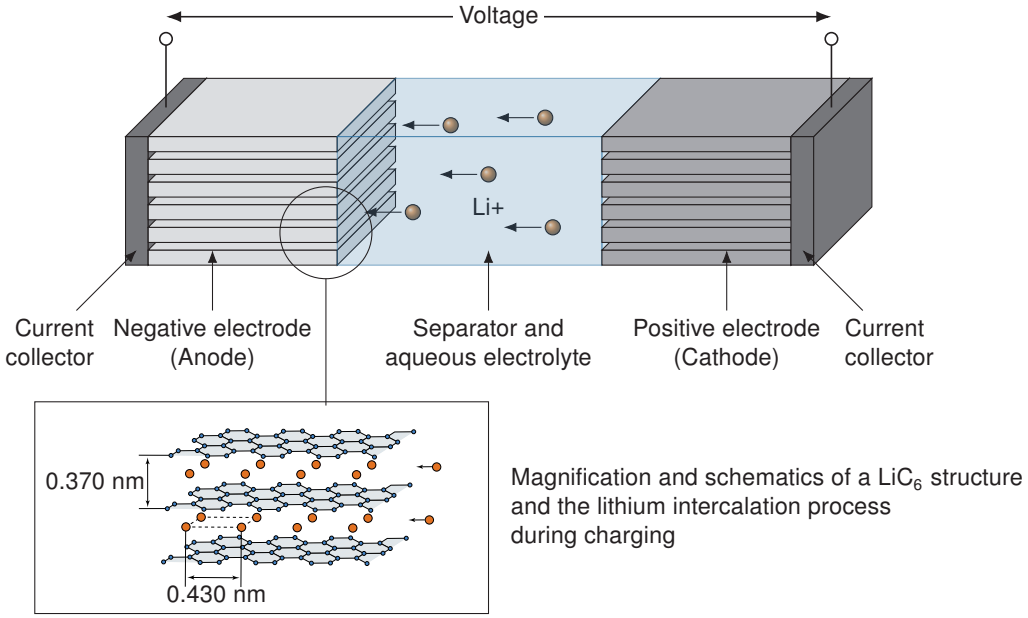

Figure 1.3: Lithium-ion cell working principle during charging. The magnified view shows the intercalation of lithium ions into a graphite host structure, as reported in the literature [35].

diffusion overvoltage. Finally, electrons are transferred from the anode to the cathode via the current collectors and an external circuit leading to an ohmic overvoltage.

Lifting this phenomenological description to measurable quantities, the intercalation of lithium ions into or lithiation of the graphite host structure yields a descending open-circuit potential (OCP) vs. Li/Li+ of the anode. At the same time, the cathode is delithiated leading to an ascending OCP vs. Li/Li+. In total, both electrodes create a potential difference that is composed to a voltage in the lithium-ion cell, known as open-circuit voltage (OCV), describing the lithium-ion cell state at rest (Figure 1.4(a)). If the lithium-ion cell is subjected to transient cycling by applying a current at the cell's terminals, overvoltages superimpose the OCV depending on the charge or discharge direction, as explained before, which is measurable as a transient voltage at the lithium-ion cell tabs (Figure 1.4(b)).

During the charging and discharging, the change in OCV and overvoltages lead to a reversible entropic and irreversible *Joule* heat, respectively, further leading to an observable temperature change with time of the lithium-ion cell, as the dominant mechanisms described by Bernardi et al. [39]. The changing temperature of the lithium-ion cell hereby interferes with the previously mentioned electrochemical processes occurring due to accelerated reaction kinetics with larger temperatures and *vice versa*.

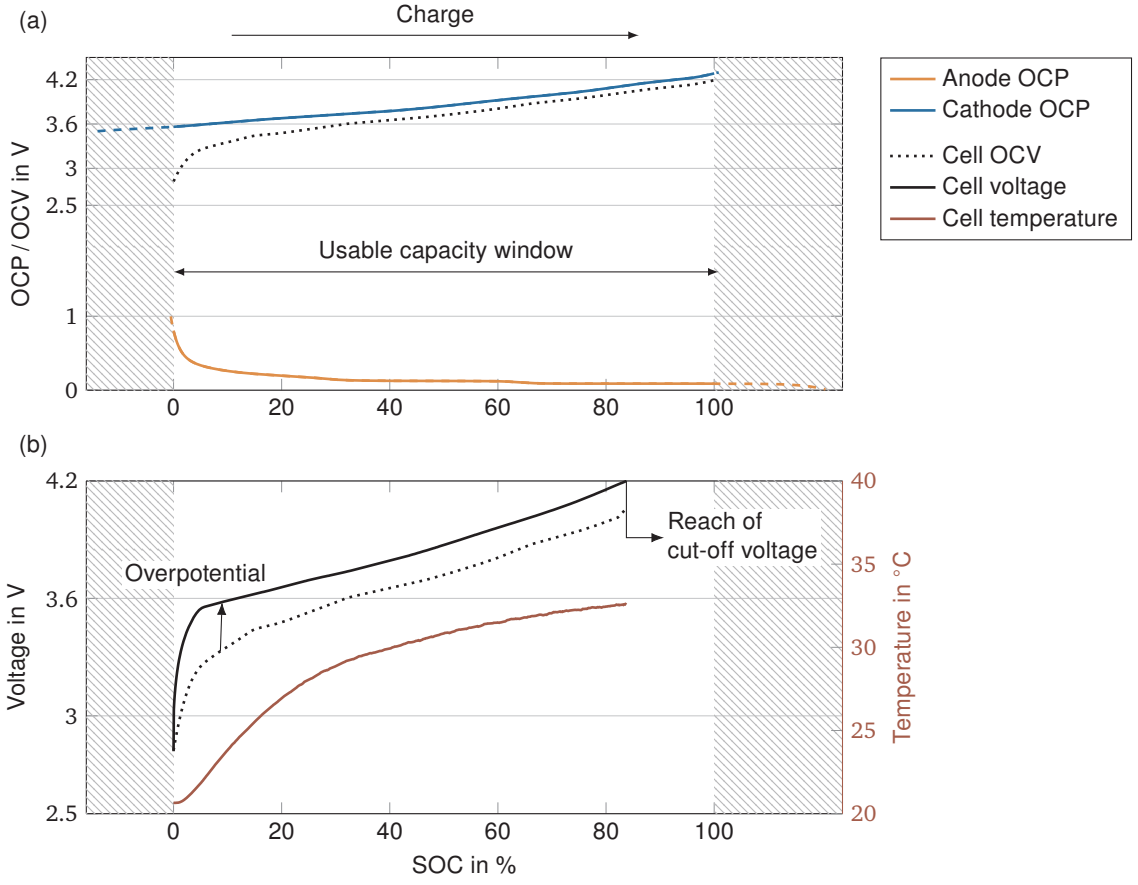

Figure 1.4: Lithium-ion cell OCV and the cell's electro-thermal behavior during charging. (a) Cell OCV as a superposition of both electrode OCPs, (b) cell terminal voltage as a superposition of the cell's OCV and cell's overpotenial, leading to a temperature rise during a 2.5 A charge (2.5 Ah cell) at 20 °C ambient temperature. All graphs are based on measurements from prior studies by the author [37, 38].

To quantitatively describe and compare the physical processes occurring in lithium-ion cells, different terms and definitions exist. To prevent any misinterpretations of the results in later sections, fundamental definitions are specified below.

- **Current rate (C-rate)**
  As a commonly and broadly used definition in the literature, the current applied to a lithium-ion cell is often translated to a current rate (C-rate) in 1/h according to

$$\text{C-rate} = \frac{I}{Q_\text{N}}, \tag{1.1}$$

  where I is the current measured in A, and Q_N is the nominal capacity measured in Ah, usually given by the cell manufacturer. This definition provides a normalized quantity for comparing the charging time and current stress across different lithium-ion cell capacities. A lithium-ion cell charged with a 1 C takes 1 h to be fully charged, independently of its capacity.

- **Capacity**
  The maximum amount of electrical charge drained from a lithium-ion cell is called capacity Q in Ah. This definition may vary, depending on the operating voltage window of the deployed lithium-ion cells, and it differs to the nominal capacity Q_N. While multiple definitions exist in the literature, the cell capacity is defined in this work as the current integral over the charging time according to

$$Q = \int_0^t I(t)\,dt, \tag{1.2}$$

  with the time t during a discharge from 4.2 V to 2.5 V at 20 °C until an absolute cut-off current of less than 1/50 C is reached during the constant voltage sequence at 2.5 V. Therefore, the capacity is independent of the current rate, temperature, and resistance, as overpotentials only have a marginal impact on the measurement procedure. Lithium-ion cells' capacity used in automotive applications usually ranges from approximately 2 Ah (small format cells) to about 160 Ah (large format cells).

- **State of charge (SOC)**
  To get a relative estimate of the remaining capacity during the usage of lithium-ion cells, the state of charge (SOC) is defined according to

$$\text{SOC} = \text{SOC}_\text{initial} + \int_0^t I(t)\,dt \tag{1.3}$$

  with $\text{SOC}_\text{initial}$ as the SOC at the beginning of a charge or discharge. The SOC is usually expressed in %, where 100 % stands for fully charged (commonly 4.2 V at cell level) and 0 % for a fully discharged (commonly 2.5 V at cell level) lithium-ion cell. The SOC visible in BEVs is usually slightly higher than the SOC definition commonly used during the development stage due to cell-to-cell drifts and range anxiety margins, which is why it is referred to as state of charge displayed in the user interface (UI-SOC) to clearly distinguish both quantities hereafter.

- **Resistance**
  The resistance R of a lithium-ion cell defines how the terminal voltage U evolves during a current excitation, originating in the previously described superposition of the individual overpotentials in the lithium-ion cell (Figure 1.4). If not otherwise noted, the internal resistance R is defined in this work as the ratio of the voltage drop ΔU to the applied current I over a specific time span Δt at $20\,^{\circ}$C, formally as

$$R_{1\mathrm{C},10\mathrm{s},50\%} = \frac{\Delta U}{I} = \frac{U_{\mathrm{t=10s}} - U_{\mathrm{t=0s}}}{I} \tag{1.4}$$

  as example for a $1\,$C current excitation for $10\,$s at 50 % SOC, whereas different current excitations I and different pulse durations Δt at different SOC levels can be applied, depending on the scope of consideration. The resistance R of a lithium-ion cell is often measured in mΩ and usually lies in a range of 0.1 mΩ (high capacity, large format cells) to 50 mΩ (low capacity, small format cells), depending on the cell material and format.

- **State of health (SOH)**
  The capacity and resistance of lithium-ion cells commonly change over the cycle life, often referred to as aging [40] or degradation [17] in the literature and discussed in more detail later on in Section 1.2. Both quantities are commonly tracked over the cycle life as the state of health (SOH) [41]. The capacity-related SOH, $\mathrm{SOH_C}$, and the resistance-related SOH, $\mathrm{SOH_R}$, are defined as

$$\mathrm{SOH_C} = \frac{Q}{Q_{\mathrm{initial}}} \qquad \mathrm{SOH_R} = \frac{R}{R_{\mathrm{initial}}} \tag{1.5}$$

  as a fraction of the actual capacity Q to the initial capacity Q_{initial} and the actual resistance R to the initial resistance R_{initial}, respectively. Both quantities are used with different definitions, depending on the aging-related capacity and resistance definition in the literature. Likewise, to the SOC the SOH is usually defined in %, where 100 % stands for a completely new and 0% for a failed lithium-ion cell or pack from a capacity-related SOH perspective. BEV manufacturers usually consider a $\mathrm{SOH_C}$ of below 70 % as a system, which cannot ensure safe operation anymore.

1.1.2 Materials, formats, and system architectures in electric vehicles

The fundamental principles of a lithium-ion cell can be put into practice using different electrode material combinations and geometrical formats. In the past, various electrode materials of lithium-ion cells have been discussed and deployed to optimize the trade-off between performance and costs of lithium-ion battery packs in automotive applications. As an example of the state of the art, Table 1.1 lists two mass-series BEVs and their lithium-ion battery pack specifications.

Lithium-ion cells currently used in BEV applications unite the use of carbon (C)-based anodes mainly relying on graphite, due to its beneficial properties and vast availability. Graphite profits from low irreversible capacity and low volume expansion, leading to a robust cycle life and good rate capability [42]. The volume expansion during lithiation is quite low compared to other materials with approx. 10% to its initial state [35], which allows for repetitive cycling without severe material fade. The rate capability can be enhanced by careful electrode design (loading,

Table 1.1: Volkswagen ID.3 1st edition and Tesla Model 3 Standard Range (SR) and their lithium-ion battery pack material, format, and system configuration used for the lithium-ion battery pack. Data originates from own observations and measurements of onsite-available vehicles.

Manufacturer	**Model**	**High-voltage lithium-ion battery pack**			
		Size	Cell material	Cell format	System architecture
Tesla	Model 3 SR	55 kWh	C/LFP	Prismatic	106s1p
Volkswagen	ID.3 Pro 1st edition	62 kWh	C/NMC	Pouch	108s2p

C: Carbon, NMC: Nickel manganese cobalt oxide, LFP: Lithium iron phosphate

thickness, and porosity of the electrode) to meet the required discharge rates in the automotive environment [43]. With the evolution of graphite as anode material in electrified automotive applications, R&D efforts were made to further optimize the energy density and performance. For example, the properties of graphite can be enhanced using synthesized or artificial graphite, which improves the cyclic performance of the lithium-ion cell [44]. Another and most recent option is adding silicon ($3579\,\mathrm{mAh\,g^{-1}}$) to graphite ($372\,\mathrm{mAh\,g^{-1}}$) to improve the overall energy density of the lithium-ion cells [42]. However, those advancements are rare in current BEVs, as prior work reported that the anode of a lithium-ion pouch cell from the Volkswagen ID.3 relies on graphite, most probably natural graphite due to its appearance, without any silicon content added [45].

At the cathode side, nickel cobalt aluminum oxide (NCA) was one of the most important early active materials, e.g., with its use in the first-generation mass-series Tesla Model S [46]. NCA cathodes benefit from their durability and, therefore, high rate capability and cycle life [47]. However, cyclic stability at large depth of discharge (DOD) operating windows had been reported to be poor [48], leading to fast capacity fade and resistance rise. Development pathways emerge to further decrease the cobalt content due to economic and environmental concerns by increasing the nickel content to further elevate the cyclic stability issues, which is why new material combinations are searched to improve the stability of Ni-rich NCA cells [49, 50].

Another prominent nickel-rich cathode material is seen in nickel manganese cobalt oxide (NMC), which is currently the most dominant cathode active material in BEVs [51]. Compared to NCA, NMC has almost the same specific capacity and raw material costs but slightly lower process costs [52], which renders NMC a more cost-effective material for automotive use cases. The trend to less use of cobalt and more use of nickel is also present here, leading to the development of Ni-rich NMC cells. Like NCA, the substitution of cobalt with more nickel is limited due to cyclic stability issues [53].

With the increasing awareness of economic and ethical concerns regarding the sourcing of cobalt, lithium iron phosphate (LFP) has been increasingly used as cathode material in mass-series BEVs, e.g., in the Tesla Model 3 SR (Table 1.1). LFP is inexpensive, abundant in nature, and has good cyclic stability without using cobalt [54]. On the downside, LFP suffers from a low energy density compared to NMC or NCA due to its flat lower potential at approximately $3.5\,\mathrm{V}$. In consequence, it is currently used in cost-sensitive vehicle segments with priority in high cycle life instead of high energy density [55].

Based on this brief overview of the different active materials currently deployed in automotive applications, it becomes apparent that no material is superior to another, and a co-existence of the various materials depending on the use case is the present scenario at the time of writing.

The various combinations of graphite-based anodes with NCA, NMC, or LFP cathodes can be realized using various packaging formats. Most prominently, these anode and cathode materials are countered to working lithium-ion cells within cylindrical, prismatic, or pouch cell designs. While the first two are contained within a solid aluminum envelope, the latter is sealed within a soft polymer bag. Similar to the active material use, there is still no consensus in industry and academia on which format may be superior to the others, which is why all formats are currently used in industrial practice depending on the individual applications.

To achieve the high energy and power densities required in automotive applications, many lithium-ion cells are connected in series and parallel. With a voltage range between 2.5–4.2V approximately 100 lithium-ion cells in series reach a common direct current (DC) voltage level of 400 V and, if doubled, a level of 800 V.

With many lithium-ion cells connected to larger systems reaching high voltage levels and large capacities, high charging power can be applied to quickly recharge the individual cells. Figure 1.5 shows an overview of the fast charging imes of available mass-series BEVs in the European market at the time of writing. While some manufacturers reach charging times as low as 18 min for a fast charge between 10–80 % SOC, other manufactures double or even triple these numbers. Apparently, fast charging of energy-dense battery packs poses technical challenges across all cell materials and segments, which must overcome by advanced fast charging strategies.

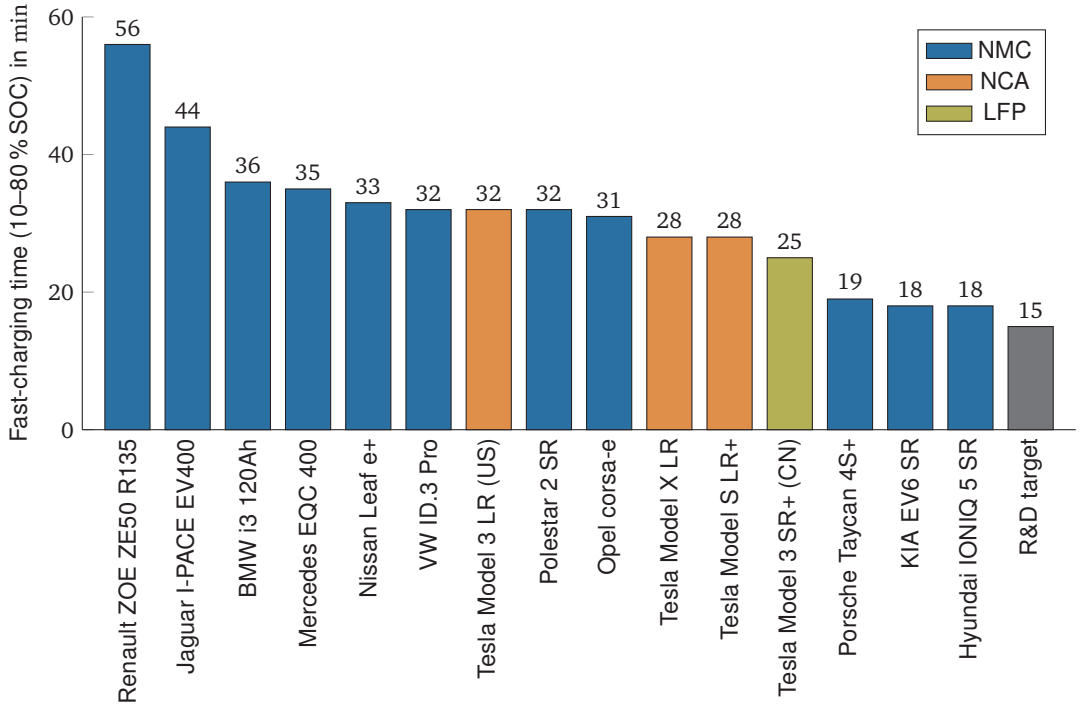

Figure 1.5: Fast charging time (10–80 % SOC) of an excerpt of available mass-series BEVs in the European market. Data is based on prior work [57]. The illustrated R&D target is based on the declared fast charging time target of less than 15 min between 10–80 % until 2028 by the United States Department of Energy (DOE) [14] and the similar fast charging target of 3.5 C between 0–80 % until 2030 by the European Council for Automotive Research and Development (EUCAR) [15].

1.1.3 Fast charging strategies of state-of-the-art electric vehicles

The capability to fast-charge lithium-ion battery packs is imperative to reach shorter charging times. In the most straightforward and customary manner, lithium-ion battery packs are charged with constant power and the charging power can be increased to reach faster charging times. Unfortunately, this approach comes at the cost of an early failure of the lithium-ion battery pack, as increasing the charging power leads to harsh conditions and accelerates aging, as explained in more detail below, in Section 1.2.1. Therefore, BEVs manufacturers pursue advanced strategies for current control during fast-charging events.

Figure 1.6 shows fast charging events starting at $0\,\%$ UI-SOC for two BEVs with strategies strictly differing from common constant power (CP) control principles. For example, the Volkswagen ID.3 Pro 1st edition (NMC) reaches its peak fast charging power of $100\,$kW after a few seconds, followed by a rapidly declining charging power until a constant current (CC) control plateau at approximately $70\,\%$ SOC. The CC sequence is held until a SOC of around $80\,\%$. Note that the UI-SOC generally differs to the true SOC, as the UI-SOC includes cell-to-cell drifts and/or range anxiety safety margins.

Likewise, the Tesla Model 3 SR (LFP) follows a similar strategy of an upfront larger charging current, but almost doubling the charging current. Once reaching a CP level of approximately $165\,$kW after a few seconds limiting the maximum fast charging power, the fast charging current is transiently, almost linearly, declining to $80\,\%$ SOC. Due to the flat voltage plateau of the LFP lithium-ion cells, the slope of the power and the current follow a similar pattern at this stage. In contrast to the VW ID.3 Pro 1th edition, no CC stage is reached during the fast-charging event and the current is controlled in a transient manner to $80\,\%$ SOC.

The control variables of these strategies can only be hypothesized without in-depth knowledge of the manufacturer's control strategies, which were not publicly shared. It can be assumed that the initial CP sequence is set due to the limited power capability of the high-voltage bus as power losses are proportional to the charging current, according to $P = R \cdot I^2$, which is likely to fast exceed the thermal limits of $400\,$V architecture components at these continuous current rates. For the transient current sequence of both vehicles, it is assumed that an advanced strategy must control the charging current (here, most likely by analytical functions or look-up tables due to the low computational effort) as no other measurable signal is held constant during the transient current control sequence, such as power, voltage, or temperature. The unique terminating CC sequence of the VW ID.3 1st edition may be set because the lithium-ion cell's maximum CC charging rate limit may be reached.

The fast charging strategies of both vehicles have in common that they rely on advanced control principles, such as the definition of triggering conditions for control inflection points (e.g., CP to transient current control or CC sequences) and the definition of the transient current control sequence. These must be identified during the development stage. The implications of fast charging for lithium-ion cells are discussed below, for a sound understanding of the mechanisms behind these advanced current control strategies.

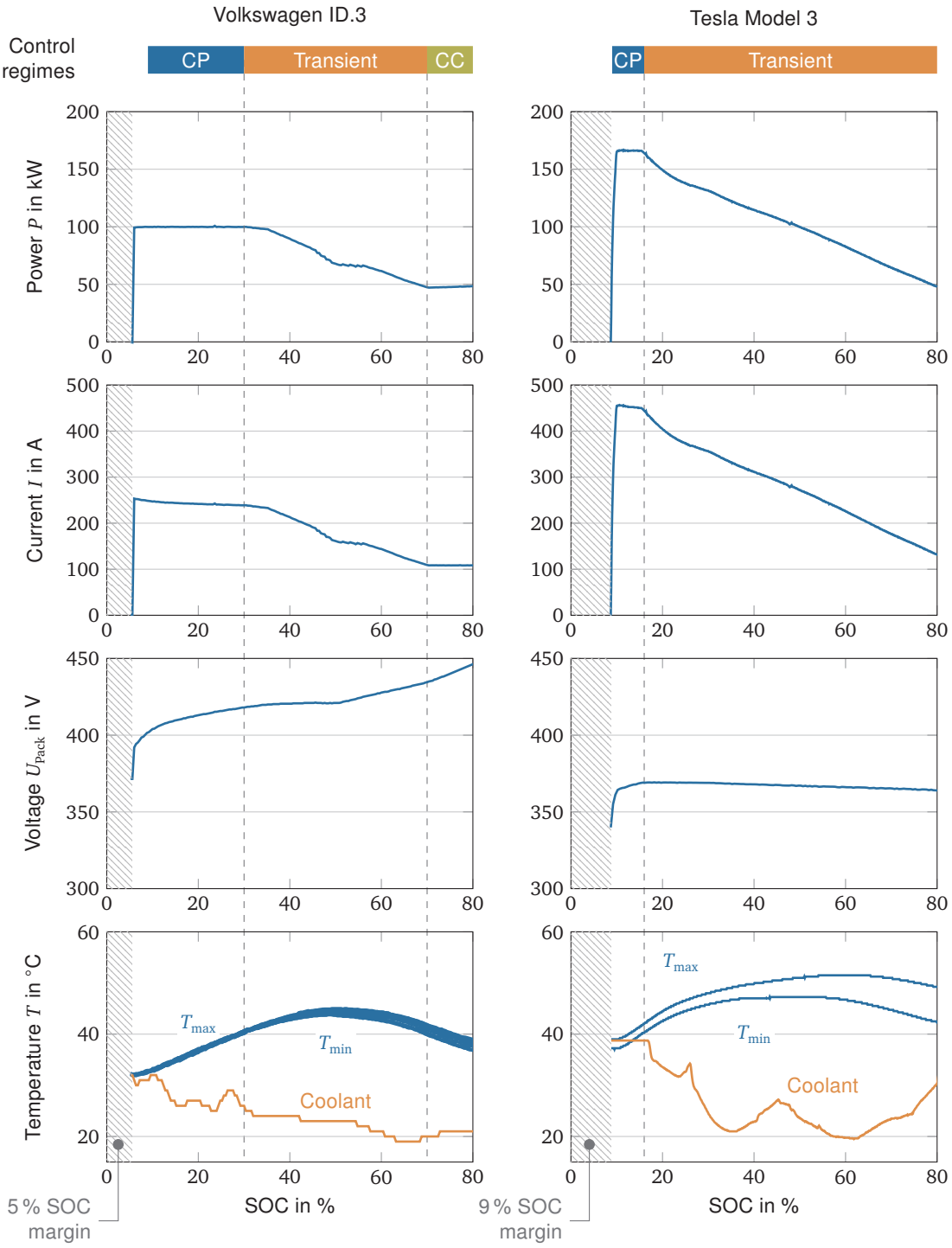

Figure 1.6: Fast charging events (starting at 0 % UI-SOC) of a Volkswagen ID.3 Pro 1st edition (NMC) and a Tesla Model 3 SR (LFP). (a) Charging power P, (b) current I, (c) voltages $U_{\text{cell}}/U_{\text{pack}}$, and (d) minimum and maximum temperature $T_{\text{min}}/T_{\text{max}}$ of the lithium-ion cells and pack. Expected control regimes are annotated on top of each group of sequences. Note that the shown SOC represents the actual SOC, which differs from the UI-SOC. The data displayed is recorded during a preconditioned fast-charging event of a Volkswagen ID.3 Pro 1st edition and Tesla Model 3 SR reproduced from prior work [58–60] and data acquisition [61].

1.2 Implications of fast charging for lithium-ion cells

Theoretically and ideally, lithium-ion cells can be fast charged by increasing the charging current to reach the desired fast charging time. In reality, increasing the charging current leads to declining performance of the lithium-ion cells, known as aging [40] or degradation [17], in turn, leading to a rapid reach of the end of life (EOL). The diminishing performance is commonly observable in a capacity loss, i.e., loss of range of a BEV, and resistance increase, i.e., loss of power capability of the BEV, which is usually a jointly observed phenomenon [62]. Most critical, the aging rate is not proportional to the applied charging current rate, as aging processes may self-amplify at a certain point, leading to a rapid failure of the lithium-ion cell or pack, commonly described as, e.g., rollover [63], knee [64, 65], or nonlinear aging [66–70]. Since the latter is the more frequently used terminology in the literature, it is used in the remainder of this work.

Figure 1.7 provides experimental data, which shows that increasing the charging rate with conventional CC charging principles leads to a rapid loss of available capacity and a steep increase in resistance. Whilst the trend is linear in the initial phase, a transition appears after a specific charge throughput or cycling in which the aging trend becomes nonlinear and self-reinforcing for the cell charged with 1.5 C. The lithium-ion cell rapidly reaches a capacity decay of $30\,\%$ to a remaining SOH of $70\,\%$, which is a common EOL and warranty criterion by BEV manufacturers.

In the following, implications for applying fast charging currents to lithium-ion cells are outlined by summarizing the main mechanisms limiting the fast charging current and—if these limits are not obeyed—leading to in-operation and safety-critical aging of the lithium-ion cells (Section 1.2.1). Metallic lithium deposition as the most critical aging mechanism, commonly known as *lithium plating*, is introduced (Section 1.2.2) and its influencing factors are summarized (Section 1.2.3), to derive requirements for thorough battery management (Section 1.2.4).

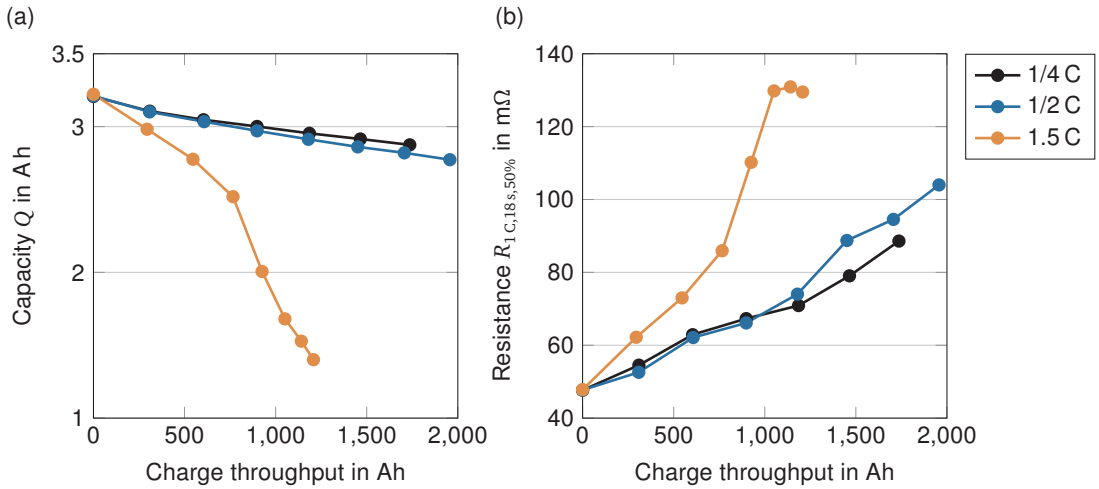

Figure 1.7: Capacity fade over charge throughput of a 3.2 Ah C/NCA lithium-ion cell (Sanyo 18650 BL) during charging with increasing C-rate beyond the manufacturer datasheet limits [71]. The lithium-ion cells were repeatedly discharged with 1 C to 2.5 V and charged with $1/4$ C, $1/2$ C, and 1.5 C. The manufacturer charging current limit is specified as $1/2$ C in the data sheet.

1.2.1 Rate-dependent aging mechanisms

The aging mechanisms behind the capacity loss and resistance rise of lithium-ion cells are manifold and complex, as most are closely intertwined and hard to track down in practice. A brief excerpt of the rate-dependent aging mechanism, leading to severe capacity loss and resistance rise during fast charging, is given in the following. For a general overview of all identified aging mechanisms during the regular cycling of lithium-ion cells, the reader is referred to a thorough review of Birkl et al. [17].

Historically, rate-dependent aging mechanisms have been intensively investigated for the anode because intercalation kinetics has been reported to be more critical than deintercalation kinetics from the cathode [72, 73]. Following this argumentation and the earlier work of Schindler et al. [74], three major aging mechanisms are reported in the literature, which should be avoided or inhibited if fast charging strategies are to be designed.

- **Lithium plating and dendrite formation**
  As lithium intercalation into the graphite is a diffusion-limited process, only a fraction of available lithium ions can intercalate into the host material at a time. If charging currents rise and solid-state transport kinetics are slower than lithium ions available for intercalation, lithium can plate as lithium metal on the graphite surface [75, 76]. Aging mechanisms inhibiting the lithium intercalation increase the likelihood of metallic lithium deposition [77].
- **Particle cracking**
  Particle cracking may be critical as severe cracks may cause exposure of the anode surface, additional solid electrolyte interphase (SEI) growth, and a loss of electrically connected active material participating in the charging process [78, 79]. Indirectly, particle cracking at the cathode may also arise, leading to transition metal dissolution, which may diffuse through the separator layer and foster SEI growth at the anode, especially for NMC cathode materials [53, 80]. Particle cracking is associated with increasing charging currents, as high currents lead to inhomogeneous stress to the electrodes, which may cause the particle to fracture [81]. While this occurs due to the natural volume expansion of graphite during lithium intercalation at the anode, it may be a particularly strong case for doped graphite anodes, e.g., with silicon with a particle volume expansion from 300 % [82] to 400 % [83] relative to its initial state. High-temperature gradients may foster inhomogeneous stress [84].
- **Electrolyte decomposition and depletion**
  Electrolyte decomposition describes the parasitic consumption of electrolytes due to potential or temperature exceedance, leading to the accelerated formation of electrode surface films, such as SEI on the anode [85], and gas evolution [86]. Electrolyte decomposition is accelerated by poorly passivated lithium deposits [87] or elevated temperatures [88], usually present during fast charging. The consumption of electrolytes has been seen as a major limitation during fast charging, in a later stage of life, if lithium deposition is avoided [89]. Moreover, lithium concentration gradients are established throughout the liquid phase at high charge rates, which

may lead to a salt depletion at the negative electrode in the worst case, rendering former active material sites inactive [25, 90].

The appearance of nonlinear aging strictly depends on the occurrence of a manifold combination of the various aging mechanisms during fast charging. Recently, Attia et al. [65] provided an in-depth review of the complex origins of nonlinear aging, linking the observable nonlinear capacity fade to a combination of different aging mechanisms and modes known from the state of the art. While many different pathways exist, lithium plating has been linked to all paths resulting in nonlinear aging. It is—as an anode-centered mechanism—associated with the charging of lithium-ion cells. Consequently, lithium plating at the anode is focused on within this work and further assessed, while the others are kept in mind for later analysis of experimentally aged lithium-ion cells.

1.2.2 Lithium plating mechanism

Lithium plating is a parasitic process describing the loss of available lithium for charge transfer by the metallic deposition of lithium ions on the anode surface, as illustrated in Figure 1.8. Lithium plating occurs if lithium-ion cells are charged under harsh conditions. With increasing charging current, the charge acceptance of the graphite anode material is constrained. Limited solid diffusion in the graphite particles may lead to surface concentration saturation [91]. Also, limited charge transfer in the solid phase can constrain lithium intercalation [92]. In both cases, lithium plating is thermodynamically favored against the lithium intercalation reaction into the graphite host structure.

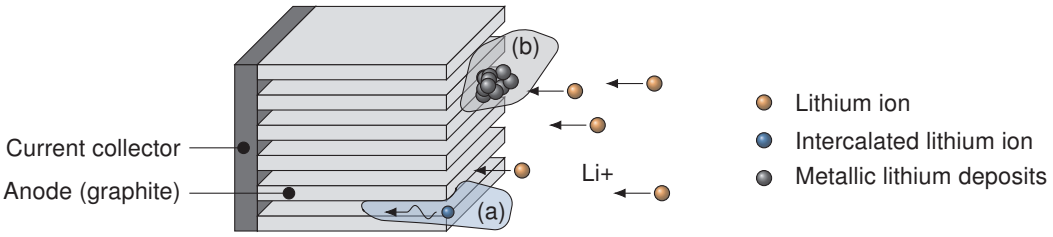

Figure 1.8: Simplified illustration of lithium plating at the anode surface. (a) Regular lithium intercalation into the graphite host structure during charging, (b) limited lithium intercalation, accumulating lithium ions, and the onset of metallic lithium deposition as a consequence.

Lithium plating has been reported to be triggered on the basis of different hypotheses. Most prominently, lithium plating has been reported to occur when the anode potential drops below $0\,\mathrm{V}$ vs. Li/Li+ [93]. Figure 1.9 shows the relationship between the anode potential and lithium plating. During a fast charge, the anode potential ϕ_{OCP}^{-} may reach negative potentials, which thermodynamically favors lithium plating in theory. The onset of lithium plating at negative anode potentials has been widely investigated and proven in the past by various techniques [92, 94]. However, experimental studies showed that graphite tolerates negative potentials at short time spans without the onset of metallic lithium deposits [95–97]. Gao et al. [91] reported that with a closer look at the lithium-ion cell dynamics, the potential criterion is only a necessary condition for the onset of lithium plating but not a sufficient one. However, both criteria are linked via the influence of concentration gradients on cell kinetics and, thus, local potentials [96]. Consequently, the voltage criterion is preferred in the literature because it also captures non-concentration-driven effects [92].

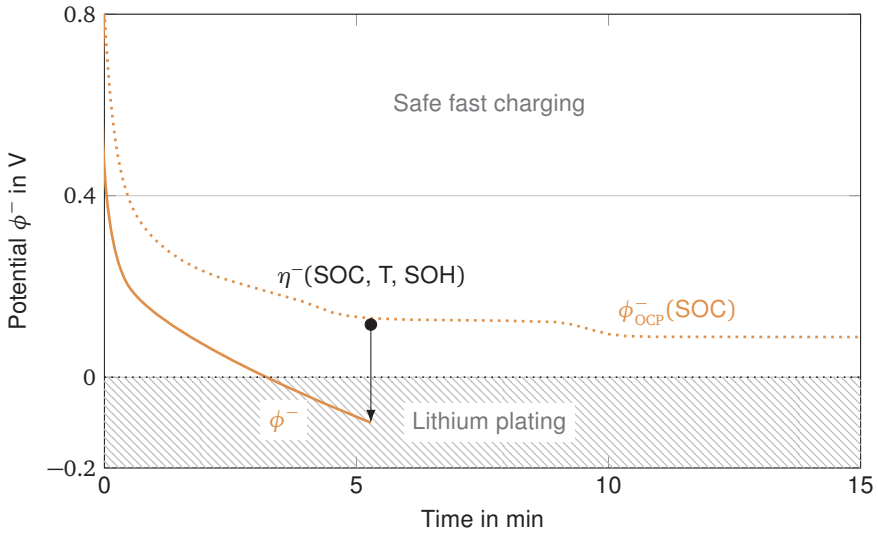

Figure 1.9: Anode potential over time during charging with respect to critical negative anode potentials thermodynamically favoring lithium plating at the anode surface.

In real-world applications, electrode current stress is inhomogeneous due to production scattering or varying local electrode conditions during operation [98]. Lithium plating is, therefore, most likely to occur locally at specific spots onto the anode layer within a lithium-ion cell.

Once lithium plating occurs, it can be reversed by either a rest period or a subsequent discharge of the lithium-ion cell [99]. This reversible process is also known as *lithium stripping* [100]. During rest, the metallic lithium deposits with an electrically conductive connection to the anode surface reintercalate to the graphite structure while the concentration at the interface drops. During discharge, they undergo a charge transfer reaction into the electrolyte and participate in the charge transfer again.

Although lithium plating is theoretically reversible, metallic lithium deposits grow over time in a dendrite-shaped pattern, which may electrically isolate by missing its conductive connection to the graphite structure and further passivate by secondary SEI growth [101]. While dendrites of metallic lithium may pierce the separator and induce a short-circuit within the cell leading to a thermal runaway, the contained lithium in isolated deposits is no longer available for change transfer. Consequently, the lithium-ion cell's capacity fades and the resistance rises—an irreversible process that should be avoided at all cost during operation.

1.2.3 Factors influencing lithium plating

Phenomenologically, multiple factors influence the occurrence of lithium plating. The previous section introduced the link between metallic lithium deposition and anode potential, with negative anode potentials leading to lithium plating. If the slope of the anode OCP in Figure 1.3 is superimposed by an overvoltage during charging, as shown in Figure 1.9, negative anode potentials can be easily reached during charging. Consequently, all lithium-ion cell conditions influencing the anode potential during operation may limit the maximum charging current: the SOC, the temperature, and the SOH. Figure 1.10 illustrates this causality for each factor.

High SOC regions increase the likelihood of lithium deposition during charging. With increasing lithiation of the anode during charging, the anode OCP is steadily lowered in the already narrow

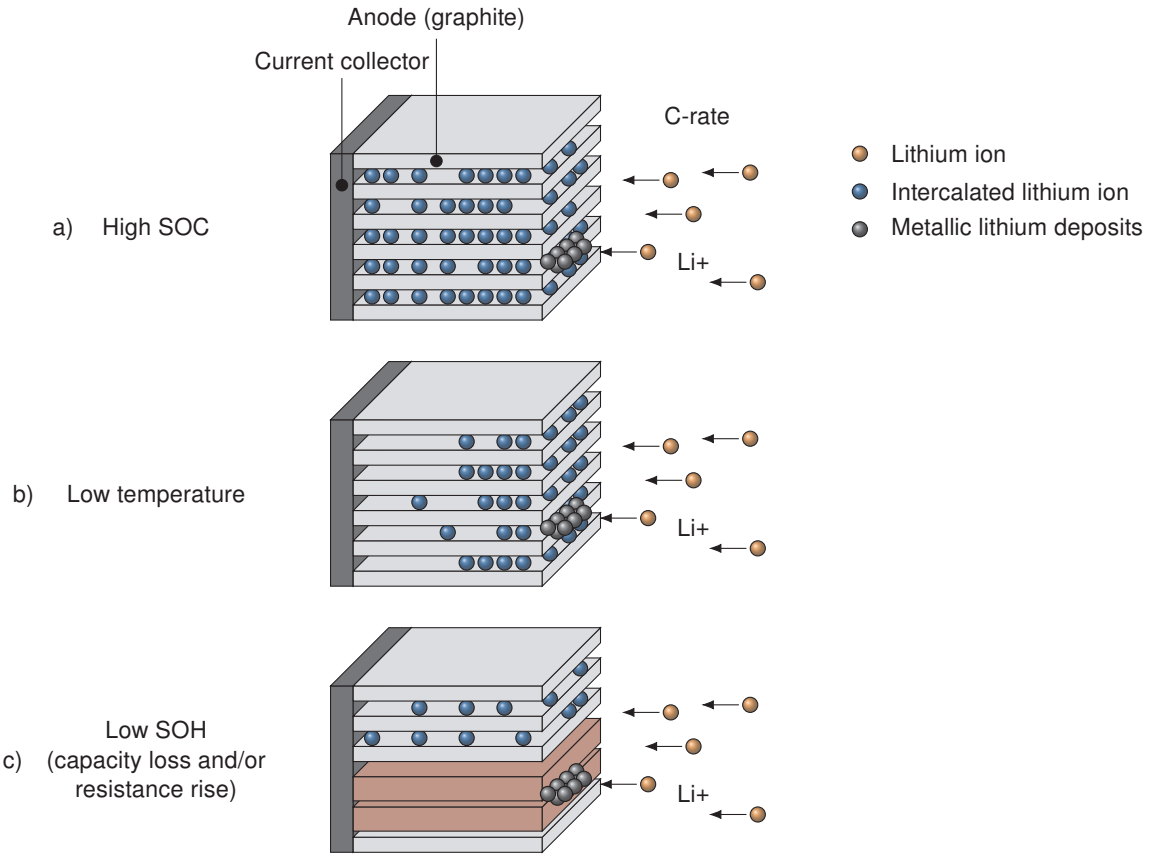

Figure 1.10: Operating conditions as factors limiting the charging current or provoking lithium plating during charging of lithium-ion cells. Following the causality of lithium plating, theoretically relying on negative anode potentials [93], the changing factors during operation, that is, (a) the SOC, the (b) temperature, and the (c) SOH, are limiting the fast-charging current.

range of up to 800 mV in the operating voltage range of the lithium-ion cell. With increasing OCP, also the overpotential increases due to the lowered diffusion with fewer vacant sites for lithium-ion intercalation [102, 103], as shown in a simplified form in Figure 1.10(a).

Likewise, low cell temperatures increase the risk of lithium plating during charging. Lowered solid-state kinetics within the graphite particles is hampered at low temperatures [104], leading to an agglomeration of lithium at the particle surface. Similar to a locally high SOC, as shown in Figure 1.10(b), lithium intercalation is inhibited, which lowers the anode potential.

Over operating time, aging most dominantly manifests as a growth of SEI at the anode during regular BEV operation [105], resulting in a capacity fade due to a loss of lithium inventory and a resistance rise at the particle surface of the graphite. Likewise, this SEI thickness and resistance increase elevate the anode overpotential, as lithium intercalation faces additional resistance, as shown in Figure 1.10(c), again increasing the risk of lithium plating. Similar, aging mechanisms triggering a capacity loss, may amplify the current density at the remaining vacant sites, leading to an overpotential rise.

The factors leading to lithium plating during operation are complex and closely intertwined. Moreover, if lithium plating is to be avoided, all factors must be considered, and the current properly controlled at the application level, in a pragmatic and feasible manner.

1.2.4 Requirements for the fast charging control strategy

The onset of non-linear aging due to lithium plating and all factors causing the onset must be prevented by adjusting the charging current through physics-motivated battery management during operation. Battery management systems (BMSs) are deployed to fulfill this task and ensure safe and sustainable operation during the usage of BEVs [106]. A function controlling the charging current at the edge of the physical limits of lithium-ion cells, from now on referred to as *fast charging control strategy*, is needed and meets the following requirements:

1. **Prevent the onset of nonlinear aging.**
   The onset of non-linear aging by, e.g., lithium plating, and all factors causing the onset, need to be prevented by adjusting the charging current through a physics-informed fast charging strategy.
2. **Maximize accuracy while minimizing time and resource effort.**
   Fast charging strategies must be highly accurate while requiring minimal time and resource effort during development. A reasonable balance must be found to maintain effectiveness while leveraging the method's potential for use in cost-sensitive automotive environments.
3. **Enabling flexibility to different cell materials and formats.**
   Lithium-ion cell materials and formats are frequently subject to change due to material innovations, material availability, or cost targets in different segments. The changing parameters of the design strategies must be easily transferable to the fast charging strategy so that the lithium-ion cell design can be diversified without having to repeat the entire development procedure multiple times.
4. **Adapt to the conditions present in the lithium-ion cell.**
   Many influencing factors change during the operation and must be considered in the fast charging strategy. The fast charging strategy must adapt to these changes to hedge against unintended critical fast-charging events.
5. **Extrapolate to all operating conditions.**
   The fast charging control strategy must be able to extrapolate accurately as not all operating conditions can be tested with reasonable time and resource effort in the laboratory.

Based on these requirements, the different methods to detect, predict, and prevent the onset or trigger conditions of lithium plating are summarized and discussed in the following.

1.3 Detection of lithium plating

Ideally, the online detection and quantification of the onset of lithium deposition during operation could enable the adjustment of the fast charging current and the prevention of severe capacity loss. Several methods have been reported in the past, which can be classified into two categories:

- Methods based on advanced sensing capability.
- Methods based on conventional sensing capability.

Methods based on advanced sensing include techniques to track down the occurrence of metallic lithium deposits by, e.g., optical or electron microscopy. In general, these methods need advanced sensing devices. They are partly invasive as the lithium-ion cell under study must be opened, and laboratory samples must be derived for the assessment. These methods are mainly used to understand the basic principles of the lithium deposition mechanism, i.e., their quantification, localization, and morphology. However, they can also indicate a recent lithium plating occurrence during the practical operation of a cell by *post-mortem* investigation.

Methods based on conventional sensing involve techniques for which lithium plating is measurable on other signals, which enables observability of the original lithium plating mechanism. These methods can be applied to lithium-ion cells during operation by evaluating the conventional current, voltage, or temperature signals.

In the following, the identified relevant methods are outlined (Section 1.3.1) and their implications critically discussed (Section 1.3.2).

1.3.1 Methods

Table 1.2 provides an overview of commonly used methods to detect the onset of lithium plating. The available methods are briefly introduced in the following.

Table 1.2: Overview of methods to detect lithium deposition. Methods are clustered according to their invasive or non-invasive nature, based on a previous literature study [107].

Category	Name	References
Methods based on advanced sensing Require additional measurement devices, cell modifications, and/or *post mortem* samples.	Optical microscopy	[108–111]
	Scanning electron microscopy (SEM)	[96, 108]
	Transmission electron microscopy	[111]
	X-ray microscopy	[112]
	Glow-discharge optical emission spectroscopy	[113, 114]
	Nuclear magnetic resonance	[115]
	Electron paramagnetic resonance	[116]
	Raman spectroscopy	[117]
	Neutron diffraction	[118]
	Reference electrode	[119–121]
	Dilatation tracking	[122, 123]
Methods based on conventional sensing Require improved accuracy, resolution, or sampling of conventional signals (U, I, T).	High precision coulometry	[109, 124]
	Differential voltage- & incremental capacity analysis (DVA/ICA)	[125, 126]
	Stripping discharge	[127–131]
	Voltage relaxation	[96, 130, 132]
	Calorimetry	[133, 134]
	Electrochemical impedance spectroscopy (EIS)	[132, 135]

Within the group of methods based on advanced sensing, optical microscopy is one of the oldest and frequently used techniques [111]. With this, a lithium-ion cell is discharged, opened in an argon-filled glove box, and the anode electrode layer is isolated and imaged, as seen in Figure 1.11. Areas with lithium plating residuals can be identified by their glossy light-gray color on the dark-gray graphite surface [109]. The nature of this method limits the informative value concerning the morphology and quantification of the metallic lithium deposits. A higher resolution with more ground for a detailed morphology analysis can be achieved by applying scanning electron microscopy (SEM), which uses electron beams to visualize metallic lithium

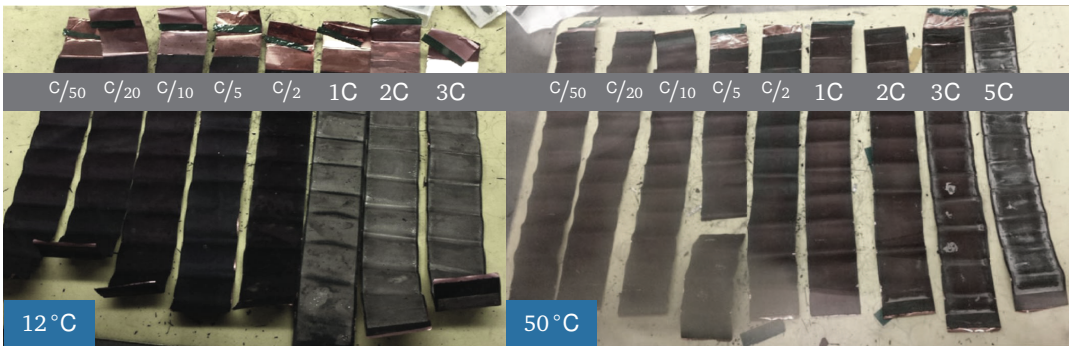

Figure 1.11: *Post-mortem* images of a graphite anode cycled with different charging C-rates at (left) 12 °C and (right) 50 °C ambient temperature and opened under Argon atmosphere reproduced and modified from Burns et al. [109]. Lithium plating can be identified as a light-colored coating onto the gray graphite electrode (*cf.* 1C–3C at 12 °C), which does not occur if higher temperatures are applied.

deposits as a mossy, net-like structure on the active material [96]. Since lithium dendrites are destroyed during the anode layer isolation from the separator, this method only indicates residues of the lithium plating [96]. A combination with energy-dispersive X-ray analysis to quantify the amount of deposited metallic lithium is impossible due to the insensitivity of the method to light elements such as lithium [114]. Further improved resolution but also increased complexity can be reached by applying transmission electron microscopy, X-ray microscopy, or glow-discharge optical emission spectroscopy. However, this also necessitates the production of more complex laboratory samples, a smaller field of view, and increased likelihood for artifacts in the measurement signal [111]. An even more precise detection can be achieved by nuclear magnetic resonance or electron paramagnetic resonance, in which a frequency offset due to metallic lithium is detected in a high-frequency magnetic field applied to a specific sample. Wandt et al. [116] successfully applied electron paramagnetic resonance to quantify and time-resolve the occurrence of lithium plating in laboratory samples. Also, neutron diffraction has been employed to monitor the onset of lithium plating, requiring a neutron source for the experiments [118]. In general, all methods above involve advanced sensing capability, which is beneficial for in-depth analysis of lithium plating mechanisms in fundamental science, but cannot be transferred to practical automotive applications.

A more practical and less resource-intensive way of tracking down the onset of lithium plating can be achieved by inserting an artificial reference electrode into the anode [119–121], as lithium plating can then be estimated by the anode potential drop below 0 V, which thermodynamically favors the reaction. Unfortunately, this approach is of an invasive nature, as the lithium-ion cell is opened, which changes the overall system properties and may lead to an overpotential overestimation of the anode [136].

Another practical approach has been seen in measuring the mechanical dilatation of lithium-ion cells. During lithiation, the graphite undergoes a reversible volume expansion, which dominates the dilation behavior of the cell [122]. If lithium plating takes place, a sudden irreversible rise of dilatation occurs, which can be measured, e.g., with a gauge in the study of Bitzer et al. [122]. Rieger et al. [137] built upon this study and extended the measurement setup by a localized laser scanning device to measure the dilatation spatial- and time-resolved during lithium plating. Other studies of the same group used this method to associate the onset of non-linear aging with an irreversible local dilatation of the cell [138] and to determine maximum charging currents

based on these results [139]. Precise dilatation measurement devices are required to apply this method, devices which are usually unavailable in automotive applications.

In contrast, methods based on conventional sensing, i.e., current-, voltage-, and temperature signals, have been frequently reported to track down lithium plating in lithium-ion cells.

High precision coulometry has been increasingly used for lithium plating detection, mainly by Dahn's group [109]. It is based on the principle that the charge and discharge capacity must result in efficiency above approximately 99 %. Otherwise, side reactions such as lithium plating take place and consume the available lithium for charge transfer. If lithium plating occurs, the charge capacity does not match the discharge capacity drawn from the battery. To apply this detection method, a high current measurement accuracy of around $\pm 0.02\% + 200\,\mathrm{nA}$ is needed [134], which is only possible with dedicated and precise measurement equipment and the investigated lithium-ion cell placed in isothermal ambient environments [124].

Besides, also differential voltage analysis (DVA) is intensively used to track down different aging modes. Here, a slow charge or discharge sequence is performed, and the voltage signal is differentiated to the charge throughput according to

$$\frac{dU}{dQ} = \frac{dU}{dt} \cdot \frac{dt}{dQ} = \frac{dU}{dt} \cdot I^{-1} \tag{1.6}$$

with the voltage U, the charge throughput Q, time t, and the applied current I [107]. Characteristic peaks can be found in the DVA and associated with the individual electrodes, as flat two-phase regions show up as minima, and steep phase transitions show up as maxima [140–142]. Therefore, anode-related aging mechanisms, such as lithium plating, can be qualitatively detected. Likewise, the reciprocal of the DVA is used defined as the incremental capacity analysis (ICA). The inverse minima/maxima behavior is observable based on the same physical principle. Multiple studies linked the onset of lithium plating to a declining anode-related minimum [125] or turning point of the anode-related maxima growth with cycles [126]. Unfortunately, charge or discharge sequences over the entire SOC window are rarely found in practice [143], which hampers their use in practical applications.

Another prominently used technique is devised by analyzing the voltage relaxation after a charge sequence. Once lithium plating has occurred, lithium can partly reintercalate into the graphite host structure which leads to a potential superimposing of the overall cell voltage signal, observable as a mixed-potential [96]. Figure 1.12 shows a lithium-ion cell of a Volkswagen ID.3 1st edition (C/NMC) charged with 1C and increasing SOC-window, performed in a prior study [144], where a distinct voltage plateau can be observed in the voltage signal, with distinct minima in the differential voltage. With minima shifting to later relaxation times, the technique approximates the amount of deposited metallic lithium [130]. However, the reliability of this method is based on a high and precise sampling of the voltage signal for further differentiation, which is usually not possible due to the low sampling rates and low resolution of automotive BMSs in high-voltage lithium-ion battery packs.

Similar to the voltage relaxation, a mixed-potential voltage signal can be observed during slow discharge directly after a fast charge event, known as lithium stripping [100]. If the cell is discharged immediately after the occurrence of lithium plating, which is usually the case for automotive applications after a fast charge event, the oxidation of the lithium deposits is

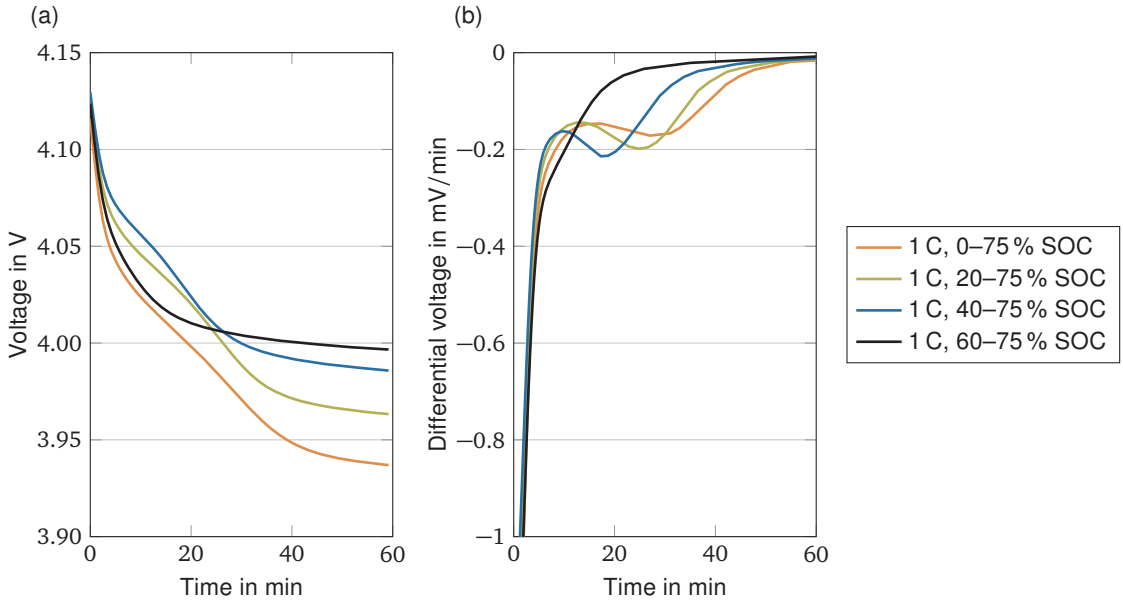

Figure 1.12: Indirect detection of the onset of lithium plating during a fast-charging sequence of a 78 Ah C/NMC lithium-ion pouch cell from a Volkswagen ID.3 at 0 °C ambient temperature [144]. With increasing charge throughput, a voltage plateau manifests in the subsequent relaxation sequence due to the lithium stripping mechanism (a), which could be used for the online detection of lithium plating by local minima identification of the differential voltage signal (b).

thermodynamically favored against the reintercalation into the graphite host structure leading to a superimposed voltage signal observable as a voltage plateau [145]. Multiple studies revealed the observability of lithium plating after a charge sequence at subzero temperatures [127, 128, 131]. In later studies, the quantification of the deposited metallic lithium was also shown to be quantifiable by evaluating the duration of the mixed potential [129, 130]. Campbell et al. [146] investigated how reliable lithium plating can be detected with this method regarding thermal influences as well as their unambiguity. The authors showed that lithium plating might occur even when it could not be detected in the voltage signal of the subsequent discharge, which was also assumed earlier by Waldmann et al. [75], questioning the reliability and practical implementation of this method. For further details, the reader is referred to the provided analysis within the studies mentioned.

Besides using the voltage signal, the thermal effect of lithium plating and their observability in the cell temperature signal have been investigated, known as calorimetry [133]. This method measures the energy produced from parasitic cell reactions to track down ongoing lithium plating processes. Downie et al. [134] observed a small endothermic response during the onset of lithium plating for C/NMC cells. The authors suggest that this thermal response could also be measurable in the thermal measurement signal of automotive larger-format lithium-ion cells. This has been confirmed by other studies, which applied a thermal sensor matrix to a large format pouch cell to localize the thermal gradient in the cell [147]. Even though this method is non-invasive, a precise isothermal calorimeter or susceptible temperature measurement device is required to accurately quantify the onset of lithium plating, whose reliability and practicality is questioned by other studies due to the multitude of cells used in automotive applications [145].

Electrochemical impedance spectroscopy (EIS) has also been used for lithium plating detection. Here, a sinusoidal voltage (potentiostatic EIS) or current profile (galvanostatic EIS) is imposed

on a lithium-ion cell under study, and the response is evaluated in the frequency domain. The individual curve sections to higher or lower frequencies are assigned to different cell effects in the literature [36]. Studies proved that characteristic frequency ranges correlate with lithium plating validated with voltage relaxation [132, 135] or *post-mortem* cell investigations [148]. However, to the best of the author's knowledge, there is yet no EIS-capable BMS in use in automotive applications.

1.3.2 Implications

All discussed methods based on advanced sensing offer the potential to conclusively identify and partly quantify the onset of lithium plating. However, these methods are unsuitable for online lithium plating identification during BEVs' operation due to their invasive nature or intensive resource demand. On the other hand, methods based on conventional measurement signals provide a more practical way to identify lithium plating during vehicle operation. This is achieved by tracking down the occurrence of lithium deposits through observations of secondary processes, i.e., lithium stripping, and the resulting mixed-potential observable in the voltage signal. However, these methods commonly rely on conventional sensing capability with high accuracy, resolution, and sampling, usually unavailable in automotive applications or unreliable under varying ambient conditions, which are known to differ broadly in automotive environments.

Following this comparison, it becomes apparent that no method exists to date, which enables a precise, reliable, and applicable online detection for the onset of lithium plating. Moreover, if the onset of lithium plating could be detected online by non-destructive methods, the irreversible part of the reaction has already manifested. It cannot be reversed, increasing the likelihood of further onsets in the subsequent fast charging event. Therefore, the onset of lithium plating has to be predicted in advance to avoid any acceleration of degradation and failure of the lithium-ion battery pack during fast charging events.

1.4 Prediction of lithium plating

Multiscale modeling of lithium-ion cells has been seen as a mandatory approach to tackle the problems associated with the detection of the critical aging mechanisms by predicting critical parameters of control and projecting them from the nanoscale (electrode level) to the macroscale (cell and pack level) [149]. This empowers the BMS to control the charge current, e.g., at the edge of the lithium plating process, which is quantifiable by anode potential predictions before lithium plating can physically occur. Lithium-ion cell models, often referred to as *digital twins*, enable this projection. A broad variety of modeling approaches exists, as visible in Figure 1.13.

In the following, the main methods of electrochemical modeling (Section 1.4.1), physics-enhanced equivalent circuit modeling (Section 1.4.2), and data-driven modeling (Section 1.4.3) are explained in more detail.

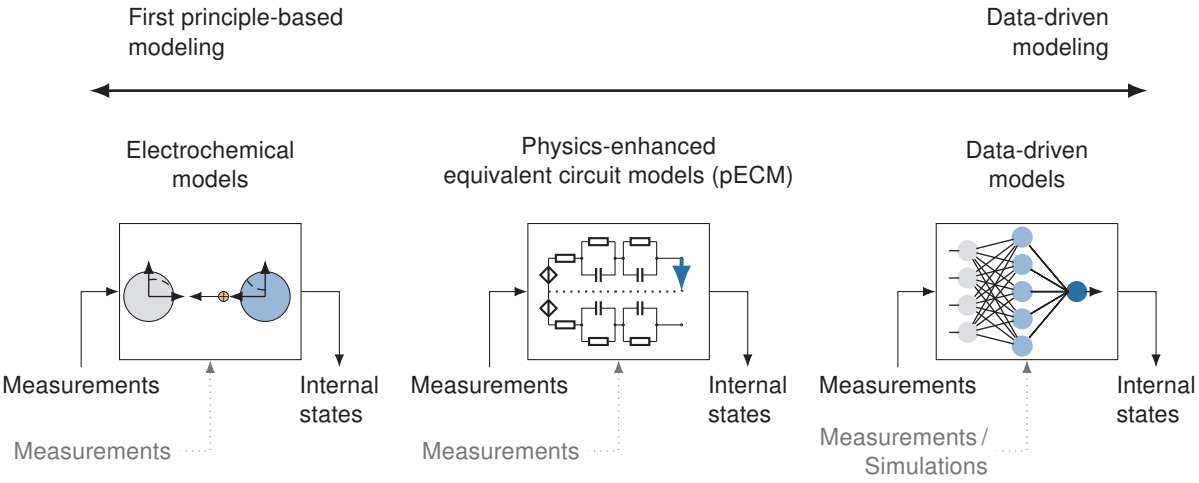

Figure 1.13: Multiscale modeling approaches of lithium-ion cells to predict critical control parameters and project them from the nanoscale to the macroscale. Many approaches exist, ranging from data-driven modeling, i.e., look-up tables or black-box models, to first principles modeling, i.e., describing the physical relations of the electrochemical reactions of lithium-ion cells.

1.4.1 Electrochemical modeling

One of the most popular modeling approaches lies in the pseudo-two-dimensional (P2D) electrochemical model originally developed by Doyle, Fuller, and Newmann [150]. Here, a lithium-ion cell is modeled based on coupled physical and electrochemical differential equations representing the material interactions within a lithium-ion cell. The porous structure of the lithium-ion cell is reduced to a one-dimensional problem across the different cell component layers. Additionally, a pseudo dimension in the radial direction is introduced to describe the solid-phase diffusion within the active material particles. Figure 1.14 shows a schematic view of the model. The spatial dimension across the porous layers is shown (x-dimension), and the radial dimension through the particle (r-dimension). The physical laws of this model are the theory of concentrated solutions and the theory of porous electrodes. The lithium-ion concentration can be calculated throughout the cell, which yields electrical potentials of the respective domains, which can then be summarized into a general cell voltage. For the sake of simplicity, a more detailed mathematical derivation is omitted at this point. The interested reader is referred to the original work in the dissertation of Doyle [151] or relevant literature in that field, e.g., Plett [152].

Due to its high accuracy and detailed representation of the internal electrochemical processes, the model has been used in multiple studies. For example, Sturm et al. [153] deployed a P2D for more accurate SOC estimation. Gao et al. [154] applied the P2D for co-estimating the SOC and SOH. A few studies investigated capacity fade during the use of lithium-ion cells coupling a P2D with an aging model [155, 156].

Other studies extended the P2D model in the two dimensions of the electrode layer to allow for enhanced spatial resolution within the cell. These models coupled multiple P2D models for a single lithium-ion cell which enables to account for the electrical and thermal inhomogeneities within lithium-ion cells. Furthermore, thermal models introducing a thermodynamic energy balance were added to allow for a coupled electrothermal simulation. The resulting models are used to investigate the impact of different tab designs [157–159] or study the current and thermal inhomogeneity of large format cells [159–161] to optimize cell design and thermal management

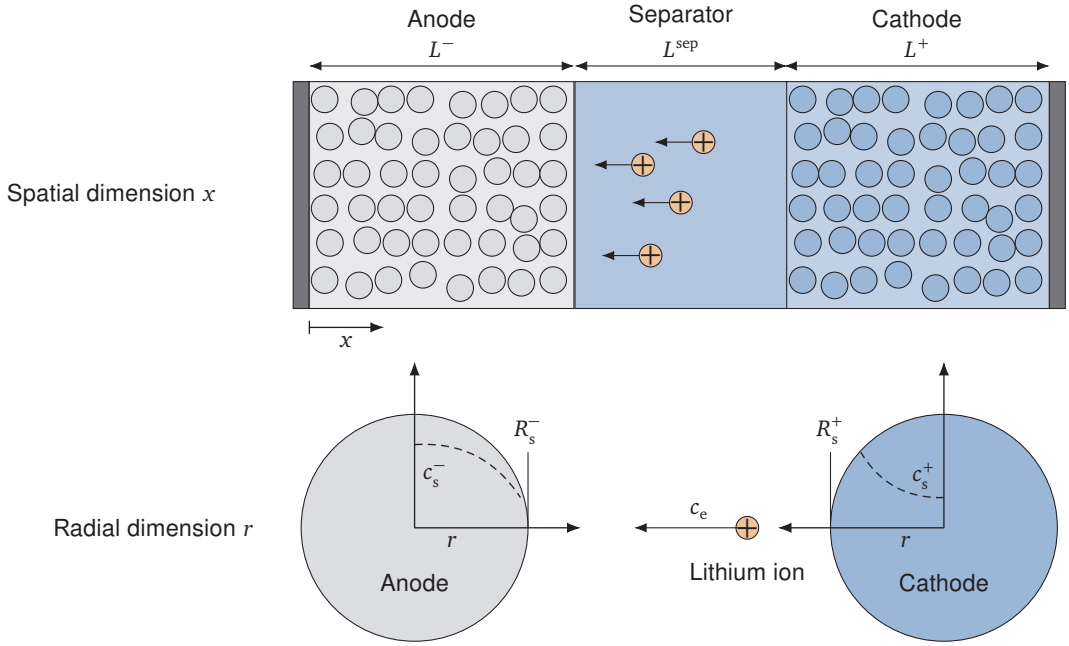

Figure 1.14: Schematics of the pseudo two-dimensional (P2D) lithium-ion cell model with the spatial dimension (x-dimension) and the pseudo radial dimension through the active material particles (r-dimension). The spatial dimension is captured by the layer thicknesses for the anode L_-, separator L_{sep}, and cathode L_+. The radial dimension is captured by the particle radii for the anode R_s^- and cathode R_s^+ with the lithium-ion concentrations c_s^-, c_e, c_s^+ in the respective solid (s) or electrolyte (e) domain.

interfaces. Despite their power, these models are computationally complex and hamper any downstream use in online applications.

With the rise of electrochemical models based on the originally developed P2D, the computational complexity limited their use for online battery management applications, as mentioned in multiple studies reviewing the state of the art [162–164]. Many authors proposed model-order reductions to reduce the computational effort but maintain sufficient accuracy. An excellent overview of state-of-the-art model-order reduction methods is presented by Ringbeck [165].

The single particle model (SPM) is a wide-spread model-order reduction of the original P2D model. It is assumed that the porous electrodes consist of uniform particles that are exposed to the same conditions, regardless of their location. As a result, the reactions on the particles are assumed to be homogeneous. By doing so, the complex electrode model can be simplified by using a single spherical particle, thus setting the particle count to one ($n_r = 1$). This reduces the complexity to only one numerical solution of a single particle in each material. The interested reader is referred to relevant literature discussing the derivation from the P2D in detail, e.g., in Plett [152].

The SPM was first mentioned by Ning and Popov [166], who introduced the model for aging analysis. Despite the computational improvements due to employing a single particle per electrode, computational complex differential equations are required for the diffusion phenomena in the solid and liquid phases. Therefore, many downstream studies investigated model-order reduction techniques to further ease the computational demand. Santhanagopalan et al. [167] used polynomials to approximate the solid-phase diffusion in the electrode models of the SPM. Guo et al. [168] applied an Eigenfunction expansion with similar motivation. Tanim et al. [169]

simplified the SPM using a quadratic polynomial function to model the electrolyte concentration across the anode, separator, and cathode. The results showed good agreement to high-fidelity P2D simulations. Similarly, Li et al. [170] applied second-order polynomial approximations for the electrolyte concentration across all layers mentioned earlier. Note that model-order reductions are likewise applicable with the high-fidelity P2D model; as such, applying the model-order reduction again to all simulated particles.

Consequently, electrochemical models of reduced order promise a high level of accuracy as they maintain the physical interpretability of the individual cell reactions, but still inherit implementation challenges due to their high computational power requirement.

1.4.2 Physics-enhanced equivalent circuit modeling

To further reduce the complexity of electrochemical and reduced-order models, physics-enhanced equivalent circuit models (pECMs) have been investigated to predict internal states while being solvable analytically without intensive parameter identification. In contrast to the previously introduced reduced-order models, they originate from the commonly applied approach to model the phenomenological electro-thermal behavior of lithium-ion cells, i.e., demanding a current input and providing a voltage output by a series of look-up tables and resistor/capacitor elements, but address their shortcomings of modeling cell level effects only by crafting two individual equivalent circuit models for each electrode.

Srbik et al. [171] first proposed such a model based on a complex network of equivalent circuits to mimic the characteristics of electrochemical models. In their study, three particles in each electrode and three spatial discretizations in the separator are modeled, parameterized with literature data, and validated against experimental data.

Merla et al. [172] extended this approach by providing a guideline for the parameter identification of these models using OCV determination techniques and EIS. Similar to Srbik et al. [171], the presented pECM depicts a complete replication of the individual electrode behavior following the electrochemical modeling approaches. Given the initial incentive to ease the modeling effort, several parameters still need to be determined with the presented approach. The authors, however, highlight the potential for the simulation of internal states if multiple lithium-ion cells must be considered because of their computational efficiency and stability.

This approach was further developed by authors such as Li et al. [173], who proposed a pECM relying on ordinary differential equations (ODEs) without algebraic constraints to enable fast computation in real-world implementations. The model has been tested against experimental data at different temperatures and aging states. Geng et al. [174] proposed a similar model but with further reduced modeling circuits focusing on electrode particle modeling.

Attempting further simplification, other authors reduced the remaining complexity of the multi-particle modeling to single electrode equivalent circuit networks, representing the electrode particle of the overall lithium-ion cell without any enhanced resolution of, e.g., spatial particle concentrations. As an example, Figure 1.15 illustrates the schematics of this model. These models still depend on the identification of electrode and cell-level parameters, but eliminate the use of many literature values whose accuracy cannot be guaranteed.

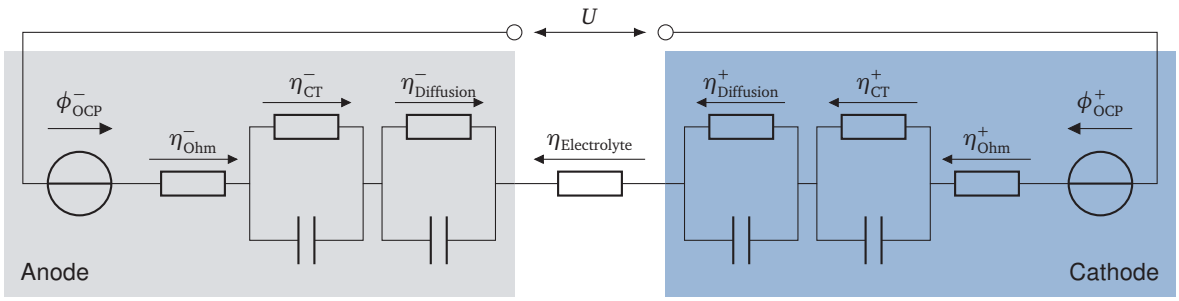

Figure 1.15: Schematics of a pECM lithium-ion cell model able to predict internal states while being computationally efficient with the compromise of reduced physical interpretability. Electrodes are modeled by a voltage source element to represent the electrode's OCP (ϕ_{OCP}) and a finite number of RC-elements to represent the electrode's dynamic behavior (ohmic resistance η_{Ohm}, charge transfer η_{CT}, diffusion $\eta_{Diffusion}$). Likewise, the electrolyte overpotential $\eta_{Electrolyte}$ can be added with equivalent circuit elements between both electrode submodels (here, as an ohmic resistance).

Drees et al. [175, 176] proposed such a simplified pECM for anode potential prediction by modeling the individual electrode with a series resistance and one RC-circuit dependent on the SOC and temperature, which were scaled for the use of larger cell formats. It was shown that these models could be parameterized with pseudo-open-circuit voltage (pOCV) and current pulse tests but still rely on three-electrode measurements to allow for insights into the electrode behavior. Zhao et al. [177] and Zhang et al. [178] extended this method by inserting a reference electrode into a pouch and a cylindrical lithium-ion cell, respectively.

While the model order reduction of pECMs allows for computational efficiency and lesser parameters to identify, the model loses physical interpretability and adaptability due to the approximation of the electrochemical cell behavior with equivalent circuits.

1.4.3 Data-driven modeling

A promising approach to handling the physical and computational complexity of the models mentioned earlier are data-based models. Here, measurements or simulations at the electrode level are used to train data-driven models and deploy them for internal state prediction.

Lin [179] first proposed a long short-term neural network capable of predicting the anode potential during different charging sequences. The model was trained with simulated data of a reduced-order electrochemical model. As such, four different discharge cycles and five different CC charging cycles were simulated to generate a broad training dataset. While the trained model showed good validity, the validation was carried out against the reduced-order electrochemical model response only, as experimental validation was out of scope in this study.

Based on the work of Lin [179], Hamar et al. [180] investigated three different regression models to evaluate their impact on the model's computational performance and accuracy for use in real-world applications. Likewise, high-fidelity P2D simulations were tested to train the models without further experimental validation of the trained data-driven model. It was shown that a trade-off exists between the yielded prediction accuracy and the amount of stored data, as the random forest method achieved the highest accuracy but also posed the most extensive data storage requirement.

Li et al. [181] extended the long short-term memory prediction to other battery internal states beyond the sole prediction of the anode potential. The model validation was extended to unknown ambient temperatures and different measurement noise levels, with maximum relative errors of below 2.9 %. Experimental validation was carried out for measurable states at the cell level but not for the electrode level.

Whilst only a few studies exist for internal state prediction of lithium-ion batteries with data-driven modeling, large datasets are needed for training, which can only be derived utilizing models of higher fidelity as experimental data, in general, is sparse. Furthermore, the complexity in modeling and parameter identification is shifted to complexity in choosing adequate model training techniques, as a broad variety of methods exists.

1.5 Research gaps

In conclusion, fast charging is strictly limited by the physical processes present in the lithium-ion battery system. These limits are specific to a given lithium-ion cell type and cannot be overcome without rapidly declining battery pack performance and the rise of safety-critical conditions. By nature of the detection methods, it is apparent that severe aging mechanisms have already occurred when they can be detected online during the BEV operation. However, the fast-charging current can be controlled by model-based state predictions to operate at these limits to minimize the charging time while prolonging the life of the battery system. To prevent high-voltage energy storage failures and dangerous safety-critical situations at an early stage, the anode potential must be predicted and controlled with model-based fast charging control functions by the BMS.

With the rise of the importance of fast charging in the automotive sector, many studies in the literature proposed methods to determine the fast charging limits. Therefore, this work seeks to give an overview of the different techniques and model usage to answer the question:

(1) *What are the remaining challenges in fast charging control?*

The key findings are used to derive a method in determine health-aware fast charging strategies and to overcome the identified remaining challenges. Electrochemical models of reduced order have a promising potential in upscaling lithium plating trigger conditions from the electrode level to the application level and allow for safe current control. Moreover, these models enable a fast transfer to various lithium-ion cell types, i.e., chemistries and formats, by adjusting changing parameters without requiring extensive experimental testing. In the literature, however, there is still no consensus on how to approach a given commercial lithium-ion cell to extract relevant single material-, geometrical- or electrode properties and parameters for modeling. Therefore, this work proposes an approach to extend the present state-of-the-art by answering the question:

(2) *How can lithium-ion cells be characterized to identify essential parameters for electrochemical modeling?*

With the derived parameters at hand, the subsequent step includes using them for electrochemical modeling. If the measurements and obtained parameters are added to an electrochemical model of reduced order, which inherits a given degree of abstraction, the model response may

strongly diverge from the complex real-world behavior of the lithium-ion cell or system. As many effects are interdependent, it is difficult to isolate the origin of the error if the parameter identification procedure should be kept lean. It is, therefore, essential to balance the required measurements and precision at the electrode level and the necessary effects at the cell or system level. This work proposes a novel hybrid model parameter identification method as expressed by the question:

(3) *How can electrochemical models be systematically parameterized for fast charging control?*

The developed model can now mimic the behavior of the lithium-ion cell or system while giving access to control quantities at the electrode level. It is still unclear how the crafted and validated model can be transferred from theory to a health-aware fast charging strategy applicable to a real-world laboratory environment. Extensive cycle life studies are sparse but relevant to provide a proof-of-concept of the strategy. Also, the remaining aging mechanism occurring if lithium-ion cells are fast charged repeatedly, are not well understood. To shed light onto the penciled procedure and missing insights, the following question is answered:

(4) *How to deploy electrochemical models for health-aware fast charging control and which aging mechanism do occur?*

Finally, the results in a controlled laboratory environment must be upscaled to harsh application environments. Here, the serial and parallel connection of many lithium-ion cells poses additional disturbances due to their electrical contact resistances. It still needs to be understood entirely how electrical contact resistance may interfere with lithium-ion cells in test and real-world applications, in particular, if larger currents are applied. Consequently, the following question is raised:

(5) *How do electrical contacts in lithium-ion battery packs influence lithium-ion cell performance during fast charging?*

1.6 Outline

Based on the research gaps, Chapter 2 and the core contributions of this work is structured as shown in Figure 1.16 and are outlined in the paragraphs below.

Section 2.1 presents a clustering of existing methods to determine fast charging strategies for battery management systems in the literature. All studies are compared and critically discussed. The remaining research gaps are identified and the focus of this work is set.

Section 2.2 proposes an approach to perform parameter identification of lithium-ion battery models capable of controlling the fast-charging current at the edge of the physical limits. A tear-down and characterization procedure is outlined for a cylindrical lithium-ion cell. The parameters are used to differentiate individual electrode behavior in downstream modeling and parameter identification to enable accurate anode potential predictions.

Section 2.3 derives an electrochemical model of reduced order capable of controlling the anode potential at a given limit during fast charging events. A novel method is presented, hybridizing the parameter identification procedure of those models by trading off required measurements

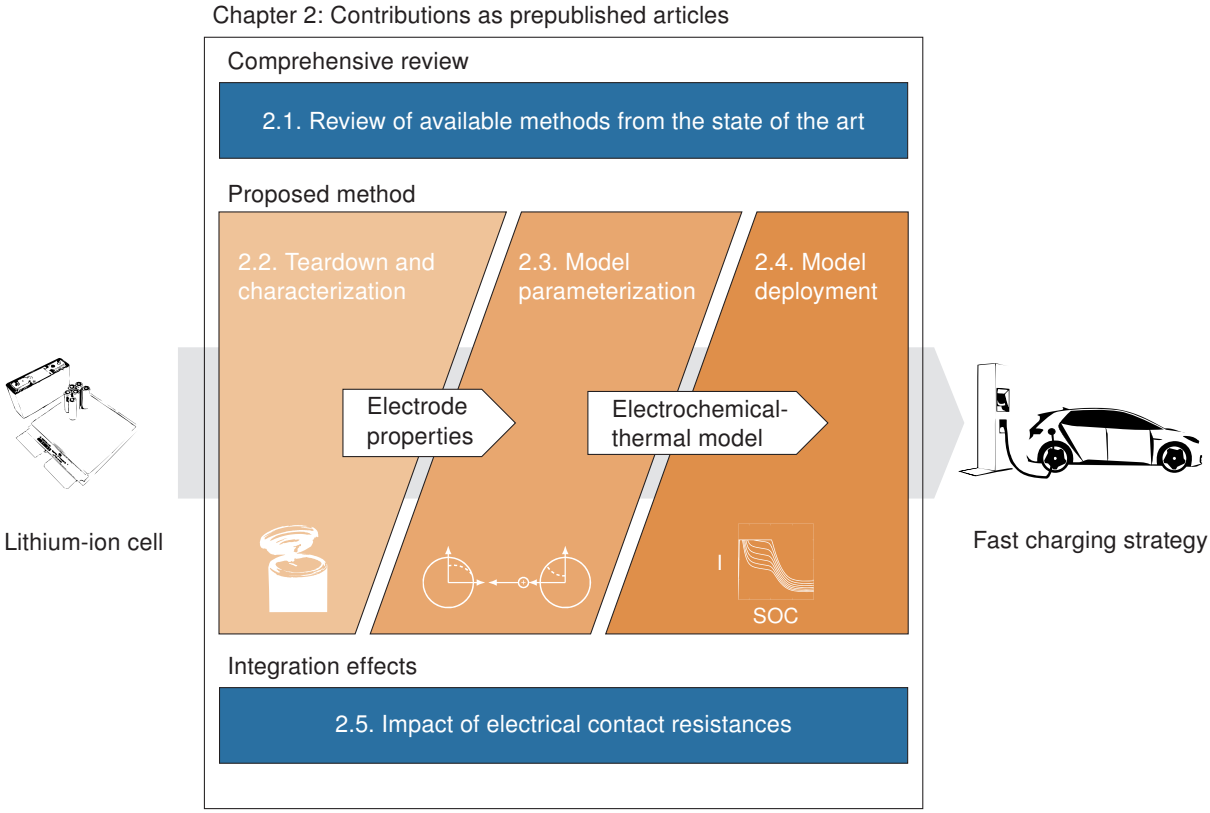

Figure 1.16: Layout of the contributions presented in this work. Methods to determine model-based fast charging strategies from the state of the art are reviewed, a novel method is proposed, and electrical contact resistance as a pack-level effect is investigated.

at the electrode level with numerical methods at the cell and pack level. Moreover, a sensitivity analysis of the parameters and their impact on anode potential control strategies is provided. The model is validated for varying charging currents in a broad ambient temperature range and with a 12s2p configuration.

Section 2.4 uses the validated electrochemical model of reduced order to derive a health-aware fast charging control strategy. The strategy is deployed in a laboratory environment to fast-charge a lithium-ion cell with real-time model predictions to mitigate the risk of lithium plating and nonlinear aging. The step-by-step procedure for putting a theoretical electrochemical model of a lithium-ion battery for a health-aware fast-charge control system into practice is described in particular detail. Extensive cycle life tests are carried out for an experimental evaluation of the strategy.

Section 2.5 extends the analysis by comparing the experimental results of single-cell fast charging studies from laboratory environments to the pack level. The parasitic thermal impact of electrical contact resistances is quantified for contact pins widely used in laboratory environments. The self-heating of the lithium-ion cells with these contact pins and laser-welded joints commonly used in automotive applications are compared during fast charging.

After presenting the individual contributions of this work, the proposed method is critically and comprehensively discussed in Chapter 3, cross-referencing the partial results achieved and taking into account results that have not been included in the prior publications.

Finally, Chapter 4 summarizes the results of this work and provides directions for future research efforts in the field of model-based fast charging control of lithium-ion batteries and their transfer and deployment in real-world applications.

2 Contributions

In the following sections, prior publications as part of this work are presented and assigned to the individual steps of the proposed method. Each publication is summarized and the key conclusions are drawn to highlight the contributions made to the present state of the art.

2.1 Remaining challenges in fast charging control of electric vehicles

With the growing demand for shorter charging times, a number of studies in the literature investigated how charging current can be controlled to avoid excessive aging of lithium-ion batteries during fast charging events. Still, a consensus is yet to be found on optimally determining a fast-charging strategy enabling short charging times while ensuring a prolonged cycle life without the risk of severe safety hazards during the operation of lithium-ion cells or systems.

This section reviews the state of the art of fast charging control strategies. It derives the remaining key challenges associated with fast charging from a cell perspective, referring to an earlier study by the author [57] and literature assessments [182]. The fast charging capability of mass-series BEVs was analyzed to reveal that R&D targets posed by governmental institutions still need to be reached in practice. The lithium-ion battery pack current, voltage, and temperature of a Volkswagen ID.3 1st edition and Tesla Model 3 Standard Range are recorded during a fast-charging event and analyzed. Both manufacturers apply a fast charging current control strategy, but with different characteristics, as their lithium-ion cells are made of different materials (NMC vs. LFP) and form factor (pouch vs. prismatic), highlighting the necessity of adaptive methods. Based on the incentive to minimize development and testing time, studies determining fast charging control strategies are identified, categorized, and evaluated. A novel clustering is derived based on the quantities used for current control and, within model-based studies, the differentiation between observable and unobservable states. It is revealed that heuristic studies involve large experimental testing matrices including considerable testing effort. Model-based approaches reduce the testing efforts by the inherited physical nature and interpretability. In addition, model-based studies enable a fast transfer to different lithium-ion cell materials and formats because only a limited number of parameters must be identified in advance. However, most studies do not apply model-based fast charging strategies to a broad experimental validation in a real-time environment at different ambient temperatures. Moreover, a coupled derating with aging is rarely performed, while it has been shown to increase the cycle life of lithium-ion cells and systems drastically.

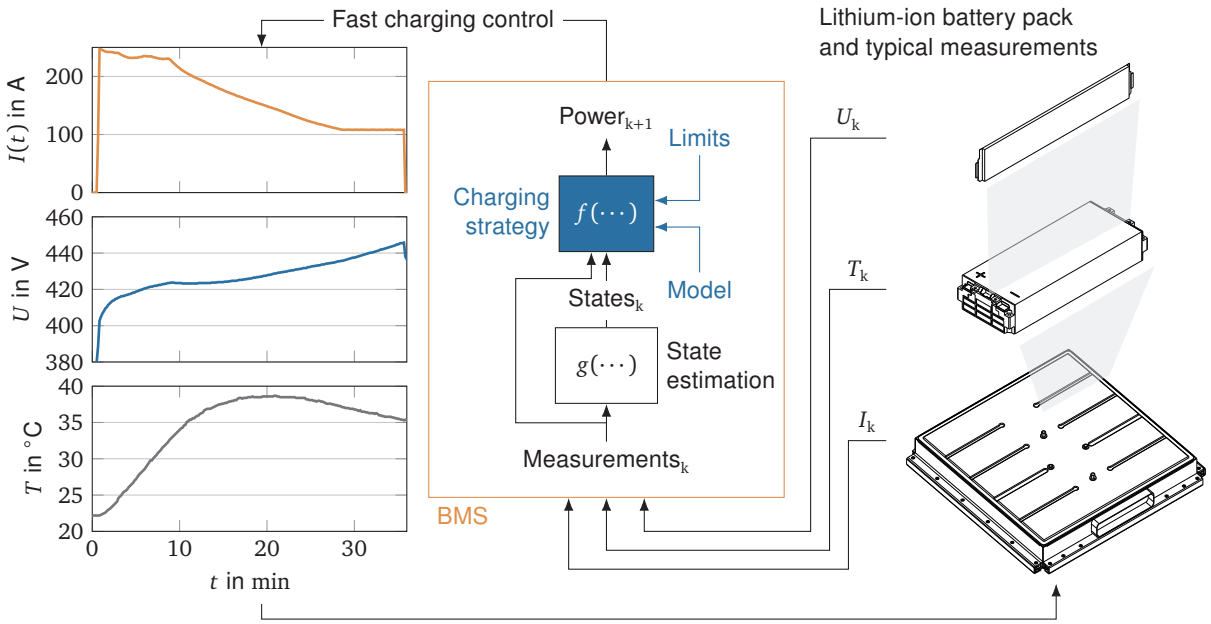

Figure 2.1: Architecture, interactions, and dependencies of the fast charging strategy. The measurements shown is recorded during a fast-charging event of a Volkswagen ID.3 1st edition reproduced from prior work [58–60] and data acquisition [61].

The results of the presented study pave the way for the further investigation and development of electrochemical model-based fast charging current control strategies, as they show promising potential to adapt the strategy to the changing lithium-ion cell states during operation. Within this field of model-based approaches, the article points out that the parameter identification of electrochemical models is still challenging. Systematic parameter identification procedures are needed to boost the modeling process during the development phase, trading off the required lab effort with the required accuracy. Moreover, broad experimental model validation is usually neglected, questioning the flexibility of electrochemical models. Concerning the usage of electrochemical models of reduced order, the article shows that the adaption to the actual SOH of the battery is rarely investigated, and methods are needed to link the SOH to electrochemical models during fast charging current control. Based on the observations, the subsequent contributions of this work span the remaining challenges and intend to propose solutions to the issues involved.

Author contribution: General conceptualization, method development, investigation, validation, data curation, and visualization were performed by Nikolaos Wassiliadis. Jakob Schneider supported in writing parts of the upscale to pack level section. Alexander Frank was involved in writing and editing the theoretical background section. Andreas Jossen and Markus Lienkamp provided resources and supervision for this work. All authors, including Leo Wildfeuer and Xue Lin, reviewed and edited the manuscript.

Review of fast charging strategies for lithium-ion cell systems and their applicability for battery electric vehicles

Nikolaos Wassiliadis, Jakob Schneider, Alexander Frank, Leo Wildfeuer, Xue Lin, Andreas Jossen, Markus Lienkamp

Journal of Energy Storage 44, 2021.
Digital Object Identifier: 10.1016/j.est.2021.103306

Journal of Energy Storage 44 (2021) 103306

Contents lists available at ScienceDirect

Journal of Energy Storage

journal homepage: www.elsevier.com/locate/est

Review article

Review of fast charging strategies for lithium-ion battery systems and their applicability for battery electric vehicles

Nikolaos Wassiliadis [a,*], Jakob Schneider [a], Alexander Frank [b], Leo Wildfeuer [a], Xue Lin [a], Andreas Jossen [b], Markus Lienkamp [a]

[a] Technical University of Munich (TUM), School of Engineering & Design, Department of Mobility Systems Engineering, Institute of Automotive Technology, Germany
[b] Technical University of Munich (TUM), School of Engineering & Design, Department of Energy and Process Engineering, Institute for Electrical Energy Storage Technology, Germany

ARTICLE INFO

Keywords:
Battery electric vehicles
Fast charging
Lithium-ion battery
Battery aging
Lithium plating
Advanced battery management systems

ABSTRACT

Despite fast technological advances, world-wide adaption of battery electric vehicles (BEVs) is still hampered—mainly by limited driving ranges and high charging times. Reducing the charging time down to 15 min, which is close to the refueling times of conventional vehicles, has been promoted as the solution to the range anxiety problem. However, simply increasing the charging current has been known to accelerate battery aging disproportionally, leading to severe capacity and power fade while posing an unacceptable safety hazard during operation. Many different approaches have been taken to develop new fast charging strategies for battery management systems to solve the dilemma between charging speed and battery aging. To date, there is no consensus on how to optimally determine a fast and health-aware charging strategy. From an application-oriented perspective, the questions arise of what the advantages and disadvantages of the various methods are and how they can be applied. This article presents a comprehensive review and novel approach for classification of over 50 studies in fast charging strategy determination of the state of the art. We evaluate and compare all studies according to the underlying parameterization effort, the battery cell under study, and whether a proof of concept with conditions close to real-world applications has been performed. The advantages and disadvantages of the analyzed methods are critically discussed and evaluated with regard to their cost–benefit ratio. Finally, the finding are used to identify remaining research gaps in order to enable a transfer to electric vehicle applications.

1. Introduction

As electric mobility has been identified as key for improving urban air quality and reducing the dependence on fossil fuels, many efforts are being taken in academia and industry to enable world-wide adoption of battery electric vehicles (BEVs). Even though BEV sales are increasing, sales numbers fall considerably short of expectations in countries with limited political incentives [1]. Over the last decade, range anxiety has been identified as one of the largest barriers [2], although today's generation of BEVs partially achieve electric driving ranges beyond 500 km, far outperforming the common daily travel requirement of today's individual mobility [3]. Also, commonly provided charging times of above 4 h prevent the acceptance of a big market share in the automotive sector; that is, individual mobility without the ability to charge at home, as it is present in densely populated metropolitan areas, or heavy-duty commercial vehicle applications, which commonly have to meet the requirement of a high degree of utilization. It is expected that the problem of range anxiety will only be resolved if charging times match refueling times of conventional vehicles [4–8]. As a consequence, R&D goals have been set from regulative institutions on achieving fast charging times comparable to refueling times of conventional vehicles, e.g., the United States Department of Energy (DOE) in 2017 with a targeted fast charging time of below 15 min in 2028 [9] or a proposal of the European Technology and Innovation Platform (ETIP) aligned with the European Commission's Strategic Energy and Technology Plan (SET-Plan) with a targeted fast charging time of below 20 min by 2030 [10]. Fast charging is therefore used hereinafter as terminology, describing a charging procedure operating at the boundaries of the physical limits of a lithium-ion battery in order to compete with the refueling times of combustion-powered vehicles.

Recently, car manufacturers have headed to even faster charging times of announced BEVs, as shown in Table 1 for an excerpt of state-of-the-art BEVs. Besides technological advancements, charging times are

* Corresponding author.
E-mail address: nikolaos.wassiliadis@tum.de (N. Wassiliadis).

https://doi.org/10.1016/j.est.2021.103306
Received 28 July 2021; Received in revised form 21 September 2021; Accepted 22 September 2021
Available online 2 November 2021

Table 1
Extract of BEVs in the European market ranked by their capability of fast charging, here specified as a fast charging index with respect to the vehicle WLTP range. Data based on Blomgren et al. [11] and Schmuch et al. [12], extended with recently announced models with information provided by BEV manufacturers and ev-database.org [13]. Chemistry and supplier information is estimated from publicly known cooperations of BEV manufacturers with cell manufacturers and their product portfolio.

Battery electric vehicle model	Battery size	Battery chemistry	Battery supplier	WLTP range	Fast charging capability		
	Brutto kWh			km	Power kW	Time[a] min	Speed[b] km/min
Tesla Model S Long Range Plus	95	C-NCA	Panasonic/Tesla	652	250	28	16.3
Kia Soul EV 6 Standard Range 2WD	62	C-NMC	SK Innovation	394	175	18	15.3
Hyundai IONIQ 5 Standard Range 2WD	62	C-NMC	SK Innovation	384	175	18	14.9
Tesla Model X Long Range	95	C-NCA	Panasonic/Tesla	580	250	28	14.5
Porsche Taycan 4S Plus	93.4	C-NMC	LG Chem.	389	262	19	14.3
Tesla Model 3 Long Range (US)	82	C-NCA	Panasonic/Tesla	614	250	32	13.4
Tesla Model 3 Standard Range Plus (CN)	55	C-LFP	CATL	440	145	25	12.3
Polestar 2 Standard Range Single Motor	64	C-NMC	LG Chem.	420	125	32	9.2
Fiat 500e Hatchback	42	C-NMC	Samsung SDI	320	85	25	9.0
VW ID.3 Pro	62	C-NMC	LG Chem.	420	100	33	8.9
VW ID.4 Pure	55	C-NMC	LG Chem.	341	100	29	8.2
Mercedes EQC 400 4MATIC	85	C-NMC	LG Chem./Farasis	411	112	35	8.2
Audi e-tron 50 quattro	71	C-NMC	LG Chem.	283	120	25	7.9
Nissan Leaf e+	62	C-LMO/NMC	AESC	385	100	35	7.7
Peugeot e-208	50	C-NMC	LG Chem.	339	99	31	7.7
Jaguar I-PACE EV400	90	C-NMC	LG Chem.	470	104	44	7.5
Opel corsa-e	50	C-NMC	LG Chem.	330	99	31	7.5
BMW i3 120Ah	42.2	C-NMC	Samsung SDI	308	49	36	6.0
BMW Mini Cooper SE	32.6	C-NMC	CATL	203	49	29	4.9
Renault Zoe ZE50 R135	54.7	C-NMC	LG Chem.	385	46	56	4.8
VW e-Golf	35.8	C-NMC	Samsung SDI	231	40	36	4.5
Opel Ampera-e	62.2	C-NMC	LG Chem.	423	46	66	4.5
Honda e	35.5	C-NMC	CATL	222	56	36	4.3
VW e-up!	36.8	C-NMC	LG Chem.	258	40	48	3.8

[a]Fast charging between 10%–80% SOC, except where otherwise noted.
[b]Calculated according to Speed = Range · SOC range (see a)/fast charging time.

still above the aforementioned fast charging time thresholds, with the fastest charging time currently achieved by the Porsche Taycan 4S Plus model with around 21 min for a fast charge between a 10 to 80 % SOC. However, fast charging time depends, in the simplest way, on the charging time limit which could be tightened per design, i.e., by adjusting the accessible capacity during a fast charge event, which makes this quantity difficult to compare over different vehicles with different battery sizes and net battery capacities. Here, we use a calculated fast charging speed in km/min to achieve a more user-oriented and comparative figure over different vehicle sizes. This measure compares the charging time with the vehicle range and represents the distance a user can cover per charging minute. If a fast charging speed of 32 km/min is exceeded, it is assumed to satisfy over 80 % of all long-distance trips [14]. The Tesla Model S then leads the comparison in charging speed with 16.3 km/min, taking into account the vehicle's standardized range determined by the Worldwide Harmonised Light Vehicle Test Procedure (WLTP). If these results are directly compared to a quickly estimated combustion-powered vehicle with, e.g., 50 L fuel capacity, 8 L/100 km fuel consumption and a similar, but rather long refueling time of 15 min yielding 41.7 km/min refueling speed, it becomes apparent that BEVs are still far from meeting comparative figures to combustion-powered vehicles in terms of charging or refueling speed, respectively. A trade-off may arise, as additional lithium-ion battery cells can increase the net system's fast charging power while keeping the current rate at the cell level constant, but the concurrently increasing high energy storage weight reduces the overall vehicle efficiency, thus reducing the fast charging speed in terms of km/min. In addition, costs are also drastically increased. Simply increasing the size of the energy storage system is therefore not a sustainable solution.

Decreasing the fast charging time of lithium-ion batteries is not an easy task and requires charging rates operating at the physical limits of the lithium-ion battery chemistry. Furthermore, the charging rates must adapt to varying conditions, such as temperature variations [15,16]. It is well understood that simply increasing the constant charging current leads to unproportional battery aging [17], which may lead to a fast decline in capacity and value of the most expensive component in BEVs [18], and—in the worst case—to safety hazards during operation. In common lithium-ion battery applications, the charging conditions have a larger impact on the aging behavior than the discharge conditions [19]. Consequently, the fast charging current has to be precisely controlled by the battery management system (BMS) to enable fast but also health-aware charging during operation. Many researchers are therefore heading towards new physically-motivated fast charging strategies.

Currently, many different methods exist for the determination of health-aware fast charging strategies. Each method has its own benefits and drawbacks, making it difficult to decide what is the most suitable approach for a given application. Moreover, there is no consensus in the literature on which mechanisms are the limiting effects of varying cell chemistries during fast charging and on how to craft appropriate fast charging strategies accordingly.

1.1. Contributions

Many excellent reviews on fast charging and its influences have been presented. Fast charging and its application has been reviewed at the material level [20–22] and at the cell [22–24] and system level [23], from a charging algorithm perspective [25,26] and intensively across multiple research domains within the BEV context [4–8]. In addition to the aforementioned studies, this review focuses on the fast charging strategy determination procedures of the state of the art from a BMS/BEV perspective, assuming a given commercial lithium-ion battery cell and system for which a health-aware fast charging strategy should be developed. Special consideration is given to a clear clustering structure of existing approaches and identification of the remaining barriers hampering the deployment of the investigated fast charging strategies in real-world automotive applications. Based on the analysis, research gaps have been identified to enable further development in the field and a higher technological readiness level of the investigated solutions. A broad overview of current research activities is given and

evaluated according to their advantages and disadvantages. From an application-oriented perspective, fields of future research are identified. The main contributions of this study can be summarized as follows:

1. **Summary of critical limitations during fast charging and derivation of critical parameter to control**.
   The origins of limitations on the vehicle level are traced back to the electro-thermal limitations on the cell component level. Critical parameters for thorough control by the BMS are discussed.
2. **Classification and comparison of over 50 approaches to determine health-aware fast charging strategies for lithium-ion batteries in the literature**.
   A literature overview of state-of-the-art methods to determine health-aware fast charging strategies is given and each method is evaluated and compared, according to the underlying motivation and the initially required effort for determination, whether an experimental proof of concept was performed or not and the ability to scale to the application level.
3. **Evaluation of research gaps and recommendations for further development to reach the application level**.
   Based on the performed literature review, potential research gaps have been derived and the need for further research is highlighted.

1.2. Structure of the article

The remainder of this article is organized as follows: Section 2 provides a brief summary of the challenges and origins of fast charging. Current limiting effects are traced back to the electro-chemical origins to the main cell components. The key mechanisms for accelerated battery aging during fast charging are highlighted and the possibilities to control those mechanisms are discussed. In Section 3, different methods for fast charge strategy determination are presented and compared. Section 4 discusses the different approaches and emphasizes research gaps to lever higher charging speeds while maintaining battery life. The key conclusions are summarized in Section 5.

2. Theoretical background

The fast charging capability of battery packs depends on various factors, which are interdependent and can be traced back from the application level to the electro-chemical behavior occurring on the cell component level. In the following sections, the general fast charging limitations on the vehicle level are presented and are gradually traced back to the main origins of the lithium-ion battery, lithium deposition, and heat generation. Finally, the need for intelligent, electro-thermal motivated and model-based fast charging strategies is emphasized.

2.1. Fast charging strategies and challenges

Ideally, a battery pack in an electric vehicle is able to accept high charging currents independent of the conditions present in the battery pack, while providing a long lifetime to keep maintenance costs low and sustainability high. Unfortunately, these ideals usually pose several trade-offs in reality.

In the past, several electric vehicle manufacturers have had technical problems associated with the fast charging capability of their BEVs. Most prominently, early generations of the Nissan Leaf suffered under excessive fast charging power derating on long-distance trips, which was traced back to insufficient battery thermal management. Fast charging with the advertised speed was only possible once, if the conditions were right, indicating an underestimation of the thermal behavior of the cells under fast charging procedures [6]. Synchronously, Nissan Leaf battery packs were prone to accelerated aging if temperatures were high [27], leading to the assumption that frequently fast-charged Nissan Leafs may also suffer under accelerated battery aging because of an increased battery system temperature. When Porsche first introduced their new concept study, Mission-E, as a predecessor of the series model, Taycan, a fast charging time of 15 min at 350 kW was advertised [28]. In a later release towards the start of production, the charging power had been decreased to 270 kW (peak) and the charging time has been increased to above 21 min if a narrow temperature corridor was obeyed. Recently, Hyundai experienced a series of charging-related electric vehicle fires. The incidents were first traced back to damaged anode tabs of the installed lithium-ion batteries by the electric vehicle manufacturer, later supplemented with a contradictory statement by the cell manufacturer that the fast charging logic had been falsely applied to the BMS [29]. While the reasons for this issue are still being clarified at the time of writing, it becomes clear that fast charging still poses a major challenge for electric vehicle manufacturers.

Fast charging time can be decreased in the simplest way by increasing the charging current within the operational boundaries. Hereby, current, voltage, and temperature are controlled within a tight operational window to prohibit excessive aging, known as the safe operating area (SOA) [30]. These limits are usually static (e.g., maximum voltage and temperature) or controlled based on simple rules (e.g., maximum current adjustment to temperature) [30] and provided with cell qualifications from the cell manufacturer. Charging current guidelines from cell manufacturers are usually kept conservative [31] and underrate the non-damaging fast charging capabilities of lithium-ion batteries. If these limits are to be exceeded, more elaborate strategies are needed, as it can be seen in Fig. 1 for a DC fast charging event of a VW ID.3 and a Tesla model 3, increasing the complexity and risk of false implementation or unintentional abuse. If the battery system is to operate at the physical boundaries of the lithium-ion battery, battery aging and abuse trigger conditions have to be considered individually and the fast charging current controlled according to the targeted application.

Overall, battery aging mechanisms always take place at the cell component level [32], emphasizing the need to understand the malicious short- and long-term aging behavior and mechanisms present during fast charging procedures. This knowledge has to be scaled up to develop health-aware fast charging control algorithms at an application level.

2.2. Indications for major cell aging mechanisms during fast charging and relevant control parameter

Health-aware fast charging current control strategies necessarily require measured or predicted quantities to incorporate them into a control-loop during the fast charging procedure. To minimize severe aging phenomena, these quantities must be kept within the critical and tolerated limits of malicious cell reactions during operation. This simple task description is complex and difficult to realize in practice, since battery aging mechanisms are manifold, interdependent, and occur at each component in the cell; that is, the anode, cathode, and electrolyte [33]. In the following sections, a brief overview of the most critical aging phenomena including their onset conditions reported in the literature and the possibilities to control them in practice are explained. Note that many further aging mechanisms take place, which are, however, still under investigation concerning their severity during fast charging procedures by many researchers. Since there is no consensus on how to control these effects by the BMS yet, we focus on the currently most dominating mechanisms and consensus in the literature, that is, lithium deposition and heat generation.

2.2.1. Lithium deposition and control

In lithium-ion batteries in general, lithium-ions are transferred from the cathode via the liquid electrolyte to the anode during charging. Alongside, as apparent from Table 1, all commercially deployed lithium-ion battery systems unite graphite as the anode material, which makes it a universal bottleneck during charging independent of the

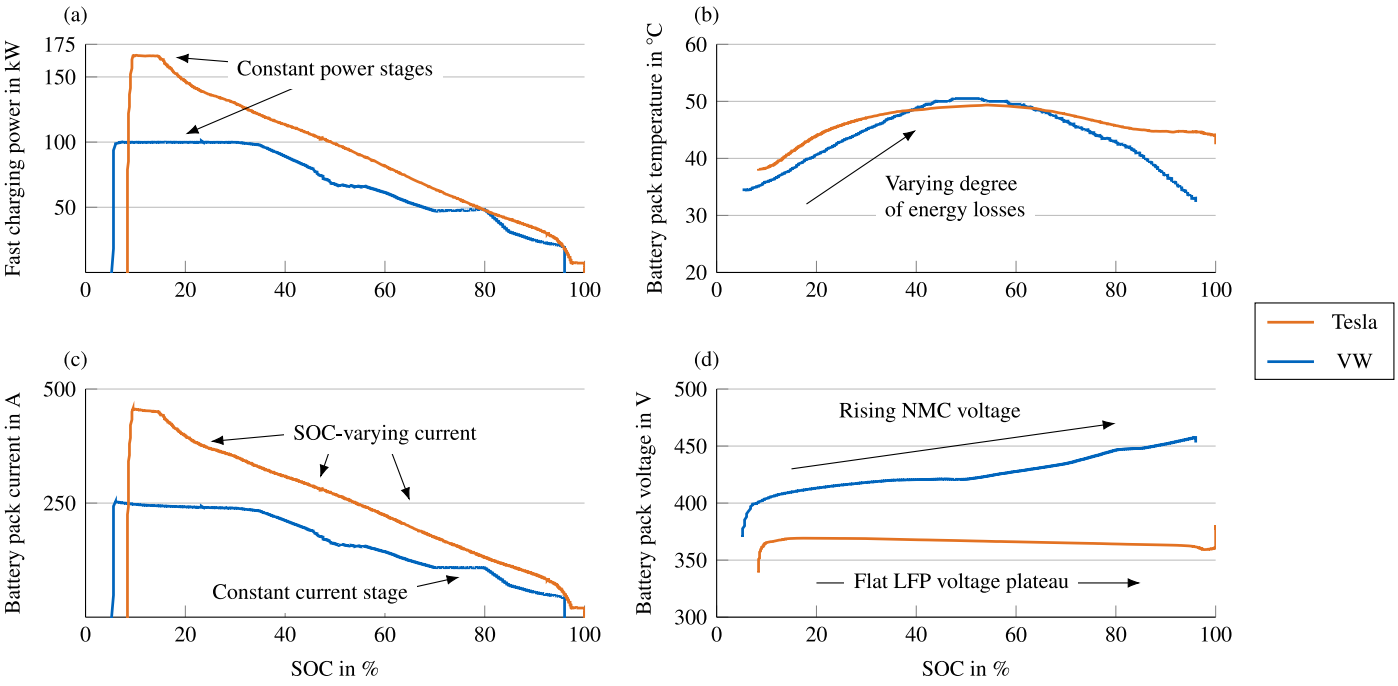

Fig. 1. Fast charging of a VW ID.3 Pro Performance and a Tesla Model 3 Standard Range Plus (CN). On-board measurements of the battery system (a) fast charging power, (b) temperature, (c) current and (d) voltage for both vehicles recorded during a fast charging event at a 350 kW charging pile starting from 0% SOC displayed at the vehicle user interface until the fast charging event was stopped by the vehicle. Note that the illustrated SOCs correspond to the actual SOC of the battery pack, as it does not contain safety margins of the vehicle.

cathode chemistry. Recent research has therefore mainly focused on graphite anode limitations. Under normal circumstances, only the desired intercalation of lithium-ions into the carbon lattice occurs. However, the charge acceptance of anode material is limited and confirmed as the major limiting component during fast charging [34]. If excessive charge rates are applied to lithium-ion batteries with graphite anodes, the desired intercalation reaction directly competes with the metallic deposition reaction of lithium at the intercalation surface, also known as *lithium plating*. This side reaction is undesired and hazardous, as it is thermodynamically unstable and further reacts with electrolyte compounds to side products [35], reducing the amount of usable lithium-ions during charging and discharging.

Fig. 2 further illustrates the operational conditions which favor the lithium deposition reaction at the anode/electrolyte interface in argumentation order. As summarized by Waldmann et al. [36,37], at low temperatures (Fig. 2(a)), due to *Arrhenius* law, the intercalation kinetics and diffusion processes in the active material are inhibited. This leads to an accumulation of lithium-ions at the particle surface, which in turn further hinders intercalation reactions and leads to an accumulation of lithium-ions at the anode–electrolyte-interface, amplifying lithium deposition.This can happen even at low C-Rates of 0.5 C [38]. If the charging current is too high (Fig. 2(b)), a similar mechanism takes place. High C-Rates can lead to an accumulation of lithium-ions close to the anode surface. This in combination with already intercalated lithium-ions accumulating at the particle surface, which hinders additional intercalation, favors the lithium deposition reaction. Also, at high SOC (Fig. 2(c)), the high local lithiation inside the anode particles leads to inhibited diffusion [39], which again amplifies lithium-ion accumulation and lithium deposition.

The lithium deposition reaction is not fully reversible [40], reducing the available lithium inventory and clogging intercalation pathways, thus reducing the available capacity and increasing the impedance of the battery, respectively [41]. The definition of excessive charge rates for lithium deposition is dependent on the anode SOC, the temperature, and the state-of-health (SOH), and thus may vary during a fast charge event. Empirical determination of the thresholds at this level of detail poses a challenging task for transferring the findings to an application level.

As one potential solution for lithium deposition prevention, the charging current can be controlled during operation if a control quantity is introduced, which summarizes all aforementioned harmful conditions [42]. Legrand et al. [43] first defined a lithium deposition criteria, which linked the occurrence of lithium deposition to the anode open-circuit potential ϕ_{OCP}^{NE} and anode overpotential η^{NE}. Note that all potentials are given vs. Li/Li^+. Following the authors, the lithium deposition process becomes thermodynamically possible if the anode overpotential η^{NE} exceeds a specific potential, which can be expressed as

$$\eta^{NE} > \phi_{OCP}^{NE} - \phi_{Li/Li+} + \eta_{Li/Li+}, \tag{1}$$

where the remaining quantities are the equilibrium potential $\phi_{Li/Li+}$ and overpotential $\eta_{Li/Li+}$ of the malicious lithium deposition reaction. With further simplification [44], lithium deposition occurs if the anode overpotential exceeds the anode open-circuit potential, expressed as

$$\phi^{NE} = \phi_{OCP}^{NE} - \eta^{NE} < 0\text{V}, \tag{2}$$

commonly known as the lithium deposition criteria. Since lithium intercalation for graphite anodes is expected to happen in a narrow potential between 5 mV to 300 mV [24] and the open-circuit potential rapidly approaches zero with increasing SOC [34], negative potentials can be easily reached during fast charging and the anode electrode potential ϕ^{NE} should be kept above a safety threshold ϕ_{limit}

$$\phi^{NE} > \phi_{\text{limit}}, \tag{3}$$

which lies above the theoretical critical threshold of 0 V, but includes safety margins for estimation errors.

Since the overpotential η^{NE} is directly coupled to the C-Rate, SOC, temperature, and SOH, all critical scenarios can be jointly prevented if the anode potential ϕ^{NE} is thoroughly controlled. Vice versa to Eq. (2), the dissolution of deposited lithium, also known as *lithium stripping* of

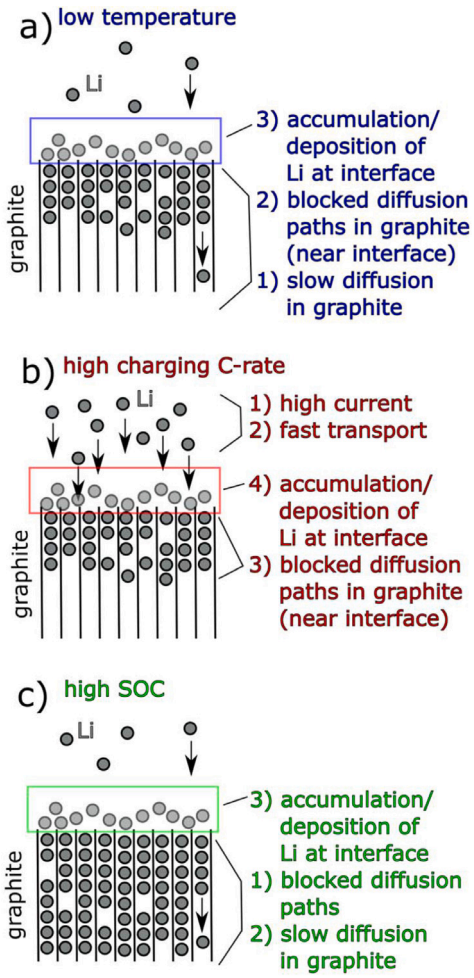

Fig. 2. Critical lithium intercalation situations during charging at various initial conditions increasing the likelihood of lithium deposition: (a) charging at lower temperatures, (b) charging with high current rates, and (c) charging at high SOC. The figure has been reproduced in its unmodified form from [36].

electrically connected lithium, may occur if the anode potential η^{NE} is positive [38,44,45].

Beyond that, the dominance of lithium deposition as a major aging mechanism was supported with experimental analysis of NMC811/Graphite pouch cells, since anode capacity fade was observed to accelerate faster than cathode capacity fade at high C-Rates, leading to conditions where lithium deposition occurs due to an electrode capacity imbalance [46]. Moreover, Zhang [47] performed several current rate tests in a NCA/Graphite coin cell setup with a lithium-metal reference. The author concluded that even though the anode may not be initially a limit for fast charging, dissolution of cathode metals due to, e.g., high temperatures or overcharge may aggravate side reactions at the anode. This in turn leads to an increase in the impedance of the anode, raising the likelihood of lithium deposition during cycle life.

Lithium deposition at the anode surface is seen as one of the most critical aging mechanisms during fast charging, since its likelihood increases over the battery lifetime [48], especially at low temperatures [49], and it is self-reinforcing [41,50,51]. If lithium depositions are present at the anode surface, an increase in resistance appears, further increasing the probability of additional deposition by increasing the required anode overpotential and thus further lowering the anode potential ϕ^{NE} [41]. Studies provided in-depth analysis, which indicates that the nonlinear aging characteristic of lithium-ion cells can be traced back to lithium deposition [52]. This adverse effect is self-reinforcing [51], which is why it must be avoided during electric vehicle operation, as it depicts a failure of the overall battery system and may lead to an internal short-circuit of the battery cell [53]. Moreover, lithium deposition increases the risk for the onset of self-heating side reactions, leading to an increased likelihood of thermal runaway [54,55].

2.2.2. Heat generation and control

From a lithium deposition perspective, the overpotential at the anode interface should be kept as low as possible under all circumstances to prevent accelerated aging conditions. As the overpotential is strictly correlated to the cell's temperature; that is, lower temperatures lead to higher overpotentials, higher temperatures could be beneficial for avoiding lithium deposition. However, high temperatures also trigger unwanted side reactions and therefore accelerated aging. The anode surface is covered by a passivation layer [56], known as solid electrolyte interphase (SEI), which forms around the active material in the first cycles after production and protects the anode material from side reactions with the electrolyte [57]. During operation of the lithium-ion battery, the SEI thickness grows even when the cell is under rest if reactive components are present [58]. Since SEI growth is a temperature-dependent process, temperature is the major influencing factor [59].

Temperatures over 25 °C were identified as a malicious condition in respect to increased SEI growth under conventional charge and discharge rates in the past [60]. However, Yang et al. [61] recently showed that an increased cell temperature may be beneficial for fast charging procedures, since higher temperatures also foster diffusion processes inside the particles and therefore can lead to reduced overpotentials at the electrode–electrolyte interface. Moreover, at low ambient temperatures, high charging C-Rates may lead to high temperature differences across the battery cell, which leads to higher currents in local hot spots and promotes accelerated local aging [62]. Temperature hot spots may further contribute to increased local volume changes in the active material, which in turn lead to mechanical tensions and particle cracking. However, elevated temperatures and C-Rates may pose the problem of accelerated electrolyte decomposition and gas evolution. Mussa et al. [63] reported extensive gas evolution during 4 C fast charging of a 25 Ah prismatic NMC/Graphite cell. The resulting swelling of the cell led to a steep increase in cell impedance due to ionic transport restrictions between the electrodes. Jalkanen et al. [64] concluded that temperature-induced SEI layer growth, drying of the electrode, electrolyte decomposition and gas evolution can even lead to lithium deposition in aged cells. Beyond that, if specific temperature limits are exceeded, hazardous thermal runaway events, such as fires and explosions, could occur [65]. In order to keep thermal induced side reactions at the tolerated limit and avoid thermal runaway due to increased thermal thresholds, cell temperature has to be precisely controlled. This is usually achieved by measuring the temperature at critical points, e.g., thermal hot spots. A general energy balance for battery systems was first given by Bernardi et al. [66], which in its reduced form gives the following equation for the total generated power loss Q_{tot},

$$\dot{Q}_{tot} = \dot{Q}_{irrev} + \dot{Q}_{rev} = I(U - U_{\mathrm{OCV}}) + I(T\frac{dU_{\mathrm{OCV}}}{dT}), \tag{4}$$

where the first term describes the irreversible heat, dependent on the charging current I, the cell's terminal voltage U, and the open-circuit-potential U_{OCV}, while the second part describes the reversible entrophic heat. For high charge rates, the reversible part is negligible [67] and the temperature increase can be defined by

$$\dot{T}_c = \frac{T_s - T_c}{RC} + \frac{\dot{Q}_{irrev}}{C}, \tag{5}$$

with the core temperature T_c, measurement point temperature T_s, the thermal resistance R, and heat capacity C between both points [68].

The temperature can then be controlled by keeping the core temperature T_c below a defined threshold T_{limit} according to

$$T_c < T_{\text{limit}}, \tag{6}$$

which depends on the allowed maximum temperature of the lithium-ion battery and includes safety reserves for model or measurement inaccuracies.

Sensing of thermal effects is therefore of utmost importance during fast charging. A direct placement of thermal sensors at the hot spots is usually limited by the dense design of the battery system. As a result, differences between the cell core or hot spot and the cell case or measurement point occur, hampering a close temperature control of the cell. In the past, differences have been reported within various cell formats, which is especially critical if fast charging currents are applied and irreversible heat generation overtakes thermal conduction to sensor placing points. While earlier studies reported differences of up to 2 °C in cylindrical 18650 cells at 3C charging rates and 20 °C ambient temperature [69], up to 5 °C difference were measured *in operando* in cylindrical 18650 cells [31] and up to 10 °C difference in cylindrical 26650 cells with cell core measurements [68]. Pouch cells usually have a larger surface area than cylindrical cells and a relatively small thickness. On the surface, hot spots develop at the positive tab or at the center of the cell under load [70–72]. Previous studies have focused on the temperature inhomogeneity during discharge, whereby Grandjean et al. [70] found that temperature gradients and hot spots are independent of the current direction. For a 20 Ah pouch cell at 20 °C ambient temperature, temperature differences of 3 °C were measured for a 3C charge. Comparable results have been attained by Waldmann et al. [73] with a slightly smaller pouch cell of 16 Ah, with gradients of 4 °C for 3C and 11 °C for 8C. The temperature difference can be expected to increase with a declining surface-to-volume ratio of cell formats, e.g., the trend of larger radii of cylindrical formats or larger volumes of prismatic and pouch cells. A densely packed battery system and parallel connected cells can further increase inhomogeneity. It is therefore of particular importance to account for the heat transfer between the point of power loss and temperature measurement from an application-oriented viewpoint.

In the long term, temperature-related side reactions are accompanied by a loss of lithium inventory and thus lead to an accelerated capacity decrease at elevated temperatures [74]. Furthermore, and even more critical, SEI growth increases the impedance of the cell. This leads to larger power losses and higher thermal heat generation for aged lithium-ion batteries, increasing the cooling demand of the overall battery system during its lifetime. Moreover, the internal impedance variations due to the temperature inhomogeneity and cell aging [75] may lead to increased local overpotentials in the anode, resulting in an increased probability of lithium deposition. It is therefore apparent that the temperature behavior is coupled to the mechanisms of lithium plating, making both effects and their interdependency important to consider for health-aware fast charging strategies at the application level.

2.3. Battery management system requirements

To date, methods for *in operando* detection of malicious cell reactions and their application in commercially deployed lithium-ion battery systems are still in an early stage and do not reliably provide information about the battery states for subsequent use in a real-time fast charging control strategy [76]. If battery health should be sustained as much as possible during fast charging, malicious cell reactions have to be predicted in advance to avoid abuse conditions before they are present and thus minimize aging and ensure safety over the operational service life [77]. Advanced battery management systems (ABMS) with the help of advanced battery algorithms and knowledge of the operating boundary conditions are therefore required [77–79]. The greatest challenge hereby lies in capturing the aging processes under all influencing factors at the material level and feasibly scale them to the application level without a greater loss of accuracy [80]. Methods for the determination and implementation of such fast charging strategies with a greater level of generality but sufficient accuracy are of utmost importance for the sustainable and safe operation of battery systems in electric vehicles. Those methods should be applicable to lithium-ion battery systems of the current state of the art but also scalable to different types and formats.

3. Methods for the determination of health-aware fast charging strategies for battery management systems

Over the last decade, many different approaches have been developed to determine fast and simultaneously health-aware fast charging strategies, which include further physical information for current control than conventional constant current constant voltage (CCCV) or constant power constant voltage (CPCV) charging strategies. Relevant studies were collected using the available literature in the addressed field at the time of writing. 59 studies in total were identified as relevant to the scope of the article. In general, all identified approaches can be categorized into two main groups. In the first group, the demonstrated approaches are summarized by *heuristic studies*, as experimental observations of the lithium-ion battery cycle life under different charging currents lead to the resulting fast charging strategy. The second group involves *model-supported approaches* with battery models of different kinds, which are used to control the charging current at the edge of lithium-ion battery aging stress factors. Here, we subdivide this group into model-supported approaches based on commonly measurable *external cell states* (e.g., voltage, temperature) and based on commonly non-measurable *internal cell states* (e.g., anode potential, cell core temperature). Note that the argument of measurability refers to commercially available lithium-ion battery cells at the time of writing. The latter and larger group is further subdivided into *data-driven models*, *characteristic maps*, physically-enhanced *equivalent circuit models*, and *electro-chemical models*, with rising physical interpretability but declining applicability due to increased calculational effort of the approach. All studies and methods concur that the reported health-aware fast charging strategy has to be experimentally validated and scaled up to the application level to be applicable in real-world scenarios of BEVs. Therefore, all studies are categorized to

- the lithium-ion battery cell under study,
- the parameter base, i.e., the effort required for determination of the fast charging strategy and the transferability,
- the aging test, i.e., whether a proof-of-concept aging test has been performed and under which ambient conditions,
- the aging derating strategy, i.e., the adaptation of the actual SOH of the battery,
- the scale level, i.e., the battery system architecture considered within the investigated study.

Fig. 3 gives an overview of the clustering principle and the introduced categories. Table 2 presents further details on the reviewed studies, which are discussed later in the article.

3.1. Heuristic studies

The most popular approach in determining health-aware fast charging strategies lies in a heuristic study of the achievable cycle life under different current control strategies. Hereby, many cells are cycled with a cell-specific, individual charging current strategy until a predefined cycle count or capacity retention is achieved. Subsequently, the longest-lasting battery cell with the shortest charging time sets the health-aware fast charging strategy. An overview of different fast charging strategies is given in Fig. 4.

In an early study of Notten et al. [81], it was observed that an upfront higher charging current during charging, introduced as boost

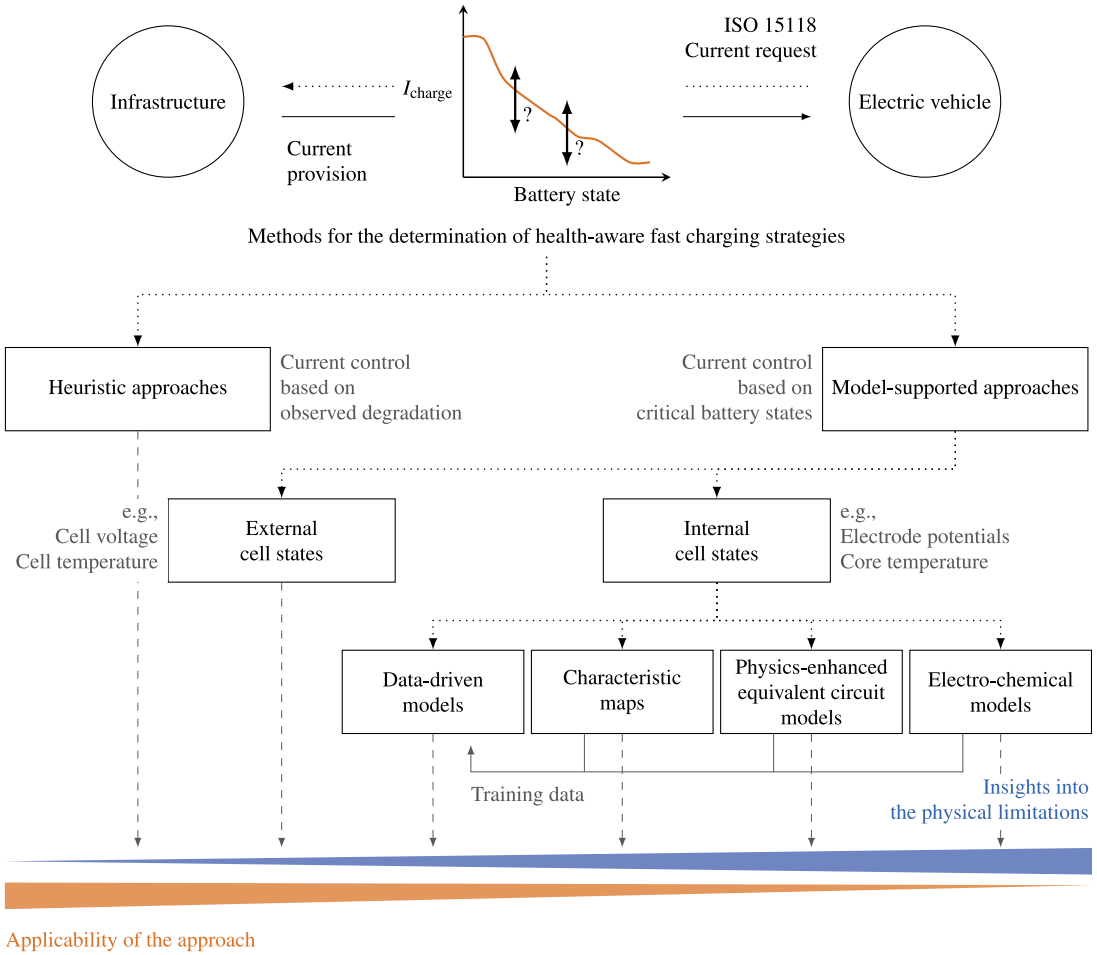

Fig. 3. Clustering of different approaches for the determination of health-aware fast charging strategies for lithium-ion batteries.

charging (BC), could prevent the occurrence of side reactions such as lithium deposition, thus enabling faster charging while keeping aging acceleration low. The strategy has been investigated for cylindrical and prismatic cells, showing that the results are independent of the lithium-ion battery format. Zhang [82] supported the results by finding that an initial higher current with a constant power control in the beginning increased the cycle life compared to an initial lower current stage. Li et al. [83] compared conventional constant current (CC) charging with pulse charge (PC) techniques in a way that the charging current is applied by short positive pulses interrupted by short negative pulses, which are understood as being the lever to reduce the probability of lithium deposition [139]. However, the PC technique requires high frequencies down to less than 1 ms to effectively inhibit lithium deposition [140], which demands additional electronics capable of high-frequency modulation within the overall charging system. With a similar motivation, negative current stages during a CC charging sequence were investigated by Abdel-Monem et al. [84,85] and compared to different fast charging strategies with varying current stages, also known as multistage constant current (MSCC) strategies. From a cycle life test it was concluded that the negative pulses reduced diffusion time constants during fast charging and thus slowed down capacity fade of the investigated lithium-ion battery (LIB). Based on the aforementioned studies, Keil and Jossen [19] carried out a broad empirical study investigating the impact on battery cycle life of a selection of popular fast charging current profiles. Parameters of CCCV charging, BC and PC, were varied according to time comparability to a conventional CCCV strategy and the effects on cycle life were evaluated. The authors concluded that lower current at high SOC and/or lower cut-off voltages may be beneficial for minimal battery aging. Based on this motivation, Mussa et al. [86] cycled cells in a long-term aging study with a CC fast charging profile to a partial SOC of 80 % and compared it to the conventional cell manufacturer specifications. The fast charging current was determined by adjusting the current to achieve 80 % SOC within 30 min. Interestingly, the larger charging current within a lower voltage window yielded an increased cycle life compared to the cell manufacturer's standard charging recommendation, giving exception to the general belief that fast charging accelerates battery aging. However, the charging rate of 1 C has been far below the currently targeted fast charging rates. In all aforementioned studies, the testing effort to determine the optimal fast charging strategy is intensive.

To determine the different current stages of the fast charging strategy with a more physical motivation and narrowing the testing scheme to the most promising fast charging strategies, Ansean et al. [87] studied different current stages during charging, known as BC strategies, parameterized on the base of the internal resistance evolution of the cell under study. By taking into account the cell impedance and adjusting the current stages accordingly, excessive heat generation can be avoided. Due to the measured internal resistance determined by a high pulse power characterization (HPPC), the stages replicate a boost profile with the highest charging current in the beginning. With a similar motivation, the upper voltage limit of CCCV charging had been increased based on the internal resistance in other studies [88]. Recent work of Sebastian et al. [89] presented a NCA-motivated approach to determine an optimal MSCC fast charging protocol. Despite the manufacturer's recommendations, the investigated cell was charged with an initial lower current and higher current ramp in the subsequent

Table 2
Summary of studies investigating different methods for the determination of fast charging strategies with extracted information about the cell under study, the fast charging strategy, and whether a proof of concept with conditions close to real-world applications had been performed.

Subcategory	Authors	Battery cell under study		Fast charging strategy determination and proof of concept			
		Manufacturer and type	Material	Parameter base	Aging test	Aging derating	Scale
Heuristic studies							
	Notten et al. [81]	Sony US18650	n/s	Arbitrarily set	✓25 °C	–	1s1p
	Notten et al. [81]	Philips LP423048	n/s	Arbitrarily set	✓25 °C	–	1s1p
	Zhang [82]	n/s	C-LCO	Comparability	✓23 °C	–	1s1p
	Li et al. [83]	Sony US18650S	C-LCO	Arbitrarily set	✓ n/s	–	1s1p
	Abdel-Monem et al. [84]	EIG 7Ah	C-LFP	Arbitrarily set	✓25 °C	–	1s1p
	Abdel-Monem et al. [85]	EIG 7Ah	C-LFP	Arbitrarily set	✓25 °C	–	1s1p
	Keil and Jossen [19]	Sanyo UR18650SA	C-LMO/NMC	Comparability	✓25 °C	–	1s1p
	Keil and Jossen [19]	Sony US18650VT1	C-LCO/NMC	Comparability	✓25 °C	–	1s1p
	Keil and Jossen [19]	A123 18650M1A	C-LFP	Comparability	✓25 °C	–	1s1p
	Mussa et al. [86]	n/s	C-NMC/LMO	Comparability	✓25 °C	–	1s1p
	Ansean et al. [87]	A123 n/s	C-LFP	Cell impedance	✓23 °C	–	1s1p
	Noh et al. [88]	PHET IFR13N0	C-LFP	Cell impedance	✓25, 45 °C	–	1s1p
	Sebastian et al. [89]	Panasonic NCR18650B	C-NCA	Cell impedance	✓23 °C	–	1s1p
	Chen et al. [90]	Sanyo UR18650W	n/s	Cell impedance	✓ n/s	–	1s1p
	Schindler et al. [91]	Samsung ICR18650-26F	C-NMC	Arbitrarily set	✓25 °C	–	1s1p
	Amanor-Boadu et al. [92]	n/s	C-LCO	Cell impedance	–	–	1s1p
	Attia et al. [93]	A123 18650M1A	C-LFP	Comparability	✓30 °C	–	1s1p
Model-based studies based on commonly measurable, external battery states							
	Lee et al. [94]	Sanyo UR14500 P	n/s	n/s	–	–	1s1p
	Liu et al. [95]	A123 26650	C-LFP	Fitting	–	–	1s1p
	Guo et al. [96]	n/s	C-LCO/NMC	Fitting	✓n/s	–	1s1p
	Xu et al. [97]	A123 ANR26650	C-LFP	tuning	–	–	1s1p
	Ye et al. [98]	Victpower LR1865SZ	n/s	n/s	–	–	1s1p
	Patnaik et al. [99]	Samsung INR18650-25R	C-NCA	n/s	–	–	1s1p
	Zhang et al. [100]	n/s	C-NMC	Arbitrarily set	✓25 °C	–	1s1p
	Jaguemont et al. [101]	n/s	LTO-NMC	Arbitrarily set	–	–	1s1p
	Jaguemont et al. [101]	n/s	C-NMC	Arbitrarily set	–	–	1s1p
	Liu et al. [102]	n/s	C-NMC	Fitting	✓24 °C	–	1s1p
Model-based studies based on commonly non-measurable, internal battery states							
Data-driven models	Lin [103]	A123 ANR26650M1B	C-LFP	SPM simulations	–	–	1s1p
	Hamar et al. [104]	n/s	C-NMC	P2D simulations	–	–	1s1p
Characteristic maps	Spingler et al. [105]	Kokam SLPB 526495	C-NMC	Volume expansion	✓25 °C	–	1s1p
	Hovestadt et al. [106]	n/s	C-NMC	Volume expansion	✓25 °C	–	1s1p
	Waldmann et al. [107]	n/s	C-NCA	3-electrode cells	✓25 °C	–	1s1p
	Sieg et al. [108]	n/s	C-n/s	3-electrode cells	✓25 °C	SOH update	96s1p
	Epding et al. [109]	Customized cells	C-NMC/LTO	3-electrode cells	✓23 °C	SOH update	–
	Shkrob et al. [110–114]	Customized cells	C-NMC	3-electrode cells	–	–	–
	Amietszajew et al. [31]	n/s	C-NCA	Reference electrode	–	–	1s1p
	Liu et al. [115]	n/s	C-NMC	Reference electrode	✓25 °C	–	1s1p
Physics-enhanced ECMs	Zou et al. [116]	A123 ANR26650M1	C-LFP	Fitting	–	–	1s1p
	Perez et al. [117]	A123 ANR26650M1	C-LFP	Fitting	✓25 °C	–	1s1p
	Remmlinger et al. [118,119]	n/s	C-NMC	Fitting	✓0 °C	–	1s1p
	Li et al. [120]	n/s	n/s-NMC	Literature	–	–	1s1p
	Drees et al. [121]	Customized cells	C-NMC	3-electrode cells	✓20 °C	–	1s1p
Electro-chemical models	Klein et al. [122]	n/s	n/s	n/s	–	–	1s1p
	Pramanik and Anwar [123]	n/s	C-LCO	Literature	–	–	1s1p
	Adam et al. [124]	n/s	C-NMC	n/s	✓15, 25 °C	SOH update	1s1p
	Xu et al. [125]	A123 26650 M1-B	C-LFP	Literature & tuning	–	–	1s1p
	Choe et al. [126]	n/s	n/s	tuning & fitting	✓25 °C	–	1s1p
	Chu et al. [127]	n/s	C-NMC	3-electrode cell fit	✓n/s	–	1s1p
	Zou et al. [128]	n/s	C-LCO	Literature & fitting	–	–	1s1p
	Song et al. [129]	n/s	n/s	tuning	✓n/s	Aging model	1s1p
	Yin et al. [130]	n/s	C-NMC	Literature & tuning	✓25 °C	Aging model	1s1p
	Yin and Choe [131]	LG Chem n/s	C-NMC	Literature & tuning	✓25 °C	Aging model	1s1p
	Yin et al. [132]	n/s	C-NMC	Literature & tuning	✓25 °C	–	1s1p
	Lin et al. [133]	n/s	C-LFP	Literature & tuning	✓n/s	–	1s1p
	Lin et al. [134]	A123 ANR26650	C-LFP	Literature & tuning	–	–	1s1p
	Hasan et al. [135]	n/s	C-NMC	Literature & tuning	–	–	1s1p
	Kolluri et al. [136]	n/s	n/s-NiOOH	Arbitrarily set	–	–	1s1p
	Ringbeck et al. [137]	Kokam SLPB 75106100	C-NCO	2-electrode cells	–	–	1s1p
	Yang et al. [138]	Kokam SLPB11543140H5	C-NMC/LCO	Literature	–	–	1s6p

n/s: not specified; s: serial; p: parallel.

step because of the internal resistance profile of the cell leading to a two-fold better lifetime. Intensive *post-mortem* material characterization supported the assumptions that—against common opinion in the literature—the cathode behavior is the key limiter during fast charging in the study. However, only 40 fast charge cycles could be achieved until end-of-life (EOL), making it difficult to obtain further conclusions on the applicability of the strategy. In a similar manner for PC strategies, Chen et al. [90] used a slightly modified PC strategy

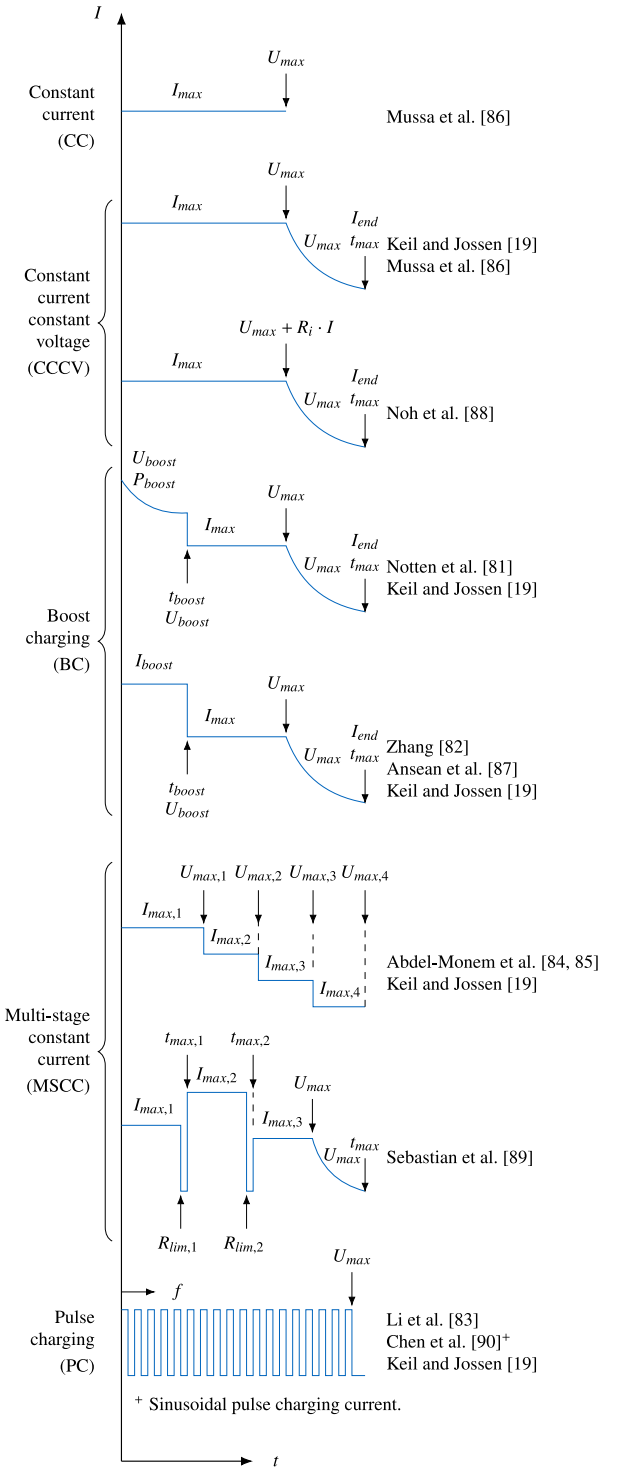

Fig. 4. Overview of fast charging current sequences in the field of heuristic studies in the literature and required limits (annotations without arrows) and trigger conditions for stage transitions (annotations with arrows).

by applying sinusoidal currents to minimize internal heat generation and determined the applied frequency from cell impedance measurements. In aging experiments, an increased cycle life was observed, most probably due to reduced heat generation. Unfortunately, the ambient temperatures of the cycle life experiments were not specified so as to be able to further evaluate on the reported results.

In order to further reduce the testing effort, many authors combined the experimental assessment with various methods for an optimal

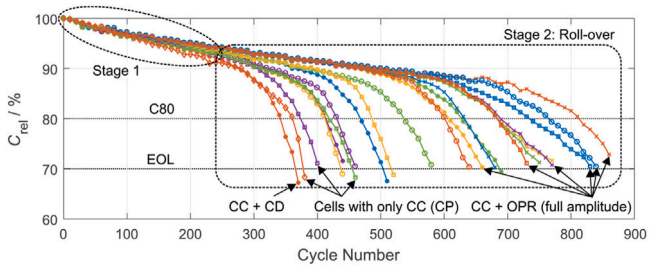

Fig. 5. Aging of cylindrical battery cells under different fast charging strategies in a heuristic study. Constant current (CC) profiles with an upfront reduced current (CD) perform significantly worse than CC profiles superimposed by an anode potential reserve (OPR) profile. The figure has been reproduced in its unmodified form from [91].

experimental test design. Schindler et al. [91] applied a design of experiments (DOE) approach in order to reduce the amount of testing and to deduce more significant conclusions of superimposed fast charging profiles of anode potential, multi-stage constant current, current interrupt, and thermal derating strategies. Interestingly, as illustrated in Fig. 5, cells cycled with anode potential reserve achieved the longest cycle life and the latest transition to nonlinear aging. Amanor-Boadu et al. [92] applied the Taguchi method to boost the experimental assessment of pulse charging profiles. However, the influence on finding the optimal fast charging strategy in terms of charging time and battery aging was not part of this study. Beyond that, Severson et al. [141] and Attia et al. [93] provided a new technique to accelerate the evaluation of heuristic studies with data-based aging prediction. Instead of intensive lab testing of multiple LIBs with variations in MSCC profiles, only a simple set of the most promising candidates was chosen and the subsequent assessment was supported with an iterative closed-loop procedure of early cycle life predictions after 100 fast charge cycles. Surprisingly, despite the commonly found monotonically decreasing stages for avoiding lithium deposition, their method reveals a not-strictly monotonically decreasing MSCC as the optimum for a fast charge of the deployed LFP battery cell. In supplementary analysis, the authors conclude that SEI layer growth may be the most dominating aging mode and a reason for the almost constant current fast charging strategy due to the high self-heating ability of the battery cells [93].

3.2. Model-supported studies based on external cell states

In addition to empirical studies, a second pathway with model-supported approaches has evolved in the literature. Here, the optimal fast charging strategy is determined by a battery model which mimics the lithium-ion battery behavior. As a major benefit, fast charging strategies can be determined with less effort, i.e., no need for intensive full fractional battery cycle life testing. The deployed models, however, require upfront battery characterization effort.

By modeling and coupling of phenomenological effects, such as the short-term electro-thermal and long-term aging behavior of a given battery cell, estimates about optimal charging profiles can be made in simulations prior to intensive testing. Many studies emphasized that thermal aspects play an important role during fast charging. Zhang et al. [100] used a thermal model to optimize the trade-off between charging time and temperature rise. The authors proposed a Pareto-optimal current profile with an upfront higher current with decreasing current over SOC. Similar capacity retention compared to a CC strategy has been observed in a single-cell aging experiment. Xu et al. [97] used a coupled electrical–thermal model to develop an energy-efficient two-step MSCC fast charging strategy to minimize the heat generation during the fast charging procedure. The highest efficiency and lowest temperature rise was achieved with an upfront high current which preheats the cell. A similar approach has been implemented by Patnaik

et al. [99], incorporating a feed-forward control with maximal temperature correction to allow for closed-loop control. In another study [94], MSCC strategies were implemented by estimating the SOC based on the input current and usage of the signal as quantity to trigger the stage transitions. Liu et al. [102] investigated the influence of battery aging on the optimality of the stage amplitudes and transitions of MSCC fast charging strategies; however, without deriving a quantifiable conclusion. In the studies of Jaguemont et al. [101], a coupled electro-thermal simulation has been used to investigate the localized temperature rise of large format pouch cells during MSCC-charging protocols at various temperatures. The authors concluded that short negative pulses during fast charging at cold temperatures can improve the fast charging capability of the cell under study. Evaluation of the impact on battery aging has not been within the scope of this study. All previously mentioned studies assume less aging due to a lower and/or more homogeneous temperature rise during fast charging.

By further adding the long-term aging behavior of a given battery cell to the electro-thermal model, estimates about optimal charging profiles can be made in simulations prior to intensive testing. Guo et al. [96] investigated a fast charging strategy coupled to a specific voltage profile optimized with an ECM at the beginning of life. The coupling of the battery voltage, as a battery response to the current, enables a current derating according to the SOH since impedance increase and capacity decrease directly correlate to the voltage response of the battery and therefore prolong the overall cycle life.

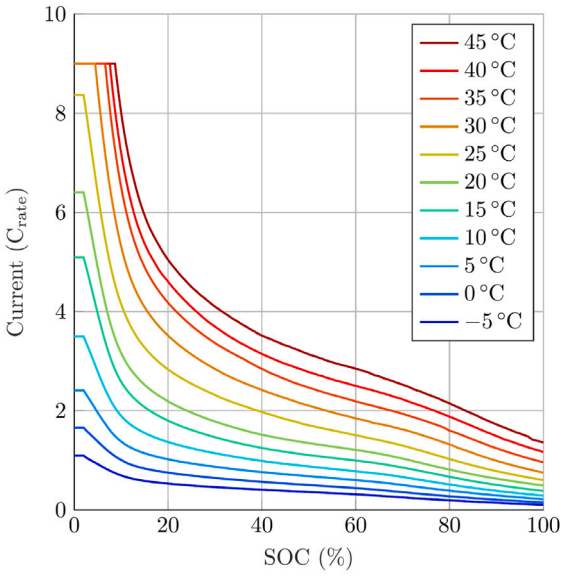

Fig. 6. Maximum fast charging current over SOC at different temperatures (characteristic map) determined by fast charging 3-electrode cells with current control to 1 mV anode potential. The figure has been reproduced in its unmodified form from [108].

3.3. Model-supported studies based on internal cell states

While battery models estimating measurable states are capable of avoiding intensive testing, a lack of physical motivation of these approaches does not allow for consideration of relevant aging mechanisms. Therefore, many researchers deployed battery models based on internal and usually not observable battery states into their fast charging current control to avoid trigger setpoints for accelerated aging.

3.3.1. Characteristic maps

A promising approach in incorporating internal battery states in an application-oriented manner is the development of characteristic maps based on the investigation of customized cells (e.g., reference electrode insertion, 3-electrode test cells) or special experimental setups (e.g., localized dilatation or temperature measurements).

As the lithium deposition process builds up a surface at the anode which leads to increased cell thickness, lithium deposition can be indirectly measured by dilatation analysis [142,143]. Rieger et al. [144] deployed a localized dilatation analysis via multi-directional laser scanning during charging. In a later study by the research group [105], those measurements were used to craft characteristic maps for health-aware fast charging control. The derived strategy was able to keep a cycle life performance far beyond a conventional CCCV strategy with a similar charging time. Based on this study, Hovestadt et al. [106] used a localized dilatation setup, including an additional localized temperature setup, for a large format automotive pouch cell. A multi-stage fast charging strategy had been deduced from lithium deposition indications such as dilatation, but also an observed endothermic temperature behavior at high SOC of the cell was used as the indication for current stage transitions. Due to the measurement principle, the method is only applicable for soft case cells, such as pouch cells.

In addition to dilatation analysis, lithium reference electrodes were also utilized for gathering insights into the battery internal states and trigger conditions. Waldmann et al. [107] deployed 3-electrode cells to study the anode potential under different charge rates. Based on the anode potential drop below 0 V at a given C-Rate, optimized fast charging strategies have been derived and applied to commercial 18650 lithium-ion batteries as a MSCC health-aware fast charging strategy. The transition points were triggered by the cell's terminal voltage. In aging tests at 25 °C an increased cycle life could be observed. Interestingly, prior aging tests indicated a dominance of lithium deposition as the main aging mechanism up to an ambient temperature of 25 °C. In the work of Sieg et al. [108], measurements also taken from a 3-electrode cell were utilized as characteristic maps to control the current according to the SOC and cell temperature of a 51 Ah pouch cell, as visualized in Fig. 6. Fast charging within 23 min could be achieved up to 80 % SOC while maintaining a cycle life of 1800 cycles until EOL if a current derating, that is, a reduction of the fast charging current due to measurement or model errors, is applied. The presented current derating is based on the SOH of the cell (taking into account both capacity and impedance). In addition, the charging current is further scaled with defined factors argued by measurement and model errors. Unfortunately, the cathode chemistry was not specified to further evaluate the results. Battery pack tests were also performed, highlighting the problem of temperature inhomogeneities if complete packs are fast charged. A similar approach with similar results had been achieved by Epding et al. [109], keeping the life cycle test at a 3-electrode cell level, which additionally revealed that aged anodes may increase the charge acceptance due to secondary aging mechanisms (i.e., particle cracking and surface expansion). Similarly, in an in-depth article series, fast charging has been followed from the material to cell level [110–114]. The authors built 3-electrode cells [110] to investigate the electrode polarization during high charge rates [111], the anode relaxation behavior [112], and the interdependency between anode overpotential and cell temperature [113], with direct measurements and the support of a pseudo-two-dimensional model (P2D). In a subsequent study [114], the authors transferred their result to demonstrate an anode potential reserve fast charging strategy deduced from the 3-electrode cell. Due to the absence of a data interface to the battery cycler, the control was implemented as a current step-back profile approximating the course of a potential controller. 3-electrode cells were experimentally fast charged from 16–80 % at 30 °C to assess whether average charge rates of 6C are technically implementable without exceeding potential thresholds for lithium deposition. The authors concluded that lithium deposition during the targeted high fast charging rates can be excluded at temperatures beyond 45 °C, however, highlighting that other aging mechanisms take place and have to be considered for health-aware fast charging. At the time of writing, the results have not been upscaled to a full cell or system level. In contrast, Amietszajew et al. [31] inserted a

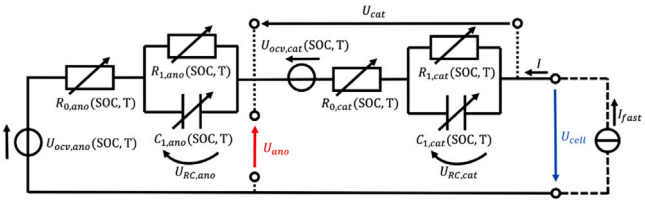

Fig. 7. Physics-enhanced ECM for fast charging control at the lithium deposition process. The overall cell voltage U_{cell} consists of the two superimposed anode U_{ano} and cathode U_{cat} potentials Both potentials are modeled with a open-circuit voltage source, an ohmic resistance, and a RC-network—all dependent on the cell's SOC and the cell's temperature. The figure has been reproduced in its unmodified form from [121].

lithium reference electrode and a cell core temperature sensor directly into a commercial 18650 lithium-ion battery. Based on different charge rates and the reference electrode of the modified cell, the authors developed a MSCC fast charging strategy. Unfortunately, a long-term aging test with unmodified cells to evaluate on the applicability was not within the scope of the study. Also, Liu et al. [115] inserted a reference electrode into a large format pouch cell and derived a fast charging strategy without any lithium deposition during the fast charging procedures while achieving twice the charging speed to the manufacturer's recommendation. The fast charging strategy follows a MSCC pattern by reducing the charging current by 1/20 C if an anode potential reserve of 10 mV is exceeded. Also here, aging tests were performed until the first 100 cycles only, limiting further evaluation of the long-term performance. However, no lithium deposition could be observed within the first 100 cycles.

3.3.2. Physics-enhanced equivalent circuit models

As insights into the physical interrelations of the stress factors and the fast charging capability are limited with characteristic maps, physically enhanced models have also been incorporated to determine and optimize the fast charging procedure in the literature. A popular approach in application-oriented modeling lies in deploying ECM, which usually maps the in- and output relation of quantities directly measurable with full cells. In the extensions for fast-charging strategies, the ECM is further physically-enhanced to either extend the thermal model to a core temperature state differing from the measured temperature or to the electrode level as, e.g., the anode potential is of particular interest for fast charging control, visualized in Fig. 7.

Zou et al. [116] coupled a lumped ECM with a lumped thermal model to optimize the fast charging strategy of a 26650 cylindrical lithium-ion battery. Besides general operating voltage bounds, the cell's core temperature has also been optimized to follow an optimized trajectory. Experimental investigations were not within the scope of the study. The authors emphasized that fast charging capability will change through the battery age and lifetime, which therefore should be considered in further studies. In a similar study of Perez et al. [117], the model is additionally coupled to a semi-empirical aging model to optimize the fast charging strategy over the battery lifetime. Similar aging but fast charging could be achieved up to the 110th cycle, however, with an increasing aging rate compared to the reference fast charging strategies. A similar approach has been taken by Liu et al. [95], but by evaluating different stages of a MSCC fast charging strategy. Here, an experimental proof of concept has been put into the outlook. All studies involve a physically-enhanced thermal ECM, but relying on a conventional electrical ECM neglecting critical control parameters for lithium deposition prevention.

From a lithium deposition viewpoint, Remmlinger et al. [118] and Tippmann et al. [119] investigated charging strategies at low temperature by crafting a physics-enhanced ECM of the anode. The anode potential was then used to control the charging current at the theoretical limit of lithium deposition. A proof of concept in an

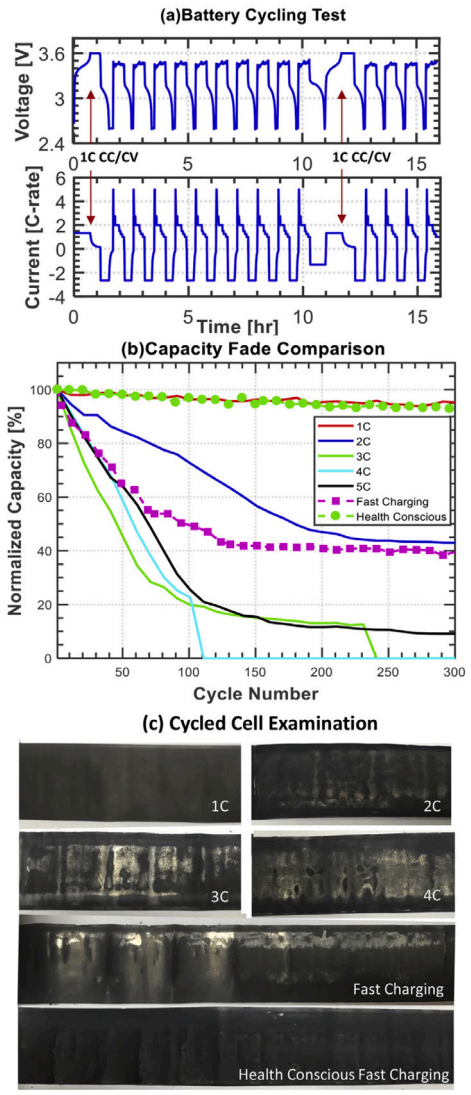

Fig. 8. Cycle life of a health-aware fast charging strategy compared to conventional strategies. (a) The applied fast charge cycle procedure leads to (b) improved cycle life due to the absence of lithium deposition as shown in (c) *post-mortem* images of the electrodes. The figure has been reproduced in its unmodified form from [133].

aging test at 0 °C was performed and discussed; unfortunately, the results were not presented in greater detail. Recently, further work on physics-based ECM modeling of full cells was carried out [145,146], leading to further application to fast charging strategy determination. Li et al. [120] applied a spatially-resolved physics-based ECM to craft a health-aware fast charging strategy incorporating critical battery-internal states, e.g., anode potential. Beyond the modeling principle, an observer and control strategy has been proposed to account for modeling errors and model deployment, respectively. However, a proof of concept in an aging study was not within the scope of this work. A similar approach has been recently deployed by Drees et al. [121] with a more simplified physics-enhanced ECM and application to the formation process in lithium-ion battery production. The model-based fast charging strategy achieved similar capacity retention by a 53 % faster charging time without any aging derating. The authors put a real-time application for health-aware fast charging control at the cell level into the outlook.

3.3.3. Electro-chemical models

Beyond physical-enhanced ECM battery models for fast charging current control and optimization, electro-chemical battery models

based on the P2D model originally developed by Doyle, Fuller, and Newman [147] incorporating the electrode physics have been intensively discussed.

In an early simulation-based study by Klein et al. [122], a P2D model was used in combination within a multi-objective optimization framework and nonlinear model predictive control to calculate the optimal fast charging current based on safety criteria specified for a fictitious lithium-ion battery, such as anode overpotential, maximum temperature, and maximum SOC. The procedure could be optimized offline and then applied as a look-up table. However, a proof of concept was not part of this study. Similarly, Pramanik and Anwar [123] determined the fast charging current according to a minimum anode potential reserve and the maximum cell temperature in an offline optimization routine. The objective function is tuned in a way that the current is controlled close to the weighted thresholds synchronously minimizing the charging time. A proof of concept in an aging study was not part of the study. By also using a full-order P2D, Adam et al. [124] recently deduced MSCC profiles by keeping the current above an anode potential threshold of 0 V or higher. A life cycle test has been performed by not only applying fast charging cycles, but by also investigating different combinations of fast charging cycles and normal charging cycles, which may be more likely during real-world BEV operation. Different non-invasive methods for online detection of lithium deposition have been investigated to avoid intensive testing for fast charging strategy determination. Interestingly, online detection of lithium deposition was not possible for the current profile derived from the electro-chemical model with anode potential control. Furthermore, the cell under study clearly showed lithium depositions in a *post-mortem* study, which underscores the need for anode potential reserve control above the theoretical limits, if this control scheme is upscaled to the cell or system level, even though the authors did not directly specify whether 0 V or a value larger than that had been used for determination of the strategy. Xu et al. [125] investigated the interdependencies of electrical and thermal behavior of lithium-ion batteries during fast charging procedures. An offline dynamic programming optimization was performed to optimize the current stages of a MSCC fast charging strategy over battery age. While the optimization led to an upfront higher charging current to avoid lithium deposition, the temperature optimization led to an upfront lower charging current for minimum temperature rise.

In a different approach, Sturm et al. [148] showed the benefits of a multi-dimensional modeling framework, first published and validated by Erhard et al. [149], with regard to the evaluation of charging behavior. By simulating local inhomogeneities in the anode overpotential and temperature distribution of the jelly roll in a high-energy 18650 cylindrical cell, the presented multi-dimensional modeling framework is able to more accurately predict the onset of lithium deposition compared to a standard P2D. While the use in real-time applications is not yet possible due to the required computational power, the obtained simulation data could be used to optimize the fast charging protocol of a separate P2D model by adjusting the safety criteria, e.g., the aforementioned ϕ_{Limit}. In a follow-up publication by Sturm et al. [150], the multi-dimensional modeling framework was used to study the impact of electrode and cell design on fast charging capabilities of different state-of-the-art cylindrical LIBs. By analyzing in- and through-plane voltage-drops, a dominant influence of the current collector tab design and the accompanied current density distribution on cell polarization was found. Fast charging profiles were adapted accordingly in order to prevent overheating and local onset of lithium deposition. All aforementioned studies involved offline optimization to determine a health-aware fast charging strategy.

As the originally developed P2D model is computationally expensive and can only serve as an offline optimization routine, many researchers worked on model order reductions to increase the computational speed, well known as reduced-order models (ROMs). While ROMs can improve the calculation speed of the original P2D model, simplifications may lead to an increased inaccuracy in predicting critical control quantities, e.g., the anode potential. Choe et al. [126] used a ROM for implementing a pulse-charging fast charging strategy. Based on the predicted battery model internal states, pulse widths were determined by switching at critical surface concentrations. The strategy led to a lower temperature rise during the fast charge. Additionally, similar capacity retention compared to CCCV was observed in a single aging test. Unfortunately, the cell under study was not specified and the aging study was terminated at 100 cycles with extrapolation of the results. Chu et al. [127] deployed a ROM to control the charging current according to an anode potential reserve. As one of the few in the literature, the model was validated up to 5C with *in situ* anode potential measurements by a reference electrode. A closed-loop observer was designed to account for SOC deviations during fast charging. Fast charging times of down to 52 min could be achieved with a nearly full charge of 97 % of the available capacity. The importance of the right adjustment of anode potential reserve was highlighted, which depends on cell and system inhomogeneities. In other studies, cell surface temperature and electrolyte concentration has also been added in addition to the anode potential fast charging control [128].

Other authors also included temperature-induced aging mechanisms, such as SEI growth, into their models. Song et al. [129] investigated a model-based fast charging strategy incorporating not only the anode potential as indication for lithium deposition, but also modeling additional parasitic side reactions with the electrolyte. In addition, based on the experimental results of Monem et al. [84] and lithium stripping simulation analysis, short discharge pulses were added to the beginning of charge to allow for lithium-ion recovery during charging. A direct comparison between model-based fast charging with and without discharge pulses is not made. Other studies also only considered side reaction rates [130,132]. Based on these findings, which were further optimized, Yin et al. [131] coupled a ROM with an aging model to determine a health-aware fast charge strategy considering lithium deposition and SEI growth, i.e., electrical and thermal effects. Alongside the optimal temperature slope, the 40 Ah pouch cell was actively temperature-controlled in a short time scale with Peltier devices. The utilized ROM was validated at 25 °C up to 2C. The optimal fast charging strategy further included short negative pulses in the form of a PC strategy to allow for lithium stripping, as lithium deposition may occur during the charge cycle. A similar cycle life compared to conventional 1C CCCV charging could be achieved, but by reducing the charging time by more than 50 % in the low and medium SOC range. Interestingly, the slope of the optimized fast charging current has a pattern similar to a strict anode potential control, i.e., a larger current in the beginning steadily decreasing over SOC, although both electrical and thermal effects were considered. While this study provides many helpful insights into the crafting of a health-aware fast charging strategy, the computational effort to perform the optimizations of the complex closed-loop model and the concept of a surface temperature-controlled thermal management system for a single lithium-ion battery cell is far from deployment in real-world automotive applications. In a study by Lin et al. [134], a SPM was coupled with a thermal core model to optimize the charging current according to the temperature rise and overpotential-induced charging losses. An aging test was not within the scope of the study. In another publication [133], the most dominant aging modes, SEI layer growth and lithium deposition, were modeled and coupled to a SPM to optimize health-aware fast charging strategies with promising results concerning the overall cycle life, as illustrated in Fig. 8. The objective function is set up as a weighted balance between both side reaction rates. The health-aware fast charging strategy achieved major improvements in cycle life compared to conventional CCCV charging. However, it is not clear whether the strategy has been deployed in real time responding to the actual cell states.

With many fast-charging protocols determined at ambient temperatures, studies at subzero temperatures have gained increasing interest. Hasan et al. [135] derived a PC fast charging protocol from a P2D

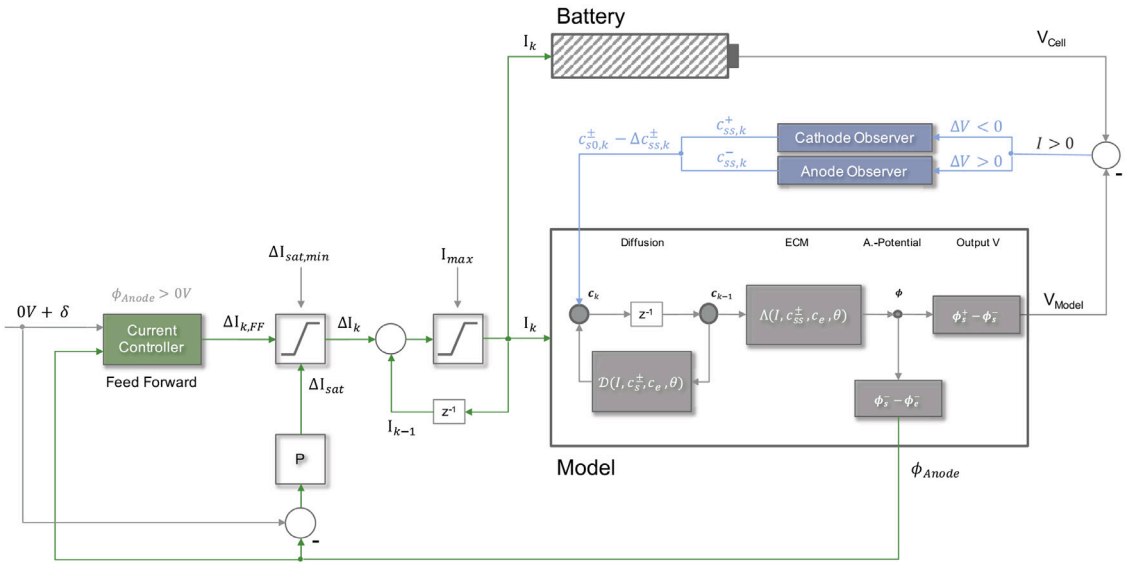

Fig. 9. Functional control loop structure of a health-aware fast charging strategy based on anode potential reserve control incorporating a reduced order electro-chemical model. The figure has been reproduced in its unmodified form from [137].

model to keep the anode saturation close to its maximum in the beginning of subzero fast charging. The study mainly focused on design parameter rather than lifetime assessment for a specific lithium-ion battery, but revealed that subzero temperatures hamper current acceptance of the anode material, supporting preheating strategies of lithium-ion battery systems prior to fast charging.

Recent studies have further investigated the integration of the aforementioned models into control schemes. Kolluri et al. [136] emphasized the necessity for a closed-loop charging control if electro-chemical models are deployed in an advanced battery management system (ABMS). They proposed a nonlinear model predictive control strategy to fast charge according to an anode potential reserve in a closed-loop control. As the control framework behind the strategy was the focus of this study, a battery with a nickel hydroxide electrode was modeled and no experimental validation was given. A similar approach has been taken by Ringbeck et al. [137], presenting a complete closed-loop model framework for real-time control with an anode/cathode open circuit voltage (OCV) observer structure (Fig. 9). A model order reduction to one particle per electrode has been performed, as the computational burden could be drastically decreased. In contrast to previous publications, an in-depth parameter determination at the electrode level has been used for model parameterization, leading to undesirable model predictions during the upscale to cell level. Aging tests were put into the outlook.

Recently, Yang et al. [138] investigated system effects and their control during fast charging. Six SPMs with a coupled thermal and aging model were used in parallel to predict the anode potential of each cell within a 1s6p pouch cells battery system (Fig. 10). As already pointed out by Liu et al. [95] in a former study with a similar setup, inhomogeneities within the system may lead to large current differences of the parallel cells. In the study of Yang et al. [138], the cell closest to the cell tabs experienced the largest current and therefore the highest likelihood of lithium deposition, if not individually controlled. However, an experimental proof of concept was not within the scope of the study.

3.3.4. Data-driven models

With the rise of data processing techniques and computing power, data-driven approaches have also gained increasing interest for fast charging strategy determination. As the aging mechanisms are complex to model and computationally expensive to deploy, data-driven models provide a convenient way to map the in- and output relations of high fidelity electro-chemical models, e.g., P2D, and transfer it to real-time environments.

Lin [103] deployed an enhanced SPM to predict the anode potential under varying battery conditions and fed the results into the training of a long short-term memory (LSTM). As the error to the data source model was of major concern for the study, the prediction accuracy of the LSTM model was investigated under different charge and discharge conditions. For the special case of charging at high current rates, a prediction accuracy of a maximum 3.73 mV root mean squared error (RMSE) was achieved. Further assessment of the robustness of the LSTM model was put into the outlook. The LSTM model required 345 MB of memory space, while a full-order model required about 866 MB of memory space. The author argues that in contrast to electro-thermal modeling, there is no need for complex modeling, parameterization, and electro-chemical knowledge. However, the deployed data-based model itself relies on training data of such a model. Building on the previous study, Hamar et al. [104] further developed this approach to study the efficiency, accuracy, and suitability of the algorithm for online implementation. The authors developed a random forest model and achieved an anode potential prediction accuracy down to 2.6 mV RMSE, as illustrated in Fig. 11. Again, model training and validation has been performed with a P2D battery model only. The hardware implementation of the model has been addressed for further studies. From a real-time deployment perspective, the model achieving the lowest anode potential prediction error was stated to require approximately 100 MB of memory space. As can be seen in the aforementioned studies, data-driven models have not been used for anode potential reserve control in real-time experimental setups yet, but show promising potential in increasing the benefit-cost relation due to decreased calculational requirements.

4. Discussion

While many approaches proposed solutions to issues associated with the determination of health-aware fast charging strategies, many aspects have still not been investigated comprehensively, but offer the potential to successfully transfer research results into automotive applications if investigated. The subsequent sections will summarize the main points of interest from an application-oriented perspective.

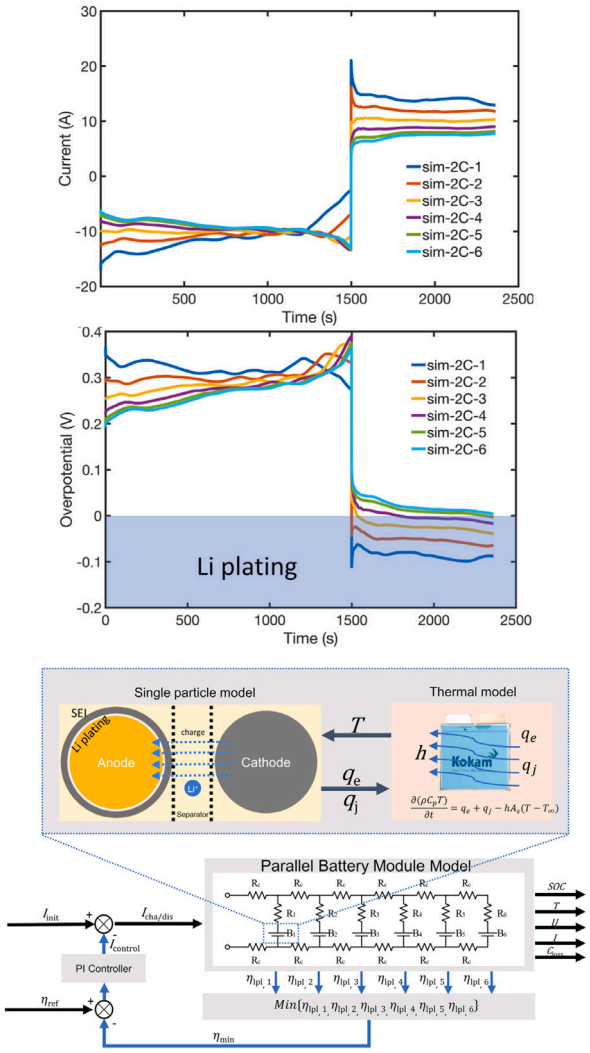

Fig. 10. Model-based evaluation of the anode potential of all cells in a 1s6p battery module during fast charging. Currents of the individual cells (top figure) with their corresponding anode potentials exceeding the theoretical limit for lithium deposition below 0 V (center figure). The deployed model consists of a SPM coupled to a thermal model embedded into a system model and an anode potential control loop (bottom figure). The figures have been reproduced in its unmodified form from [138].

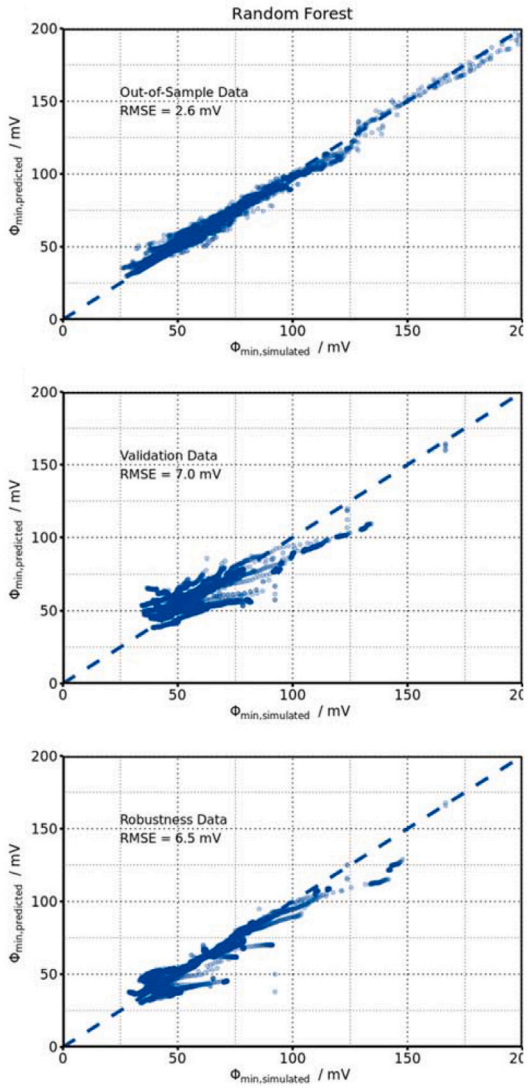

Fig. 11. Excerpt of the validation of a data-based model showing the predicted anode potential $\Phi_{\text{min,predicted}}$ over the reference simulation $\Phi_{\text{min,simulated}}$ for three different validation scenarios (top to bottom). The figure has been reproduced in its unmodified form from [104].

4.1. Adaptability of fast-charging strategy determination methods

The projection to other cell types of currently developed approaches is still time- and resource-intensive, in particular if heuristic studies are carried out. Design of experiment (DOE) approaches are frequently used, e.g. [91], to ease the fast charge strategy determination by deploying lesser cells than in a full fractional approach. However, many battery cells still have to be cycled until their EOL to reveal and identify the most promising fast charging strategies. Recent research, e.g. [93,141], tackled the problem of heuristic studies with machine learning-based lifetime estimations; however, the developed procedure still demands appropriate machine learning models to be crafted involving appropriate data and hyperparameter tuning, which has to be assessed prior to cycle life projection and is dependent on available data of the investigated cell chemistry and type. Also, it is still not completely clarified how those data-driven models have to be trained and applied to achieve reliable results and should be addressed by future research.

On the other hand, model-supported approaches offer the potential of performing less aging tests due to their physical motivation; however, intensive cell characterization effort is needed upfront to model deployment to achieve an accurate replica of the cell behavior. Many parameters must be determined and can only be separated if half-cells of both electrodes are built in laboratory-scaled samples and their properties are experimentally determined. Beyond the considered electrode-specific limitations, ionic concentration dynamics must be considered and are usually fitted from literature values to full cell measurements. Moreover, thermal behavior of the investigated cell has to be characterized alongside by repeating the characterization procedure at various temperature levels. If a new cell chemistry is investigated, this approach has to be repeated. In contrast to heuristic approaches, however, after parallelizable effort upfront to deployment, a carefully crafted model then enables health-aware fast charging without the need for many aging experiments with broad parameter variations.

Further research is needed to develop methods to determine fast charging strategies, keeping the characterization effort at a minimum, e.g., for model-supported approaches, and avoiding the need for multiple cells in long-term cycle life experiments, e.g., heuristic approaches. Novel methods, which are adaptive to any lithium-ion battery type, offer the potential to speed up the fast-charging strategy determination

process. This may be helpful for an early assessment of the fast charging capability of new cell types or BMS developers, which do not have the opportunity of long-term cycle life experiments and *post-mortem* cell investigation. Since model-supported approaches inherently provide for these possibilities, these approaches are particularly promising. In here, reduced order models or data-driven models fed by simulation and/or real-world data can further simplify the implementation effort, increasing the practicality of model-based fast charging strategies and investigations should therefore be intensified in this field of research.

4.2. Consideration of electro-thermal interdependencies

As internal impedance of lithium-ion batteries rises with lower temperatures, lithium deposition is more likely to occur. If electro-thermal interdependencies are modeled, internal cell preheating leads to a fast decrease in anode overpotential and high cell temperatures during a fast charge event. Therefore, thermal limitations can be identified as a major reason for accelerated battery aging at high ambient temperatures. However, lower ambient temperatures during a fast charging event can also be expected during operation, in particular if battery electric vehicles are frequently fast charged due to missing an overnight charging opportunity and/or cannot be thermally conditioned fast enough. While higher ambient temperatures primarily lead to thermal limitations as overpotentials are degraded but SEI growth is accelerated, lower ambient temperatures primarily lead to anode overpotential limitations due to slow diffusion kinetics in the active material. As revealed within this review, studies mainly focused on a single effect, either electrical or thermal, without considering both parameters concurrently. We hypothesize that the optimal fast charging control in terms of either anode potential or thermal losses lead to a similar charging current profile; that is, an upfront higher current steadily decreasing with SOC. Beyond that, also the effect of the cell's initial condition (e.g., initial SOC, temperature) on the health-awareness are not yet studied comprehensively.

Further studies are needed which incorporate both electrical and thermal effects and proof their approach for different initial cell states and in different scenarios, i.e., a subzero and a preconditioned scenario.

4.3. Accuracy-performance dilemma of model-supported strategies

At first glance, the model fidelity of model-based fast charging strategies should be high to achieve accurate model predictions. However, high degrees of model discretization concurrently lead to increased computational effort to solve the involved partial differential equations [137]. A dilemma arises, which poses the question of whether algorithms should aim at high model fidelity, taking into account longer calculational times but achieving more accurate predictions of, e.g., anode potential, or whether algorithms should aim at yielding low calculational effort to increase accuracy by higher sampling, as illustrated in Fig. 12.

To date, no robust real-time application benchmark of model-based fast charging strategies has been performed, highlighting the need to assess the performance in online setups. Comparative studies of different model fidelities are required to map model accuracy on battery lifetime performance.

4.4. Parameterization and validation of model-supported approaches

Model-supported approaches promise high accuracy and consequently maximum exploited fast charging potential of the lithium-ion batteries due to their electro-chemical motivation and their possibility to adapt to a specific cell behavior. The accuracy of model-supported approaches mainly depends on the accuracy of its parameter determination, which is usually done by relying on literature values, e.g., [135], or by a thorough material and tear-down analysis of the single cell components, e.g., [137]. Both techniques rely on measurements, which

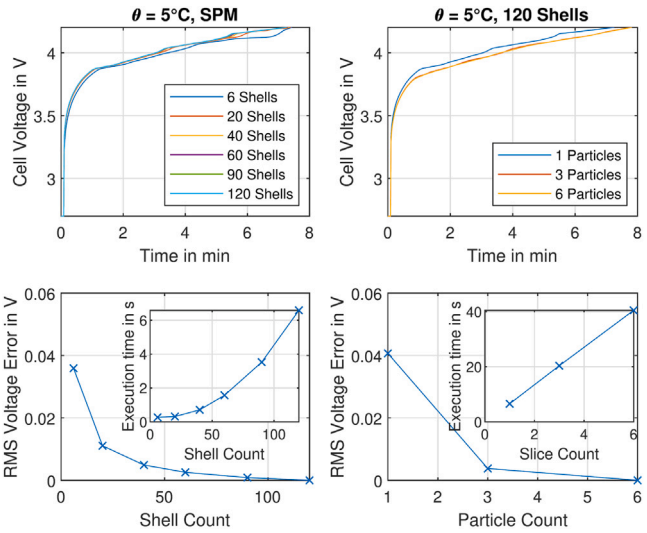

Fig. 12. Model error in voltage prediction of different degrees of model reduction. With decreasing calculational burden, i.e., less discretizations within the active material (shell count, left) or less particles simulated (particle/slice count, right), model accuracy is also reduced, which may interfere with the subsequent fast charging current control. The figures have been reproduced in their unmodified form from [137].

are performed on the cell component level and are measured with the underlying assumption that the results are still accurate if scaled from a fractional cell to a full-scale lithium-ion battery or system. Model response may therefore be inaccurate on the first try and because of this many authors manually tune the critical parameter to adapt cell and system behavior, e.g. [127,129,132].

Yet, a method has to be developed in order to accurately parameterize electro-chemical models with a specifically defined procedure which separates half cell behavior but does not neglect the to-be-achieved full cell behavior of the lithium-ion battery. Hybridization of the different modeling approaches and parameterization techniques may help to dissolve this dilemma and should be further investigated. Moreover, broad validation has to be carried out and the degree of accuracy of the model response to measurements must be discussed in fast charging studies, as inaccuracies have a major lever on, e.g., the theoretical lithium deposition criteria. Accessible cloud-based data can serve as an additional validation opportunity to adjust model parameter and extent the validation during operation of the battery system.

4.5. Closed-loop model design for model-supported strategies

Despite the open-loop nature of heuristic approaches, many of the presented model-based studies also investigate fast charging strategies, which are set up open-loop and do not capture disturbances of real-world applications. Especially studies that capture model-supported approaches based on external cell states are often only optimized offline to a specific cell state. If variations to the parameters occur, e.g., due to different electric and thermal loads in the application, the optimality may be jeopardized. However, real-time model-based fast charging strategies based on internal cell states are also affected. On a short-term scale, model initialization and parameterization coupled with measurement bias, error, and distortions might lead to incorrect prediction of the cell behavior and therefore hazardous control of the charging current. Here, a critical condition evolves at the beginning of the fast charge, as the SOC has to be initialized correctly to yield an accurate anode potential prediction which is directly fed into the current control loop. On a long-term scale, aging effects may further reduce the model accuracy. The latter is a special case addressed in Section 4.6 hereinafter.

Based on the analysis and discussion provided, there is no consensus on how to account for parameter and measurement errors and the resulting influence on the health-aware fast charging strategies during the lithium-ion battery life cycle. Additional studies investigating the aforementioned issues are required.

4.6. Aging consideration and derating strategies

For both heuristic and model-supported approaches, varying cell condition and behavior over the battery life have to be considered, as it directly influences the fast charging capability of the lithium-ion batteries under study. Since the longest-lasting battery is chosen within heuristic studies and model-supported approaches without a coupled derating strategy, especially in the beginning of the cycle life, the fast charge capability of the battery may be underestimated. To the best of the authors' knowledge, only a few authors include derating strategies to directly reduce the applied fast charging current based on the actual SOH of the cell in their studies [108,109,124]. However, only a relative capacity decline and resistance increase determined in the time-domain has been considered. Two other studies directly couple aging models with the fast charging control [129,133], while it is not clear whether those aging models are superior to an update based on the actual SOH commonly determined online in BEV applications.

Derating strategies should be further investigated, tackling the evolving differences in capacity, impedance, and electrode balancing over age and investigating the impact of derating strategy over the battery life, i.e., fast charging times over battery life.

4.7. Proof of concept and upscale to the application level

Almost all fast-charging studies, except [108,138], do not scale their fast charging strategies to the higher system or application level. Many effects at the system level may deteriorate the cycle life achieved at the cell level, impeding the transfer of those strategies to the application level.

As BMSs only control the charging current at a few spots distributed through the module, electrical and thermal variations in serial and parallel connections are difficult to consider within the control strategy and may lead to unobserved cell behavior [151]. The imbalance in serial connection might be easier to control for closed-loop model-supported approaches, since terminal voltages on each level are measured and can be fed back. However, imbalances in parallel connections might be more difficult to trace, due to the absence of a cell-specific measurement signal. Splitting current in parallel connections may lead to an underestimation of battery states and therefore overestimation of the acceptable fast-charging current. For example, if two parallel connected cells with a varying capacity are fast charged, the current distribution over time will change due to differences in SOC and impedance. This can lead to the current control limits being exceeded. These varying battery states arise in part by inter-cell resistances and their non-uniform electrical contact overpotentials. In the case of pulse or cyclic charging methods, these effects cannot compensate the mentioned differences, because the time it takes the parallel string to redistribute the load is in the order of hundreds of seconds and is expected to take even longer with rising cell capacity [152]. Non-uniform overpotentials may also lead to uneven thermal losses [153]. As discussed by Yang et al. [138], the placement of the load point in a battery system also results in differences of inter-cell resistances, which then lead to different fast-charging currents for each cell. Furthermore, as already pointed out by Chu et al. [127] and Ringbeck et al. [137], parameter deviations, model and state errors and ambiguities, and measurement errors must be considered, especially for model-based anode potential reserve strategies: the theoretical limit of 0 V may not be sufficient from an application-oriented perspective. All these effects mentioned above can result in a non-uniform load and temperature distribution, which may lead to an earlier aging of the overall system compared to the single cell. Tanim et al. [154] demonstrated the severity of evolving parameter deviations in a battery system over time, mainly traced back to thermal inhomogeneities, if only 50 kW CCCV fast charging is applied to a 24 kW h battery system with passive thermal management. The study shows that thermal effects pose a strong influence on the fast charging strategy and have to be considered when scaling up from the cell to system level.

In addition to the thermal and electric interactions between multiple cells, there are also indirect control opportunities for battery cells at the application level, such as active battery thermal management system (BTMS) strategies, which have a large lever on the optimality of the fast charging strategy. The battery system temperature can differ from −20 °C up to 50 °C during operation, because of the varying ambient temperature in different climatic regions. Therefore, heating or cooling, depending on the ambient temperature, to a specific narrow temperature window prior to or during a fast-charge event has to be considered if fast charging strategies are investigated. Here, it is still not completely clear how the thermal management interacts with advanced fast charging strategies and how to properly set the thermal control limits over time. As battery system cooling is commonly realized by vapor compression cycles [155,156], active thermal management control strategies in combination with advanced fast charging strategies should be further investigated. While external heating strategies have benefits in their low system costs and reliability, disadvantages in energy efficiency and temperature uniformity are present [157]. Therefore, internal heating strategies, like mutual pulse heating [158], show more promising results in these aspects, but are still not completely understood with regard to their aging effect in the context of fast charging.

Many aspects of system interdependencies of many cells integrated in electric powertrains are still unknown, which is why model-based electro-thermal optimizations and proof of concepts at the application level are needed in order to increase the cycle life and maintain the safety of fast-charged battery systems. In addition, the boundary conditions of thermal management systems have to be considered to draw reliable conclusions for real-world scenarios.

5. Conclusions and further need for research

This work summarized recent research in the field of health-aware fast charging from an application-oriented perspective. An overview on today's limitations on the battery cell and system level is given, emphasizing the need for model-supported design strategies and advanced algorithms for battery management in electric vehicles. Over 50 approaches tackling the challenge of determining health-aware fast charging strategies have been summarized, clustered, and compared. Potential research gaps for further development have been deduced and can be summarized as follows:

- **Further development, implementation and utilization of adaptive model-supported approaches.**
  Heuristic studies have been widely performed to determine health-aware fast charging strategies in the past. The lack of physical insights during crafting of the test procedures poses the need for extensive lab testing and impede an effective approach. We believe that efforts should be shifted to model-supported approaches based on battery internal states, as it closes the link between the physical battery behavior and fast charging current control and enables the reaction to rapidly changing cell properties, which may be an early-indicator for hazardous safety risks. Also, such models can be easily customized to other active material combinations and formats, enabling flexibility to new materials and better adjustments to the impact of design, e.g., increased inhomogeneities in large-format cells. Here, research is needed to clarify how those models should be crafted or hybridized and adjusted to be the most suitable for real-world applications. Furthermore, electro-thermal interdependencies have to be modeled if fast charging strategies are investigated.

- **Simplified parameterization and extended validation.**
  Model-supported approaches including the use of battery-internal states still lack an applicable parameterization technique. While parameter determinations at the material level lead to high inaccuracies in scaling at the cell and system level, top-down approaches by generic fitting methods at the cell and system level suffer from inaccuracies caused by state ambiguities at the material level. Comprehensible procedures are needed to determine model parameter as precise as necessary while putting the achieved parameter into context with the measurable quantities at the cell and system level. Lab effort has to be kept at a minimum to sustain fast development speed despite rapidly changing battery system chemistries, formats, and architectures.
- **Experimental proof of concepts.**
  Experimental investigation of health-aware fast charging strategies has been mainly presented for ambient temperatures around 25 °C only, while common automotive applications operate in a wider temperature range; usually between −20 °C to 50 °C. If the results are not projected to other temperature levels, it is unclear whether the fast charging strategy is capable of avoiding critical operating conditions. Thus, the robustness of the determined strategy cannot be sufficiently evaluated from an application perspective. The case of low to subzero ambient temperatures especially should be considered, as impedance rise to lower temperatures render this scenario most challenging for health-aware fast charging strategies.
- **Investigation of derating strategies.**
  The importance of the adaption of fast charging strategies to the actual SOH of the battery has been recently emphasized in the literature as degrading performance impacts the fast charging capability of the cell. However, only a few studies consider derating strategies and their impact on the cycle life during fast charging. Further studies are needed on how to effectively derate the charging current of lithium-ion batteries to sustain a health-aware fast charging strategy over the cycle life of the battery system.
- **Upscale to the system and application level.**
  Many effects present at the system level, such as unbalanced currents in parallel and serial connected cells, different thermal management systems, thermal control strategies, or thermal interdependencies with other powertrain components, and their impact on fast charging are still unknown. High currents at the beginning of a fast charge may lead to inhomogeneous thermal behavior of cells connected in serial and parallel, resulting in high thermal gradients within the system and the risk of local overcharge situations. Also, thermal management systems may increase the likelihood of lithium deposition at the cooling interface, which is not considered if cell tests without thermal control are only performed. The projection of health-aware fast charging strategies to the system level plays an important role in increasing the technology maturity for real-world applications.

We believe that major steps towards an automotive fast charging time target of below 15 min without severe aging, reliable safety, and overall satisfactory vehicle range can be made today, if the right commercial battery cells are chosen and the fast charging strategy deployed in the BMS takes into account critical battery states and system interdependencies.

CRediT authorship contribution statement

Nikolaos Wassiliadis: Conceptualization, Methodology, Investigation, Validation, Data curation, Writing – original draft, Visualization. **Jakob Schneider:** Writing – original draft. **Alexander Frank:** Writing – original draft. **Leo Wildfeuer:** Writing – review & editing. **Xue Lin:** Writing – review & editing. **Andreas Jossen:** Writing – review & editing, Resources, Supervision. **Markus Lienkamp:** Writing – review & editing, Resources, Supervision.

Declaration of competing interest

The authors declare that they have no known competing financial interests or personal relationships that could have appeared to influence the work reported in this paper.

Acknowledgments

The authors would like to thank Florian Schmid for providing the opportunity to record data of the VW ID.3 and Tesla Model 3. Also, we thank Jakob Weiss and Ann-Sophie Zollner for their contributions to the electric vehicle benchmark during their Master's studies. This research was partly funded by the German Federal Ministry for Economic Affairs and Energy (BMWi) within the project "ultraBatt" under grant number 01MV21015D, within the project "NEFTON" under grant number 01MV21004A and partly funded by the German Federal Ministry of Education and Research (BMBF) within the project "InnoCase" under grant number 03XP0207F.

References

[1] European Environment Agency, Electric Vehicles in Europe, EEA Report, European Environment Agency, Copenhagen, 2021, URL http://www.worldcat.org/oclc/967495004. [accessed on 21.07.2021].

[2] D. Pevec, J. Babic, A. Carvalho, Y. Ghiassi-Farrokhfal, W. Ketter, V. Podobnik, A survey-based assessment of how existing and potential electric vehicle owners perceive range anxiety, J. Clean. Prod. 276 (2020) 122779, http://dx.doi.org/10.1016/j.jclepro.2020.122779.

[3] N.S. Pearre, W. Kempton, R.L. Guensler, V.V. Elango, Electric vehicles: How much range is required for a day's driving? Transp. Res. C 19 (6) (2011) 1171–1184, http://dx.doi.org/10.1016/j.trc.2010.12.010.

[4] C. Michelbacher, S. Ahmed, I. Bloom, A. Burnham, B. Carlson, F. Dias, E.J. Dufek, A.N. Jansen, M. Keyser, A. Markel, A. Meintz, M. Mohanpurkar, A. Pesaran, D. Scoffield, M. Shirk, T. Stephens, T. Tanim, R. Vijayagopal, J. Zhang, Enabling fast charging – Introduction and overview, J. Power Sources 367 (2017) 214–215, http://dx.doi.org/10.1016/j.jpowsour.2017.08.008.

[5] S. Ahmed, I. Bloom, A.N. Jansen, T. Tanim, E.J. Dufek, A. Pesaran, A. Burnham, R.B. Carlson, F. Dias, K. Hardy, M. Keyser, C. Kreuzer, A. Markel, A. Meintz, C. Michelbacher, M. Mohanpurkar, P.A. Nelson, D.C. Robertson, D. Scoffield, M. Shirk, T. Stephens, R. Vijayagopal, J. Zhang, Enabling fast charging – A battery technology gap assessment, J. Power Sources 367 (2017) 250–262, http://dx.doi.org/10.1016/j.jpowsour.2017.06.055.

[6] M. Keyser, A. Pesaran, Q. Li, S. Santhanagopalan, K. Smith, E. Wood, S. Ahmed, I. Bloom, E. Dufek, M. Shirk, A. Meintz, C. Kreuzer, C. Michelbacher, A. Burnham, T. Stephens, J. Francfort, B. Carlson, J. Zhang, R. Vijayagopal, K. Hardy, F. Dias, M. Mohanpurkar, D. Scoffield, A.N. Jansen, T. Tanim, A. Markel, Enabling fast charging – Battery thermal considerations, J. Power Sources 367 (2017) 228–236, http://dx.doi.org/10.1016/j.jpowsour.2017.07.009.

[7] A. Meintz, J. Zhang, R. Vijayagopal, C. Kreutzer, S. Ahmed, I. Bloom, A. Burnham, R.B. Carlson, F. Dias, E.J. Dufek, J. Francfort, K. Hardy, A.N. Jansen, M. Keyser, A. Markel, C. Michelbacher, M. Mohanpurkar, A. Pesaran, D. Scoffield, M. Shirk, T. Stephens, T. Tanim, Enabling fast charging – Vehicle considerations, J. Power Sources 367 (2017) 216–227, http://dx.doi.org/10.1016/j.jpowsour.2017.07.093.

[8] A. Burnham, E.J. Dufek, T. Stephens, J. Francfort, C. Michelbacher, R.B. Carlson, J. Zhang, R. Vijayagopal, F. Dias, M. Mohanpurkar, D. Scoffield, K. Hardy, M. Shirk, R. Hovsapian, S. Ahmed, I. Bloom, A.N. Jansen, M. Keyser, C. Kreuzer, A. Markel, A. Meintz, A. Pesaran, T.R. Tanim, Enabling fast charging – Infrastructure and economic considerations, J. Power Sources 367 (2017) 237–249, http://dx.doi.org/10.1016/j.jpowsour.2017.06.079#.

[9] D. Howell, S. Boyd, B. Cunningham, S. Gillard, L. Slezak, Enabling Fast Charging: A Technology Gap Assessment, Technical Report, 2017, http://dx.doi.org/10.2172/1416167.

[10] European Technology and Innovation Platform, Batteries - towards a competitive European industrial battery value chain for stationary applications and e-mobility: Draft proposal, 2021, URL https://ec.europa.eu/info/sites/info/files/research_and_innovation/funding/documents/ec_rtd_he-partnerships-european-industrial-battery-value-chain.pdf. (accessed on 21.07.2021).

[11] G.E. Blomgren, The development and future of lithium ion batteries, J. Electrochem. Soc. 164 (1) (2017) A5019–A5025, http://dx.doi.org/10.1149/2.0251701jes.

[12] J. Schmalstieg, C. Rahe, M. Ecker, D.U. Sauer, Full cell parameterization of a high-power lithium-ion battery for a physico-chemical model: Part I. Physical and electrochemical parameters, J. Electrochem. Soc. 165 (16) (2018) A3799–A3810, http://dx.doi.org/10.1149/2.0321816jes.

[13] ev-database.org, Electric vehicle database, 2020, URL https://ev-database.org/. (accessed on 21.07.2021).

[14] T.S. Bryden, G. Hilton, A. Cruden, T. Holton, Electric vehicle fast charging station usage and power requirements, Energy 152 (2018) 322–332, http://dx.doi.org/10.1016/j.energy.2018.03.149.

[15] Y. Motoaki, W. Yi, S. Salisbury, Empirical analysis of electric vehicle fast charging under cold temperatures, Energy Policy 122 (2018) 162–168, http://dx.doi.org/10.1016/j.enpol.2018.07.036.

[16] G. Trentadue, A. Lucas, M. Otura, K. Pliakostathis, M. Zanni, H. Scholz, Evaluation of fast charging efficiency under extreme temperatures, Energies 11 (8) (2018) 1937, http://dx.doi.org/10.3390/en11081937.

[17] J. Vetter, P. Novák, M.R. Wagner, C. Veit, K.-C. Möller, J.O. Besenhard, M. Winter, M. Wohlfahrt-Mehrens, C. Vogler, A. Hammouche, Ageing mechanisms in lithium-ion batteries, J. Power Sources 147 (1–2) (2005) 269–281, http://dx.doi.org/10.1016/j.jpowsour.2005.01.006.

[18] A. König, L. Nicoletti, D. Schröder, S. Wolff, A. Waclaw, M. Lienkamp, An overview of parameter and cost for battery electric vehicles, World Electr. Veh. J. 12 (1) (2021) 21, http://dx.doi.org/10.3390/wevj12010021.

[19] P. Keil, A. Jossen, Charging protocols for lithium-ion batteries and their impact on cycle life—An experimental study with different 18650 high-power cells, J. Energy Storage 6 (2016) 125–141, http://dx.doi.org/10.1016/j.est.2016.02.005.

[20] Y. Liu, Y. Zhu, Y. Cui, Challenges and opportunities towards fast-charging battery materials, Nature Energy 4 (7) (2019) 540–550, http://dx.doi.org/10.1038/s41560-019-0405-3.

[21] H. Zhao, L. Wang, Z. Chen, X. He, Challenges of fast charging for electric vehicles and the role of red phosphorous as anode material: Review, Energies 12 (20) (2019) 3897, http://dx.doi.org/10.3390/en12203897.

[22] W. Xie, X. Liu, R. He, Y. Li, X. Gao, X. Li, Z. Peng, S. Feng, X. Feng, S. Yang, Challenges and opportunities toward fast-charging of lithium-ion batteries, J. Energy Storage 32 (2020) 101837, http://dx.doi.org/10.1016/j.est.2020.101837.

[23] A. Tomaszewska, Z. Chu, X. Feng, S. O'Kane, X. Liu, J. Chen, C. Ji, E. Endler, R. Li, L. Liu, Y. Li, S. Zheng, S. Vetterlein, M. Gao, J. Du, M. Parkes, M. Ouyang, M. Marinescu, G. Offer, B. Wu, Lithium-ion battery fast charging: A review, ETransportation 1 (2019) 100011, http://dx.doi.org/10.1016/j.etran.2019.100011.

[24] S.S. Zhang, Challenges and strategies for fast charge of li-ion batteries, ChemElectroChem 7 (17) (2020) 3569–3577, http://dx.doi.org/10.1002/celc.202000650.

[25] W. Shen, T.T. Vo, A. Kapoor, Charging algorithms of lithium-ion batteries: An overview, in: 2012 7th IEEE Conference on Industrial Electronics and Applications (ICIEA), IEEE, 2012, pp. 1567–1572, http://dx.doi.org/10.1109/ICIEA.2012.6360973.

[26] Y. Gao, X. Zhang, Q. Cheng, B. Guo, J. Yang, Classification and review of the charging strategies for commercial lithium-ion batteries, IEEE Access 7 (2019) 43511–43524, http://dx.doi.org/10.1109/ACCESS.2019.2906117.

[27] D. Myall, D. Ivanov, W. Larason, M. Nixon, H. Moller, Accelerated Reported Battery Capacity Loss in 30 kWh Variants of the Nissan Leaf, 2018, http://dx.doi.org/10.20944/preprints201803.0122.v1.

[28] A.G. Porsche, Mission e, Christopherus (387) (2018) URL https://newsroom.porsche.com/en/products/porsche-taycan-mission-e-drive-unit-battery-charging-electro-mobility-dossier-sportscar-production-christophorus-387-15827.html. accessed on 21.07.2021.

[29] H. Yang, J. Lee, Hyundai Motor to replace battery systems in $900 mln electric car recall, 2021, URL https://www.reuters.com/article/us-hyundai-motor-electric-recall-idUSKBN2AO0JS. (accessed on 21.07.2021).

[30] W. Waag, C. Fleischer, D.U. Sauer, Critical review of the methods for monitoring of lithium-ion batteries in electric and hybrid vehicles, J. Power Sources 258 (2014) 321–339, http://dx.doi.org/10.1016/j.jpowsour.2014.02.064.

[31] T. Amietszajew, E. McTurk, J. Fleming, R. Bhagat, Understanding the limits of rapid charging using instrumented commercial 18650 high-energy Li-ion cells, Electrochim. Acta 263 (2018) 346–352, http://dx.doi.org/10.1016/j.electacta.2018.01.076.

[32] M. Dubarry, B.Y. Liaw, M.-S. Chen, S.-S. Chyan, K.-C. Han, W.-T. Sie, S.-H. Wu, Identifying battery aging mechanisms in large format Li ion cells, J. Power Sources 196 (7) (2011) 3420–3425, http://dx.doi.org/10.1016/j.jpowsour.2010.07.029.

[33] C.R. Birkl, M.R. Roberts, E. McTurk, P.G. Bruce, D.A. Howey, Degradation diagnostics for lithium ion cells, J. Power Sources 341 (2017) 373–386, http://dx.doi.org/10.1016/j.jpowsour.2016.12.011.

[34] S.S. Zhang, K. Xu, T.R. Jow, Study of the charging process of a LiCoO2-based Li-ion battery, J. Power Sources 160 (2) (2006) 1349–1354, http://dx.doi.org/10.1016/j.jpowsour.2006.02.087.

[35] M.W. Verbrugge, B.J. Koch, The effect of large negative potentials and overcharge on the electrochemical performance of lithiated carbon, J. Electroanal. Chem. 436 (1–2) (1997) 1–7, http://dx.doi.org/10.1016/S0022-0728(97)00031-4.

[36] T. Waldmann, B.-I. Hogg, M. Kasper, S. Grolleau, C.G. Couceiro, K. Trad, B.P. Matadi, M. Wohlfahrt-Mehrens, Interplay of operational parameters on lithium deposition in lithium-ion cells: Systematic measurements with reconstructed 3-electrode pouch full cells, J. Electrochem. Soc. 163 (7) (2016) A1232–A1238, http://dx.doi.org/10.1149/2.0591607jes.

[37] T. Waldmann, B.-I. Hogg, M. Wohlfahrt-Mehrens, Li plating as unwanted side reaction in commercial Li-ion cells – A review, J. Power Sources 384 (2018) 107–124, http://dx.doi.org/10.1016/j.jpowsour.2018.02.063.

[38] C. von Lüders, J. Keil, M. Webersberger, A. Jossen, Modeling of lithium plating and lithium stripping in lithium-ion batteries, J. Power Sources 414 (2019) 41–47, http://dx.doi.org/10.1016/j.jpowsour.2018.12.084.

[39] K. Persson, V.A. Sethuraman, L.J. Hardwick, Y. Hinuma, Y.S. Meng, A. van der Ven, V. Srinivasan, R. Kostecki, G. Ceder, Lithium diffusion in graphitic carbon, J. Phys. Chem. Lett. 1 (8) (2010) 1176–1180, http://dx.doi.org/10.1021/jz100188d.

[40] J. Wandt, P. Jakes, J. Granwehr, R.-A. Eichel, H.A. Gasteiger, Quantitative and time-resolved detection of lithium plating on graphite anodes in lithium ion batteries, Mater. Today 21 (3) (2018) 231–240, http://dx.doi.org/10.1016/j.mattod.2017.11.001.

[41] Q. Liu, C. Du, B. Shen, P. Zuo, X. Cheng, Y. Ma, G. Yin, Y. Gao, Understanding undesirable anode lithium plating issues in lithium-ion batteries, RSC Adv. 6 (91) (2016) 88683–88700, http://dx.doi.org/10.1039/c6ra19482f.

[42] Z. Li, J. Huang, B. Yann Liaw, V. Metzler, J. Zhang, A review of lithium deposition in lithium-ion and lithium metal secondary batteries, J. Power Sources 254 (2014) 168–182, http://dx.doi.org/10.1016/j.jpowsour.2013.12.099.

[43] N. Legrand, B. Knosp, P. Desprez, F. Lapicque, S. Raël, Physical characterization of the charging process of a Li-ion battery and prediction of Li plating by electrochemical modelling, J. Power Sources 245 (2014) 208–216, http://dx.doi.org/10.1016/j.jpowsour.2013.06.130.

[44] S. Hein, A. Latz, Influence of local lithium metal deposition in 3D microstructures on local and global behavior of Lithium-ion batteries, Electrochim. Acta 201 (2016) 354–365, http://dx.doi.org/10.1016/j.electacta.2016.01.220.

[45] D. Ren, K. Smith, D. Guo, X. Han, X. Feng, L. Lu, M. Ouyang, J. Li, Investigation of lithium plating-stripping process in li-ion batteries at low temperature using an electrochemical model, J. Electrochem. Soc. 165 (10) (2018) A2167–A2178, http://dx.doi.org/10.1149/2.0661810jes.

[46] C. Mao, R.E. Ruther, J. Li, Z. Du, I. Belharouak, Identifying the limiting electrode in lithium ion batteries for extreme fast charging, Electrochem. Commun. 97 (2018) 37–41, http://dx.doi.org/10.1016/j.elecom.2018.10.007.

[47] S.S. Zhang, Identifying rate limitation and a guide to design of fast-charging Li-ion battery, InfoMat 2 (5) (2020) 942–949, http://dx.doi.org/10.1002/inf2.12058.

[48] S.-B. Son, D. Robertson, Z. Yang, Y. Tsai, S. Lopykinski, I. Bloom, Fast charge-driven Li plating on anode and structural degradation of cathode, J. Electrochem. Soc. 167 (14) (2020) 140506, http://dx.doi.org/10.1149/1945-7111/abc031.

[49] G. Zhang, X. Wei, G. Han, H. Dai, J. Zhu, X. Wang, X. Tang, J. Ye, Lithium plating on the anode for lithium-ion batteries during long-term low temperature cycling, J. Power Sources 484 (2021) 229312, http://dx.doi.org/10.1016/j.jpowsour.2020.229312.

[50] M. Petzl, M. Kasper, M.A. Danzer, Lithium plating in a commercial lithium-ion battery – a low-temperature aging study, J. Power Sources 275 (2015) 799–807, http://dx.doi.org/10.1016/j.jpowsour.2014.11.065.

[51] X.-G. Yang, Y. Leng, G. Zhang, S. Ge, C.-Y. Wang, Modeling of lithium plating induced aging of lithium-ion batteries: Transition from linear to nonlinear aging, J. Power Sources 360 (2017) 28–40, http://dx.doi.org/10.1016/j.jpowsour.2017.05.110.

[52] T.C. Bach, S.F. Schuster, E. Fleder, J. Müller, M.J. Brand, H. Lorrmann, A. Jossen, G. Sextl, Nonlinear aging of cylindrical lithium-ion cells linked to heterogeneous compression, J. Energy Storage 5 (2016) 212–223, http://dx.doi.org/10.1016/j.est.2016.01.003.

[53] X. Lai, C. Jin, W. Yi, X. Han, X. Feng, Y. Zheng, M. Ouyang, Mechanism, modeling, detection, and prevention of the internal short circuit in lithium-ion batteries: Recent advances and perspectives, Energy Storage Mater. 35 (2021) 470–499, http://dx.doi.org/10.1016/j.ensm.2020.11.026.

[54] T. Waldmann, J.B. Quinn, K. Richter, M. Kasper, A. Tost, A. Klein, M. Wohlfahrt-Mehrens, Electrochemical, post-mortem, and ARC analysis of li-ion cell safety in second-life applications, J. Electrochem. Soc. 164 (13) (2017) A3154–A3162, http://dx.doi.org/10.1149/2.0961713jes.

[55] J. Du, Y. Liu, X. Mo, Y. Li, J. Li, X. Wu, M. Ouyang, Impact of high-power charging on the durability and safety of lithium batteries used in long-range battery electric vehicles, Appl. Energy 255 (2019) 113793, http://dx.doi.org/10.1016/j.apenergy.2019.113793.

[56] R. Fong, U. von Sacken, J.R. Dahn, Studies of lithium intercalation into carbons using nonaqueous electrochemical cells, J. Electrochem. Soc. 137 (7) (1990) 2009–2013, http://dx.doi.org/10.1149/1.2086855.

[57] S. Choi, G. Jung, J.E. Kim, T. Kim, K.S. Suh, Lithium intercalated graphite with preformed passivation layer as superior anode for lithium ion batteries, Appl. Surf. Sci. 455 (2018) 367–372, http://dx.doi.org/10.1016/j.apsusc.2018.05.229.

[58] S.J. An, J. Li, C. Daniel, D. Mohanty, S. Nagpure, D.L. Wood, The state of understanding of the lithium-ion-battery graphite solid electrolyte interphase (SEI) and its relationship to formation cycling, Carbon 105 (2016) 52–76, http://dx.doi.org/10.1016/j.carbon.2016.04.008.

[59] M.-T.F. Rodrigues, F.N. Sayed, H. Gullapalli, P.M. Ajayan, High-temperature solid electrolyte interphases (SEI) in graphite electrodes, J. Power Sources 381 (2018) 107–115, http://dx.doi.org/10.1016/j.jpowsour.2018.01.070.

[60] T. Waldmann, M. Wilka, M. Kasper, M. Fleischhammer, M. Wohlfahrt-Mehrens, Temperature dependent ageing mechanisms in Lithium-ion batteries – A Post-Mortem study, J. Power Sources 262 (2014) 129–135, http://dx.doi.org/10.1016/j.jpowsour.2014.03.112.

[61] X.-G. Yang, C.-Y. Wang, Understanding the trilemma of fast charging, energy density and cycle life of lithium-ion batteries, J. Power Sources 402 (2018) 489–498, http://dx.doi.org/10.1016/j.jpowsour.2018.09.069.

[62] Y. Zhu, J. Xie, A. Pei, B. Liu, Y. Wu, D. Lin, J. Li, H. Wang, H. Chen, J. Xu, A. Yang, C.-L. Wu, H. Wang, W. Chen, Y. Cui, Fast lithium growth and short circuit induced by localized-temperature hotspots in lithium batteries, Nature Commun. 10 (1) (2019) 2067, http://dx.doi.org/10.1038/s41467-019-09924-1.

[63] A.S. Mussa, A. Liivat, F. Marzano, M. Klett, B. Philippe, C. Tengstedt, G. Lindbergh, K. Edström, R.W. Lindström, P. Svens, Fast-charging effects on ageing for energy-optimized automotive LiNi1/3Mn1/3Co1/3O2/graphite prismatic lithium-ion cells, J. Power Sources 422 (2019) 175–184, http://dx.doi.org/10.1016/j.jpowsour.2019.02.095.

[64] K. Jalkanen, J. Karppinen, L. Skogström, T. Laurila, M. Nisula, K. Vuorilehto, Cycle aging of commercial NMC/graphite pouch cells at different temperatures, Appl. Energy 154 (2015) 160–172, http://dx.doi.org/10.1016/j.apenergy.2015.04.110.

[65] Q. Wang, P. Ping, X. Zhao, G. Chu, J. Sun, C. Chen, Thermal runaway caused fire and explosion of lithium ion battery, J. Power Sources 208 (2012) 210–224, http://dx.doi.org/10.1016/j.jpowsour.2012.02.038.

[66] D. Bernardi, E. Pawlikowski, J. Newman, A general energy balance for battery systems, J. Electrochem. Soc. 132 (1) (1985) 5–12, http://dx.doi.org/10.1149/1.2113792.

[67] A. Nazari, S. Farhad, Heat generation in lithium-ion batteries with different nominal capacities and chemistries, Appl. Therm. Eng. 125 (2017) 1501–1517, http://dx.doi.org/10.1016/j.applthermaleng.2017.07.126.

[68] C. Forgez, D. Vinh Do, G. Friedrich, M. Morcrette, C. Delacourt, Thermal modeling of a cylindrical LiFePO4/graphite lithium-ion battery, J. Power Sources 195 (9) (2010) 2961–2968, http://dx.doi.org/10.1016/j.jpowsour.2009.10.105.

[69] K. Onda, T. Ohshima, M. Nakayama, K. Fukuda, T. Araki, Thermal behavior of small lithium-ion battery during rapid charge and discharge cycles, J. Power Sources 158 (1) (2006) 535–542, http://dx.doi.org/10.1016/j.jpowsour.2005.08.049.

[70] T. Grandjean, A. Barai, E. Hosseinzadeh, Y. Guo, A. McGordon, J. Marco, Large format lithium ion pouch cell full thermal characterisation for improved electric vehicle thermal management, J. Power Sources 359 (2017) 215–225, http://dx.doi.org/10.1016/j.jpowsour.2017.05.016.

[71] D.-C. Lee, J.-J. Lee, J.-S. Kim, S. Cho, C.-W. Kim, Thermal behaviors analysis of 55 ah large-format lithium-ion pouch cells with different cell aspect ratios, tab locations, and C-rates, Appl. Therm. Eng. 175 (2020) 115422, http://dx.doi.org/10.1016/j.applthermaleng.2020.115422.

[72] S. Tang, Z. Wang, H. Guo, J. Wang, X. Li, G. Yan, Quantifying the temperature distribution and thermal characteristics of a 4.35 v LiCoO2/graphite pouch cell by modeling and experiments, Electrochim. Acta 366 (2021) 137465, http://dx.doi.org/10.1016/j.electacta.2020.137465.

[73] T. Waldmann, G. Bisle, B.-I. Hogg, S. Stumpp, M.A. Danzer, M. Kasper, P. Axmann, M. Wohlfahrt-Mehrens, Influence of cell design on temperatures and temperature gradients in lithium-ion cells: An in operando study, J. Electrochem. Soc. 162 (6) (2015) A921–A927, http://dx.doi.org/10.1149/2.0561506jes.

[74] S.S. Zhang, K. Xu, T.R. Jow, Optimization of the forming conditions of the solid-state interface in the li-ion batteries, J. Power Sources 130 (1–2) (2004) 281–285, http://dx.doi.org/10.1016/j.jpowsour.2003.12.012.

[75] M. Baumann, L. Wildfeuer, S. Rohr, M. Lienkamp, Parameter variations within li-ion battery packs – Theoretical investigations and experimental quantification, J. Energy Storage 18 (2018) http://dx.doi.org/10.1016/j.est.2018.04.031.

[76] I.D. Campbell, M. Marzook, M. Marinescu, G.J. Offer, How observable is lithium plating? Differential voltage analysis to identify and quantify lithium plating following fast charging of cold lithium-ion batteries, J. Electrochem. Soc. 166 (4) (2019) A725–A739, http://dx.doi.org/10.1149/2.0821904jes.

[77] M.S. Hossain Lipu, M.A. Hannan, T.F. Karim, A. Hussain, M.H.M. Saad, A. Ayob, M.S. Miah, T.M. Indra Mahlia, Intelligent algorithms and control strategies for battery management system in electric vehicles: Progress, challenges and future outlook, J. Clean. Prod. 292 (2021) 126044, http://dx.doi.org/10.1016/j.jclepro.2021.126044.

[78] N. Chaturvedi, R. Klein, J. Christensen, J. Ahmed, A. Kojic, Algorithms for advanced battery-management systems, IEEE Control Syst. 30 (3) (2010) 49–68, http://dx.doi.org/10.1109/MCS.2010.936293.

[79] H. Rahimi-Eichi, U. Ojha, F. Baronti, M.-Y. Chow, Battery management system: An overview of its application in the smart grid and electric vehicles, IEEE Ind. Electron. Mag. 7 (2) (2013) 4–16, http://dx.doi.org/10.1109/MIE.2013.2250351.

[80] Y. Wang, J. Tian, Z. Sun, L. Wang, R. Xu, M. Li, Z. Chen, A comprehensive review of battery modeling and state estimation approaches for advanced battery management systems, Renew. Sustain. Energy Rev. 131 (2020) 110015, http://dx.doi.org/10.1016/j.rser.2020.110015.

[81] P.H. Notten, J.H.O.h. Veld, J.R. van Beek, Boostcharging li-ion batteries: A challenging new charging concept, J. Power Sources 145 (1) (2005) 89–94, http://dx.doi.org/10.1016/j.jpowsour.2004.12.038.

[82] S.S. Zhang, The effect of the charging protocol on the cycle life of a Li-ion battery, J. Power Sources 161 (2) (2006) 1385–1391, http://dx.doi.org/10.1016/j.jpowsour.2006.06.040.

[83] J. Li, E. Murphy, J. Winnick, P.A. Kohl, The effects of pulse charging on cycling characteristics of commercial lithium-ion batteries, J. Power Sources 102 (1–2) (2001) 302–309, http://dx.doi.org/10.1016/S0378-7753(01)00820-5.

[84] M. Abdel Monem, K. Trad, N. Omar, O. Hegazy, B. Mantels, G. Mulder, P. van den Bossche, J. van Mierlo, Lithium-ion batteries: Evaluation study of different charging methodologies based on aging process, Appl. Energy 152 (2015) 143–155, http://dx.doi.org/10.1016/j.apenergy.2015.02.064.

[85] M. Abdel-Monem, K. Trad, N. Omar, O. Hegazy, P. van den Bossche, J. van Mierlo, Influence analysis of static and dynamic fast-charging current profiles on ageing performance of commercial lithium-ion batteries, Energy 120 (2017) 179–191, http://dx.doi.org/10.1016/j.energy.2016.12.110.

[86] A.S. Mussa, M. Klett, M. Behm, G. Lindbergh, R.W. Lindström, Fast-charging to a partial state of charge in lithium-ion batteries: A comparative ageing study, J. Energy Storage 13 (2017) 325–333, http://dx.doi.org/10.1016/j.est.2017.07.004.

[87] D. Anseán, M. González, J.C. Viera, V.M. García, C. Blanco, M. Valledor, Fast charging technique for high power lithium iron phosphate batteries: A cycle life analysis, J. Power Sources 239 (2013) 9–15, http://dx.doi.org/10.1016/j.jpowsour.2013.03.044.

[88] M.H. Noh, P.X. Thivel, C. Lefrou, Y. Bultel, Fast-charging of lithium iron phosphate battery with ohmic-drop compensation method, J. Energy Storage 8 (2016) 160–167, http://dx.doi.org/10.1016/j.est.2016.10.005.

[89] S.S. Sebastian, B. Dong, T. Zerrin, P.A. Pena, A.S. Akhavi, Y. Li, C.S. Ozkan, M. Ozkan, Adaptive fast charging methodology for commercial Li-ion batteries based on the internal resistance spectrum, Energy Storage 2 (4) (2020) e141.

[90] L.-R. Chen, S.-L. Wu, D.-T. Shieh, T.-R. Chen, Sinusoidal-ripple-current charging strategy and optimal charging frequency study for li-ion batteries, IEEE Trans. Ind. Electron. 60 (1) (2013) 88–97, http://dx.doi.org/10.1109/TIE.2012.2186106.

[91] S. Schindler, M. Bauer, H. Cheetamun, M.A. Danzer, Fast charging of lithium-ion cells: Identification of aging-minimal current profiles using a design of experiment approach and a mechanistic degradation analysis, J. Energy Storage 19 (2018) 364–378, http://dx.doi.org/10.1016/j.est.2018.08.002.

[92] J.M. Amanor-Boadu, A. Guiseppi-Elie, E. Sanchez-Sinencio, Search for optimal pulse charging parameters for li-ion polymer batteries using taguchi orthogonal arrays, IEEE Trans. Ind. Electron. 65 (11) (2018) 8982–8992, http://dx.doi.org/10.1109/TIE.2018.2807419.

[93] P.M. Attia, A. Grover, N. Jin, K.A. Severson, T.M. Markov, Y.-H. Liao, M.H. Chen, B. Cheong, N. Perkins, Z. Yang, P.K. Herring, M. Aykol, S.J. Harris, R.D. Braatz, S. Ermon, W.C. Chueh, Closed-loop optimization of fast-charging protocols for batteries with machine learning, Nature 578 (7795) (2020) 397–402, http://dx.doi.org/10.1038/s41586-020-1994-5.

[94] C.-H. Lee, M.-Y. Chen, S.-H. Hsu, J.-A. Jiang, Implementation of an SOC-based four-stage constant current charger for li-ion batteries, J. Energy Storage 18 (2018) 528–537, http://dx.doi.org/10.1016/j.est.2018.06.010.

[95] X. Liu, Y. He, G. Zeng, J. Zhang, X. Zheng, State-of-power estimation of li-ion batteries considering the battery surface temperature, Energy Technol. 6 (7) (2018) 1352–1360, http://dx.doi.org/10.1002/ente.201700680.

[96] Z. Guo, B.Y. Liaw, X. Qiu, L. Gao, C. Zhang, Optimal charging method for lithium ion batteries using a universal voltage protocol accommodating aging, J. Power Sources 274 (2015) 957–964, http://dx.doi.org/10.1016/j.jpowsour.2014.10.185.

[97] M. Xu, R. Wang, B. Reichman, X. Wang, Modeling the effect of two-stage fast charging protocol on thermal behavior and charging energy efficiency of lithium-ion batteries, J. Energy Storage 20 (2018) 298–309, http://dx.doi.org/10.1016/j.est.2018.09.004.

[98] M. Ye, H. Gong, R. Xiong, H. Mu, Research on the battery charging strategy with charging and temperature rising control awareness, IEEE Access 6 (2018) 64193–64201, http://dx.doi.org/10.1109/ACCESS.2018.2876359.

[99] L. Patnaik, A.V. Praneeth, S.S. Williamson, A closed-loop constant-temperature constant-voltage charging technique to reduce charge time of lithium-ion batteries, IEEE Trans. Ind. Electron. 66 (2) (2019) 1059–1067, http://dx.doi.org/10.1109/TIE.2018.2833038.

[100] C. Zhang, J. Jiang, Y. Gao, W. Zhang, Q. Liu, X. Hu, Charging optimization in lithium-ion batteries based on temperature rise and charge time, Appl. Energy 194 (2017) 569–577, http://dx.doi.org/10.1016/j.apenergy.2016.10.059.

[101] J. Jaguemont, N. Omar, M. Abdel-Monem, P. van den Bossche, J. van Mierlo, Fast-charging investigation on high-power and high-energy density pouch cells with 3D-thermal model development, Appl. Therm. Eng. 128 (2018) 1282–1296, http://dx.doi.org/10.1016/j.applthermaleng.2017.09.068.

[102] J. Liu, Q. Duan, H. Chen, J. Sun, Q. Wang, An optimal multistage charge strategy for commercial lithium ion batteries, Sustain. Energy Fuels 2 (8) (2018) 1726–1736, http://dx.doi.org/10.1039/C8SE00235E.

[103] X. Lin, Real-time prediction of anode potential in li-ion batteries using long short-term neural networks for lithium plating prevention, J. Electrochem. Soc. 166 (10) (2019) A1893–A1904, http://dx.doi.org/10.1149/2.0621910jes.

[104] J. Hamar, C. Zoerr, S.V. Erhard, A. Jossen, Anode potential estimation in lithium-ion batteries using data-driven models for online applications, J. Electrochem. Soc. 168 (3) (2021) 030535, http://dx.doi.org/10.1149/1945-7111/abe721.

[105] F.B. Spingler, W. Wittmann, J. Sturm, B. Rieger, A. Jossen, Optimum fast charging of lithium-ion pouch cells based on local volume expansion criteria, J. Power Sources 393 (2018) 152–160, http://dx.doi.org/10.1016/j.jpowsour.2018.04.095.

[106] L. Hovestadt, K. Wildermann, A. Sahhary, R. Hanke-Rauschenbach, Investigation of temperature and pressure behaviour of constrained lithium ion cell under lithium plating conditions, J. Electrochem. Soc. 167 (11) (2020) 110540, http://dx.doi.org/10.1149/1945-7111/aba550.

[107] T. Waldmann, M. Kasper, M. Wohlfahrt-Mehrens, Optimization of charging strategy by prevention of lithium deposition on anodes in high-energy lithium-ion batteries – Electrochemical experiments, Electrochim. Acta 178 (2015) 525–532, http://dx.doi.org/10.1016/j.electacta.2015.08.056.

[108] J. Sieg, J. Bandlow, T. Mitsch, D. Dragicevic, T. Materna, B. Spier, H. Witzenhausen, M. Ecker, D.U. Sauer, Fast charging of an electric vehicle lithium-ion battery at the limit of the lithium deposition process, J. Power Sources 427 (2019) 260–270, http://dx.doi.org/10.1016/j.jpowsour.2019.04.047.

[109] B. Epding, B. Rumberg, M. Mense, H. Jahnke, A. Kwade, Aging–optimized fast charging of lithium ion cells based on three–electrode cell measurements, Energy Technol. 8 (10) (2020) 2000457, http://dx.doi.org/10.1002/ente.202000457.

[110] M.-T.F. Rodrigues, K. Kalaga, S.E. Trask, D.W. Dees, I.A. Shkrob, D.P. Abraham, Fast charging of li-ion cells: Part I. Using Li/Cu reference electrodes to probe individual electrode potentials, J. Electrochem. Soc. 166 (6) (2019) A996–A1003, http://dx.doi.org/10.1149/2.0401906jes.

[111] I.A. Shkrob, M.-T.F. Rodrigues, D.W. Dees, D.P. Abraham, Fast charging of li-ion cells: Part II. Nonlinear contributions to cell and electrode polarization, J. Electrochem. Soc. 166 (14) (2019) A3305–A3313, http://dx.doi.org/10.1149/2.0561914jes.

[112] I.A. Shkrob, M.-T.F. Rodrigues, D.P. Abraham, Fast charging of li-ion cells: Part III. Relaxation dynamics and trap-controlled lithium ion transport, J. Electrochem. Soc. 166 (16) (2019) A4168–A4174, http://dx.doi.org/10.1149/2.0511916jes.

[113] M.-T.F. Rodrigues, I.A. Shkrob, A.M. Colclasure, D.P. Abraham, Fast charging of li-ion cells: Part IV. Temperature effects and “safe lines” to avoid lithium plating, J. Electrochem. Soc. 167 (13) (2020) 130508, http://dx.doi.org/10.1149/1945-7111/abb70d.

[114] I.A. Shkrob, M.-T.F. Rodrigues, D.P. Abraham, Fast charging of li-ion cells: Part V. Design and demonstration of protocols to avoid li-plating, J. Electrochem. Soc. 168 (1) (2021) 010512, http://dx.doi.org/10.1149/1945-7111/abd609.

[115] J. Liu, Z. Chu, H. Li, D. Ren, Y. Zheng, L. Lu, X. Han, M. Ouyang, Lithium–plating–free fast charging of large–format lithium–ion batteries with reference electrodes, Int. J. Energy Res. 45 (5) (2021) 7918–7932, http://dx.doi.org/10.1002/er.6375.

[116] C. Zou, X. Hu, Z. Wei, X. Tang, Electrothermal dynamics-conscious lithium-ion battery cell-level charging management via state-monitored predictive control, Energy 141 (2017) 250–259, http://dx.doi.org/10.1016/j.energy.2017.09.048.

[117] H.E. Perez, X. Hu, S. Dey, S.J. Moura, Optimal charging of li-ion batteries with coupled electro-thermal-aging dynamics, IEEE Trans. Veh. Technol. 66 (9) (2017) 7761–7770, http://dx.doi.org/10.1109/TVT.2017.2676044.

[118] J. Remmlinger, S. Tippmann, M. Buchholz, K. Dietmayer, Low-temperature charging of lithium-ion cells Part II: Model reduction and application, J. Power Sources 254 (2014) 268–276, http://dx.doi.org/10.1016/j.jpowsour.2013.12.101.

[119] S. Tippmann, D. Walper, L. Balboa, B. Spier, W.G. Bessler, Low-temperature charging of lithium-ion cells part I: Electrochemical modeling and experimental investigation of degradation behavior, J. Power Sources 252 (2014) 305–316, http://dx.doi.org/10.1016/j.jpowsour.2013.12.022.

[120] Y. Li, M. Vilathgamuwa, E. Wikner, Z. Wei, X. Zhang, T. Thiringer, T. Wik, C. Zou, Electrochemical model-based fast charging: Physical constraint-triggered PI control, IEEE Trans. Energy Convers. (2021) 1, http://dx.doi.org/10.1109/TEC.2021.3065983.

[121] R. Drees, F. Lienesch, M. Kurrat, Fast charging lithium-ion battery formation based on simulations with an electrode equivalent circuit model, J. Energy Storage 36 (2021) 102345, http://dx.doi.org/10.1016/j.est.2021.102345.

[122] R. Klein, N.A. Chaturvedi, J. Christensen, J. Ahmed, R. Findeisen, A. Kojic, Optimal charging strategies in lithium-ion battery, in: Proceedings of the 2011 American Control Conference, IEEE, 2011, pp. 382–387, http://dx.doi.org/10.1109/ACC.2011.5991497.

[123] S. Pramanik, S. Anwar, Electrochemical model based charge optimization for lithium-ion batteries, J. Power Sources 313 (2016) 164–177, http://dx.doi.org/10.1016/j.jpowsour.2016.01.096.

[124] A. Adam, J. Wandt, E. Knobbe, G. Bauer, A. Kwade, Fast-charging of automotive lithium-ion cells: In-situ lithium-plating detection and comparison of different cell designs, J. Electrochem. Soc. 167 (13) (2020) 130503, http://dx.doi.org/10.1149/1945-7111/abb564.

[125] M. Xu, R. Wang, P. Zhao, X. Wang, Fast charging optimization for lithium-ion batteries based on dynamic programming algorithm and electrochemical-thermal-capacity fade coupled model, J. Power Sources 438 (2019) 227015, http://dx.doi.org/10.1016/j.jpowsour.2019.227015.

[126] S.-Y. Choe, X. Li, M. Xiao, Fast charging method based on estimation of ion concentrations using a reduced order of electrochemical thermal model for lithium ion polymer battery, World Electr. Veh. J. 6 (3) (2013) 782–792, http://dx.doi.org/10.3390/wevj6030782.

[127] Z. Chu, X. Feng, L. Lu, J. Li, X. Han, M. Ouyang, Non-destructive fast charging algorithm of lithium-ion batteries based on the control-oriented electrochemical model, Appl. Energy 204 (2017) 1240–1250, http://dx.doi.org/10.1016/j.apenergy.2017.03.111.

[128] C. Zou, X. Hu, Z. Wei, T. Wik, B. Egardt, Electrochemical estimation and control for lithium-ion battery health-aware fast charging, IEEE Trans. Ind. Electron. 65 (8) (2018) 6635–6645, http://dx.doi.org/10.1109/TIE.2017.2772154.

[129] M. Song, S.-Y. Choe, Fast and safe charging method suppressing side reaction and lithium deposition reaction in lithium ion battery, J. Power Sources 436 (2019) 226835, http://dx.doi.org/10.1016/j.jpowsour.2019.226835.

[130] Y. Yin, Y. Bi, Y. Hu, S.-Y. Choe, Optimal fast charging method for a large-format lithium-ion battery based on nonlinear model predictive control and reduced order electrochemical model, J. Electrochem. Soc. 167 (16) (2020) 160559, http://dx.doi.org/10.1149/1945-7111/abd607.

[131] Y. Yin, S.-Y. Choe, Actively temperature controlled health-aware fast charging method for lithium-ion battery using nonlinear model predictive control, Appl. Energy 271 (2020) 115232, http://dx.doi.org/10.1016/j.apenergy.2020.115232.

[132] Y. Yin, Y. Hu, S.-Y. Choe, H. Cho, W.T. Joe, New fast charging method of lithium-ion batteries based on a reduced order electrochemical model considering side reaction, J. Power Sources 423 (2019) 367–379, http://dx.doi.org/10.1016/j.jpowsour.2019.03.007.

[133] X. Lin, X. Hao, Z. Liu, W. Jia, Health conscious fast charging of Li-ion batteries via a single particle model with aging mechanisms, J. Power Sources 400 (2018) 305–316, http://dx.doi.org/10.1016/j.jpowsour.2018.08.030.

[134] X. Lin, S. Wang, Y. Kim, A framework for charging strategy optimization using a physics-based battery model, J. Appl. Electrochem. 49 (8) (2019) 779–793, http://dx.doi.org/10.1007/s10800-019-01322-1.

[135] M.F. Hasan, C.-F. Chen, C.E. Shaffer, P.P. Mukherjee, Analysis of the implications of rapid charging on lithium-ion battery performance, J. Electrochem. Soc. 162 (7) (2015) A1382–A1395, http://dx.doi.org/10.1149/2.0871507jes.

[136] S. Kolluri, S.V. Aduru, M. Pathak, R.D. Braatz, V.R. Subramanian, Real-time nonlinear model predictive control (NMPC) strategies using physics-based models for advanced lithium-ion battery management system (BMS), J. Electrochem. Soc. 167 (6) (2020) 063505, http://dx.doi.org/10.1149/1945-7111/ab7bd7.

[137] F. Ringbeck, M. Garbade, D.U. Sauer, Uncertainty-aware state estimation for electrochemical model-based fast charging control of lithium-ion batteries, J. Power Sources 470 (2020) 228221, http://dx.doi.org/10.1016/j.jpowsour.2020.228221.

[138] S. Yang, X. Gao, Y. Li, W. Xie, B. Guo, L. Zhang, X. Liu, Minimum lithium plating overpotential control based charging strategy for parallel battery module prevents side reactions, J. Power Sources 494 (2021) 229772, http://dx.doi.org/10.1016/j.jpowsour.2021.229772.

[139] B.K. Purushothaman, U. Landau, Rapid charging of lithium-ion batteries using pulsed currents, J. Electrochem. Soc. 153 (3) (2006) A533, http://dx.doi.org/10.1149/1.2161580.

[140] A. Aryanfar, D. Brooks, B.V. Merinov, W.A. Goddard, A.J. Colussi, M.R. Hoffmann, Dynamics of lithium dendrite growth and inhibition: Pulse charging experiments and Monte Carlo calculations, J. Phys. Chem. Lett. 5 (10) (2014) 1721–1726, http://dx.doi.org/10.1021/jz500207a.

[141] K.A. Severson, P.M. Attia, N. Jin, N. Perkins, B. Jiang, Z. Yang, M.H. Chen, M. Aykol, P.K. Herring, D. Fraggedakis, M.Z. Bazant, S.J. Harris, W.C. Chueh, R.D. Braatz, Data-driven prediction of battery cycle life before capacity degradation, Nature Energy 334 (2019) 928, http://dx.doi.org/10.1038/s41560-019-0356-8.

[142] B. Bitzer, A. Gruhle, A new method for detecting lithium plating by measuring the cell thickness, J. Power Sources 262 (2014) 297–302, http://dx.doi.org/10.1016/j.jpowsour.2014.03.142.

[143] C. Birkenmaier, B. Bitzer, M. Harzheim, A. Hintennach, T. Schleid, Lithium plating on graphite negative electrodes: Innovative qualitative and quantitative investigation methods, J. Electrochem. Soc. 162 (14) (2015) A2646–A2650, http://dx.doi.org/10.1149/2.0451514jes.

[144] B. Rieger, S.F. Schuster, S.V. Erhard, P.J. Osswald, A. Rheinfeld, C. Willmann, A. Jossen, Multi-directional laser scanning as innovative method to detect local cell damage during fast charging of lithium-ion cells, J. Energy Storage 8 (2016) 1–5, http://dx.doi.org/10.1016/j.est.2016.09.002.

[145] Y. Merla, B. Wu, V. Yufit, R.F. Martinez-Botas, G.J. Offer, An easy-to-parameterise physics-informed battery model and its application towards lithium-ion battery cell design, diagnosis, and degradation, J. Power Sources 384 (2018) 66–79, http://dx.doi.org/10.1016/j.jpowsour.2018.02.065.

[146] Y. Li, M. Vilathgamuwa, T. Farrell, S.S. Choi, N.T. Tran, J. Teague, A physics-based distributed-parameter equivalent circuit model for lithium-ion batteries, Electrochim. Acta 299 (2019) 451–469, http://dx.doi.org/10.1016/j.electacta.2018.12.167.

[147] M. Doyle, T.F. Fuller, J. Newman, Modeling of galvanostatic charge and discharge of the lithium/polymer/insertion cell, J. Electrochem. Soc. 140 (6) (1993) 1526–1533, http://dx.doi.org/10.1149/1.2221597.

[148] J. Sturm, H. Ennifar, S.V. Erhard, A. Rheinfeld, S. Kosch, A. Jossen, State estimation of lithium-ion cells using a physicochemical model based extended Kalman filter, Appl. Energy 223 (2018) 103–123, http://dx.doi.org/10.1016/j.apenergy.2018.04.011.

[149] S.V. Erhard, P.J. Osswald, P. Keil, E. Höffer, M. Haug, A. Noel, J. Wilhelm, B. Rieger, K. Schmidt, S. Kosch, F.M. Kindermann, F. Spingler, H. Kloust, T. Thoennessen, A. Rheinfeld, A. Jossen, Simulation and measurement of the current density distribution in lithium-ion batteries by a multi-tab cell approach, J. Electrochem. Soc. 164 (1) (2017) A6324–A6333, http://dx.doi.org/10.1149/2.0551701jes.

[150] J. Sturm, A. Frank, A. Rheinfeld, S.V. Erhard, A. Jossen, Impact of electrode and cell design on fast charging capabilities of cylindrical lithium-ion batteries, J. Electrochem. Soc. 167 (13) (2020) http://dx.doi.org/10.1149/1945-7111/abb40c.

[151] A. Pozzi, M. Torchio, R.D. Braatz, D. Raimondo, Optimal charging of an electric vehicle battery pack: A real-time sensitivity-based MPC approach, ArchivX 2019 (2019).

[152] B. Wu, V. Yufit, M. Marinescu, G.J. Offer, R.F. Martinez-Botas, N.P. Brandon, Coupled thermal–electrochemical modelling of uneven heat generation in lithium-ion battery packs, J. Power Sources 243 (2013) 544–554, http://dx.doi.org/10.1016/j.jpowsour.2013.05.164.

[153] N. Wassiliadis, M. Ank, L. Wildfeuer, M.K. Kick, M. Lienkamp, Experimental investigation of the influence of electrical contact resistance on lithium-ion battery testing for fast-charge applications, Appl. Energy 295 (2021) 117064, http://dx.doi.org/10.1016/j.apenergy.2021.117064.

[154] T.R. Tanim, M.G. Shirk, R.L. Bewley, E.J. Dufek, B.Y. Liaw, Fast charge implications: Pack and cell analysis and comparison, J. Power Sources 381 (2018) 56–65, http://dx.doi.org/10.1016/j.jpowsour.2018.01.091.

[155] G. Xia, L. Cao, G. Bi, A review on battery thermal management in electric vehicle application, J. Power Sources 367 (2017) 90–105, http://dx.doi.org/10.1016/j.jpowsour.2017.09.046.

[156] A.R.M. Siddique, S. Mahmud, B. van Heyst, A comprehensive review on a passive (phase change materials) and an active (thermoelectric cooler) battery thermal management system and their limitations, J. Power Sources 401 (2018) 224–237, http://dx.doi.org/10.1016/j.jpowsour.2018.08.094.

[157] X. Hu, Y. Zheng, D.A. Howey, H. Perez, A. Foley, M. Pecht, Battery warm-up methodologies at subzero temperatures for automotive applications: Recent advances and perspectives, Progr. Energy Combust. Sci. 77 (2020) 100806, http://dx.doi.org/10.1016/j.pecs.2019.100806.

[158] Y. Ji, C.Y. Wang, Heating strategies for Li-ion batteries operated from subzero temperatures, Electrochim. Acta 107 (2013) 664–674, http://dx.doi.org/10.1016/j.electacta.2013.03.147.

2.2 Teardown and characterization procedure for commercial lithium-ion cells

A model-based fast charging control strategy requires a carefully crafted electrochemical model of the lithium-ion cell. As pointed out in Section 2.1, many parameters of electrochemical models cannot be determined at the cell level due to the parameter ambiguity of the electrode behavior. For example, the OCV of the lithium-ion cell U_{OCV} is composed of a simple superposition of the electrode OCPs U^{+}/U^{-} according to $U_{\mathrm{OCV}} = U^{+} - U^{-}$. Consequently, both electrode OCPs cannot be determined without further knowledge of the individual electrode OCPs at the cell level. If an electrochemical model for a commercial lithium-ion cell with unknown electrode parameters must be developed, a teardown of the lithium-ion cell and investigation of the electrochemical performance of the individual electrodes is inevitable [103, 104, 183, 184].

To tackle these challenges, this section introduces an approach to gain the essential electrode parameters for electrochemical model development from a commercial cylindrical lithium-ion cell and to avoid ambiguities in the downstream identification of the remaining parameters at the cell level. The approach was published in prior work [185] and is visualized in Figure 2.2. This work extends earlier studies, e.g., by Illig [186], Waldmann et al. [187], or Schindler [188], by providing an alternative approach with additional insights. Prior to the teardown procedure, the lithium-ion cell was scanned with computed tomography (CT) to identify optimal access points to the cell core without penetrating the active material layer. The lithium-ion cell was opened under an inert gas atmosphere (O_2, $H_2 < 0.1$ ppm), and the individual electrodes were harvested. The electrode layer and tab dimensions were measured. Two-electrode half cells were built from circular electrode stamps countered with a lithium-metal electrode and filled with LP30 electrolyte. After sealing and a minimum electrolyte soaking time of 24 h, all two-electrode cells underwent a post-formation to guarantee stable behavior during the assessment. In the following, half-cells were subjected to OCP identification using various techniques, i.e., pOCV and galvanic intermediate titration technique (GITT) at different ambient temperatures (-10 °C to 50 °C). The half-cells were also subjected to EIS to identify the individual loss processes occurring at the cell level and to track down the limiting electrode by quantifying the impedance behavior of both electrodes.

The results revealed that if two-electrodes half cells are built from carefully harvested electrodes, only three post-formation cycles can be sufficient to reach stable electrode cycling behavior, which may help to reduce the impact of calendar aging as it is well-known that manually built lab-scale cells are prone to early failure [189]. Using GITT measurements leads to a more accurate determination of the electrode OCP with lower overpotential deterioration compared to the pOCV technique, even compared to a pOCV performed with a current rate as low as C/100. However, as discussed in Section 1.1.1, stage transitions are not depicted with high resolution due to the missing continuity of the voltage signal, which, however, are important to match for downstream electrochemical modeling. It was shown in a subsequent investigation that if both electrode OCPs are balanced and aligned to the cell's OCV, using the GITT measurements yielded a better fit if the OCV domain (voltage error) is used in the objective function. In contrast, the use of pOCVs measurements yielded a better fit if either a vertical shifting parameter is added to the optimization and the DVA domain (differential voltage error) is used in the objective function. Wanzel [164] showed that only the charge direction of the GITT measurement is

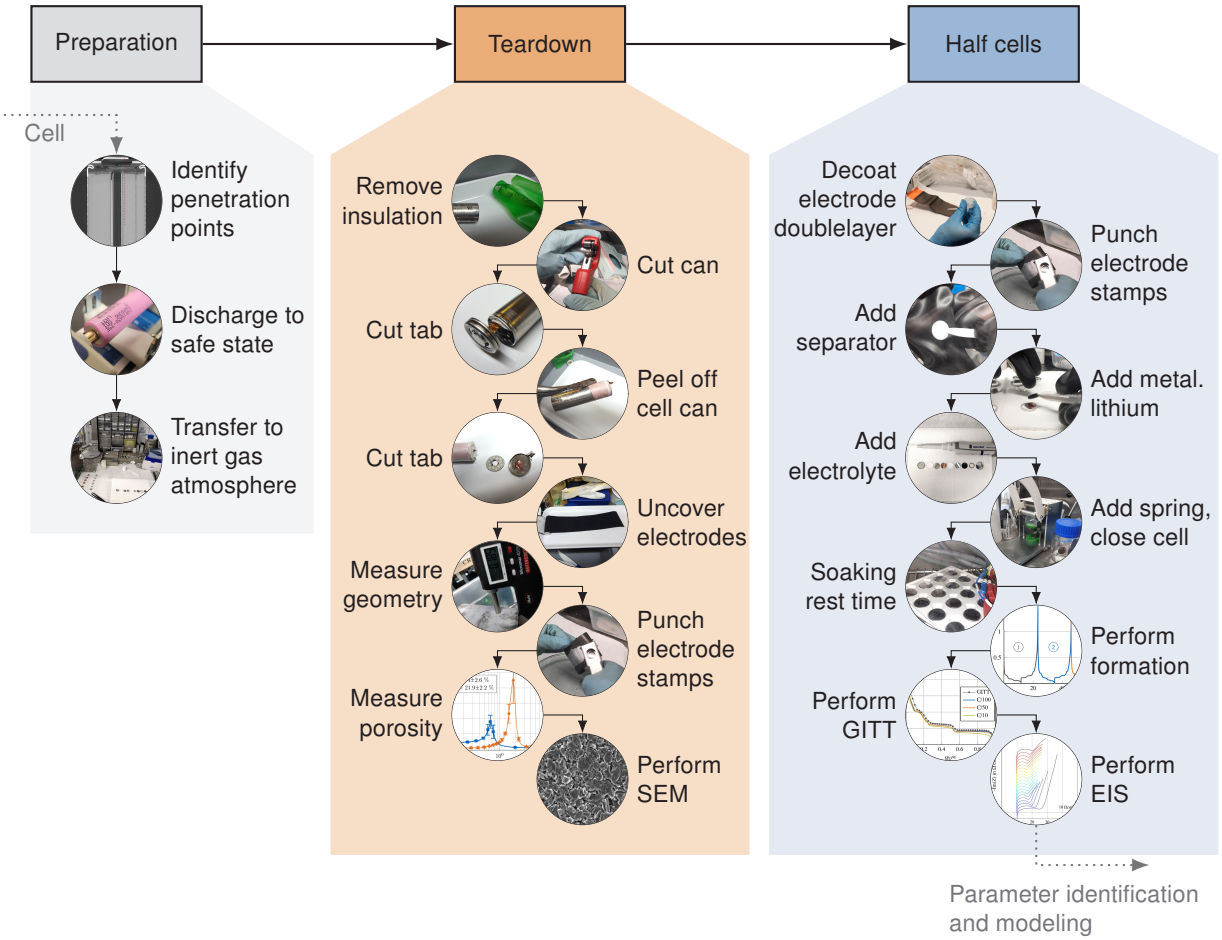

Figure 2.2: Step-by-step teardown and characterization procedure of a commercial lithium-ion cell with unknown properties to gather essential measurements for downstream model parameter identification and fast charging control.

sufficient for fast charging current control and benefits from mitigating fitting deteriorations due to the hysteresis behavior of the cell in low SOC regions. Beyond that, no clear temperature dependence of the OCV of the cell and half-cells could be observed. With regard to the dynamic electrode behavior and fast charging capability, the impedance spectra determined with EIS also revealed that the anode suffers under a more significant impedance than the cathode with increasing SOC [190]. The overall procedure was examined for a cylindrical cell with half cells sealed in mini pouch bags but has also been proven to be likewise applicable to other cell formats, such as automotive-scale pouch cells, with half cells sealed in hard-case coin cells [45].

Author contribution: Leo Wildfeuer and Nikolaos Wassiliadis jointly carried out the teardown of the lithium-ion cell under study, built the half cells, and performed the characterization, investigation, curation, and validation of the experimental results as equal first authors. Alexander Karger supported parts of this study with evaluation algorithms. Fabian Bauer provided resources for and assisted with the CT scans. Markus Lienkamp provided resources and supervision for this work. All authors reviewed and edited the manuscript.

Teardown analysis and characterization of a commercial lithium-ion cell for advanced algorithms in battery electric vehicles

Leo Wildfeuer†, Nikolaos Wassiliadis†, Alexander Karger, Fabian Bauer, Markus Lienkamp
† Both authors contributed equally as first authors.

Journal of Energy Storage 48, 2022.
Digital Object Identifier: 10.1016/j.est.2021.103909

Journal of Energy Storage 48 (2022) 103909

Contents lists available at ScienceDirect

Journal of Energy Storage

journal homepage: www.elsevier.com/locate/est

Research papers

Teardown analysis and characterization of a commercial lithium-ion battery for advanced algorithms in battery electric vehicles

Leo Wildfeuer [a,c,*,1], Nikolaos Wassiliadis [a,1], Alexander Karger [b,c], Fabian Bauer [d,e], Markus Lienkamp [a]

[a] Technical University of Munich, School of Engineering and Design, Department of Mobility Systems Engineering, Institute of Automotive Technology, Germany
[b] Technical University of Munich, School of Engineering and Design, Department of Energy and Process Engineering, Institute for Electrical Energy Storage Technology, Germany
[c] TWAICE Technologies GmbH, Munich, Germany
[d] Technical University of Munich, School of Engineering and Design, Department of Materials Engineering, Institute of Non-destructive Testing, Germany
[e] Siemens Corporate Technology, Munich, Germany

ARTICLE INFO

Keywords:
Lithium-ion batteries
Teardown analysis
Si-doped graphite anode
Ni-rich NCA cathode
Half cells
Electrochemical impedance spectroscopy

ABSTRACT

In recent years, in-depth analysis of the manifold properties of commercial lithium-ion batteries has gained increasing attention, as it fosters optimized design and operational strategies of battery-powered applications such as battery electric vehicles. However, various properties are not easily accessible and experimental determination requires intensive efforts in the battery lab. In this study, we have performed a tear-down analysis of a commercially available lithium-ion cell with a silicon-doped graphite anode and a Ni-rich NCA cathode. Enhanced by computed tomography (CT) scans, we reveal the cell's internal geometrical properties. Furthermore, mini pouch half cells of the anode and cathode have been built to examine their electrochemical properties in context with full cell measurements. In particular, we examined the open circuit voltage with different measurement methods and for different temperatures and performed reconstruction of the full cell via fitting of electrode potentials. We give detailed insights into the kinetics of the cell by analyzing the distribution of relaxation times (DRT) calculated from electrochemical impedance spectroscopy (EIS). Individual loss processes are assigned to either electrode and their polarization resistances and time constants are quantified over a large SOC and temperature range. A comprehensive open-source dataset of the investigated cell is provided to propel international research activities in the development of advanced models and algorithms for lithium-ion batteries.

1. Introduction

The success of lithium-ion batteries (LIBs) in battery-powered applications has lead to intensive efforts towards maximizing their efficiency as an energy source. In the case of battery electric vehicles (BEVs), it constitutes the most expensive component [1], which is why optimized design and operation of battery systems is of high importance. To this end, capacity retention and battery aging is a crucial phenomenon that has been tackled by many researchers in the past [2–5]. Aging results from complex physical and chemical degradation mechanisms at the cell components [5]. From an engineering perspective, it is necessary to understand the influence of these different degradation mechanisms and scale this knowledge to effects on the application level such as loss of available energy and power, as illustrated in Fig. 1.

In order to lever untapped potential of the battery system's performance and to prolong its lifetime advanced models, algorithms and operational strategies have to be designed, which require tear-down analysis of LIBs to gather in-depth knowledge about the electrochemical system.

1.1. Previous publications

In the past, many authors assessed the electrochemical properties of anode [6–13] or cathode [11,12,14–18] materials. Besides the analysis of individual cell component properties, it is important to understand their behavior in a full cell assembly to project the results to real-world applications. An extract of publications, which perform cell tear-down

* Corresponding author at: Technical University of Munich, School of Engineering and Design, Department of Mobility Systems Engineering, Institute of Automotive Technology, Germany.
E-mail addresses: leo.wildfeuer@tum.de (L. Wildfeuer), nikolaos.wassiliadis@tum.de (N. Wassiliadis).
[1] L.W. & N.W. contributed equally as first authors.

https://doi.org/10.1016/j.est.2021.103909
Received 26 April 2021; Received in revised form 3 December 2021; Accepted 22 December 2021
Available online 21 January 2022

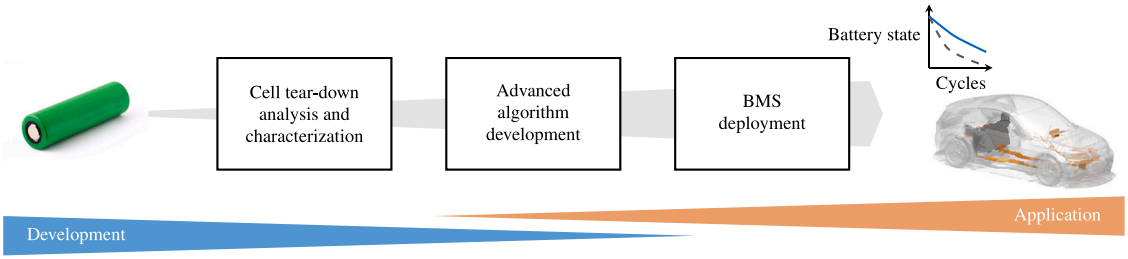

Fig. 1. Pipeline for the development of advanced algorithms for the deployment in Battery Management Systems (BMSs) of battery electric vehicles. This study focuses on the in-depth analysis and characterization of a lithium-ion cell.

and in-depth component analysis on the electrode level and provide comprehensive investigations of corresponding full cell properties, is given in the following.

Safari and Delacourt [10] analyzed the electrochemical properties of an LFP-based LIB and compared the electrode properties to the full cell, thus providing a fundamental dataset for an electrochemical battery model. However, their measurements were performed before 2011, compromising the comparability to today's battery cell generations. Sabet et al. [19,20] analyzed the predominant processes in the impedance spectra of commercial NMC- and NCA-based LIBs, respectively. Schmalstieg et al. [21] provided an electrochemical analysis of the electrode properties of a high-power LIB which they used to parameterize a physico-chemical model of the full cell. Kovachev et al. [22] performed an in-depth material and design analysis of NMC pouch cells, using a battery cell from an unknown manufacturer. Also, first generation Nissan Leaf LMO pouch cells were analyzed from a material recycling perspective [23]. Unfortunately, the investigation was restricted to material analysis only. Lain et al. [24] investigated many commercially available cylindrical LIBs with varying chemistries according to their geometrical and active material properties and compared different design strategies of manufacturers. An electrochemical performance analysis was not in the scope of the work. Recently, Liebig et al. [25] and Chen et al. [26] investigated a prismatic and cylindrical NMC cell, respectively, at the material, electrode and full cell level. They performed scanning electron microscope (SEM) images of the electrodes, geometrical measurements, and further characterization of the electrochemical performance (e.g., EIS). The parameters were used to parameterize an electro-chemical model with thermal dynamics.

It can be concluded that in present literature, only a few studies performed an in-depth investigation of commercially-available battery cells from the electrode to the full cell level, hampering downstream usage of the results for modeling, algorithm design and validation. Further systematic investigations providing insights into the properties of commercially available battery cells from the electrode to the full cell level at various ambient temperatures are needed to avoid time- and resource-intensive rework.

1.2. Contributions

We performed an in-depth analysis of a commercial 18650 LIB (Sony US18650VTC5 A) involving various state-of-the-art characterization methods. The main contributions can be summarized as follows:

1. **Tear-down analysis, half cell building, and investigation of the geometrical properties**
   The design and geometrical properties of the electrodes and of the full cell are investigated via destructive and non-destructive methods.
2. **Analysis of half cell and full cell open-circuit voltages**
   The open-circuit voltages of electrode half cells are analyzed with different measurement methods over a broad temperature range and the results are scaled to full cell level via electrode balancing and alignment.
3. **Analysis of half cell and full cell dynamics**
   The cell's behavior under dynamic conditions is analyzed via electrochemical impedance spectroscopy. The observed loss processes are assigned to either half cell via analysis of the DRT.
4. **Open-source access to the experimental data**
   All measurement data and analysis results are provided open-source alongside the article.

The results of this study can be used to develop and parameterize advanced battery analytics functionality such as physics-enhanced equivalent circuit models (ECMs) for on-line estimation of the impedance throughout the lifetime [27], P2D or reduced-order models to be used in model-based fast charging strategies [28], or determination of degradation modes through the tracking of electrode balancing over lifetime [5].

1.3. Layout

The remainder of this paper is structured as follows: Section 2 introduces the employed methods and boundary conditions for the battery dissection and building of the half cells. In Section 3, the geometrical properties of the investigated cell are stated and discussed. The static behavior of the cell, i.e., OCV of the half cells and fitting to the full cell's OCV, is presented and discussed in Section 4. The assessment of the dynamic cell behavior is presented in Section 5. In Section 6, we summarize the main insights of the article.

2. Cell tear down and building of half cells

In this section, the disassembly of a commercial 18650 cell (Sony US18650VTC5 A with a Si-doped graphite anode, NCA cathode, and 2.5 Ah nominal capacity [24]) and the building of anode and cathode half cells against metallic lithium is described.

2.1. Dissection of the cell

In the first step, a pristine cell was taken from a new manufacturing batch and was constant current constant voltage (CCCV) discharged to 2.5 V to minimize the energy contained within the cell and thus minimize the severity in the case of an unintended short-circuit. Then, the cell top was removed with a pipe cutter tool under inert gas atmosphere, while ensuring that the tool did not get in contact with the electrode materials. After opening, the outer anode cell internal copper tab could be seen, as shown in Fig. 2(a). The visible pierced layer of plastic material may help to avoid any vibration- or shock-induced internal short circuit between the negative electrode layers and the top positive battery tab. The battery cell steel can was then thoroughly unwound from the cell internal materials to expose the active material layers, as visible in Fig. 2(b) and (c), respectively. Once the jelly roll was extracted from the cell can, the electrode layers could be analyzed. Unwrapping the jelly roll revealed the electrode tab positions, as shown in Fig. 2(d).

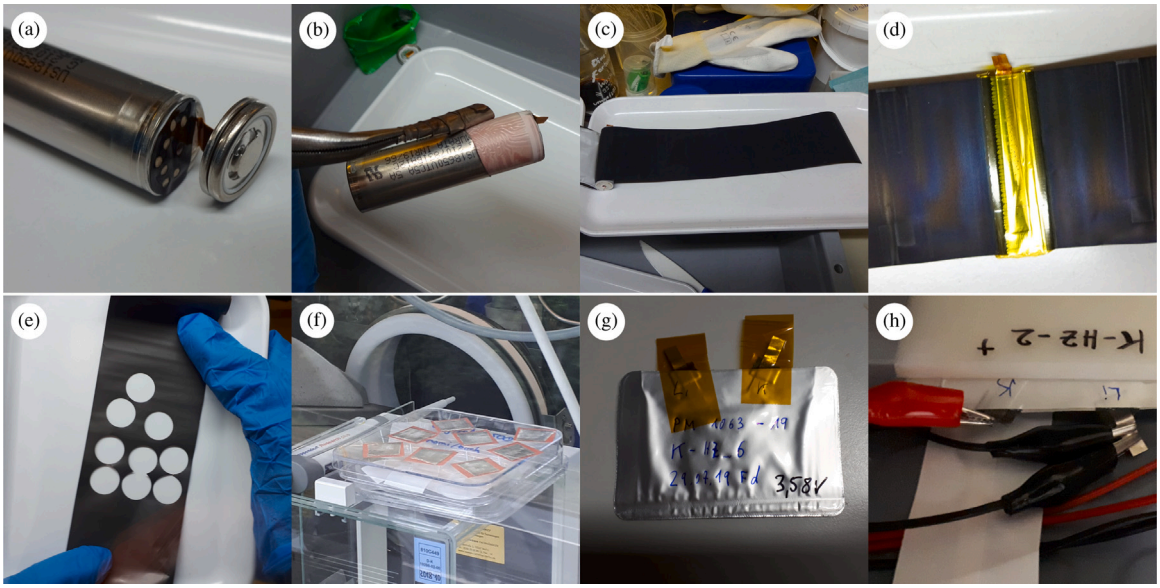

Fig. 2. Preparation of half cells under inert gas atmosphere. The cell disassembly under inert gas atmosphere can be seen in figures (a)–(d), the half cell preparation process with sample stamping of each electrode can be seen in figures (e)–(h).

2.2. Half cell assembly

To test different operating scenarios with pristine half cells and to provide spares in case of defects resulting from the manual process [29,30], we built five plus three half cells per electrode. In the first step, coins of 16 mm diameter were punched out of the now exposed electrode layer, as visible in Fig. 2(e). Since both electrodes are doubled-coated with active material, one side of the electrode was cleaned by mechanically removing the coating from the carrier material with the aid of NMP solvent at 20 °C ambient temperature. In a subsequent step, all electrode stamps were covered with a Celgard Polypropylene mono-layer separator and countered with a layer of metallic lithium, as seen in Fig. 2(f). The final half cell was then equipped with current collectors and placed in a mini pouch bag. To enable charge transfer between the electrodes, each pouch cell was filled with 500 µL of LP30 electrolyte (1M $LiPF_6$ in EC:DMC (1:1, v/v)). In the final step, the mini pouch bag was sealed with a Multivac vacuum machine. After sealing, the half cells were stored for over 24 h to guarantee that the electrolyte completely soaked into the pores of the cell components.

2.3. Formation of half cells

To allow the formation of a solid electrolyte interphase (SEI) at the electrode–electrolyte interface, a formation procedure was undertaken with all half cells by cycling in charge and discharge direction. The formation cycles are plotted in Fig. 3 for both half cells. Stable voltage traces and a coulombic efficiency over 99% was reached after three cycles for all half cells.

During formation, the minimum and maximum voltage limits for the anode were set to 10 mV and 1.5 V, respectively, as voltage gradients steeply ramp up beyond those limits and critical voltages are avoided. The cathode limits were likewise set to 2.5 V and 4.25 V. C/10 was chosen as the charge and discharge current. The resulting current was calculated using the down-scaled areal capacity (Fig. 5) of the electrode section according to:

$$I_{HC} = (16\,\text{mm}/2)^2 \cdot \pi \cdot 0.024\,\text{mAh/mm}^2 \cdot 0.1\,\text{h}^{-1} = 0.481\,\text{mA}. \quad (1)$$

For mini pouch bags, areal pressure has to be considered to make sure that volume changes do not lead to inhomogeneous contact or even internal disconnects. A target pressure of 0.1 MPa was set by placing the half cells with an active area of $(16\,\text{mm}/2)^2 \cdot \pi = 201\,\text{mm}^2$ between two square polymer contact plates and stressing the plates with a weight of 2 kg.

3. Geometrical parameters

In addition to the cell disassembly described in the previous section, we applied computed tomography (CT) to support the geometrical measures with data from the pristine cell. The non-invasive images (Fig. 4) reveal the internal structure of the full cell. The jelly roll has 27 electrode double layers with a total thickness of approximately 100 µm. Note that a more precise digital measurement was not possible due to the limited scan resolution of approximately 50 µm voxel size. The active volume, i.e., the volume which is occupied by the electrode layers including the pore volume, approximates to 87 % of the total cell volume.

The geometric properties and tab placement on the individual electrodes are illustrated in Fig. 5. On the anode, two current collector tabs are placed on uncoated copper foil at both ends. As previous studies pointed out [24], this design offers the potential to minimize resistance and heat generated in the cell core, since heat can be easily transferred from the cell core to the cell can over the center collector. Out of a total anode length of 947 mm, one side of the outer surface shows a larger area with uncoated copper foil (50 mm), which is left out during coating as it wraps the remaining cathode inside the winding and has no countering active material. At the inner surface, the coated area is larger and has a total length of 925 mm.

The cathode has one similar-sized current collector of aluminum, which is placed close to the center of the electrode. The slight offset towards the cell core may be a design feature to further increase the heat flow out of the cell core [24], which appears to be of higher priority than minimum resistance due to equidistant current paths through the cell. Both sides of the cathode are coated equally with NCA.

Both electrodes are wrapped up with a hollow center pin of 2.6 mm in diameter. Beyond production reasons, center pins allow for fast heat transfer out of the cell core during operation [31]. The slight over-sizing of the anode compared to the cathode is known as anode overhang, a design measure to ensure that the cathode is always countered with anode active material [32]. As a consequence, Li-ions can be accepted during charging even if electrodes are slightly misaligned during cell production. Hereby, the risk of local lithium plating at the electrode

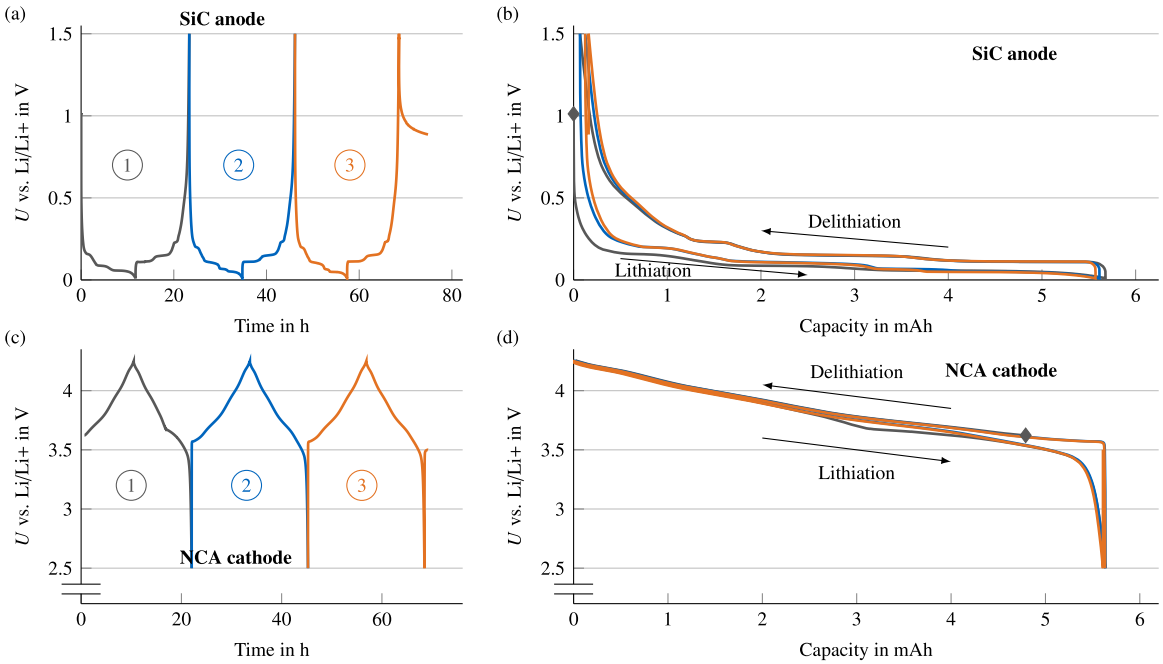

Fig. 3. Formation of the half cells until a stable voltage trace is reached. Voltage over time in (a)/(c) and voltage over capacity in (b)/(d) for anode and cathode half cells, respectively. Colored curves represent the three consecutive charge/discharge cycles, with gray markers indicating the formation starting point.

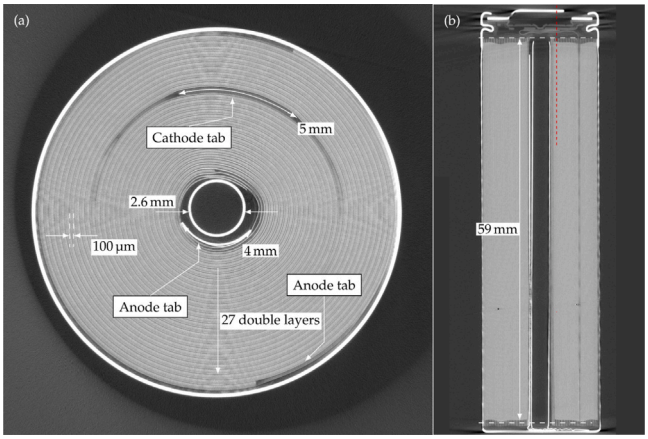

Fig. 4. CT scans of the investigated cell with digital measurements taken in myVGL (Volume Graphics GmbH, Germany). (a) provides a lateral and (b) the axial view into the cell through the cell center and reveals properties of the jelly roll.

edges is avoided. Contradictorily, many studies pointed out that the overhang leads to diffusion of lithium-ions into the overhang edges, which may aggravate inhomogeneous current densities during cycling, further provoking local lithium plating at the edges [29]. According to Lewerenz et al. [33], the ratio of the overhang can be calculated to approximately 7% of the total active area.

4. Open-circuit behavior

In this section, the voltage of the full cell and the constructed half cells at thermodynamic equilibrium are analyzed. For this, different OCV measurement methods are discussed in the first step. In the second step, the temperature dependency of the OCV is investigated between −10 °C and 50 °C. In the last step, both half cell OCVs are used to reconstruct the full cell OCV and reveal the electrode balancing. All measurements were performed with a BaSyTec CTS Lab.

4.1. Influence of measurement methods

There are two common methods for measuring the OCV of a cell, the galvanostatic intermittent titration technique (GITT) and the measurement of a pOCV with a low current rate [34]. To analyze the impact of these methods on the results for the tested cell type, pOCV measurements were performed with a C-rate of C/10, C/50 and C/100 at a reference temperature of 20 °C and GITT measurements with a relaxation time of 2 h at 40 state-of-charge (SOC) steps. The top row of Fig. 6 shows the results for the different methods for the full cell and the two half cells, respectively. Small voltage deviations between the different methods are present, which are caused by different overpotentials during the measurement. The voltage during the pOCV measurements is higher with the increasing current and is generally higher than the voltage measured during GITT.

Additionally, differential voltage analysis (DVA) of each measurement was performed and the results are shown in the bottom row of Fig. 6. The positions of the characteristic peaks in the DVA resulting from stage transitions in the anode [35,36] and cathode [37] (marked in Fig. 6(d)—(f)) are in good accordance for all measurement methods with small deviations propagating from the discussed OCV differences. Despite the limited amount of sampling points of the GITT measurement, the derived DVA curve also matches the stage transitions well. However, information losses occur in regions with higher voltage dynamics, e.g., anode stage IV. As a result, we conclude that for the investigated cell type, a pOCV measured with C/10 is sufficient to identify electrode characteristics and stage transitions at specific SOCs at the cost of higher overpotentials compared to GITT. In doing so, lab testing times, especially when tracking the pOCV during aging studies, can be reduced.

4.2. Temperature dependency

We performed pOCV measurements over a broad temperature range (−10 °C, 5 °C, 20 °C, 35 °C and 50 °C) to investigate the temperature dependence of the full cell's and half cell's OCV [38]. To minimize the influence of increased overpotentials at low temperatures, we chose a current of C/50. For this analysis, five different cells were used.

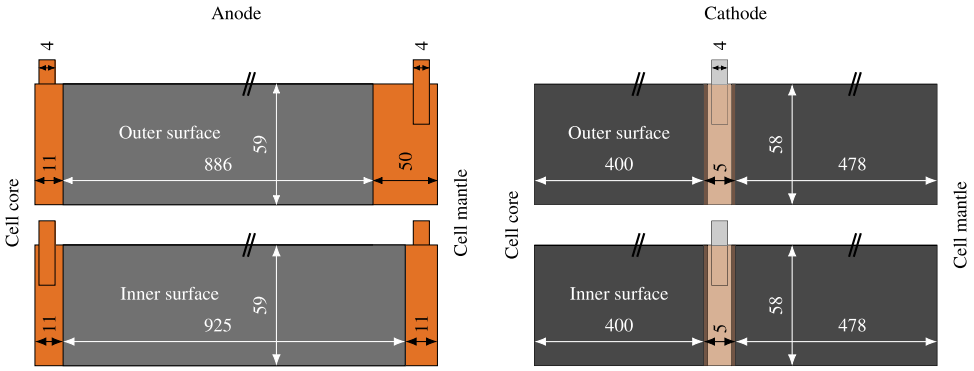

Fig. 5. Cell electrode design: The anode (left) is coated with Si-doped graphite, except for the contacting area of the two current collectors and the anode overlap at the outer surface close to the cell housing. The NCA cathode (right) is designed with a single current collector at the center. The NCA coating covers the remaining electrode wrap. All measures are in mm.

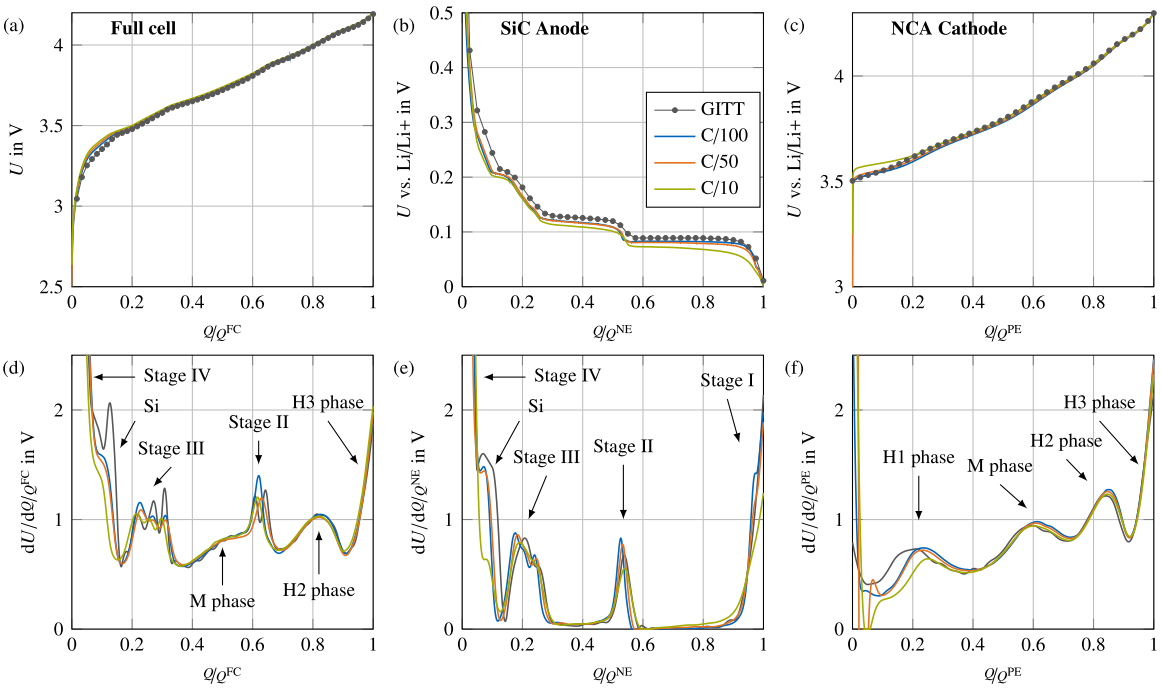

Fig. 6. Influence of different OCV measurement methods on the pseudo-OCV (top row) and corresponding DVA (bottom row) for the full cell (left column), anode (center column), and cathode (right column) over normalized capacity Q/Q^{FC}, Q/Q^{NE}, and Q/Q^{PE}, respectively. The actual measured capacities Q^{FC}, Q^{NE}, and Q^{PE} were used for normalization. OCV curves were measured in charge direction of the full cell at 20 °C. Additionally, lithiation stages and phases of the active material labeled.

Whereas intrinsic parameter variations due to production tolerances of the individual samples are expected to be negligible for the commercial full cell [39–41], these intrinsic variations might increase during manual half cell assembly and subsequent formation. However, Schmid et al. [42] showed that similar orders of magnitude of parameter variations are achievable for manually built half cells, which is why we chose to conduct the measurements with different samples, as subsequent testing of one sample would also influence the measurement results due to degradation of the half cells [30]. Experimental results are presented in Fig. 7. Again, the differential voltage is also plotted to investigate a shift of the characteristic peaks with varying temperature.

At low SOC, the OCV curves fan out and the voltage increases with decreasing temperature. In the DVA of the full cell and the anode, the stage transitions at approx. 10 % SOC (which is assumed to be caused by silicon in the anode [36]) disappears. However, no clear answer can be given as to whether this behavior results from an altered behavior of silicon at low temperatures or from increased overpotentials. This temperature effect is still visible at the stage III transition of graphite. Additionally, directly after the stage III transition, between 30 % SOC and 40 % SOC, an extra peak starts to develop for temperatures higher than 20 °C, which can be attributed to the anode. Apart from these observations, the voltage curves behave consistently over the entire temperature range.

4.3. Electrode balancing

Up to now, all voltage and differential voltage curves have been plotted over their normalized capacity Q/Q^{Cell}. However, to reconstruct the full cell voltage and understand the electrode balancing, the voltage curves of anode and cathode need to be scaled and aligned. In the following, this process is referred to as half cell fitting and the results are shown in Fig. 8. Based on the previous findings of the influence of measurement methods, we chose the C/10 curves for half cell fitting.

Half cell fitting can directly be done by using the OCV curves [5]. However, using derivatives such as incremental capacity analysis (ICA) curves [43] or DVA curves [44] might be beneficial to properly match the characteristic transition phases of the individual electrodes. In theory, all methods should yield the same results. In practice, however,

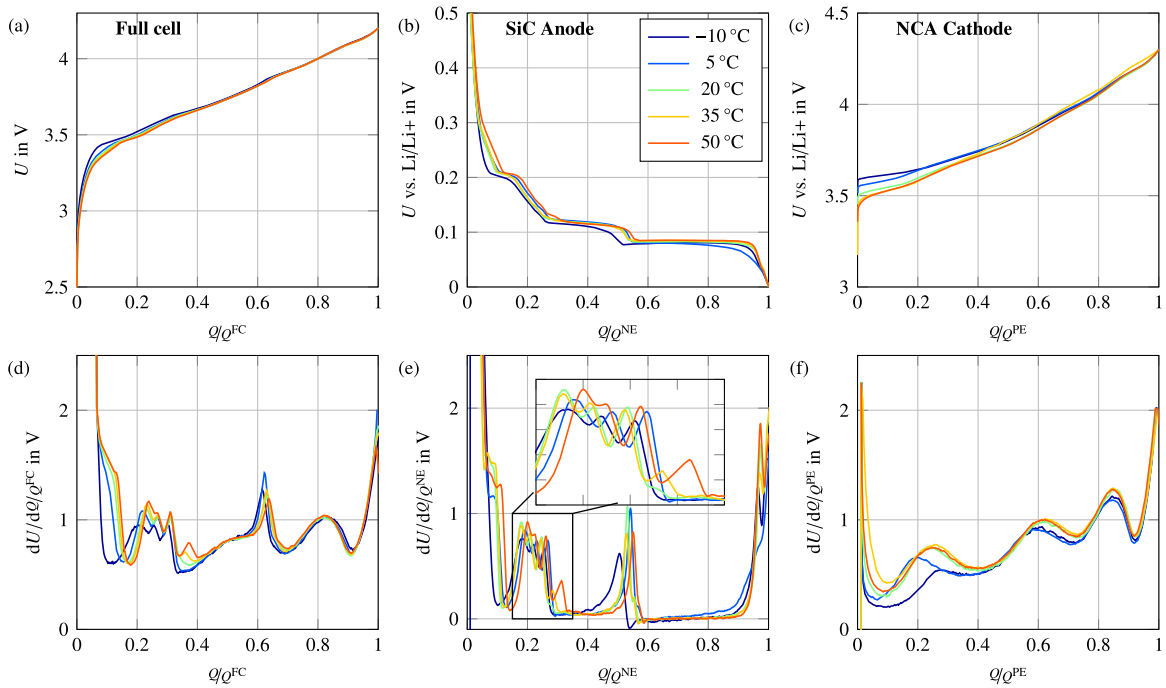

Fig. 7. Temperature dependency of the pseudo-OCV (top row) and corresponding DVA (bottom row) for the full cell (left column), anode (center column), and cathode (right column) over normalized capacity Q/Q^{FC}, Q/Q^{NE}, and Q/Q^{PE}, respectively. The actual measured capacities Q^{FC}, Q^{NE}, and Q^{PE} were used for normalization. pOCVs curves were recorded in charge direction with a current of C/50.

slight differences in the algorithm and the processed data will lead to deviating results. Therefore, half cell fitting was performed in the OCV domain as well as in the DVA domain.

The first step of the half cell fitting is to nondimensionalize the capacities of all potential curves to between 0 and 1. This is necessary because the half cells consist of only a fraction of the full cell's active material. Nondimensionalizing is allowed because the measured half-cell potentials are a material property and independent of the amount of active material.

In the next step, a fitting range is defined to exclude certain SOC ranges, which has been reported to increase the quality of the fit [5]. At low SOC, the voltage curve of the anode is especially steep. Thus the DV increases towards large values, causing a fitting procedure to minimize the error mainly in this range. Furthermore, due to the fast change in anode potential without much charge throughput, this range is highly sensitive to the measurement procedure, which could further distort the results. Thus, by excluding the outer SOC-ranges from the fitting, special attention can be paid to accurately fit the stage transitions of graphite. The difference between the upper bound x_{ub} and lower bound x_{lb} is defined as the fitting range ϑ_{fit}:

$$\vartheta_{\mathrm{fit}} = x_{\mathrm{ub}} - x_{\mathrm{lb}}. \tag{2}$$

In the OCV-domain, the electrode balancing is performed by minimizing the cost function $f_{\mathrm{cost,OCV}}$:

$$f_{\mathrm{cost,OCV}} = \int_{x_{\mathrm{lb}}}^{x_{\mathrm{ub}}} \left({U_{\mathrm{OC}}}^{\mathrm{FC}}(x_{\mathrm{FC}}) - {U_{\mathrm{sim}}}^{\mathrm{FC}}(x_{\mathrm{FC}}) \right) \rightarrow \min. \tag{3}$$

Here, the fitting is performed by computing a simulated full-cell OCV ${U_{\mathrm{sim}}}^{\mathrm{FC}}(x_{\mathrm{FC}})$ via

$$\begin{aligned} {U_{\mathrm{sim}}}^{\mathrm{FC}}(x_{\mathrm{FC}}) = {U_{\mathrm{OC}}}^{\mathrm{PE}}\left(\alpha^{\mathrm{PE}} x_{\mathrm{FC}} - \nu^{\mathrm{PE}}\right) \\ - {U_{\mathrm{OC}}}^{\mathrm{NE}}\left(\alpha^{\mathrm{NE}} x_{\mathrm{FC}} - \nu^{\mathrm{NE}}\right) - \delta_{\mathrm{volt}}. \end{aligned} \tag{4}$$

The fitting parameters $\alpha^{\mathrm{PE/NE}}$ and $\nu^{\mathrm{PE/NE}}$ determine the horizontal scaling and shifting of the cathode and anode voltage curves, respectively, and are dimensionless. The fitting parameters δ_{volt} carries the unit [V] and is introduced to equalize the difference in internal resistance within the experimental half cells compared to the full cell.

Without the introduction of δ_{volt}, which lies between 14 mV and 20 mV in the case of C/10 measurements, the optimization algorithm would be forced to compensate the existing difference in internal resistance by shifting the electrode's potential curves in the x-direction. This could lead to a mismatch of characteristic stage and phase transitions of the measured and simulated full cell curve. A positive value of δ_{volt} means that the resistances of one or both half cells is higher compared to the full cell, even though it is normalized to the active surface area. This is the case and it is visible in the impedance spectra shown in the next section.

In the DVA-domain, the cost function has to be formulated as:

$$f_{\mathrm{cost,DVA}} = \int_{x_{\mathrm{lb}}}^{x_{\mathrm{ub}}} \left(\frac{d{U_{\mathrm{OC}}}^{\mathrm{FC}}}{dx_{\mathrm{FC}}}(x_{\mathrm{FC}}) - \frac{d{U_{\mathrm{sim}}}^{\mathrm{FC}}}{dx_{\mathrm{FC}}}(x_{\mathrm{FC}}) \right) \rightarrow min, \tag{5}$$

with

$$\begin{aligned} \frac{d{U_{\mathrm{sim}}}^{\mathrm{FC}}}{dx_{\mathrm{FC}}}(x_{\mathrm{FC}}) = \frac{\alpha^{\mathrm{PE}}}{\nu_{\mathrm{fit}}} \left(\frac{d{U_{\mathrm{OC}}}^{\mathrm{PE}}}{dx_{\mathrm{FC}}}(\alpha^{\mathrm{PE}} x_{\mathrm{FC}} - \nu^{\mathrm{PE}}) \right) \\ - \frac{\alpha^{\mathrm{NE}}}{\nu_{\mathrm{fit}}} \left(\frac{d{U_{\mathrm{OC}}}^{\mathrm{NE}}}{dx_{\mathrm{FC}}}(\alpha^{\mathrm{NE}} x_{\mathrm{FC}} - \nu^{\mathrm{NE}}) \right). \end{aligned} \tag{6}$$

The effect of a different resistance on the differential potential curves is much lower, as shown in the previous section. Therefore, the optimization algorithm does not need a vertical adjustment parameter such as δ_{volt} to match the stage and phase transitions well.

There are three main factors influencing the fitting results: (i) the measurement procedure (ii) the fitting domain (OCV-domain or DVA-domain), and (iii) the fitting range. To investigate these influencing factors, we performed the fitting for each combination of $x_{\mathrm{lb}} \in [0{:}0.005{:}0.15]$ and $x_{\mathrm{ub}} \in [0.9{:}0.005{:}1]$ in the OCV domain and the DVA domain for both, C/10 and C/50, pOCV measurements. For each configuration, the RMSE was calculated in the OCV domain (with the unit mV) and the DVA domain (with the unit mV/Ah) over the full SOC range (0–1), denoted as ϵ_{full}, and over the reduced SOC range (0.15–0.9), denoted as $\epsilon_{\mathrm{range}}$. The error measures and fitting parameters are

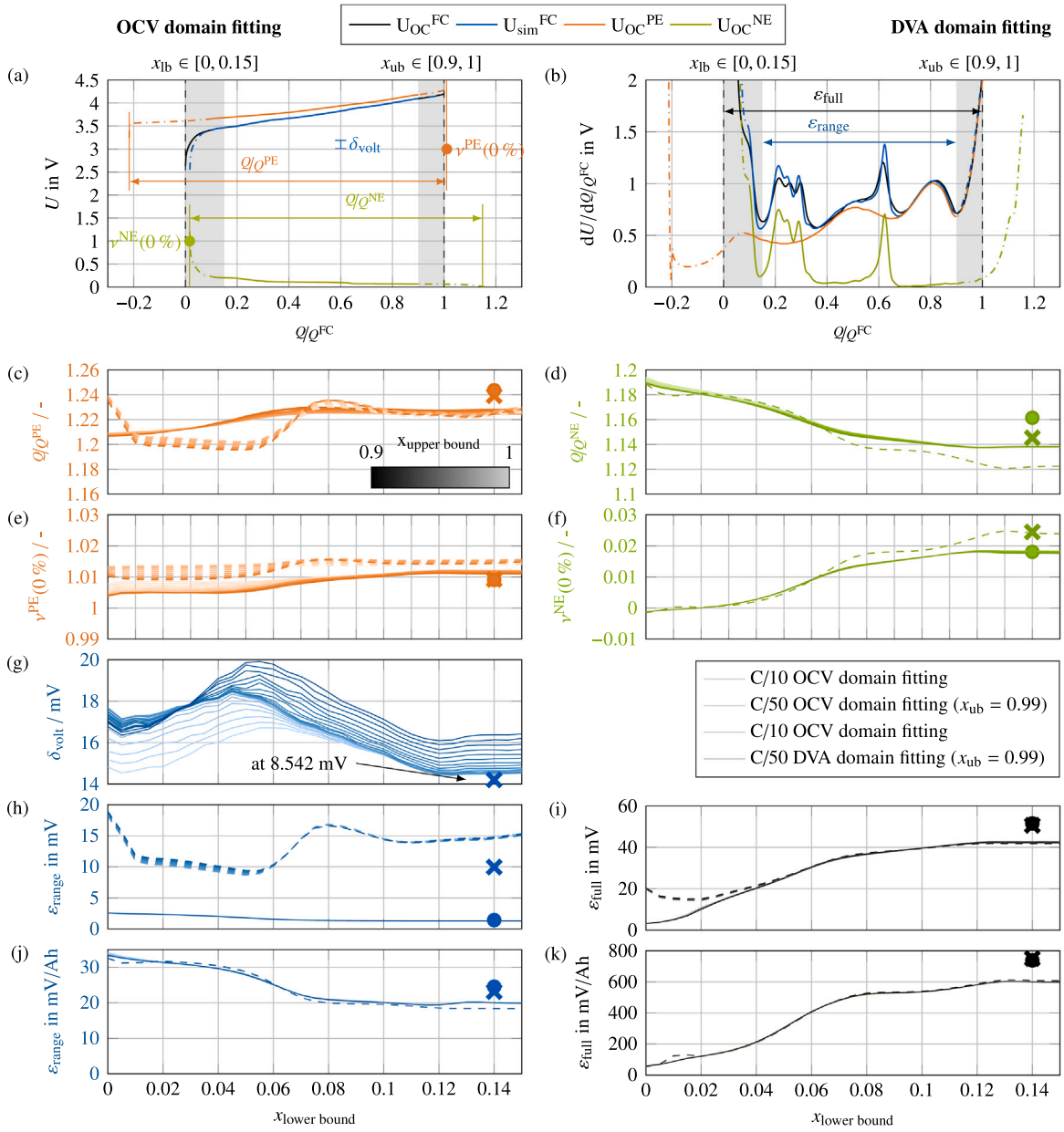

Fig. 8. Full cell OCV and DVA reconstruction from individual electrode potentials. 1st row: Results for fitting in the OCV domain (a) and fitting in the DVA domain (b) pOCV curves with C/10 at 20 °C for x_{lb} = 0.1 and x_{ub} = 0.9. The fitting parameters $\alpha^{PE/NE}$ and $\nu^{PE/NE}$ are additionally illustrated: $Q/Q^{PE/NE}$ are the normalized electrode capacities resulting from $\vartheta_{fit}/\alpha^{PE/NE}$. The shifting parameters $\nu^{PE/NE}(0\%)$ are illustrated at the state, where the respective electrode is fully delithiated. For the anode it is calculated as $\nu^{NE}(0\%) = (\vartheta_{fit}/\alpha^{PE/NE} \cdot (0 - \nu^{PE/NE})) + x_{lb}$. For the cathode it is calculated as $\nu^{PE}(0\%) = (\vartheta_{fit}/\alpha^{PE} \cdot (1 - \nu^{PE})) + x_{lb}$. 2nd–6th row: Fitting parameters and fitting errors dependent on the fitting domain (solid vs. dashed lines), the lower fitting bound x_{lb} (along the x-axis) and the upper fitting bound x_{ub} (different color shading). 2nd–3rd row: Fitting parameters of the cathode (c) and (e), and the anode (d) and (f). 4th row: The parameter δ_{volt} (g) only exists for fitting in the OCV domain. 5th row: RMSE in the OCV domain for the reduced SOC range of 0.15–0.9 (h) and the full SOC range from 0–1 (i). 6th row: RMSE in the DVA domain for the reduced SOC range of 0.15–0.9 (j) and the full SOC range from 0–1 (k). Both. ε is calculated as the root mean square error (RMSE).

presented in Fig. 8. Since the dependency on the lower and upper fitting bound is similar for the C/50 pOCV measurements, only the results for x_{lb} = 0.14 and x_{ub} = 0.99 are shown for better visibility.

In general, the trend is similar for fitting in the OCV domain compared to fitting in the DVA domain and the absolute values only differ slightly. The OCV errors ε_{range} and ε_{full}, which are much higher for the fitting in the DVA domain, reveal the missing parameter δ_{volt} and confirm the need for this additional vertical adjustment parameter in order to find physically reasonable scaling and shifting parameters $\alpha^{PE/NE}$ and $\nu^{PE/NE}$ in the OCV domain. The parameter δ_{volt} is equally dependent on the lower and upper fitting bound and no clear trend is identified. This suggests that the resistance's difference is not uniform across the whole SOC range. For the other fitting parameters and the error measures, the influence of the lower fitting bound x_{lb} is much higher compared the upper bound x_{ub}. The following observations lead to the assumption that this is due to fact that the harvested anode half cell shows different behavior compared to the pristine full cell, especially in the low SOC area.

The RMSE of the reduced range ε_{range} decreases with increasing x_{lb}, whereas the RMSE of the full range ε_{full} increases with increasing x_{lb}. This is because for low values of x_{lb}, the fitting procedure has to find a trade-off between the different characteristic anode features, leading to a better match of the low SOC area at the cost of an increased distance between the anode's stage II and stage III. For higher values of x_{lb} the anode's stages in the mid-SOC area are fitted more accurately at the cost of an increased error in the low SOC area. This is also reflected in

the scaling and shifting parameters, which are highly affected by the lower fitting bound x_{lb}. Q/Q^{NE} decreases with increasing x_{lb}, confirming the trade-off between matching the different anode stages. Especially noticeable is the positive value of $v^{NE}(0\%)$ for x_{lb} above 2 % SOC, which means that the simulated full cell is not defined for very low SOC (up to 2.5 % SOC, depending on the fitting method). For values of x_{lb} towards the first local minimum of the full cell's and anode's differential voltage (at approx. 15 % SOC), the fitting parameters and error measures converge.

Since it is assumed that lithiation of the silicon mainly takes place in the low SOC area [45], our observations are in good accordance with a recent study from Schmitt et al. [45], who investigated the change in silicon–graphite potential curves during aging and observed mainly a decrease in the relative capacity contribution of the silicon. This suggests that the high impact of the lower fitting bound and the imperfect reconstruction of the full cell from the half cell's potential curve for low values of x_{lb} is mainly due to the different behavior of silicon inside the anode. For the present measurement data, we propose to use the first local minimum at approx. 15 % SOC of the differential voltage curve as a lower fitting boundary. This way, the location of the graphite's stage II and stage III are matched perfectly and the cathode's fitting parameters are not disturbed in order to compensate the mismatch of the silicon characteristics. Since the influence of the upper fitting bound on the fitting parameters and error measures is negligible for high values of x_{lb} and the H3 phase is an important feature of the cathode, x_{ub} =99 % SOC is chosen.

5. Kinetic and transport properties

After analyzing the cell's thermodynamic behavior, it is important to understand the loss processes during the dynamic operation in order to get a complete picture of the cell's performance. Since the kinetics of LIBs are highly temperature dependent, we performed EIS on the full cell and half cells at ambient temperatures between −10 °C to 60 °C. Based on the experimental results, we calculate the DRT, which enables us to assign the loss processes of the full cell to either electrode. To quantify these loss processes, we determine the time constant and polarization resistance from the DRT.

5.1. EIS measurements, DRT calculation and parameter identification

EIS was performed using a Gamry Instruments Interface 5000, whereby the hybrid EIS mode with an AC voltage of 10 mV rms, a frequency range of 5 kHz to 10 mHz for the full cells and 5 MHz to 10 mHz for the half cells and ten points per decade was used. We increased the frequency range of half cell measurements due to the occurrence of additional processes at higher frequencies. EIS was performed for every 5 % SOC with a relaxation period of 3 h after discharging to the respective SOC. Full cell impedance spectra were recorded at −10 °C, 5 °C, 20 °C, 35 °C, 50 °C and 60 °C. Half cell impedance spectra were only recorded at 20 °C, 35 °C and 50 °C.

To isolate the individual loss processes, the DRT of an impedance spectrum can be evaluated. It makes the distribution of the total polarization resistance in the continuous space of relaxation times visible and thus provides a higher frequency resolution of the dynamic processes [46–50]. Deconvolution of the DRT is based on the assumption that the impedance of an electrochemical system can be expressed by an infinite number of RC elements [46,51]. For this study, the DRT of the recorded impedance spectra were calculated with an implementation of the algorithm presented by Wan et al. [52]. Since the DRT reveals the time constant of individual relaxation processes of an electrochemical system, assignment of full cell processes to individual electrodes becomes feasible. More details on the methodology can be found in the research articles by Sabet et al. [19,20], who performed similar analysis for NCA and NMC cells.

Furthermore, in addition to the time constants τ of individual relaxation processes, which can directly be extracted from the DRT at the respective local maxima of γ, we also determined their polarization resistance R by integration of γ between the adjacent minima of detected processes. The acquired process parameters are presented over a large operating range in the following section.

5.2. Assignment of full cell processes to half cells

In Fig. 9, impedance spectra and their corresponding DRT are plotted for the full cell and both half cells, respectively. The half cell's SOC of EIS measurements is expressed with reference to the full cell SOC according to the half cell fitting. Starting from a fully delithiated half cell, where the SOC is defined as 0, the half cell was charged in 5% SOC steps according to the precedent pOCV measurement.

Visually analyzing the full cell's impedance spectra, one distinct semi-circle and the diffusive branch can clearly be identified. In contrast to this, three processes are revealed from the DRT, which are denoted as F1, F2, and F3. The first process F1 has a time constant of 1.3 ms that does not change with the SOC and its magnitude only increases slightly towards a high and low SOC. The addition of F1 and F2 form the charge transfer resistance R_{ct} of the full cell. Thereby, F2 is highly dependent on the SOC. It is only visible from 0% SOC to 20% SOC and from 90% SOC to 100% SOC with a time constant of around 10 ms. Its resistance increases strongly towards the outer SOCs. The third process F3 at about 100 ms is least pronounced with a resistance of approximately 1 $\Omega\,cm^2$. It occurs at the transition between charge transfer and diffusion and is denoted as $R_{transition}$.

By analyzing the half cell's impedance spectra and DRT, processes of the full cell can be assigned to either the cathode or the anode. The first observed processes A0 and C0 occur at frequencies which were not captured during full cell measurements and can be attributed to the lithium counter electrode of the half cells [20].

The resistance of A1 and C1 show an exact opposite trend with the SOC while A1 is more pronounced overall. Since for F1 only a small SOC dependency of the resistance was observed, it can be assumed that F1 is the superposition of A1 and C1 with the opposed SOC dependency being counterbalanced in a full cell assembly. The dominance of the anode gets more pronounced at a high SOC and decreases towards a low SOC, where the resistance at the cathode side increases. Similar conclusions have been drawn in [19]. The strong increase of the full cells R_{ct} at a high and low SOC due to F2 seems to be resulting from the cathode's process C2. The changing resistance with the SOC of C2 coincides well with F2. Only the varying time constant of C2 does not fit into the picture.

Similar processes at the transition frequency of F3 can also be observed for the two half cells. C3 on the one hand is distinguishable in the cathode's impedance spectra and shows very similar behavior as F3. A3 on the other hand shows different behavior, especially at a high SOC, where the resistance of the process increases strongly. A sudden leap can be seen in the impedance spectra of the anode at the middle of the diffusion branch, which causes the DRT algorithm to identify two separate processes within the diffusion branch of the anode. This might be caused by impurity of the anode or measurement noise of the EIS measurement. Results at 35 °C (Fig. A.11) and 50 °C (Fig. A.12) are more reasonable for the anode and no transition process is detected at the cathode. Overall, no clear conclusion can be drawn as to whether F3 should be assigned to the anode, cathode, or both and the assignment might vary for different temperatures.

5.3. Quantification of loss process parameters over SOC and temperature

After identifying meaningful processes of the full cell and discussing the assignment of them to either the anode or the cathode, the determined parameters R and τ of the full cell are now quantitatively analyzed. Results are plotted in Fig. 10, which can be read as follows:

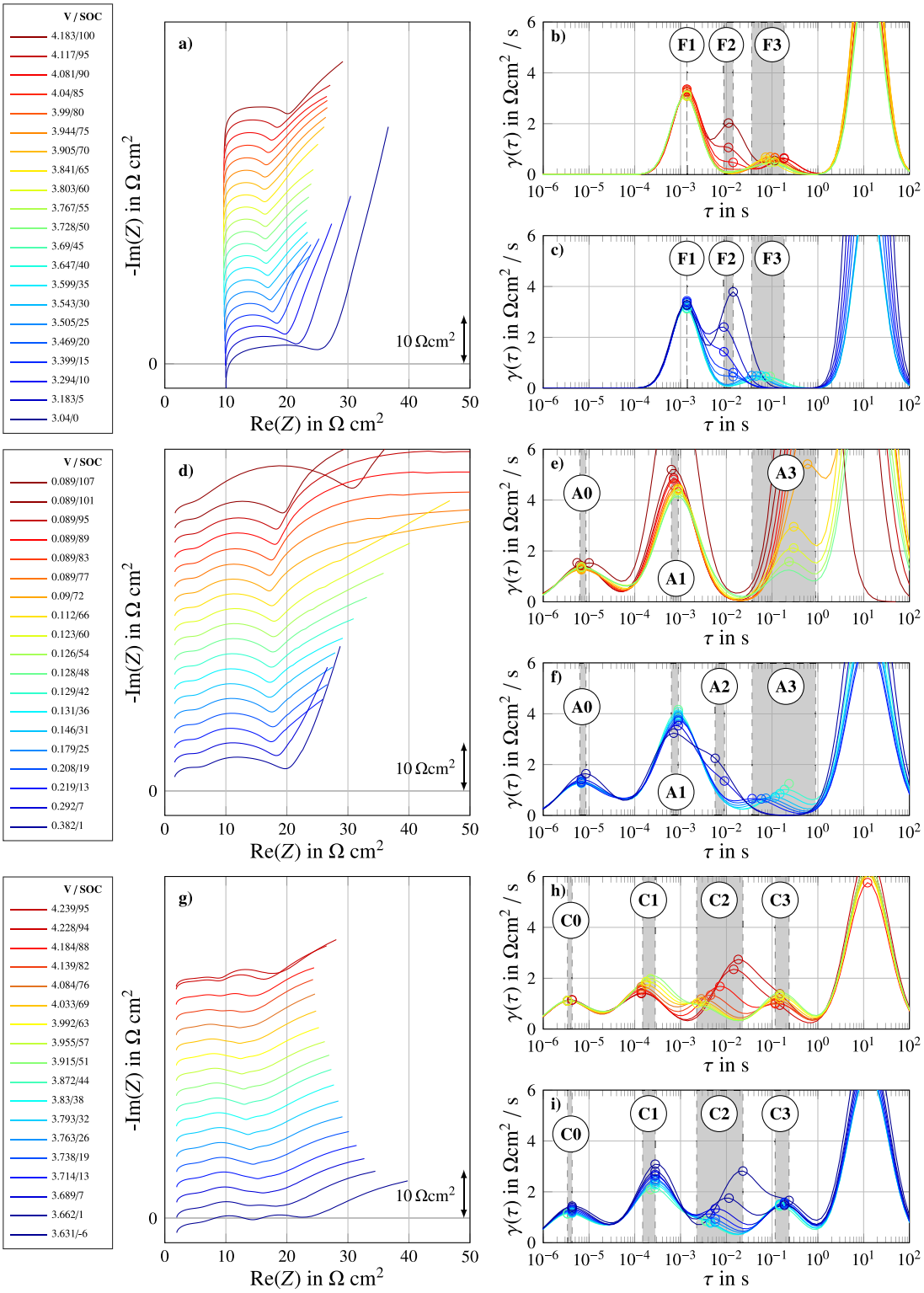

Fig. 9. Impedance spectra from EIS measurements (left column) and corresponding DRT (right column) for different SOCs at 20 °C for the full cell (top), anode (center), and cathode (bottom). DRT plots are subdivided into a high SOC area (100%–50% SOC) and low SOC area (49%–0% SOC). Impedances are normalized by the active electrode surface. SOCs of the half cells are calculated relative to the full cell according to the half cell fitting. For better visibility, impedance spectra in (a), (d), and (g) are shifted in y-direction according to the respective full cell SOC using $-\mathrm{Im}(Z) = -\mathrm{Im}(Z)+\mathrm{SOC}/2$ and the scale is indicated by the 10 Ω cm² arrow.

Resistance values of the four main identified processes are plotted in the first and second row, respectively: (1) The ohmic resistance R_{ohm}, calculated as the intersection point with the x-axis in the Nyquist plot (2) The charge transfer resistance R_{ct}, determined as the sum of all contributing sub-processes (3) $R_{\mathrm{transition}}$, which was identified around the transition frequency between charge transfer and diffusion (4) R_{diff}

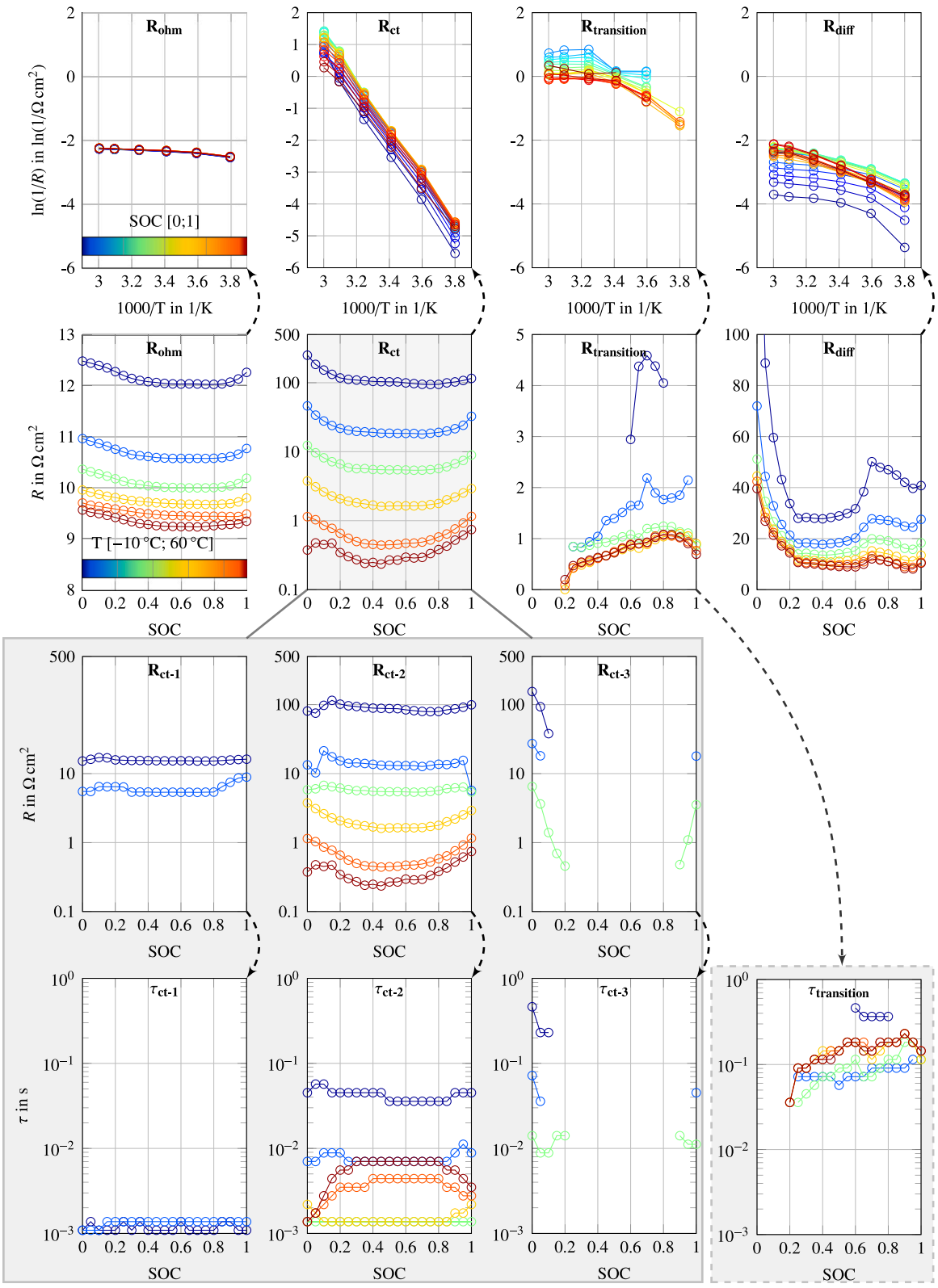

Fig. 10. Quantification of the time constant (determined at the respective local maxima of the DRT) and polarization resistance (determined by integration of the DRT between the adjacent minima) of identified loss process. Resistances are normalized by the active electrode surface. 1st row: Logarithm of the resistance over the inverse temperature according to (7) for different SOC. 2nd row: Resistance over SOC for different temperatures. 3rd row: Resistance over SOC for sub-processes of R_{ct}. 4th row: Time constants over SOC for sub-processes of R_{ct}.

representing the share of the solid state diffusion which was captured until the lowest frequency of 10 mHz.

In the first row, the logarithm of the resistance is plotted over the inverse temperature for every SOC to check for the Arrhenius

dependency according to

$$\frac{1}{R_{ct}} = A \cdot e^{\frac{-E_A}{R \cdot T}}, \quad (7)$$

with the universal gas constant R, the activation energy E_A, and the amplitude A. A linear behavior over the whole temperature range is expected for R_{ct} and R_{diff} [53]. In practice, however, confirmation of the Arrhenius dependency of solid-state diffusion is hardly possible due to the limited frequency range of EIS measurements, which is also the case for our measurements. Nevertheless, for R_{ct}, we observe a good quality of the linear fit ($R^2 > 0.996$) with resulting activation energies between $54\,kJ\,mol^{-1}$ and $65\,kJ\,mol^{-1}$.

In the second row, the resistance values are plotted over the SOC for the six different temperatures. For R_{ohm} and R_{ct}, the typical "bathtub" shape [54] is consistently observed. Thereby, R_{ct} is plotted logarithmically since it shows a strong temperature dependency with a resistance spread over several decades, reaching from below $1\,\Omega\,cm^2$ at 60 °C to above $100\,\Omega\,cm^2$ at −10 °C. The transition process shows a uniform trend with similar magnitude above 20 °C. For low temperatures, the resistance increases and is only visible in a narrow SOC interval. R_{diff} increases strongly towards a low SOC and shows characteristic behavior in the mid-SOC area, which coincides well with the stage 2 transition of graphite and can be explained by the homogenization effect [55–57].

In the third row, R_{ct} is further subdivided based on the DRT analysis. At 20 °C, two separate processes, which form the overall charge transfer resistance, have been identified. For lower temperatures (−10 °C and 5 °C) a third process is revealed by the DRT, which is assumed to be a result of the SEI. In the fourth row, the corresponding time constants τ are plotted over SOC for the three sub-processes of R_{ct} as well as for $R_{transition}$. Whereas the time constants of the charge transfer resistances vary highly with temperature, they are in the same order of magnitude for the transition process. Per definition, there is no time constant for R_{ohm} and τ_{diff} is constant due to the limited frequency range.

In this section, we complemented the study by giving detailed insights into the kinetics of the investigated cell. Thus, physically motivated design of algorithms on the application level is enabled. Based on these results, optimization algorithms, such as on-line estimation of the impedance throughout the lifetime [27], can be initialized and the number of considered loss processes, e.g., in an ECM, can be reasonably chosen.

6. Conclusions

Tear-down analysis of LIBs are essential for gathering in-depth knowledge about the systems' behavior and for enabling advanced algorithms to ensure optimal design and operation of LIBs on the application level. In this study, we presented detailed insights into the geometrical and electrochemical properties of a commercial NCA LIB with a Si-doped graphite anode.

In the first step, the cell was opened under inert gas atmosphere to yield direct measurement of the cell component's length, width, and thickness. Additionally, the battery was imaged by CT to get further insights into the geometrical structure of the jelly roll. The anode overhang was determined to approximately 7% of the total active area. Anode and cathode half cells were built for further experimental investigation of the electrode characteristics, with special focus on their interaction in a full cell assembly and for further utilization in advanced algorithms.

We compared different OCV determination techniques and found that despite small deviations due to different overpotentials, the OCV can be characterized with the GITT as well as pOCV measurements with small current rates ($> C/10$). In certain SOC ranges we observed a temperature dependency of the OCV. However, from our experimental results it is not clear whether this actually is due to temperature-dependent material properties or slower kinetics and increased overpotentials. We used the anode and cathode half cell voltage curves to reconstruct the full cell and to determine the correct balancing and alignment parameters with meaningful assignment of the electrode's characteristic material dependent stages and phases. For fitting in the OCV domain, an additional parameter accounting for different polarization in the full cell and the half cells had to be introduced. Using different configurations of the algorithms leads to slightly different results, which is why it is important to choose consistent measurements data, e.g., throughout the whole parameterization process of electrochemical models.

By analyzing the impedance spectra of the full cell and half cells, we gained detailed insights into the loss processes and their origins. The charge transfer resistance R_{ct} of the full cell at a low SOC seems to be dominated by the cathode, while it is dominated by the anode at a high SOC. R_{ct} is mainly responsible for the strong temperature dependency of the kinetic behavior and a good fit to the Arrhenius equation was confirmed (the activation energy lies between $54\,kJ\,mol^{-1}$ and $65\,kJ\,mol^{-1}$ for different SOCs). Between the charge transfer and the solid state diffusion, a transition process was observed which might, still inconclusively, be assigned to the anode. These results can further be used in physically motivated model development, e.g., by choosing a reasonable number of RC elements for an ECM. For the high frequent kinetic behavior, a minimum of two RC elements should be chosen for R_{ct}, which also could be subdivided into three RC elements, and $R_{transition}$. For the low frequent behavior, i.e., the solid state and electrolyte diffusion, further investigations, such as pulse relaxation measurements, should be performed.

Data availability

Raw measurement datasets related to this article can be found via [58], provided by mediaTUM.

CRediT authorship contribution statement

Leo Wildfeuer: Conceptualization, Methodology, Formal analysis, Investigation, Visualization, Data curation, Software, Validation, Writing – original draft, Writing – review & editing. **Nikolaos Wassiliadis:** Conceptualization, Methodology, Formal analysis, Investigation, Visualization, Data curation, Software, Validation, Writing – original draft, Writing – review & editing. **Alexander Karger:** Software, Writing – review & editing. **Fabian Bauer:** Resources, Writing – review & editing. **Markus Lienkamp:** Resources, Supervision, Writing – review & editing.

Declaration of competing interest

The authors declare that they have no known competing financial interests or personal relationships that could have appeared to influence the work reported in this paper.

Acknowledgments

This work is funded by the Bavarian Ministry of Economic Affairs, Regional Development and Energy under the project bawaii — battery analytics with artificial intelligence (IUK-1808-0013). The authors want to thank Fraunhofer ISC and especially Elena Fleder for supporting with the design and setup of the half cells. Furthermore, we want to acknowledge Matthias Wanzel and Philipp Gieler for their support.

Appendix. Impedance spectra and drt at 35 °C and 50 °C

See Figs. A.11 and A.12.

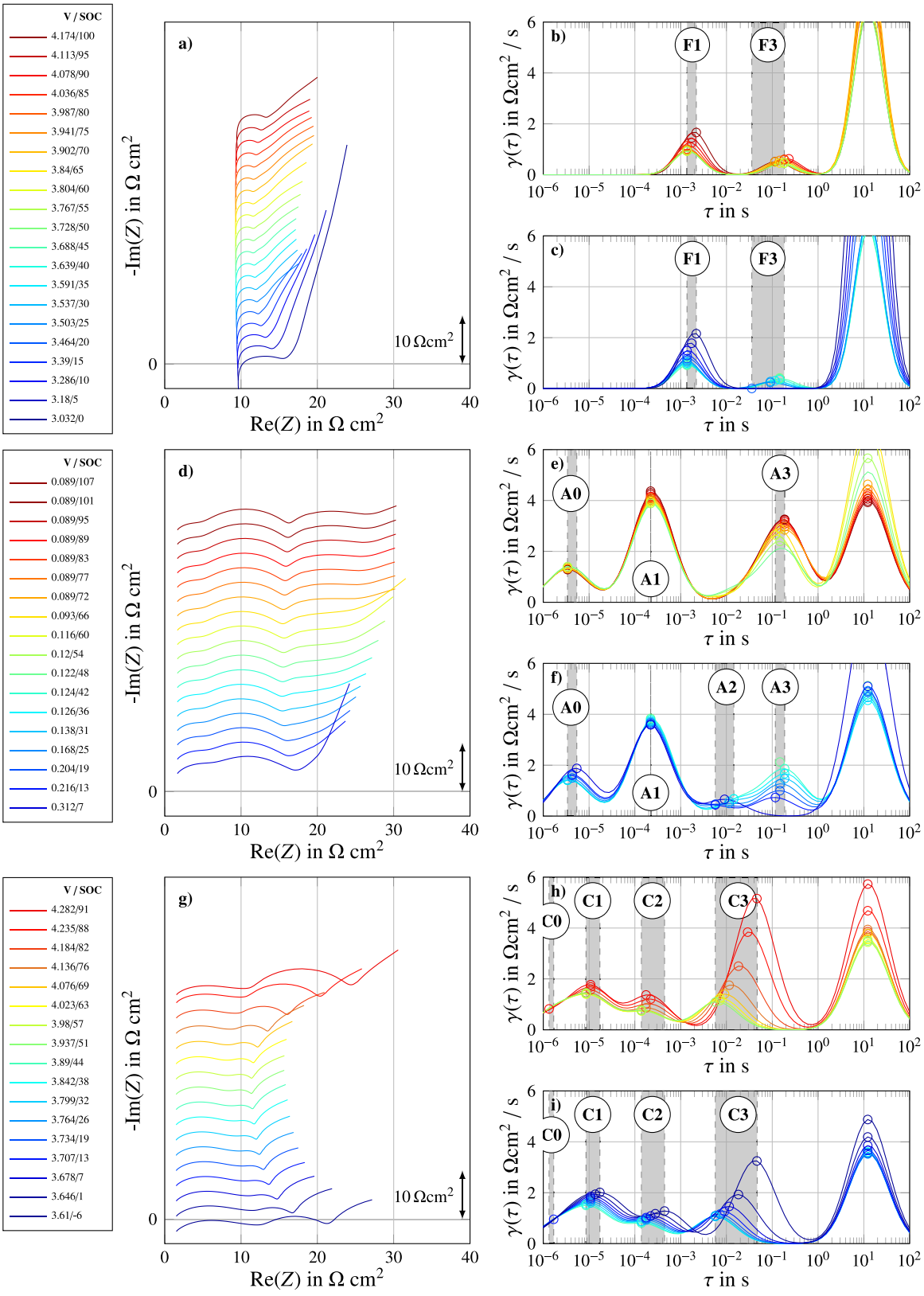

Fig. A.11. Impedance spectra from EIS measurements and corresponding DRT for different SOC at 35 °C. See Fig. 9 for detailed caption.

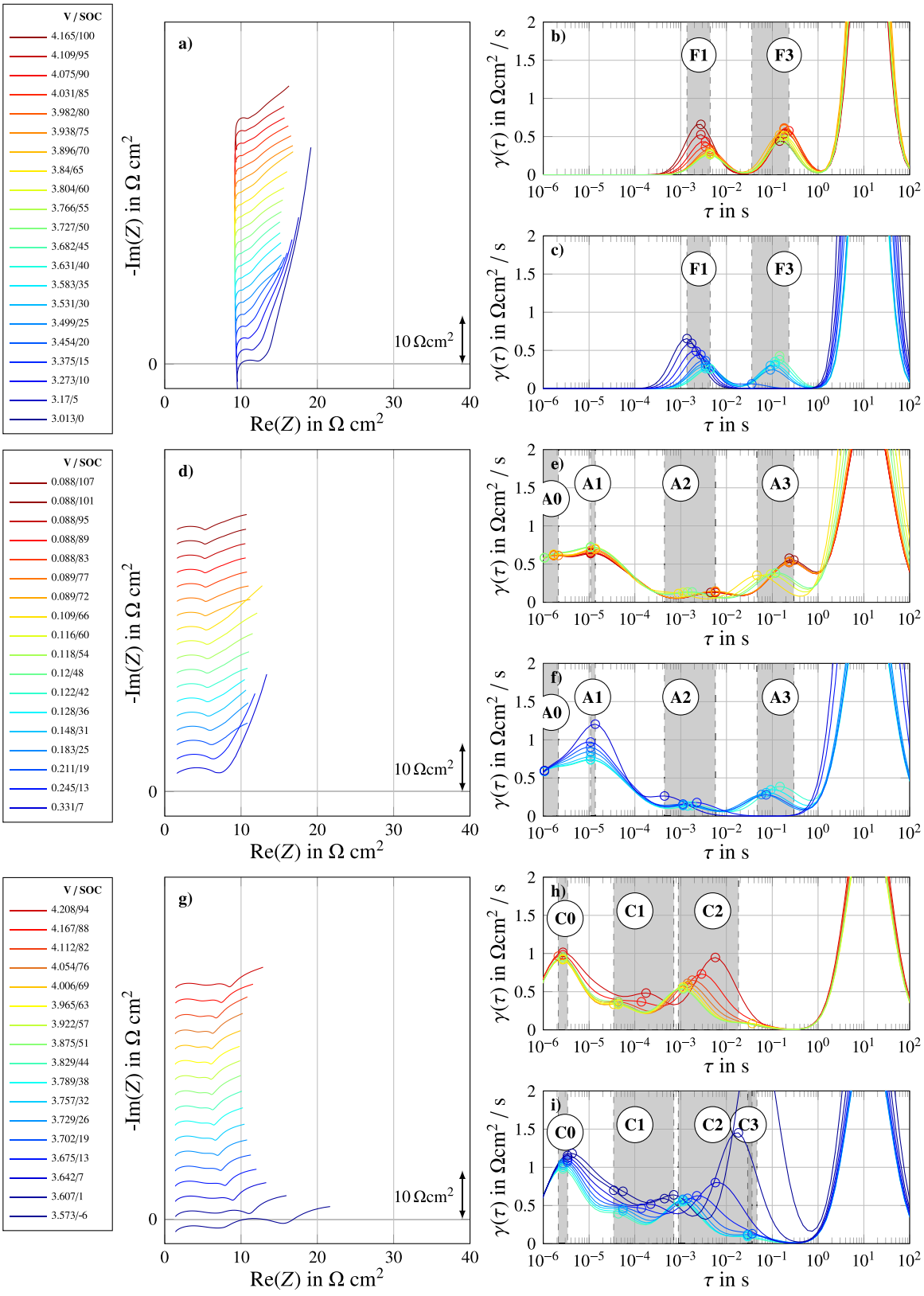

Fig. A.12. Impedance spectra from EIS measurements and corresponding DRT for different SOC at 50 °C. See Fig. 9 for detailed caption.

References

[1] A. König, L. Nicoletti, D. Schröder, S. Wolff, A. Waclaw, M. Lienkamp, An overview of parameter and cost for battery electric vehicles, World Electr. Veh. J. 12 (1) (2021) http://dx.doi.org/10.3390/wevj12010021.

[2] J. Vetter, P. Novák, M.R. Wagner, C. Veit, K.-C. Möller, J.O. Besenhard, M. Winter, M. Wohlfahrt-Mehrens, C. Vogler, A. Hammouche, Ageing mechanisms in lithium-ion batteries, J. Power Sources 147 (1–2) (2005) 269–281, http://dx.doi.org/10.1016/j.jpowsour.2005.01.006.

[3] M. Dubarry, B.Y. Liaw, M.-S. Chen, S.-S. Chyan, K.-C. Han, W.-T. Sie, S.-H. Wu, Identifying battery aging mechanisms in large format Li ion cells, J. Power Sources 196 (7) (2011) 3420–3425, http://dx.doi.org/10.1016/j.jpowsour.2010.07.029.

[4] A. Barré, B. Deguilhem, S. Grolleau, M. Gérard, F. Suard, D. Riu, A review on lithium-ion battery ageing mechanisms and estimations for automotive applications, J. Power Sources 241 (2013) 680–689, http://dx.doi.org/10.1016/j.jpowsour.2013.05.040.

[5] C.R. Birkl, M.R. Roberts, E. McTurk, P.G. Bruce, D.A. Howey, Degradation diagnostics for lithium ion cells, J. Power Sources 341 (2017) 373–386, http://dx.doi.org/10.1016/j.jpowsour.2016.12.011.

[6] M. Morita, N. Nishimura, Y. Matsuda, Charge/discharge cycling behavior of pitch-based carbon fiber in organic electrolyte solutions, Electrochim. Acta 38 (13) (1993) 1721–1726, http://dx.doi.org/10.1016/0013-4686(93)85068-A.

[7] A. Márquez, P.B. Balbuena, Molecular dynamics study of graphite/electrolyte interfaces, J. Electrochem. Soc. 148 (6) (2001) A624, http://dx.doi.org/10.1149/1.1372216.

[8] H. Yang, H.J. Bang, J. Prakash, Evaluation of Electrochemical Interface Area and lithium diffusion coefficient for a composite graphite anode, J. Electrochem. Soc. 151 (8) (2004) A1247, http://dx.doi.org/10.1149/1.1763139.

[9] H.-j. Guo, X.-h. Li, X.-m. Zhang, H.-q. Wang, Z.-x. Wang, W.-j. Peng, Diffusion coefficient of lithium in artificial graphite, mesocarbon microbeads, and disordered carbon, New Carbon Mater. 22 (1) (2007) 7–10, http://dx.doi.org/10.1016/S1872-5805(07)60006-7.

[10] M. Safari, C. Delacourt, Modeling of a commercial graphite/LiFePO4 cell, J. Electrochem. Soc. 158 (5) (2011) A562, http://dx.doi.org/10.1149/1.3567007.

[11] M. Ecker, T.K.D. Tran, P. Dechent, S. Käbitz, A. Warnecke, D.U. Sauer, Parameterization of a physico-chemical model of a lithium-ion battery, J. Electrochem. Soc. 162 (9) (2015) A1836–A1848, http://dx.doi.org/10.1149/2.0551509jes.

[12] J. Landesfeind, J. Hattendorff, A. Ehrl, W.A. Wall, H.A. Gasteiger, Tortuosity determination of battery electrodes and separators by impedance spectroscopy, J. Electrochem. Soc. 163 (7) (2016) A1373–A1387, http://dx.doi.org/10.1149/2.1141607jes.

[13] K. Pan, F. Zou, M. Canova, Y. Zhu, J.-H. Kim, Systematic electrochemical characterizations of Si and SiO anodes for high-capacity Li-Ion batteries, J. Power Sources 413 (2019) 20–28, http://dx.doi.org/10.1016/j.jpowsour.2018.12.010.

[14] D.P. Abraham, S. Kawauchi, D.W. Dees, Modeling the impedance versus voltage characteristics of LiNi0.8Co0.15Al0.05O2, Electrochim. Acta 53 (5) (2008) 2121–2129, http://dx.doi.org/10.1016/j.electacta.2007.09.018.

[15] P. Albertus, J. Christensen, J. Newman, Experiments on and modeling of positive electrodes with multiple active materials for lithium-ion batteries, J. Electrochem. Soc. 156 (7) (2009) A606, http://dx.doi.org/10.1149/1.3129656.

[16] R. Amin, D.B. Ravnsbæ k, Y.-M. Chiang, Characterization of electronic and ionic transport in Li 1-x Ni 0.8 Co 0.15 Al 0.05 o 2 (NCA), J. Electrochem. Soc. 162 (7) (2015) A1163–A1169, http://dx.doi.org/10.1149/2.0171507jes.

[17] M.A. Cabañero, N. Boaretto, M. Röder, J. Müller, J. Kallo, A. Latz, Direct determination of diffusion coefficients in commercial li-ion batteries, J. Electrochem. Soc. 165 (5) (2018) A847–A855, http://dx.doi.org/10.1149/2.0301805jes.

[18] S. Xia, F. Li, F. Chen, H. Guo, Preparation of FePO4 by liquid-phase method and modification on the surface of LiNi0.80Co0.15Al0.05O2 cathode material, J. Alloys Compd. 731 (2018) 428–436, http://dx.doi.org/10.1016/j.jallcom.2017.10.047.

[19] P. Shafiei Sabet, G. Stahl, D.U. Sauer, Non-invasive investigation of predominant processes in the impedance spectra of high energy lithium-ion batteries with Nickel-Cobalt-Aluminum cathodes, J. Power Sources (2018) http://dx.doi.org/10.1016/j.jpowsour.2018.10.024.

[20] P.S. Sabet, D.U. Sauer, Separation of predominant processes in electrochemical impedance spectra of lithium-ion batteries with nickelemanganeseecobalt cathodes, J. Power Sources 425 (2019) 121–129, http://dx.doi.org/10.1016/j.jpowsour.2019.03.068.

[21] J. Schmalstieg, C. Rahe, M. Ecker, D.U. Sauer, Full cell parameterization of a high-power lithium-ion battery for a physico-chemical model: Part I. Physical and electrochemical parameters, J. Electrochem. Soc. 165 (16) (2018) A3799–A3810, http://dx.doi.org/10.1149/2.0321816jes.

[22] Kovachev, Schröttner, Gstrein, Aiello, Hanzu, Wilkening, Foitzik, Wellm, Sinz, Ellersdorfer, Analytical dissection of an automotive li-ion pouch cell, Batteries 5 (4) (2019) 67, http://dx.doi.org/10.3390/batteries5040067.

[23] J. Marshall, D. Gastol, R. Sommerville, B. Middleton, V. Goodship, E. Kendrick, Disassembly of li ion cells—Characterization and safety considerations of a recycling scheme, Metals 10 (6) (2020) 773, http://dx.doi.org/10.3390/met10060773.

[24] Lain, Brandon, Kendrick, Design strategies for high power vs. High energy lithium ion cells, Batteries 5 (4) (2019) 64, http://dx.doi.org/10.3390/batteries5040064.

[25] Liebig, Gupta, Kirstein, Schuldt, Agert, Parameterization and validation of an electrochemical thermal model of a lithium-ion battery, Batteries 5 (3) (2019) 62, http://dx.doi.org/10.3390/batteries5030062.

[26] C.-H. Chen, F. Brosa Planella, K. O'Regan, D. Gastol, W.D. Widanage, E. Kendrick, Development of experimental techniques for parameterization of multi-scale lithium-ion battery models, J. Electrochem. Soc. 167 (8) (2020) 080534, http://dx.doi.org/10.1149/1945-7111/ab9050.

[27] A. Karger, L. Wildfeuer, A. Maheshwari, N. Wassiliadis, M. Lienkamp, Novel method for the on-line estimation of low-frequency impedance of lithium-ion batteries, J. Energy Storage 32 (August) (2020) 101818, http://dx.doi.org/10.1016/j.est.2020.101818.

[28] N. Wassiliadis, J. Schneider, A. Frank, L. Wildfeuer, X. Lin, A. Jossen, M. Lienkamp, Review of fast charging strategies for lithium-ion battery systems and their applicability for battery electric vehicles, J. Energy Storage 44 (2021) 103306, http://dx.doi.org/10.1016/j.est.2021.103306.

[29] J. Sieg, J. Bandlow, T. Mitsch, D. Dragicevic, T. Materna, B. Spier, H. Witzenhausen, M. Ecker, D.U. Sauer, Fast charging of an electric vehicle lithium-ion battery at the limit of the lithium deposition process, J. Power Sources 427 (2019) 260–270, http://dx.doi.org/10.1016/j.jpowsour.2019.04.047.

[30] A.U. Schmid, A. Ridder, M. Hahn, K. Schofer, K.P. Birke, Aging of extracted and reassembled li-ion electrode material in terms of coin cell-capabilities and limitations, Batteries 6 (2) (2020) 33, http://dx.doi.org/10.3390/batteries6020033.

[31] X.-Y. Yao, M.G. Pecht, Tab design and failures in cylindrical li-ion batteries, IEEE Access 7 (2019) 24082–24095, http://dx.doi.org/10.1109/ACCESS.2019.2899793.

[32] B. Gyenes, D.A. Stevens, V.L. Chevrier, J.R. Dahn, Understanding anomalous behavior in Coulombic efficiency measurements on li-ion batteries, J. Electrochem. Soc. 162 (3) (2015) A278–A283, http://dx.doi.org/10.1149/2.0191503jes.

[33] M. Lewerenz, G. Fuchs, L. Becker, D.U. Sauer, Irreversible calendar aging and quantification of the reversible capacity loss caused by anode overhang, J. Energy Storage 18 (2018) 149–159, http://dx.doi.org/10.1016/j.est.2018.04.029.

[34] A. Barai, K. Uddin, M. Dubarry, L. Somerville, A. McGordon, P. Jennings, I. Bloom, A comparison of methodologies for the non-invasive characterisation of commercial Li-ion cells, Prog. Energy Combust. Sci. 72 (2019) 1–31, http://dx.doi.org/10.1016/j.pecs.2019.01.001.

[35] T. Ohzuku, Y. Iwakoshi, K. Sawai, Formation of lithium-graphite intercalation compounds in nonaqueous electrolytes and their application as a negative electrode for a lithium ion (shuttlecock) cell, J. Electrochem. Soc. 140 (9) (1993) 2490–2498, http://dx.doi.org/10.1149/1.2220849.

[36] I. Zilberman, S. Ludwig, A. Jossen, Cell-to-cell variation of calendar aging and reversible self-discharge in 18650 nickel-rich, silicon–graphite lithium-ion cells, J. Energy Storage 26 (August) (2019) 100900, http://dx.doi.org/10.1016/j.est.2019.100900.

[37] K.J. Park, J.Y. Hwang, H.H. Ryu, F. Maglia, S.J. Kim, P. Lamp, C.S. Yoon, Y.K. Sun, Degradation mechanism of Ni-enriched NCA cathode for lithium batteries: Are microcracks really critical? ACS Energy Lett. 4 (6) (2019) 1394–1400, http://dx.doi.org/10.1021/acsenergylett.9b00733.

[38] A. Farmann, D.U. Sauer, A study on the dependency of the open-circuit voltage on temperature and actual aging state of lithium-ion batteries, 2017, http://dx.doi.org/10.1016/j.jpowsour.2017.01.098.

[39] M. Baumann, L. Wildfeuer, S. Rohr, M. Lienkamp, Parameter variations within Li-Ion battery packs – Theoretical investigations and experimental quantification, J. Energy Storage 18 (2018) http://dx.doi.org/10.1016/j.est.2018.04.031.

[40] K. Rumpf, M. Naumann, A. Jossen, Experimental investigation of parametric cell-to-cell variation and correlation based on 1100 commercial lithium-ion cells, J. Energy Storage 14 (2017) 224–243, http://dx.doi.org/10.1016/j.est.2017.09.010.

[41] L. Wildfeuer, M. Lienkamp, Quantifiability of inherent cell-to-cell variations of commercial lithium-ion batteries, ETransportation 9 (2021) 100129, http://dx.doi.org/10.1016/j.etran.2021.100129.

[42] A.U. Schmid, M. Kurka, K.P. Birke, Reproducibility of Li-ion cell reassembling processes and their influence on coin cell aging, J. Energy Storage 24 (2019) 100732, http://dx.doi.org/10.1016/j.est.2019.04.006.

[43] M. Dubarry, V. Svoboda, R. Hwu, B.Y. Liaw, Incremental capacity analysis and close-to-equilibrium OCV measurements to quantify capacity fade in commercial rechargeable lithium batteries, Electrochem. Solid-State Lett. 9 (10) (2006) http://dx.doi.org/10.1149/1.2221767.

[44] S. Schindler, M.A. Danzer, A novel mechanistic modeling framework for analysis of electrode balancing and degradation modes in commercial lithium-ion cells, J. Power Sources 343 (2017) 226–236, http://dx.doi.org/10.1016/j.jpowsour.2017.01.026.

[45] J. Schmitt, M. Schindler, A. Jossen, Change in the half-cell open-circuit potential curves of silicon–graphite and nickel-rich lithium nickel manganese cobalt oxide during cycle aging, J. Power Sources 506 (June) (2021) 230240, http://dx.doi.org/10.1016/j.jpowsour.2021.230240.

[46] J.P. Schmidt, P. Berg, M. Schönleber, A. Weber, E. Ivers-Tiffée, The distribution of relaxation times as basis for generalized time-domain models for Li-ion batteries, J. Power Sources 221 (2013) 70–77, http://dx.doi.org/10.1016/j.jpowsour.2012.07.100.

[47] J. Illig, M. Ender, T. Chrobak, J.P. Schmidt, D. Klotz, E. Ivers-Tiffée, Separation of charge transfer and contact resistance in LiFePO4-cathodes by impedance modeling, J. Electrochem. Soc. 159 (7) (2012) A952–A960.

[48] S. Gantenbein, M. Weiss, E. Ivers-Tiffée, Impedance based time-domain modeling of lithium-ion batteries: Part I, J. Power Sources 379 (2018) 317–327, http://dx.doi.org/10.1016/j.jpowsour.2018.01.043.

[49] E. Goldammer, J. Kowal, Determination of the distribution of relaxation times by means of pulse evaluation for offline and online diagnosis of lithium-ion batteries, Batteries 7 (2021) 36, http://dx.doi.org/10.3390/batteries7020036.

[50] L. Wildfeuer, P. Gieler, A. Karger, Combining the distribution of relaxation times from EIS and time-domain data for parameterizing equivalent circuit models of lithium-ion batteries, Batteries (2021) 1–23.

[51] D. Klotz, Characterization and modeling of electrochemical energy conversion systems by impedance techniques, (Ph.D. thesis), 2012.

[52] T.H. Wan, M. Saccoccio, C. Chen, F. Ciucci, Influence of the discretization methods on the distribution of relaxation times deconvolution: Implementing radial basis functions with DRTtools, Electrochim. Acta 184 (2015) 483–499, http://dx.doi.org/10.1016/j.electacta.2015.09.097.

[53] A. Mertens, I.C. Vinke, H. Tempel, H. Kungl, L.G.J. de Haart, R.-A. Eichel, J. Granwehr, Quantitative analysis of time-domain supported electrochemical impedance spectroscopy data of li-ion batteries: Reliable activation energy determination at low frequencies, J. Electrochem. Soc. 163 (7) (2016) H521–H527, http://dx.doi.org/10.1149/2.0511607jes.

[54] S. Gantenbein, M. Weiss, E. Ivers-Tiffée, Impedance based time-domain modeling of lithium-ion batteries: Part I, J. Power Sources 379 (January) (2018) 317–327, http://dx.doi.org/10.1016/j.jpowsour.2018.01.043.

[55] L. Wildfeuer, N. Wassiliadis, C. Reiter, M. Baumann, M. Lienkamp, Experimental characterization of li-ion battery resistance at the cell, module and pack level, in: 2019 Fourteenth International Conference on Ecological Vehicles and Renewable Energies (EVER), IEEE, 2019, pp. 1–12.

[56] J.P. Schmidt, Verfahren zur charakterisierung und modellierung von lithium-ionen zellen, (Ph.D. thesis), KIT Scientific Publishing, 2013.

[57] F.E. Hust, Physico-chemically motivated parameterization and modelling of real-time capable lithium-ion battery models : a case study on the Tesla Model S battery, (Ph.D. thesis), in: Aachener Beiträge des ISEA, 120, ISEA, 2018, pp. 1 Online–Ressource (vii, 203 Seiten) : Illustrationen, Diagramme, http://dx.doi.org/10.18154/RWTH-2019-00249.

[58] L. Wildfeuer, N. Wassiliadis, A. Karger, F. Bauer, M. Lienkamp, Teardown analysis and characterization of a commercial lithium-ion battery for advanced algorithms in battery electric vehicles, Technical University of Munich, URL https://mediatum.ub.tum.de/1639153, http://dx.doi.org/10.14459/2022mp1639153.

2.3 Systematic approach for parameter identification of electrochemical models

Advanced fast charging control strategies rely on model-based algorithms controlling the charging current at the edge of the physical limits to avoid critical aging mechanisms such as, most importantly, lithium plating during a fast charging event. The complex physical nature of lithium-ion cells requires sophisticated electrochemical models to precisely mimic the lithium-ion cell behavior and give control access to these aging trigger conditions during fast charging. As stated previously in Section 2.1, the benefit of model-based approaches lies in being flexible enough to be transferred to different cell cathode materials (e.g., NMC, LFP, NCA) and varying properties due to different cell design decisions (e.g., thin electrode in high power and thick active material layer in high energy cell designs), as the choice for cell design and materials will always depend on the targeted application (e.g., cost-efficient short distance versus superior long-distance applications, passenger vehicles versus heavy-duty vehicles, etc.). Furthermore, compared to simple look-up tables, these models can be updated to the actual state and changing parameters of the cell during operation, e.g., at rising SOC, varying ambient temperatures, and progressing age of the lithium-ion cells. Besides the various advantages, it is a highly complex challenge to precisely parameterize electrochemical models. There is still no consensus in the literature on how to do this the most efficiently, as either in-depth experimental assessments of the lithium-ion cell components and properties are carried out [103, 104, 183, 184], or parameters are grouped and step-wise identified by global numerical optimization at cell level [191–193].

To pave the way for physical-motivated modeling of lithium-ion cells in automotive applications and enable the use of these models for fast charging control algorithms, this section proposes a comprehensive approach for parameter identification of electrochemical models. Measurement-based parameter identification and fitting-based numerical parameter identification are balanced and hybridized, as published in previous work by the author [38] and visualized in Figure 2.3. The incentive lies in achieving sufficient accuracy while keeping the time and laboratory effort at a minimum. The method is applied to an electrochemical model of reduced order, namely an electrolyte-enhanced SPM originally published by Moura et al. [194], and extended with a thermal model by Perez et al. [195], to allow for later use in computational-efficient applications. Starting with material and geometrical parameters identified experimentally earlier in a tear-down study of the investigated lithium-ion cell (Section 2.2), the model is step-wise parameterized by fitting the remaining parameters systematically to explicit measurements. By systematic parameter grouping according to their electrothermal interdependence, parameter ambiguities are minimized. Note that electrolyte parameters have been extracted from the literature as it is challenging to carefully extract electrolytes from *post-mortem* commercial lithium-ion cells without contamination with other materials. In the first step, the electrode OCPs were fitted with regressions to enable meaningful extrapolation behavior and were carefully balanced and aligned to the lithium-ion cell OCVs to correctly map the electrode use in the pristine lithium-ion cell. Here, GITTs measurements have been used as they have been seen to improve the fitting accuracy compared to OCVs determination by constant current charging with low current rates (pOCVs) [196]. In a second step, the crafted model was employed to identify the parameters describing the dynamic cell behavior by fitting the single electrode model response (anode and cathode) to the pulse current excitation from the GITTs measurements at half-cell level

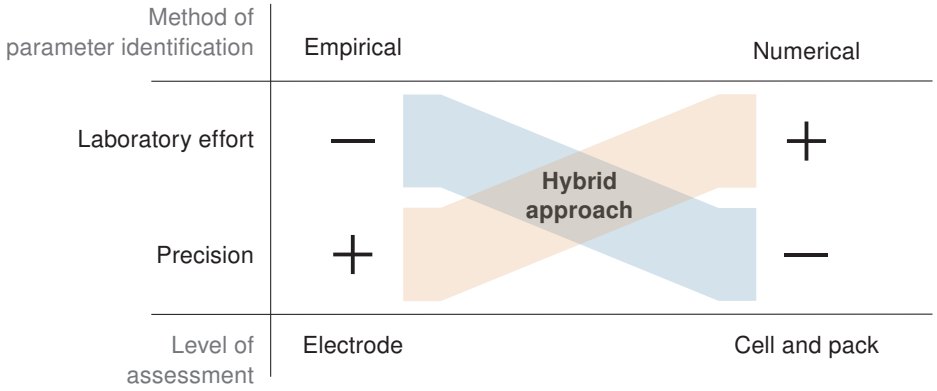

Figure 2.3: Schematics illustrating the developed systematic approach to trade-off the parameter identification task for electrochemical models with parameters determined empirically at the electrode level (empirical identification) and globally by optimization to measurements taken at the cell level (numerical identification).

and gathering SOC-dependent regressions. Then the results were used to quantify the thermal dependence by scaling and fitting the regressions to high pulse power characterizations (HPPCs) tests at different ambient temperatures at cell level. In the last step, thermal parameters were identified without interference with the electrical parameter subset [197].

A broad validation up to charging rates of 6C, ambient temperatures between $-10\,^{\circ}\mathrm{C}$ and $50\,^{\circ}\mathrm{C}$, and scale to 12s2p system level showed that the parameterized model accurately maps the cell voltage under different operating conditions. However, model accuracy decreased in low SOC regions and at subzero temperatures. The first issue can be traced back to the difficult diffusion coefficient and reaction rate quantification of the discharged cell. The latter issue has been seen to originate from a poor electrolyte parameter set [198], which highlights the need for techniques of precise characterization of the electrolyte parameter from *post-mortem* lithium-ion cells, which has been beyond the scope of this study. The model usage is restricted in the areas mentioned above for further deployment in real-time fast-charging control algorithms. The crafted model is exemplarily used for anode potential control to avoid lithium plating onset conditions during the aging of the modeled lithium-ion cell. The developed model and overall parameter identification method of electrochemical models have also been published as open source [199].

Author contribution: General conceptualization, method development, investigation, and validation within this study were pursued by Nikolaos Wassiliadis except where noted otherwise. Manuel Ank supported with the inclusion of system-level effects in the model. Preliminary tests, validation experiments, and development of parts of the algorithms were performed by Andreas Bach, Matthias Wanzel, and Ann-Sophie Zollner during their Master's studies. Nikolaos Wassiliadis, Manuel Ank, Kareem Abo Gamra, and Markus Lienkamp reviewed and edited the manuscript. Markus Lienkamp provided resources and supervision for this work.

A systematic approach for the parameter identification of electrochemical battery models for health-aware fast charging control of battery electric vehicles

Nikolaos Wassiliadis, Manuel Ank, Andreas Bach, Matthias Wanzel, Ann-Sophie Zollner, Kareem Abo Gamra, Markus Lienkamp

Journal of Energy Storage 56, 2022.
Digital Object Identifier: 10.1016/j.est.2022.105951

Journal of Energy Storage 56 (2022) 105951

Contents lists available at ScienceDirect

Journal of Energy Storage

journal homepage: www.elsevier.com/locate/est

Research papers

A systematic approach for the parameter identification of electrochemical battery models enabling health-aware fast charging control of battery electric vehicles

Nikolaos Wassiliadis *, Manuel Ank, Andreas Bach, Matthias Wanzel, Ann-Sophie Zollner, Kareem Abo Gamra, Markus Lienkamp

Technical University of Munich (TUM), School of Engineering & Design, Department of Mobility Systems Engineering, Institute of Automotive Technology, Germany

ARTICLE INFO

Dataset link: https://github.com/TUMFTM/EA_Battery_SPMparameterization

Keywords:
Electric vehicles
Fast charging
Lithium-ion battery
Electrochemical modeling
Parameter identification
Battery management systems

ABSTRACT

In industrial practice, fast charging currents are usually controlled by current stages derived from long-term lab testing at different cell integration levels — requiring intensive experimental effort prior to application. Model-based approaches exploiting knowledge of the electro-thermal behavior of the deployed lithium-ion cells promise a quicker and more targeted development of fast charging strategies with less long-term lab testing effort. However, there is still no consensus in the literature on how to quickly parameterize physics-enhanced electro-thermal battery models without a greater loss of generality. We present a systematic procedure to parameterize an electrochemical reduced-order model capable of controlling the charging current to a specific anode potential reserve at the edge of the lithium deposition process in real time for a given commercial lithium-ion cell. A broad experimental validation at charging rates ranging from 1C to 6C, ambient temperatures between −10 °C and 50 °C, and at pack level is carried out to confirm the developed method.

1. Introduction

Fast charging of battery electric vehicles has been identified as the key enabler for the wide-spread adoption of electric mobility as it promises to vanish range anxiety. In recent years, R&D goals have been focused on achieving fast charging times comparable to refueling times of conventional vehicles by many political associations, e.g. the United States Department of Energy (DOE) in 2017 with a targeted fast charging time of below 15 min in 2028 [1] or a proposal of the European Technology and Innovation Platform (ETIP) aligned with the European Commission's Strategic Energy and Technology Plan (SET-Plan) with a targeted fast charging time of below 20 min by 2030 [2].

With the parallel uprise of R&D activities in this field, many studies have revealed innovative approaches in minimizing the risk of accelerated aging due to fast charging, different to that of common battery wisdom, i.e. constant current (CC) or constant power (CP) charging. Most prominently, empirical fast charging strategies haven been studied, by applying e.g. boost- [3–5], multi-stage- [5–7], or pulse [5,8] charging currents to lithium-ion cells, choosing the fast charging strategy with minimal cell degradation. In order to avoid intensive testing, knowledge of aging mechanisms at high charge currents has been exploited for the design of fast charging strategies, with focus on the main mechanisms metallic lithium deposition, also well-known as *lithium plating*, occurring at anode potentials below 0 V [9] and temperature-induced aging mechanisms occurring beyond a cell-specific temperature threshold. Most commonly, model-based approaches have been deployed connecting measurable cell states to get a fair estimate of the immeasurable cell internal states for fast charging control at the application level [10–14], as shown in Fig. 1. One of the most promising approaches lies in deploying electrochemical models of reduced order, as they are capable of avoiding hazardous operation by scaling up knowledge of aging mechanisms at the electrode level to the pack level. Moreover, these models can be adapted to the real state of the cell during operation of a battery electric vehicle (BEV), i.e., adjusted to varying conditions.

As stated by recent review articles [15,16], one of the biggest challenges in deploying model-based strategies still lies in the parameter complexity of the involved electrochemical models and the intensive effort in yielding accurate model predictions. Even though simplifications have been made to the original and mainly used pseudo-two dimensional (P2D) electrochemical lithium-ion cell model developed by the research group of Doyle, Fuller and Newman [17], there is no consensus on how to identify the necessary parameter set in a way that achieves accuracy while keeping the required time and effort to

* Corresponding author.
E-mail address: nikolaos.wassiliadis@tum.de (N. Wassiliadis).

https://doi.org/10.1016/j.est.2022.105951
Received 11 January 2022; Received in revised form 27 September 2022; Accepted 18 October 2022
Available online 2 November 2022
2352-152X/

a minimum. From the author's perspective, two different trends for model parameter identification have been observed in the past: (1) In-depth experimental assessment of single cell components and direct parameter composition in electrochemical models on the one side [18–20], and (2) grouped or simultaneous optimization of all required material and electrode parameters to a voltage response at cell level on the other side [21–24]. While the first approach has the benefit of an accurate determination of all necessary parameters at the material and electrode level, a validated model response of a scaled-up model is usually hard to obtain. The latter approach has the advantage of fitting to measurement quantities at cell or pack level without the need for intensive electrochemical characterization, however, it loses the ability of separating the physical effects of the electrode parameters necessary for accurate fast charging current control. Hybrid approaches are needed, which enable accurate parameter identification while keeping the time and effort to a minimum.

1.1. Contributions

Model-based health-aware fast-charging control poses the challenge of incorporating an electrochemical battery model with sufficient accuracy, which is usually difficult to obtain. Many parameters must be determined in advance and evaluated according to the used cell type, additionally requiring intensive validation. The main objective of this article, therefore, is to provide a systematic parameter identification procedure of an electrochemical-thermal lithium-ion battery model valid at high charge rates, that is, an electrolyte-enhanced electro-thermal Single Particle Model (SPM), to enable a fast scaling of electrode knowledge to application level for the implementation in BMSs. Alongside this, the parameterized model is validated against measurements at high currents and temperatures and provided as an open source with this article. The main contributions of the underlying article can be summarized as follows:

- **Novel and comprehensive method for systematic parameter identification of an electrochemical-thermal model to enable scaling of electrode behavior to pack level for real-time fast-charging control**
  A comprehensive and systematic approach in determining cell-specific model parameters is presented and applied. The procedure enables a simplified model-based parameter identification for a given lithium-ion cell by separating parameter fitting into different stages and relying on reproducible and robust experimental methods.
- **Extensive validation of the crafted model at various charging currents and temperatures**
  The parameter identification procedure is applied to a commercially-available lithium-ion cell and the model is validated up to 6C charging current at −10 °C to 50 °C and 12s2p level.
- **Open-source provision of the validated model, parameterization functions and raw measurement data**
  All measurement data, processing functions, and the overall model are provided as open source alongside the article.

1.2. Organization of the article

The remainder of this article is structured as follows: Section 2 briefly introduces the governing equations of the deployed model and the lithium-ion cell under study. Subsequently, the developed characterization and systematic model parameter identification procedure is explained in Section 3, from electrode level up to pack level. In Section 4, the model accuracy is evaluated against various charging C-rates, ambient temperatures, and at pack level. A health-aware fast charging strategy is proposed in Section 5 and its sensitivity to parameter variations quantified in Section 6. Finally, Section 7 summarizes the benefits of the presented method and sheds light onto future work.

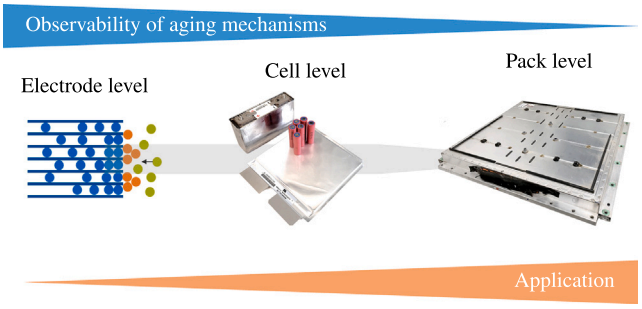

Fig. 1. Gap between electrode and pack level to account for aging mechanisms and their onset conditions for health-aware fast charging control in BMSs.

Table 1
Specifications of the lithium-ion battery under study.

Property	Value	Unit
Manufacturer	Sony/Murata	–
Type	US18650VTC5A	–
Format	18 650	–
Active material	SiC/NCA	–
Rated capacity	2.5	Ah
Voltage bounds	2.5 – 4.2	V
Weight	47.1	g
Max. charge current	6.0	A
Max. discharge current	35.0	A

2. Model and cell under study

The used electrochemical model has been developed in previous studies by Moura et al. [25] and extended with a thermal model by Perez et al. [26], which is why only the output function is outlined and the reader is referred to the corresponding publications of the mentioned authors for more details.

2.1. Cell specifications

In this study, the commercially available lithium-ion cell Sony/Murata US18650VTC5A was chosen as a representative cell candidate for lithium-ion cells with silicon-doped graphite anodes, which have been frequently deployed in the past, as silicon enables a higher energy density of lithium-ion cells [27]. The lithium-ion cell under study further contains a nickel-rich NCA cathode. The operating voltage range has been defined between 2.5 V and 4.2 V. All properties of the lithium-ion cell taken from the manufacturer data sheet are summarized in Table 1.

2.2. Electrical model

The utilized SPM is derived from simplifications of the computational complex P2D model of Newman's group [17] based on the assumption of homogeneous concentration distribution within the electrode in combination with approximations of various state variables. In here, the partial differential equations (PDEs) are discretized, which preserves both the physical–chemical description of the effects and the meaning of the parameters in the equations. The usage of several assumptions result in a model consisting of two linear PDEs which describe the diffusion behavior of the two electrodes through one spherical particle. Furthermore, it includes a quasi-linear PDE for the description of the concentration within the three spatial domains, i.e. the anode, the separator, and the cathode. These equations are combined into a nonlinear output function returning the overall battery voltage, which is calculated as a function of the concentration in the solid phase and the concentration in the liquid phase. As the model has been derived in previous work and is not within the focus of this

article, we sacrifice a detailed explanation at this point and present the overall model output equation only, highlighting the complexity of the different fragments to yield a cell voltage following a charging current excitation. For a step-by-step derivation of the model, the reader is referred to the explanation and parameter notation in Appendix A or the original articles [25,26].

The nonlinear output function of the cell voltage $U(t)$ results from the potentials of the solid phases, the overpotential of the electrode/electrolyte interfaces, the overpotential of the electrolyte and the electrode/current collector interface relationship, which can be summarized as

$$\begin{aligned} U(t) = & \underbrace{\frac{RT_\mathrm{c}}{\alpha F}\sinh^{-1}\left(\frac{I(t)}{2a^+L^+i_0^+(t)A}\right)}_{\text{Cathode overpotential}} - \underbrace{\frac{RT_\mathrm{c}}{\alpha F}\sinh^{-1}\left(\frac{-I(t)}{2a^-L^-i_0^-(t)A}\right)}_{\text{Anode overpotential}} \\ & + \underbrace{\phi_{\mathrm{OCP}}^+\left(c_{\mathrm{ss}}^+(t)\right)}_{\text{Cathode OCV}} - \underbrace{\phi_{\mathrm{OCP}}^-\left(c_{\mathrm{ss}}^-(t)\right)}_{\text{Anode OCV}} + \underbrace{\left(\frac{R_\mathrm{f}^+}{a^+L^+} + \frac{R_\mathrm{f}^-}{a^-L^-}\right)\frac{I(t)}{A}}_{\text{SEI/CEI overpotential}} \\ & + \underbrace{\frac{L^+ + 2L^{\mathrm{sep}} + L^-}{2\overline{\kappa}(T_\mathrm{c})}\frac{I(t)}{A}}_{\text{Electrolyte overpotential}} \\ & + \underbrace{\frac{2RT_\mathrm{c}}{F}\left(1-t_\mathrm{c}^0\right)\overline{k}_\mathrm{f}(t,T_\mathrm{c})\left[\ln c_\mathrm{e}(0^+,t) - \ln c_\mathrm{e}(0^-,t)\right]}_{\text{Electrolyte overpotential}} \end{aligned} \tag{1}$$

with the mathematical derivation and parameter notations detailed in Appendix A. With the above equations at hand, the overall electrical model is defined and can be applied to get a good replica of the electrical behavior of the lithium-ion cell under study while providing valuable information about the electrode states to avoid lithium deposition during fast charging current control.

2.3. Thermal model

As pointed out by recent studies, the cell's temperature at the measurement point does diverge significantly from the cell core. Amietszajew et al. [28] studied the thermal gradient for 18 650 cylindrical cells with a thermal sensor in the cell core and observed temperature differences of up to 5 K. Forgez et al. [29] investigated 26 650 cylindrical cells with a similar method in an earlier study observing temperature differences of up to 10 K. These difference are expected to diverge further with increasing charging currents, as locally occurring power losses increase quadratically with the charging current and thermal conduction is limited by the cell design. Therefore, in this study, a lumped thermal model in the lateral direction of the cell is used, based on the assumption of longitudinal homogeneity of the thermal cell behavior.

The cell core temperature T_c is calculated with the ordinary differential equation (ODE)

$$\frac{\mathrm{d}T_\mathrm{c}(t)}{\mathrm{d}t} = \frac{T_\mathrm{s}(t) - T_\mathrm{c}(t)}{R_1C_1} + \frac{\dot{Q}(t)}{C_1}, \tag{2}$$

where T_s is the measured cell surface temperature, R_1 the thermal resistance, C_1 the heat capacity, and $\dot{Q}$ the power losses within the cell core. Note that only the cell core is modeled as the cell surface temperature is measured. The heat dissipation is solely based on irreversible losses (Joule heat) defined by

$$\dot{Q}(t) = -I(t)\cdot\underbrace{\left[U(t) - \left(\phi_{\mathrm{OCP}}^+\left(\overline{c}_\mathrm{s}^+(t)\right) - \phi_{\mathrm{OCP}}^-\left(\overline{c}_\mathrm{s}^-(t)\right)\right)\right]}_{\text{Cell overpotential}} \tag{3}$$

with the charging current I, the electrode open-circuit potentials $\phi_{\mathrm{OCP}}^{\pm}$ dependent on the average particle concentration $\overline{c}_\mathrm{s}^{\pm}$, and the overall cell voltage U. Since reversible losses (e.g., entropy-related heat) are not relevant with fast charging currents [30], they are neglected within this study. For a more detailed step-by-step derivation of the thermal model, the reader is referred to the explanation and parameter notation in Appendix B.

2.4. Coupling of the physics

To ensure correct behavior of the model, close consideration has to be given to the coupling of the electrical and thermal behavior. Many parameters described in the electrical model are temperature dependent, such as the diffusion D_s and reaction rates k of both electrodes or the conductivity of the electrolyte κ. In order to ensure a correct change of these parameters due to temperature variations, the calculated cell core temperature is fed back to the electrochemical model. Hereby, the core temperature T_c is an input quantity for the calculation of the concentrations and potentials from Section 2.2 by using temperature-dependent parameters. All temperature-dependent parameters p follow the *Arrhenius* law as

$$p(T_\mathrm{c}) = p_0 \cdot e^{\frac{E_\mathrm{p}}{R}\left(\frac{1}{T_\mathrm{ref}} - \frac{1}{T_\mathrm{c}}\right)} \tag{4}$$

where T_ref is the reference temperature of the Arrhenius fitting with the reference parameter p_0, E_p is the parameter specific activation energy, R the universal gas constant at the actual cell core temperature T_c.

Note that the temperature-dependence of the open-circuit potentials due to entropy variation, as recently reported [31], has been neglected within this study as the effect is seen to be small compared to the other error sources (e.g., falsely determined electrode open-circuit potentials and false balancing and alignment of these potentials to the cell OCV). Due to the closed loop nature of the electrochemical–thermal model coupling, special detail has to be given during the parameter identification procedure, so that the identification of electrochemical parameters is not superimposed by thermal parameters and *vice versa*.

3. Characterization and model parameter identification

The characterization of the lithium-ion cell and the determination of the model parameters follow a four step procedure. In order to get access to the individual properties of the lithium-ion cell under study, a cell opening is inevitable in the beginning. In this first step, material and geometrical parameters such as mass and volume shares, widths, heights and thicknesses of the electrodes are determined. In a subsequent step, half cells are built up from stamps of the original electrodes to determine the static and dynamic behavior of the electrodes. These results are used as regressions and scaled up to cell level at various ambient temperatures. After that, the thermal parameters are identified at cell level to complete the overall procedure. The final model can be subsequently scaled to different system architectures at pack level. The overall method is described in detail in the following sections and illustrated in Fig. 2.

3.1. Parameter identification at electrode level

In a first step, the lithium-ion cell has to be analyzed according to its individual cell components. In a previous study of the authors [32], the cell under study was examined in a teardown analysis in order to yield material and geometrical parameters and reference values for the necessary characterization process. The reader is referred to the corresponding article for further reference. The used values of the lithium-ion cell under study are compared and complemented with parameters determined from material analysis by other authors [33–37].

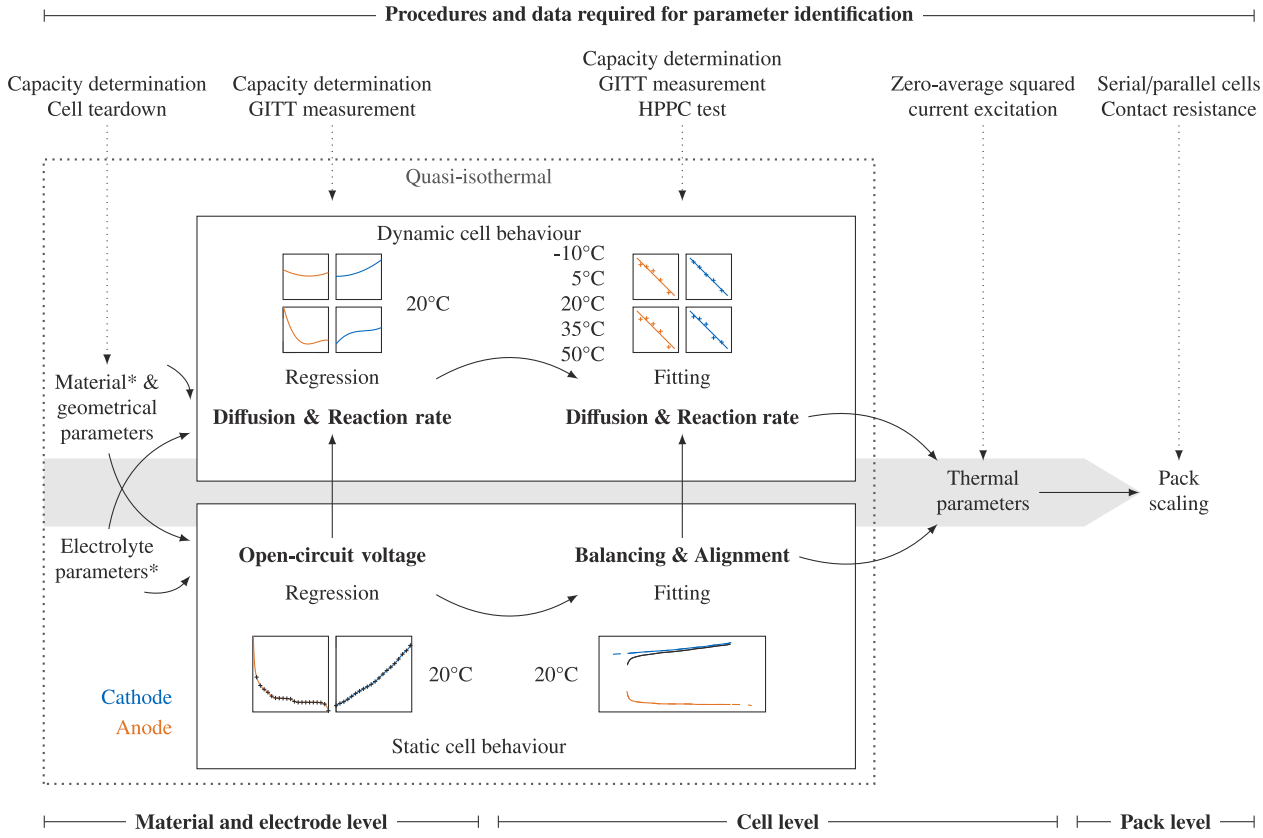

Fig. 2. Overall systematic characterization and parameter identification procedure. The battery model is scaled from electrode to pack level to enable health-aware fast charging of electric vehicle battery packs. All parameters are identified using measurements within this study, except where noted otherwise (*).

3.1.1. Material, geometrical and electrolyte parameters

Maximum concentration The maximum lithium concentration $c^{\pm}_{s,\max}$ within the active material describes the specific capacity of the material used for the electrodes. From a practical perspective, this value can be determined according to

$$c^{\pm}_{s,\max} = \frac{q^{\pm}_{s}\rho^{\pm}_{s}}{F} \tag{5}$$

with the specific capacity $q^{\pm}_{s}$, the density $\rho^{\pm}_{s}$ and the Faraday constant F. According to previous studies [33], the specific capacity of the anode active material (SiC) is 343 mAh/g and of the cathode active material (NCA) 168 mAh/g. The theoretical density of the SiC in the anode is assumed to be 2.25 g/cm^3 and the theoretical density of the NCA in the cathode is set to 4.8 g/cm^3. In total, this leads to a maximum concentration of 28 790 mol/m^3 and 30 090 mol/m^3 for the anode and cathode, respectively.

Particle radius Furthermore, the particle radii are required as they have a large leverage on the diffusion path length in the active material and therefore dynamic behavior of the battery cell. In previous studies of Lain et al. [33], the cell under study has been disassembled under inert gas atmosphere and scanning electron microscopy (SEM) measurements have been taken of the electrode surfaces. The average particle radii have been determined to be 7 µm and 2.5 µm for the anode and cathode, respectively [33].

Surface One of the most significant parameters for the model parameterization is the electrode surface A. Here, the cathode defines the active electrode surface of the battery model since the anode is usually oversized for production and safety reasons, well-known as anode overhang [38]. The surface has been determined in a previous study by the authors [39] by measuring the active electrode length (868 mm) and width (59 mm) of both electrodes of a discharged and disassembled cell leading to a double-layer surface of 1024 cm^2. This is in alignment with recent studies of the investigated cell by other authors [33].

Porosity The measured electrode surface does not directly match the measured electrode surface in practice, as electrodes consist of a material combination and, for the active material share, of millions of particle spheres of the active material applied to the electrode as a coating with gaps in between. Hence, the measured electrode surfaces have to be adjusted taking into account its active material share and porosity. Usually, this process is of theoretical nature as material shares of the slurry can only be estimated with reasonable accuracy. The active material shares $\omega^{\pm}_{s}$ have been estimated to 95% and 96% and the porosity of the electrodes $\epsilon^{\pm}_{e}$ to 27% and 13% for the anode and cathode, respectively, in a previous study [33]. The volumetric material share $\epsilon^{\pm}_{s}$ of the total electrode volume is calculated according to

$$\epsilon^{\pm}_{s} = (1 - \epsilon^{\pm}_{e}) \cdot \omega^{\pm}_{s} \tag{6}$$

resulting in 69.35% and 83.52% for anode and cathode, respectively.

Thickness Due to manufacturing tolerances, the capacity of a cell of the same type varies. The model reproduces this variation by adjusting the layer thickness of the electrode L, according to

$$L^{\pm} = \frac{C^{\pm}}{F A \epsilon^{\pm}_{s} c^{\pm}_{s,max}} \tag{7}$$

with C as the measured capacity of the investigated cell. By applying this equation to the cell under study with a measured capacity of 2.58 Ah during a CCCV discharge from 4.2 V to 2.5 V with a C/50 cut-off current, we obtain an electrode thickness of 54.66 µm and 42.77 µm for the anode and cathode, respectively. Note that this parameter has to be scaled to a specific cell in advance and requires a precise capacity determination, i.e. a low cut-off current during a full CCCV discharge.

Electrolyte and separator Beyond the active material modeling, the consideration of electrolyte overpotentials helps to increase the accuracy of the model at high current rates. The electrolyte is composed

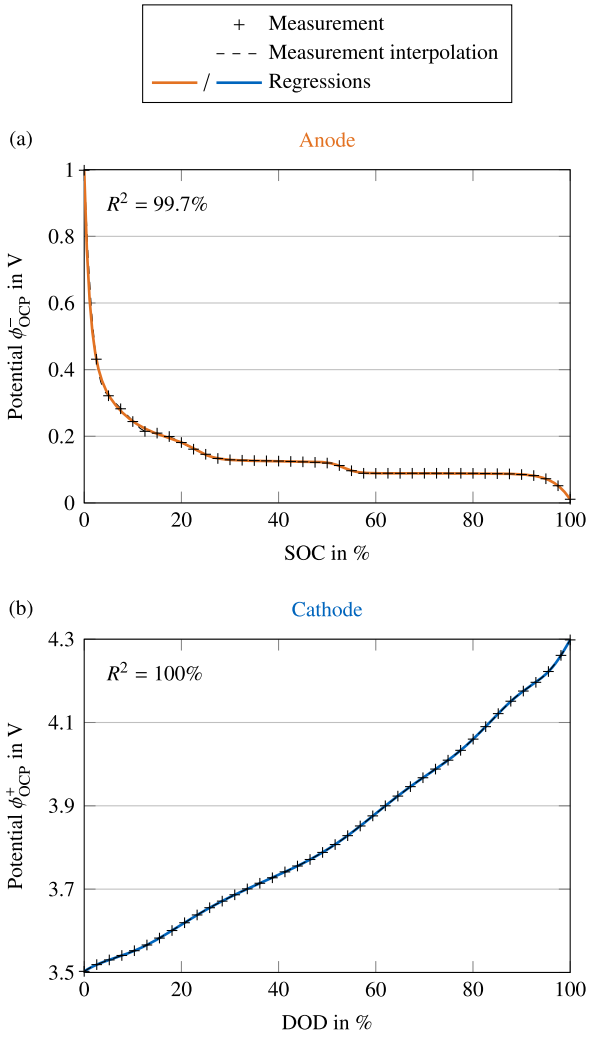

Fig. 3. Electrode open-circuit potentials (OCPs) determined with GITT measurements in charge direction. (a) Anode and (b) cathode open-circuit potentials fitted with consideration of the differential voltages to achieve accurate results with the regressions. Note that both curves are oriented counterwise as in the full cell for improved clarity, i.e., the cathode OCP is shown over the DOD instead of the SOC (mathematically, 1 – SOC).

of conducting salt, organic solvents, and additives. However, the exact composition of the solvents and their dynamic properties are usually not specified by the cell manufacturer and are hard to determine in practice (e.g., by gas chromatography of post-mortem wipe samples). Moreover, broad experimental characterizations are rarely found in literature, mostly because of the lack of established determination methods [37]. Therefore, in this work, a 1:1 (wt%) EC:EMC composition is assumed and supplemented with different empirical studies in literature. The electrical conductivity κ is composed of a modeling equation introduced by Mao et al. [34] and extended with an *Arrhenius* dependency as presented in Eq. (4) according to

$$\kappa(c_e, T) = (0.0911 + 1.9101 c_e - 1.052 c_e^2 + 0.1554 c_e^3) \cdot \exp\left(\frac{E_e}{R} \cdot \left(\frac{1}{T_{ref}} - \frac{1}{T_c}\right)\right) \tag{8}$$

with the electrolyte lithium concentration c_e, the universal gas constant R, and the activation energy E_e, which has been set to 17.120 kJ/mol based on a study by Ecker et al. [35]. The diffusion coefficient D_e is likewise composed of an empirical equation determined by Albertus et al. [36] and extended with an *Arrhenius* dependency and the activation energy of Ecker et al. [35] according to

$$D_e(c_e, T) = 6.5 \cdot 10^{-10} \cdot \exp(-0.7 c_e) \cdot \exp\left(\frac{E_e}{R}\left(\frac{1}{T_{ref}} - \frac{1}{T_c}\right)\right) \tag{9}$$

The electrolyte activity $f_{c/a}$ describes the change of properties in the presence of concentration gradients, which are expected to spread under fast charging currents. The modeling equation is taken from Lundgren et al. [37] and states

$$\frac{d \ln f_{c/a}}{d \ln c_e}(c_e) = \frac{0.2731\, c_e^2 + 0.6352\, c_e + 0.4577}{0.1291\, c_e^3 - 0.3517\, c_e^2 + 0.4893\, c_e + 0.5713} - 1\,. \tag{10}$$

For the sake of simplicity, a thermal dependency of the electrolyte activity is neglected. The transport number is set to 0.38 [40]. The remaining parameters describing the separator, namely the separator thickness L^{sep} and the porosity ϵ_e^{sep}, are set to 8 µm and 0.40, respectively, according to a study by Lain et al. [33].

3.1.2. Open-circuit voltage

The OCV of both half cells marks an essential component within the model and has to be determined experimentally. The model output voltage is crafted by a superposition of anode and cathode OCPs and therefore marks the main error source if not precisely determined, as it is omnipresent during the dynamic cell behavior parameter identification process and operation of the lithium-ion battery cell. The following two methods are commonly used for OCV determination: pseudo OCV techniques (pOCV) and relaxation measurements (GITT) [41]. As GITT measurements have been seen to more accurately match the voltage slope of the electrodes in the full cell by being less influenced by the strong voltage hysteresis of the investigated cell [42], we use this measurement technique to further parameterize the model. In a previous study of the authors [39], GITT measurements were performed on two-electrode half cells of the cell under study at 20 °C ambient temperature, as seen in Fig. 3. Both cells were fitted with a polynomial capable of reproducing the specific shape of the electrode's OCP and stage transition phases. A hyperbolic polynomial, as proposed by Safari et al. [43], has been used for the silicon graphite anode

$$\begin{aligned}\phi^-_{OCP}(SOC) =& p_1 + p_2 \exp(p_3 SOC) + p_4 \tanh\left(\frac{SOC + p_5}{p_6}\right) \\ &+ p_7 \tanh\left(\frac{SOC + p_8}{p_9}\right) + p_{10} \tanh\left(\frac{SOC + p_{11}}{p_{12}}\right) \\ &+ p_{13} \tanh\left(\frac{SOC + p_{14}}{p_{15}}\right)\end{aligned} \tag{11}$$

as it fits the measurements well and accurately reproduces the stage transitions. For the NCA cathode, a 14th degree polynomial has been used according to

$$\begin{aligned}\phi^+_{OCP}(SOC) =& p_1 SOC^{14} + p_2 SOC^{13} + p_3 SOC^{12} + p_4 SOC^{11} \\ &+ p_5 SOC^{10} + p_6 SOC^9 + p_7 SOC^8 + p_8 SOC^7 \\ &+ p_9 SOC^6 + p_{10} SOC^5 + p_{11} SOC^4 + p_{12} SOC^3 \\ &+ p_{13} SOC^2 + p_{14} SOC + p_{15}\end{aligned} \tag{12}$$

which also yield the best fit of the cathode OCP. The coefficients of both regressions are listed in Appendix C for brevity. Note that the cathode regression coefficients are large, which indicates an overfitting of the ground truth values, however, lower degree polynomials have been tested but did not improve the overall fit of the voltage curve as the characteristic gradients in the cathode OCP are most important. Both regressions fit the underlying measurement well, with a R^2 of minimum 99.7%. The regressions are subsequently used for the balancing and alignment of both electrodes to the full cell.

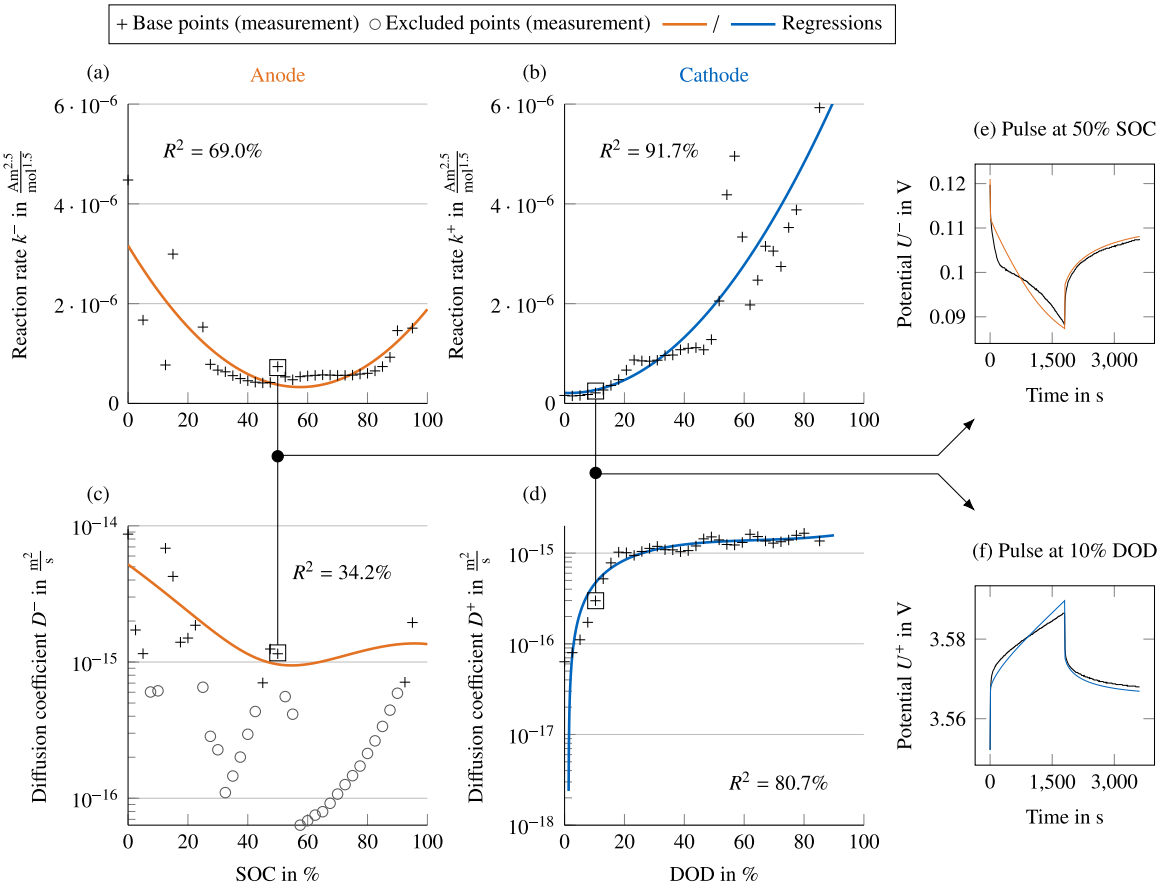

Fig. 4. Results of the half-cell pulse fitting procedure. (a)/(b) Reaction rates and (c)/(d) diffusion coefficients over the full cell SOC for anode and cathode. Examples of the pulse fitting results are illustrated in (e) for a current pulse of the anode at 50% SOC and in (f) for a current pulse of the cathode at 10% DOD according to the definition in Fig. 3.

3.1.3. Diffusion and reaction rate

After determining the OCPs of the electrodes under rest, the dynamic voltage responses of the electrodes during charging have to also be determined. This is particularly critical to determine, as half cells of commercial lithium-ion batteries are prone to an early failure under load due to the manual manufacturing process and side reactions [44]. The parameter identification approach pursued in this article is based on a qualitative characterization of the SOC-dependent parameters with model-based pulse fitting of the measured half-cell voltage response to current excitation. For this purpose, the previously determined GITT measurement serves as a base with the main advantage that now also the previously unconsidered SOC changes between the relaxation sequences are taken into account. The input current of the model is taken from the half-cell measurement and scaled to the cell level. The diffusion coefficient and the reaction rate constant are determined for each individual pulse independently using the least-squares method, based on the Levenberg–Marquardt algorithm [45–47]. The results of the fitting serve as base points to fit a regression function over the entire SOC range.

The results of the pulse fitting procedure of both electrodes are illustrated in Fig. 4. A single base point for the subsequent interpolation corresponds to the result of the parameter adjustment to match the half cell voltage response over time of one SOC specific pulse of the load profile.

With first consideration of the determined values and regression curves of the cathode reaction rate and diffusion coefficients, the regressions

$$D_s^+(\mathrm{DOD}) = p_1\mathrm{DOD}^3 + p_2\mathrm{DOD}^2 + p_3\mathrm{DOD} + p_4 \tag{13}$$

$$k^+(\mathrm{DOD}) = p_1\mathrm{DOD}^2 + p_2\mathrm{DOD} + p_3 \tag{14}$$

fit the general tendency of the base points well. Again, the coefficients of the regressions are listed in Appendix D for brevity. The overall curve slope, with an increasing value at decreasing lithiation, seems plausible, as resistance or overpotential mitigates (similar to an increase in reaction rate and diffusion coefficient) with an increasing number of vacant places for lithium-ion intercalation. Additionally, the determined range of both values matches previously reported values for NCA material in the literature, which lie in a range of 10^{-7} to 10^{-4} for the reaction rate [21,23,24,48–51] and 10^{-15} to 10^{-14} for the diffusion rate [36,52–60], respectively.

For the anode behavior, this procedure is likewise performed. Due to the nearly constant OCP during the coexisting phases of the anode OCP, as visible in Fig. 3(a), the diffusion coefficients are adjusted to implausible values which do not follow a physical pattern. The origin can be traced back to the model simplification of the SPM, replicating an open-circuit potential drop during the pulse in the model which is smeared out in the measured voltage signal by a multitude of different sized particles in reality. The base points for the regression in these SOC areas can be neglected to determine the final regression. Here, the determined values for both regressions

$$D_s^-(\mathrm{SOC}) = p_1\mathrm{SOC}^3 + p_2\mathrm{SOC}^2 + p_3\mathrm{SOC} + p_4 \tag{15}$$

$$k^-(\mathrm{SOC}) = p_1\mathrm{SOC}^2 + p_2\mathrm{SOC} + p_3 \tag{16}$$

also match previously reported value ranges and show a plausible overall curve slope for Graphite material in the literature, with 10^{-7} to 10^{-4} for the reaction rate [21,23,24,48–51] and 10^{-16} to 10^{-12} for the diffusion rate [35,61–68], respectively.

In the subsequent step, the determined static (OCV regressions) and dynamic (reaction and diffusion rate regressions) electrode behavior can be scaled to the cell level.

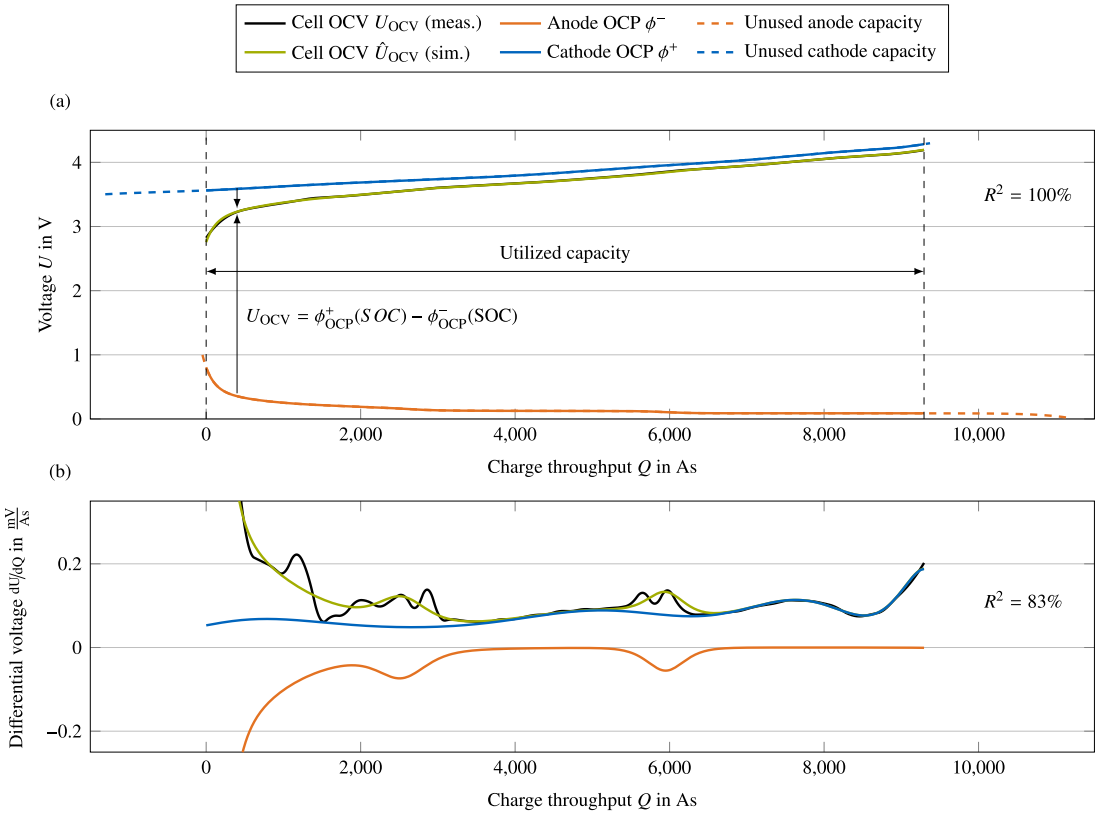

Fig. 5. Open-circuit voltage (OCV) of the model plotted against experimental data after balancing and alignment of the electrode OCPs. (a) OCPs of the individual electrodes and the superposition in comparison to the full cell OCV. (b) Differential voltage analysis (DVA) of the OCVs to analyze the positions of characteristic electrode OCP features in the full cell OCV. All OCPs/OCV measurements are determined by GITT at 20 °C ambient temperature.

3.2. Scaling to cell level

The complete definition of the static and dynamic electrode behavior has to be scaled up to cell level to yield a useful model at this stage. Here, we use the determined electrode OCP regressions and diffusion and reaction rates to scale them based on measurements performed at cell level. First, the electrode OCPs are balanced and aligned to the OCV of the full cell. Second, the reaction and diffusion reaction rate regressions are scaled to the current pulse voltage response of the full cell at ambient temperatures between −10 °C and 50 °C. In a last step, the parameters of the lumped mass thermal model are identified.

3.2.1. Balancing and alignment

The OCPs of both electrodes have to be scaled and superimposed to achieve a precise replica of the OCV of the full cell, in the latter referred to as balancing and alignment. The procedure hereby describes the share of the active anode and cathode capacity in the pristine lithium-ion cell, typically in a range of 1:1.15 to 1:1.20 with an oversized anode to prevent the occurrence of lithium deposition at the edges of the electrode active material layer [38,69]. In order to determine the electrode balancing and alignment in the pristine lithium-ion cell, the determined capacity windows of the half cells are compared to the capacity window of the full cell. Here, we apply a method similar to Honkura and Horiba [70]. By stretching or shifting the electrode OCPs, both can be adjusted so that their superposition represents the OCV of the full cell. Formally, the cell OCV U_{OCV} is calculated according to

$$\begin{aligned} U_{OCV} &= \phi^+_{OCP}(q^+) - \phi^-_{OCP}(q^-) \\ &= \phi^+_{OCP}\left(\frac{Q+\sigma^+_b}{S^+_b}\right) - \phi^-_{OCP}\left(\frac{Q+\sigma^-_b}{S^-_b}\right) \end{aligned} \tag{17}$$

and used for minimizing the objective function $\overline{f}_{obj}$ as

$$\begin{aligned} \overline{f}_{obj} &= \min_{\sigma^\pm_b, S^\pm_b} \|f(\sigma^\pm_b, S^\pm_b)\|_2^2 \\ &= \min_{\sigma^\pm_b, S^\pm_b} \left(U_{OCV} - \left(\phi^+_{OCP}\left(\frac{Q+\sigma^+_b}{S^+_b}\right) - \phi^-_{OCP}\left(\frac{Q+\sigma^-_b}{S^-_b}\right)\right)\right)^2 \end{aligned} \tag{18}$$

by using least-squares and the Levenberg–Marquardt algorithm [45–47], with the stretching factors $S^\pm_b$ and the shifting factors $\sigma^\pm_b$ over the charge throughput q of the electrodes and the charge throughput Q of the full cell.

The results of the procedure are illustrated in Fig. 5. The superposition of both electrodes achieves an almost perfect fit to the measurement data with a R^2 value of 100%. It should be noted that also the characteristic stage transitions of the electrode active materials, i.e., SiC and NCA, are accurately positioned, although the differential voltage signal was not part of the objective function. The lower R^2 value of 83% of the differential voltage can be traced back to the approximations made due to the chosen measurement technique and regression functions.

3.2.2. Diffusion and reaction rate fitting

The following procedure for scaling the determined electrode kinetics to the cell level is based on the qualitative regressions determined previously at the electrode level as a function of the electrode SOC. Now, the determined properties need to be quantified at cell level and at different ambient temperatures to allow for an accurate replica of the cell's behavior.

While the charge transfer resistance becomes almost directly visible during current excitation and is omnipresent during charging, the diffusion behavior requires a specific amount of time until it

becomes observable as an overpotential in the cell voltage signal. For the synchronous determination of both parameters, i.e., reaction rate and diffusion coefficient, both a current pulse excitation and a subsequent voltage relaxation period are, therefore, performed at different SOCs of the cell, in the latter referred to as high pulse power characterization (HPPC). This procedure is similar to the non-invasive fitting procedure presented by Namor et al. [22], but enables the determination of a reaction rate and diffusion coefficient dependent on the SOC and the temperature, as those dependencies were already earlier identified. In order to obtain the same pulse excitations over the temperatures as well as over an SOC range of 20–80%, it is necessary to limit the maximum current to 2 C in the underlying study. To avoid any interference with the still undefined thermal model parameters and assign the results to a specific temperature, we again assume constant cell temperature conditions during the short current excitations, referred to as *quasi-isothermal conditions*. To avoid over- or underestimation of the fitted parameters, both charging and relaxation phases are considered with equal time proportions. For the fitting algorithm, only positive charge pulses are considered to accurately fit the charging behavior of the cell under study. The regressions of the diffusion and reaction rate from Eq. (13) to Eq. (16) are then scaled to the full cell level using a scaling factor $s^{\pm}_{D/k}$ according to

$$D_s^{\pm} = D_s^{\pm}(SOC) \cdot s_D^{\pm} \tag{19}$$

$$k^{\pm} = k^{\pm}(SOC) \cdot s_k^{\pm} \tag{20}$$

and by minimizing the voltage error of the resulting model voltage response to the measured voltage signal at a specific ambient temperature. It should be noted that both diffusion coefficients and reaction rates are of significantly different magnitude, but are fitted synchronously during optimization, which is why a proportional scaling factor is used to ease the optimization problem. Formally, the objective function $\overline{f}_{\text{obj}}$ according to

$$\begin{aligned}\overline{f}_{\text{obj}} &= \min_{s_D^{\pm}, s_k^{\pm}} \|f(s_D^{\pm}, s_k^{\pm})\|_2^2 \\ &= \min_{s_D^{\pm}, s_k^{\pm}} \left(\sum_{P=1}^{P_{\max}} \left(U - \hat{U}(s_D^{\pm}, s_k^{\pm})\right)^2 \right)\end{aligned} \tag{21}$$

is minimized using the least-squares method, based on the Levenberg–Marquardt algorithm [45–47] and the parameter vector $\theta = [s_D^-, s_k^-, s_D^+, s_k^+]$, the investigated pulse P and the measured and simulated voltage U and $\hat{U}$, respectively. This procedure is repeated for each temperature level.

The results of the fitting at −10 °C to 50 °C ambient temperatures are illustrated in Fig. 6 for the reaction rate and diffusion coefficient of the anode and cathode. All fitted scaling factors are presented using the Arrhenius dependency from Eq. (4) and the help of a logarithmic transformation to obtain a linear dependency from the exponential function. As expected, both the reaction rate and the diffusion coefficient increase with increasing temperature, leading to a lowered overvoltage of the cell with increasing operating temperature. In this illustration, the activation energy E of the individual processes can be derived assuming an *Arrhenius* dependency. 20 °C is used as a reference temperature. The resulting activation energies are noted in Table F. The obtained values are coherent to the literature, e.g., the obtained activation energy of the anode diffusion coefficient $E_D^- = 22.5$ kJ/mol lies inbetween reported literature values between 20 [71] to approx. 50 kJ/mol [18]. Finally, the reaction rate and diffusion coefficients can be easily calculated as a function of SOC and temperature within the model.

3.2.3. Thermal parameters

The determination of the cell specific thermal model parameter introduced in Section 2.3 marks the last step in the parameter identification procedure. All temperature dependencies of the electrical

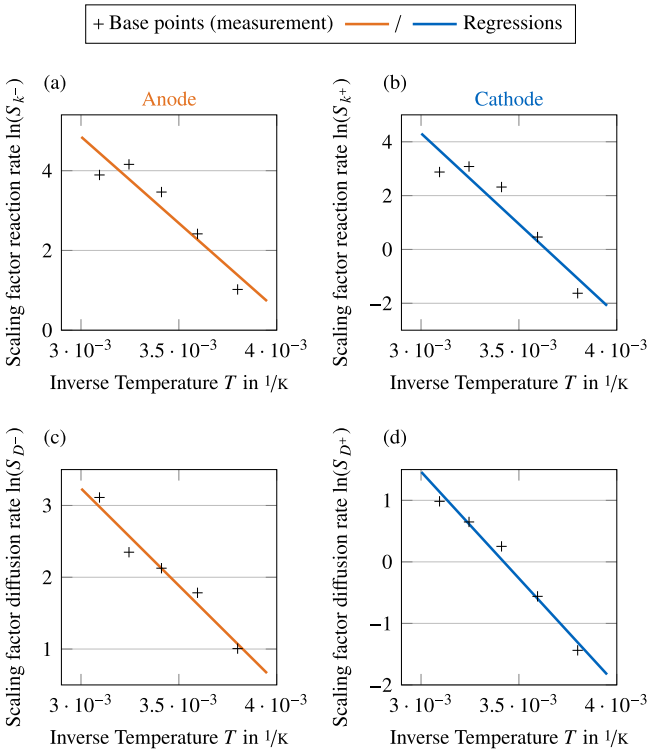

Fig. 6. Results of the full-cell pulse fitting procedure. (a)/(b) Reaction rate and (c)/(d) diffusion coefficients over temperature for anode and cathode, respectively. All regressions are based on an Arrhenius correlation.

parameter have been determined at quasi-isothermal measurement setups and are therefore assumed to be independent of the cell's thermal model parameters. For the thermal model, the determination of the heat capacity of the cell C_1 and the thermal resistance R_1 from the core to the cell surface are required. Many methods exist in the literature, which enable the determination of the thermal model parameters, such as thermal impedance spectroscopy (TIS) [72], calorimetry [73] or the decomposition of the cell and the determination of the individual material parameters [74]. All of them are subject to a certain degree of uncertainty, involve a lot of effort or require a specific type of laboratory equipment. Measuring the core temperature of a cell reliably is difficult, as inserting a temperature sensor into the cell core is laborious and changes the attributes of the pristine cell [28,29,75].

Bryden et al. [76] provided a practical method to determine the heat capacity and conduction of a lumped thermal-mass model, which has been successfully applied in downstream studies in the literature [77,78]. Consequently, this method has been also applied to the lithium-ion cell in this work. For performing the method, an extended thermal model to Eq. (2) incorporating the ambient temperature (additional thermal modeling of the surface T_s), referred to as two-point thermal mass model, was used to simulate both the cell core temperature and the cell surface temperature in order to compare it with the measured surface temperature. The extended thermal model is described by

$$\frac{T_s(t)}{dt} = \frac{\dot{Q}R_2 - T_s(t) + T_{\text{amb}}}{C_1(R_1 + R_2)} \tag{22}$$

with the surface temperature T_s, the ambient temperature T_{amb}, the heat capacity C_1, the heat generation $\dot{Q}$, the heat transfer between cell core and surface R_1, and the heat transfer between surface and ambient R_2. Before determining the unknown thermal model parameter C_1 and R_1, the heat resistance between the cell and the ambient must be found. The zero-square average current excitation was then applied for two individual cells with free (no fan) and forced (fan) convection, as seen in Fig. 7(a), to yield two measurements with different temperature

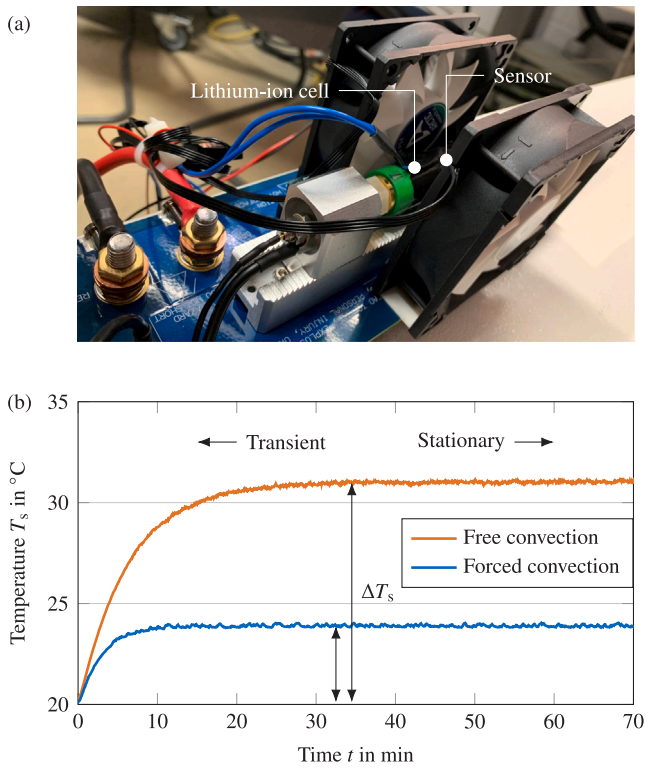

Fig. 7. Improved parameter identification of the thermal submodel. (a) Measurement setup for performing the method according to Bryden et al. [76], (b) thermal behavior of the cell under free and forced convection with the stationary temperature difference at the cell surface T_s compared to the ambient T_{amb} due to zero-average square current excitation.

evolutions over time due to the difference in the heat transfer between the cell and the environment R_2, as seen in Fig. 7(b). After approximately 30 min of the experiment, the cell surface temperature becomes stationary (dT_s/dt) and Eq. (22) simplifies to

$$R_2 = \frac{T_s - T_{amb}}{\dot{Q}}, \tag{23}$$

where the heat generation $\dot{Q}$ is calculated using the cell's OCV at the begin of the experiment and the average terminal voltage during the last 30 min of the experiment, as it enables a decoupling from the electrical submodel and parameter uncertainty error propagation. After determining the thermal resistance to the ambient R_2, the transient part of the measurement is used to fit the discretized Eq. (22) following a forward Euler method according to

$$T_s(t) = \frac{\dot{Q}R_2 + T_{amb} - T_s(t)}{C_1(R_1 + R_2)}\Delta t + T_s(t-1) \tag{24}$$

to find the remaining two parameters C_1 and R_1. With both measurements at hand, the two parameters can be determined analytically.

Fig. 8 shows the simulated and measured surface temperatures T_s during cycling with a squared zero-average current excitation at 50% SOC and an ambient temperature of 20 °C. The method results in a heat capacity C_1 of 590 J/(kg K) and a thermal resistance R_1 of 4.3 K/(W) or heat transfer coefficient h_1 of 0.23 W/(m K). Both found parameters significantly differ to the identified values from the literature (C_1 > 800 J/(kg K) [76,77] and R_1 > 30 K/(W) [73,77,79]). Reasons for the large deviation can be seen in the large uncertainties involved during thermal parameter identification, which also lead to a wide spread of literature values.

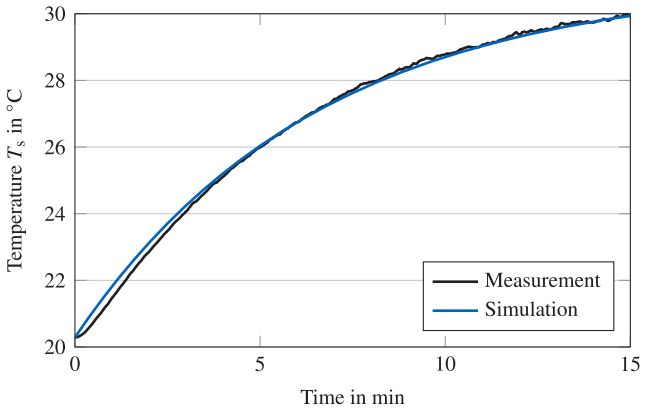

Fig. 8. Measured versus fitted cell surface temperatures T_s during cycling with zero-averaged squared current excitation and free convection, starting from a relaxed state at 50% SOC, and at 20 °C ambient temperature.

3.3. Scaling to pack level

In automotive applications, multiple lithium-ion cells are commonly connected in series and parallel to reach a specific capacity or energy level. Therefore, a scaling of the model to pack level is important to enable deployment of the model.

In the simplest and most practical way, the model inputs can be downscaled and the model outputs upscaled in accordance with the given pack configuration. Hereby, it is assumed that all cells are equally stressed and individual cell properties do not vary. Formally, the current as model input is downscaled and the voltage as model output is upscaled according to

$$I_{cell} = \frac{I_{pack}}{m} \tag{25}$$

$$U_{pack} = U_{cell} \cdot n \tag{26}$$

with the pack current I_{pack} and voltage U_{pack}, the cell current I_{cell} and voltage U_{cell}, and n serial and m parallel connected cells. To account for electrical contact resistances (ECRs), additional ohmic resistance R_{ECR} can be added to the model depending on the used cell-to-cell joint technique and resistance thereof [80].

3.4. Summary of the parameter identification procedure

The procedure leads to the overall model parameter of the investigated lithium-ion cell presented in Appendix F. The model can be used for a single lithium-ion cell or, for the application at pack level, it can be scaled to a pack of serial and parallel interconnected cells.

4. Validation

For the development of fast charging strategies, models are needed that are validated against experimental measurement data and whose accuracy is confirmed [81]. Thorough validation is an important part of model development to ensure that the model can accurately reproduce the experimental measurement data. This is especially true for simplified or reduced order models (ROMs), whose validity check has been identified as most important [82] and has been intensively investigated in the past [83,84]. To assess the accuracy and robustness of the derived electro-thermal battery model parameterized with the presented method, the model is validated at various high charging currents and ambient temperatures. The validation is based on the assumption that the electrode behavior is correctly represented if the simulated cell voltage matches the measured cell voltage, as *in operando* anode potential measurements are impossible without accepting any interference with the real-world behavior of the pristine cell. Special emphasis is given to a validation at high charge rates and low ambient temperatures, as these scenarios are the most challenging.

4.1. Low and high charging current

For each charging current validation stage, a pristine cell was used. The cell was initially CCCV discharged to 2.5 V with a cut-off current of 1/50 C to ensure a reproducible discharge to 0% SOC. After a thermal relaxation of 2 h, the charging procedure started with a constant charging current between 1 C up to 6 C until the upper voltage limit of 4.2 V was reached. During the charging procedure, the cell's surface temperature was monitored at a central point of the cylindrical cell can. For a downstream comparison to the model response, the parameterized SPM was updated with the actual capacity value determined in the initial CCCV discharge and executed with the measured current and cell surface temperature of the charging step as model input. The results of the validation at 20 °C ambient temperature are shown in Fig. 9.

Overall, the model shows a good alignment to the measured voltages of the cell under study with a RMSE between 18 mV and 29 mV at 20 °C taking into account the complex task of parameter identification and the sophisticated transient validation scenario. In the low SOC ranges below 10% SOC, especially at the beginning of charge, the largest deviations to the measured voltage occur. Consequently, special detail has to be given to the potential error if the model is deployed for fast charging strategies in a SOC region below 10%. In a SOC range between 10–60%, the relatively low absolute error is mainly due to the model simplification of the SPM. Since only one large spherical particle is simulated for both electrodes, stage transitions of the active materials (e.g. around 20% and 55% SOC, as it can be seen in Fig. 3) can be clearly identified in the cell voltage response. In reality, the steep voltage steps smear out due to millions of particles electrically connected in parallel. This inaccuracy has to be accepted if model order reductions and thus computational performance improvements are to be achieved for real-time implementation. Close to the upper cut-off voltage and generally with increasing current rates, the model error slightly increases. A potential reason can be a stronger weight and impact of the electro-thermal interdependencies, which are magnified at increasing charge rates and are generally difficult to separate during the determination procedure.

4.2. Low and high ambient temperature

To extend the validation to varying ambient temperatures, the charging procedures are performed at −10 °C, 0 °C, 5 °C, 10 °C, 15 °C, 20 °C, 35 °C, and 50 °C ambient temperature to account for typical automotive operating conditions. Each temperatures level is investigated with a new cell to exclude aging effects deteriorating the reference measurements. The RMSE of all C-rates and all ambient temperatures are illustrated in Fig. 10.

Based on the observations made at 20 °C ambient temperature, similar model behavior can be observed for varying temperatures. Especially with increasing ambient temperatures, the model accuracy can be improved. Lower overvoltages at the beginning of the charging process improve the overall accuracy, which leads to the assumption that the dynamic voltage response of the electrodes and their electro-thermal interdependency may be the main error source during parameter identification and should be accounted for if the model is deployed for fast charging control at lower temperatures. This conclusion is further supported by the larger error at high charge rates and subzero temperatures. For the worst case, namely the 6C charging at −10 °C, a steep overshoot at the beginning of charge leads to a high initial error, which becomes smaller as the cell heats itself up, however still remaining the main contributor to the large RMSE. Declining model accuracy at low temperatures is a well-known issue in literature. Therefore, special consideration has to be given to the model error if the model is deployed at subzero temperatures.

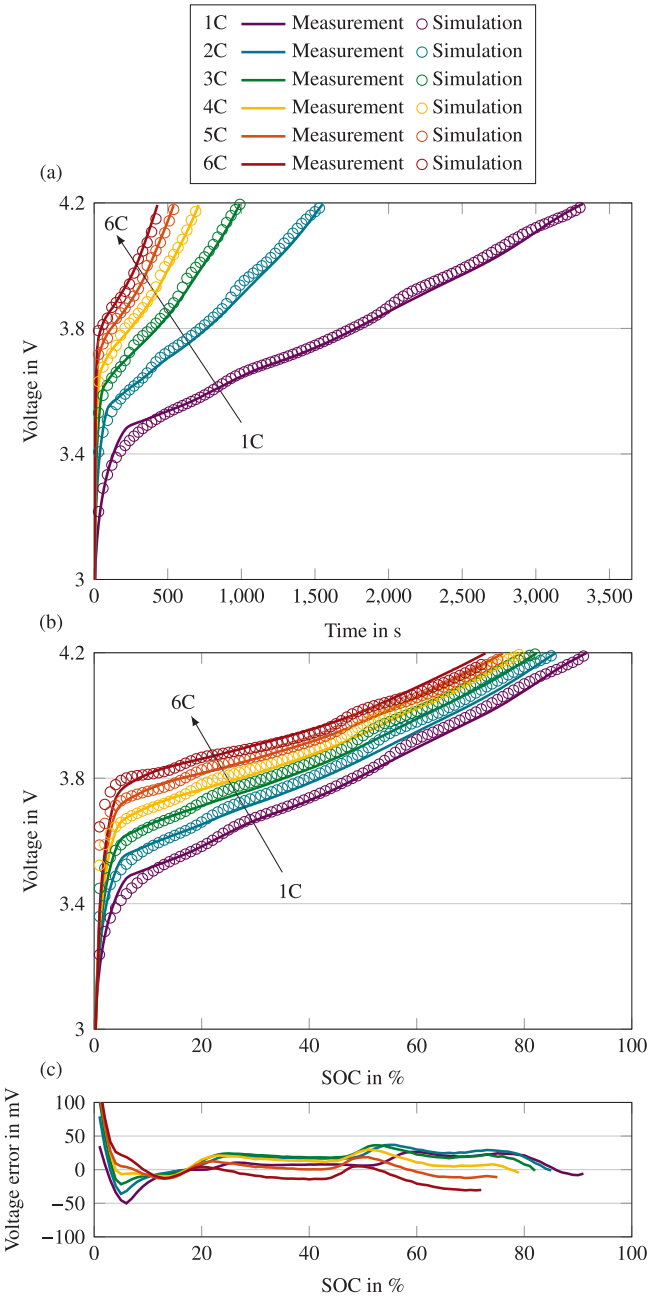

Fig. 9. Measured versus simulated cell voltage at constant charging currents from 1C to 6C. (a) Measured and simulated voltage over time. (b) Measured and simulated voltage over SOC. (c) Voltage error of the model response to the measurements over SOC. All measurements start from 0% SOC at a relaxed cell state at 20 °C ambient temperature until the upper cut-off voltage is reached.

4.3. Upscale to pack level

Validation from C/10 up to 4C at an ambient temperature of 20 °C has been performed with a laser-welded 12s2p module as a representative level for lithium-ion modules in automotive applications. All 24 cells originate from one production batch and were initially characterized revealing a capacitance scatter of 0.79% and a DC resistance scatter of 1.22%, as shown in Appendix E.

The procedure follows the experimental approach in Section 4.1, i.e., each charge sequence started from 0% SOC and a fully relaxed cell state with >2 h relaxation. Four temperature sensors placed at equidistant positions through the module were averaged, as visible

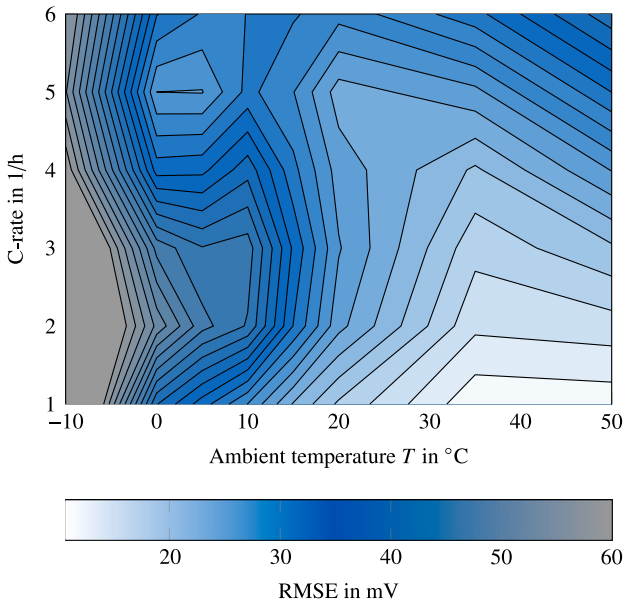

Fig. 10. Voltage error heat map at charging currents from 1 C to 6 C and ambient temperatures between −10 °C and 50 °C. The voltage error is evaluated with the RMSE over the full charge sequence. Note that the lithium-ion cell's temperature increases during the procedure to allow for validation of the complex electro-thermal interdependence.

in Fig. 11(a)–(b), and fed as input to the model. In addition to the recording of the overall system voltage, all individual cell voltages were monitored in order to check for inappropriate and improper voltage deviations. The input current is scaled with the number of cells in parallel and the output voltage is scaled with the number of cells in series.

The comparison of the measured and simulated voltage is illustrated in Fig. 11(c)–(e). Despite the scaling and the cell-to-cell interdependencies during fast charging, the model achieves a robust estimate of the overall system voltage. The added electrical contact resistances (ECRs) of the copper–steel joints connecting the individual cell pairs did not contribute a large additional overpotential as the largest overpotential can be traced back to cell-internal mechanisms. As no larger deviation to the cell-level errors is observed, the model can be easily scaled to pack level of any architecture if laser-welded copper–steel joints or other low impedance connections are utilized.

5. Fast charging control strategy

After parameter identification, the model can be used for fast charging control during lifetime of the lithium-ion cell, e.g., control of the anode potential as proposed by many prior studies, e.g. [10–14]. The anode potential ϕ^-, defined by

$$\phi^- = \phi^-_{\mathrm{OCP}} + \eta^- + \eta^{\mathrm{SEI}}, \tag{27}$$

is commonly controlled at a specific threshold to avoid any metallic deposition of lithium during charging. In theory, the critical threshold lies at 0 V [9]. In practice, charging current control algorithms start to decrease the charging current if a specified anode potential reserve (APR) is reached [10] to account for model and measurement uncertainties [14]. E.g., the anode potential can be controlled during a fast charging event of a lithium-ion cell or pack, as illustrated in Fig. 12 for a arbitrarily set anode potential limit.

Initially, the charging current is limited to the model validation boundary or a customized current limit during a constant current (CC) sequence to limit the losses and heat rate within the lithium-ion cell. If the anode potential reaches a specified limit, current is controlled

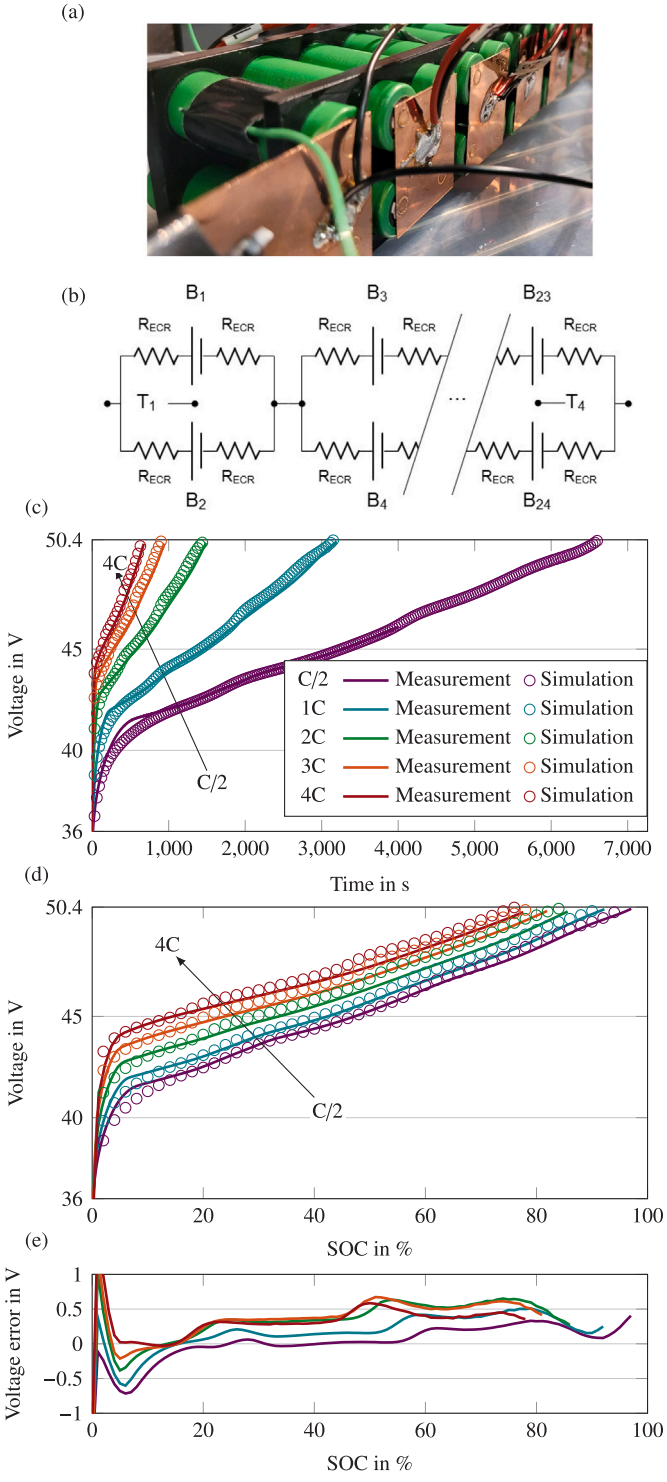

Fig. 11. Validation at pack level. (a) Image and (b) equivalent circuit of the 12s2p lithium-ion module with 24 lithium-ion cells B_n, electrical contact resistances R_{ECR}, and temperature measurements T_x. (c)–(d) Measured versus simulated voltage at constant charging currents from 1C to 4C. (e) Error between measurement and simulation. All measurements start from 0% SOC at a relaxed state at 20 °C ambient temperature.

to a constant anode (CA) potential. With rising age of the lithium-ion cell and update of the state of health to the model (here, we adjust the capacity and SEI resistance, the latter leading to a SEI overpotential η_{SEI} rise for visualization purposes), the inevitable SEI growth leads to an earlier reach of the CA sequence, even though anode potential reserve

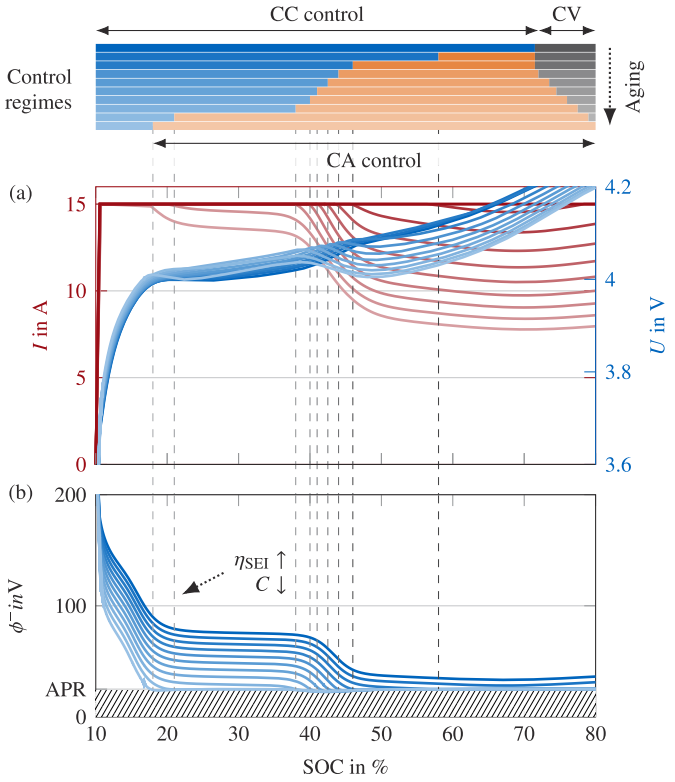

Fig. 12. Fast charging strategy with current control to a arbitrarily set anode potential limit (CA) of 25 mV adaptive to, e.g., a falling capacity C (from 100% to 80%) and rising SEI overpotential η^-_{SEI} (from 100% to 200%) in the model during lifetime of a single lithium-ion cell. (a) Current and voltage over time and (b) and anode potential during a fast charging event with increasing age of the cell (in here, the cell capacity has been reduced with 2% steps and the SEI resistance has been increased with 10% steps as an example). Prior to each event, a constant current (CC) sequence is applied to remain within the model boundaries determined during model validation, which is subsequently followed by a constant anode potential (CA) sequence, if the specified limit is reached. All simulations were carried out at 20 °C cell surface temperature.

violations did not occur with a pristine cell. By regular update of the model, the changing properties of the lithium-ion cell can be accounted for during fast charging control and improve their lifetime.

6. Control sensitivity to parameter variations

For a downstream usage of the model for fast-charge applications, it is important to quantify the sensitivity of the model outputs to varying parameters in order to highlight the inherited uncertainty of the parameter identification procedure and evaluate the required accuracy of the parameters. Many studies in the literature already performed such an analysis [31,85,86], however relying on the full cell voltage and temperature response. As fast charging control with an anode potential reserve is our major objective, we define a new quantity for further sensitivity analysis. Formally, we therefore define a current control inflection point SOC^-_{lim} as

$$SOC^-_{lim} = SOC(\phi^- < APR) \tag{28}$$

which defines the starting point for current control by the BMS. This limit is monitored while single parameters of the model are varied during the analysis. The remaining parameter set is held constant. The parameters were sorted into four groups according to the parameter identification steps presented in Fig. 2, that is, (1) material and geometric, (2) static, (3) dynamic and (4) thermal model parameters, were put into the scope of the analysis, with the originally determined values as the baseline scenario (ground truth assumption). Regressions

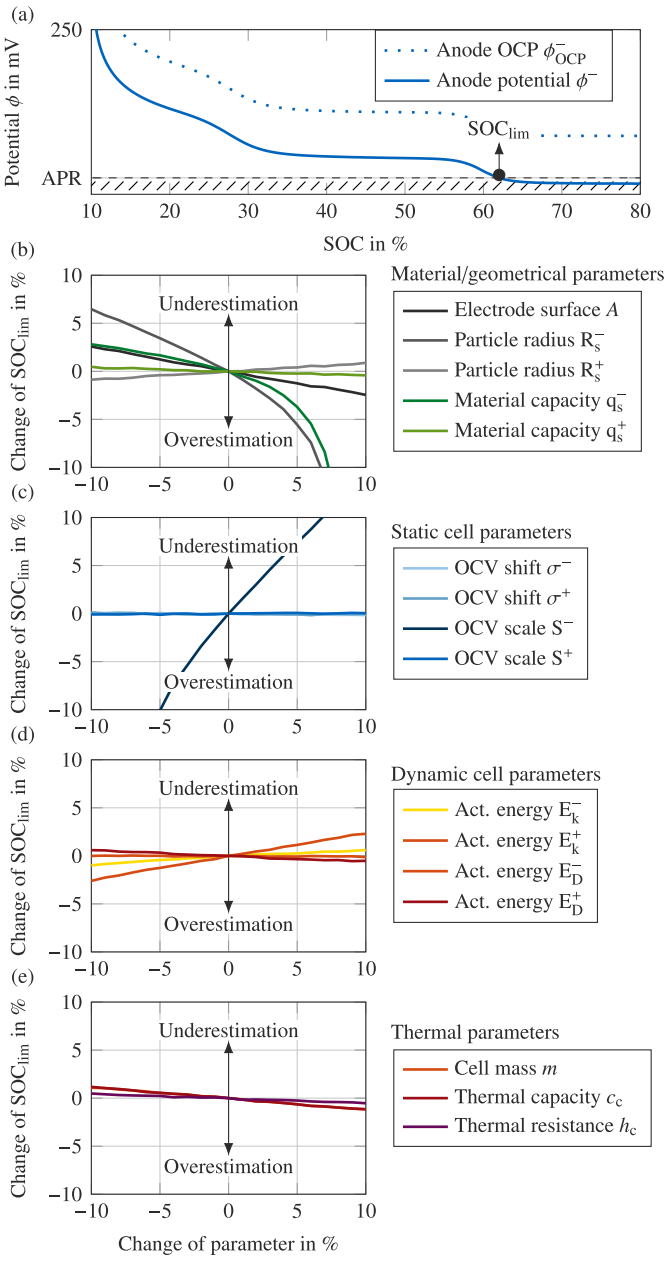

Fig. 13. Parameter sensitivity to the charging control as an effect of model-based control of an anode potential reserve (APR). (a) Definition of the abuse prevention control point SOC^-_{lim} at an arbitrarily set anode potential reserve of 25 mV and a starting charging current of 6C. (b)–(e) Sensitivity of the defined control point SOC^-_{lim} relative to (b) material, (c) static, (d) dynamic and (e) thermal parameter variations. All simulations were carried out at 20 °C constant cell surface temperature.

over the SOC, e.g., the OCV, were varied by shifting and/or scaling the regressions as during the parameter identification procedure.

The results are illustrated in Fig. 13 for an exemplary harsh 6C charging scenario at 20 °C constant cell temperature. Note that a negative change of SOC^-_{lim} leads to a more conservative current control as the limit is reached earlier, while a positive change of SOC^-_{lim} leads to a critical control situation as the abuse limit is reached without notice. As expected, the scale factor S^- of the determined anode OCV has the largest impact on the anode potential and charging current control, which emphasizes the necessity of an accurate determination of both the electrode and full cell OCV during the parameterization procedure. Furthermore, it should be mentioned that the cathode also has an isolated influence on the anode potential via the thermal model,

albeit a much lower one. Besides, the particle radius R_s^- of the anode during material characterization and the activation energy of the anode diffusion coefficient E_D^- strongly influence the anode potential control. Thermal model parameters, however, can be seen as less sensitive to determination uncertainties, as the cell warms up fast during aggressive fast charging and the change of overpotential-relevant parameter is slowed down. These results have to be taken into account for the discussion of the validity of these models, since a rather large uncertainty in model determination does not directly question the usability of the overall model for fast-charge control applications.

7. Summary and conclusions

The development of health-aware fast charging strategies for advanced battery management systems relies on knowledge of battery internal states for current control. An electrochemical battery model of reduced order has been developed and validated alongside a novel parameter identification framework for rapid knowledge scaling of electrode aging trigger conditions, e.g. lithium deposition, to pack level. The carefully crafted model has been validated in a broad operating range, between −10 °C to 50 °C ambient temperature and up to 6C charging rates, in order to yield a precise replica of the cell's behavior at fast charging rates and account for inherited model errors. The model enables real-time fast-charge control of typically unobservable internal cell states at the application level, reducing fast-charge time while minimizing lithium-ion cell degradation. Moreover, as the model parameter change over age of the lithium-ion cell and need to be accounted for in the model [87–90], the aging state can be updated by, e.g., adjusted capacity, electrode charge balance, and resistance.

In future work, the developed method will be deployed to parameterize electrochemical lithium-ion cell models for real-time fast charging current control in order to avoid critical aging mechanisms during the lifetime. The results will give helpful insights on the advantages and disadvantages of model-based fast charging strategies.

CRediT authorship contribution statement

Nikolaos Wassiliadis: Conceptualization, Methodology, Software, Validation, Formal analysis, Investigation, Data curation, Writing – original draft, Writing – review & editing, Visualization, Project administration. **Manuel Ank:** Validation, Writing – review & editing. **Andreas Bach:** Investigation, Software. **Matthias Wanzel:** Investigation, Software. **Ann-Sophie Zollner:** Investigation, Software. **Kareem Abo Gamra:** Writing – review & editing. **Markus Lienkamp:** Writing – review & editing, Resources, Supervision.

Declaration of competing interest

The authors declare that they have no known competing financial interests or personal relationships that could have appeared to influence the work reported in this paper.

Data availability

All measurements, implemented parameter identification functions, and the validated electrochemical model are provided as open source alongside the underlying article, accessible via GitHub: https://github.com/TUMFTM/EA_Battery_SPMparameterization.

Acknowledgments

This research received funding by the German Federal Ministry for Economic Affairs and Climate Action (BMWK) within the project "ultraBatt" under grant number 01MV21015 and by the German Federal Ministry of Education and Research (BMBF) within the project "OptiPro" under grant number 03XP0364B. Special thanks to our colleague Alessandro Sommer for supporting the study with coin cells and Michael Kick for supporting the study with a laser-welded lithium-ion battery pack. Also, we would like to thank Florian Biechl and the staff of our electric lab for their support. We acknowledge the work of Jakob Weis, who analyzed the thermal dependencies of the electrolyte parameters during his master's studies. Furthermore, we would like to thank Jan Veeh for partly performing the single-cell validation measurements as part of his master's studies.

Appendix A. Governing electrochemical model equations

The first equations of the model use the aforementioned assumptions to display the charge flux density $j_n(t)$ as proportional to the applied current $I(t)$ to the system, as described by

$$j_n^+(t) = \frac{I(t)}{Fa^+L^+A} \tag{A.1}$$

$$j_n^-(t) = \frac{-I(t)}{Fa^-L^-A} \tag{A.2}$$

for both, the negative (−) and positive (+) terminals. F hereby denotes the Faraday constant, a the specific interfacial surface area, L the electrode thickness and A the active electrode area. By using the assumption that the concentration of the solid phase within the electrodes is constant in the spatial dimension x and *Fick*'s law, the lithium diffusion within the solid phase $c_s^\pm$ can be formulated as

$$\frac{\partial c_s^\pm}{\partial t}(r,t) = \frac{1}{r^2}\frac{\partial}{\partial r}\left[D_s^\pm(T_c) r^2 \frac{\partial c_s^\pm}{\partial r}(r,t)\right] \tag{A.3}$$

where r denotes the particle radii, $D_s^\pm$ the diffusion coefficient in the solid phase and T_c the cell core temperature. For solving the PDE, the corresponding boundary conditions can be defined by using Eqs. (A.1) and (A.2), resulting in

$$\frac{\partial c_s^\pm}{\partial t}(0,t) = 0 \tag{A.4}$$

$$\frac{\partial c_s^\pm}{\partial t}(r^\pm,t) = \mp \frac{1}{D_s^\pm(T_c)Fa^\pm L^\pm}\frac{I(t)}{A}. \tag{A.5}$$

Accordingly, the lithium concentration in the liquid phase c_e of the spatial domains, i.e., anode, separator, and cathode, are defined with PDEs along their axial direction through the electrode layers x as

$$\frac{\partial c_e^-}{\partial t}(x,t) = \frac{\partial}{\partial x}\left[\frac{D_{e,\mathrm{eff}}(c_e^-,T_c)}{\varepsilon_e^-}\frac{\partial c_e^-}{\partial x}(x,t)\right] - \frac{1-t_c^0}{\varepsilon_e^- FL^-}\frac{I(t)}{A} \tag{A.6}$$

$$\frac{\partial c_e^{\mathrm{sep}}}{\partial t}(x,t) = \frac{\partial}{\partial x}\left[\frac{D_{e,\mathrm{eff}}(c_e^{\mathrm{sep}},T_c)}{\varepsilon_e^{\mathrm{sep}}}\frac{\partial c_e^{\mathrm{sep}}}{\partial x}(x,t)\right] \tag{A.7}$$

$$\frac{\partial c_e^+}{\partial t}(x,t) = \frac{\partial}{\partial x}\left[\frac{D_{e,\mathrm{eff}}(c_e^+,T_c)}{\varepsilon_e^+}\frac{\partial c_e^+}{\partial x}(x,t)\right] + \frac{1-t_c^0}{\varepsilon_e^+ FL^+}\frac{I(t)}{A} \tag{A.8}$$

where $D_{e,\mathrm{eff}}$ denotes the effective electrolyte diffusion coefficient based on the porosity ε of the deployed materials and the transfer coefficient t_c^0. For the defined PDEs, the following coupling boundary conditions exist similar to the boundary conditions of the original P2D model

$$\frac{\partial c_e^-}{\partial x}(0^-,t) = \frac{\partial c_e^+}{\partial x}(0^+,t) = 0 \tag{A.9}$$

$$D_{e,\mathrm{eff}}^-\left(c_e(L^-),T_c\right)\frac{\partial c_e^-}{\partial x}(L^-,t) = D_{e,\mathrm{eff}}^{\mathrm{sep}}\left(c_e(0^{\mathrm{sep}}),T_c\right)\frac{\partial c_e^{\mathrm{sep}}}{\partial x}(0^{\mathrm{sep}},t) \tag{A.10}$$

$$D_{e,\mathrm{eff}}^{\mathrm{sep}}\left(c_e(L^{\mathrm{sep}}),T_c\right)\frac{\partial c_e^{\mathrm{sep}}}{\partial x}(L^{\mathrm{sep}},t) = D_{e,\mathrm{eff}}^+\left(c_e(L^+),T_c\right)\frac{\partial c_e^+}{\partial x}(L^+,t) \tag{A.11}$$

$$c_e(L^-,t) = c_e(0^{sep},t) \tag{A.12}$$

$$c_e(L^{sep},t) = c_e(L^+,t) \tag{A.13}$$

The overall potential of both electrodes is then defined by

$$\phi_s^{\pm}(x,t) = \phi_{OCP}^{\pm}\left(c_{ss}^{\pm}(t)\right) + \eta^{\pm}(t) + \phi_e^{\pm}(x,t) + FR_f^{\pm}j_n^{\pm}(t) \tag{A.14}$$

where $\phi_{OCP}^{\pm}\left(c_{ss}^{\pm}(t)\right)$ denotes the OCV of the electrode with the particle surface concentration $c_{ss}^{\pm}(t)$, $\eta^{\pm}(t)$ the overpotential at the electrode–electrolyte interface, $\phi_e^{\pm}(x,t)$ the potential of the electrolyte, and $FR_f^{\pm}j_n^{\pm}(t)$ the passivation film ohmic resistance.

Considering the assumptions that (A1) the exchange current density $i_0^{\pm}(t)$ can be approximated by its average value $\overline{i}_0^{\pm}(t)$, which is independent of the spatial x-dimension, (A2) charge conservation applies to the liquid and solid domains, which leads to $j_n^{\pm}(t)$ being proportional to $I(t)$, and the *Butler–Volmer* equation

$$j_n^{\pm}(x,t) = \frac{i_0^{\pm}(x,t)}{F}\left[\exp\left(\frac{\alpha_a F}{RT_c}\eta^{\pm}(x,t)\right) - \exp\left(-\frac{\alpha_c F}{RT_c}\eta^{\pm}(x,t)\right)\right] \tag{A.15}$$

with the assumption that (A3) the outward and backward reactions are symmetrical $\alpha_a = \alpha_c$, the overpotential at the electrode–electrolyte interface $\eta^{\pm}(t)$ can be calculated according to

$$\eta^{\pm}(t) = \frac{RT_c}{\alpha F}\sinh^{-1}\left(\frac{\pm I(t)}{2a^{\pm}L^{\pm}\overline{i}_0^{\pm}(t)A}\right) \tag{A.16}$$

The remaining potential of the electrolyte can then be determined by integrating the expression

$$\begin{aligned}\int_{0^-}^{0^+}\frac{\partial\phi_e^{\pm}}{\partial x}(x,t)\,\mathrm{d}x &= \int_{0^-}^{0^+}\frac{i_e^{\pm}(x,t)}{\kappa_{eff}(c_e)}\mathrm{d}x \\ &+ \int_{0^-}^{0^+}\frac{2RT_c}{F}\left(1-t_c^0\right)\left(1+\frac{\mathrm{d}\ln f_{c/a}}{\mathrm{d}\ln c_e}(x,t)\right)\frac{\partial\ln c_e}{\partial x}(x,t)\,\mathrm{d}x\end{aligned} \tag{A.17}$$

which further simplifies with a linear approximation if it is assumed (A4) that the activity of the electrolyte $k_f(x,t) = 1 + \mathrm{d}\ln f_{c/a} / \mathrm{d}\ln c_e(x,t)$ is constant in the respective spatial domain and results from the averaged concentration $\overline{k}_f(t) \approx k_f(x,t)$, and (A5) the conductivity in the liquid phase is constant in the respective spatial domain and results from the averaged concentration $\overline{\kappa} \approx \kappa_{eff}(c_e)$, leading to

$$\begin{aligned}\phi_e^+(0^+,t) - \phi_e^-(0^-,t) &= \frac{L^+ + 2L^{sep} + L^-}{2\overline{\kappa}(T_c)}I(t) \\ &+ \frac{2RT_c}{F}\left(1-t_c^0\right)\overline{k}_f(t)\left[\ln c_e(0^+,t) - \ln c_e(0^-,t)\right].\end{aligned} \tag{A.18}$$

In sum, the overall cell voltage $U(t)$ can be formulated from the electrode potentials of the solid phase $\phi^{\pm}$ taking into account the overpotential $\eta^{\pm}$, the electrolyte potential $\phi_e^{\pm}$, according to

$$\begin{aligned}U(t) &= \phi(0^+,t) + \phi(0^-,t) \\ &= \underbrace{\frac{RT_c}{\alpha F}\sinh^{-1}\left(\frac{I(t)}{2a^+L^+i_0^+(t)A}\right)}_{\text{Cathode overpotential}} - \underbrace{\frac{RT_c}{\alpha F}\sinh^{-1}\left(\frac{-I(t)}{2a^-L^-i_0^-(t)A}\right)}_{\text{Anode overpotential}} \\ &+ \underbrace{\phi_{OCP}^+\left(c_{ss}^+(t)\right)}_{\text{Cathode OCV}} - \underbrace{\phi_{OCP}^-\left(c_{ss}^-(t)\right)}_{\text{Anode OCV}} + \underbrace{\left(\frac{R_f^+}{a^+L^+} + \frac{R_f^-}{a^-L^-}\right)\frac{I(t)}{A}}_{\text{SEI/CEI overpotential}} \\ &+ \underbrace{\frac{L^+ + 2L^{sep} + L^-}{2\overline{\kappa}(T_c)}\frac{I(t)}{A}}_{\text{Electrolyte overpotential}} \\ &+ \underbrace{\frac{2RT_c}{F}\left(1-t_c^0\right)\overline{k}_f(t,T_c)\left[\ln c_e(0^+,t) - \ln c_e(0^-,t)\right]}_{\text{Electrolyte overpotential}}.\end{aligned} \tag{A.19}$$

For a more detailed explanation of the governing equations and their physical origin, the reader is referred to existing literature in the field of P2D modeling and the derivation of the introduced reduced-order model [25,91].

Appendix B. Governing thermal model equations

1D thermal models of lithium-ion cells can be derived by subdividing the thermal dynamics into heat generation and heat transfer. The first can be derived from a energy balance of the lithium-ion cell according to Bernardi et al. [92] following

$$\dot{Q} = \dot{Q}_{irr} + \dot{Q}_{rev} + \dot{Q}_{react} + \dot{Q}_{mix} \tag{B.1}$$

with the irreversible losses Q_{irr}, the reversible losses Q_{rev}, the enthalpy of reaction Q_{react}, and the enthalpy of mixing Q_{mix}. In contrast to the first two, the last two loss terms represent only a minor share of the overall losses and are difficult to be modeled precisely, which is why they are often neglected in the literature. The relevance of reversible losses due to entropy changes is controversial discussed. While the relative share on the total heat generation may be relatively large for specific anode/cathode combinations at cell formats [93], studies pointed out that the negligence at small charging C-rates beyond 1 C is reasonable [30]. Therefore, reversible losses are neglected for the case of fast charging. Conclusively, the heat generation can be calculated by

$$\dot{Q}(t) = -I(t)\left[U(t) - U_{OCV}\right] = -I(t)\left[U(t) - \left(\phi_{OCP}^+ - \phi_{OCP}^-\right)\right] \tag{B.2}$$

with the charging current I and the overpotential of the cell as a subtraction of the cell's terminal voltage U and the cell's OCV U_{OCV}. Hereby, the cell's OCV U_{OCV} is composed of both electrode OCPs $\phi_{OCP}^{\pm}$.

For the heat transfer, we simplify the model to the radial direction of the lithium-ion cell, which usually poses the largest thermal gradient and reaches the mounted temperature sensor at the cell can. Once power losses occur, heat is transferred through the material to the surroundings of the cell. By conducting an energy balance at the cell core, the heat is equal to the heat generated at the core minus the heat transferred in the radial direction, following

$$C_1\frac{dT_c}{dt} = \dot{Q} - \frac{1}{R_1}(T_c - T_s) \tag{B.3}$$

with the thermal capacity C_1, the internal thermal resistance R_1, the core temperature T_c, and the surface temperature T_s. By solving Eq. (B.3) for T_c, we yield the final ODE

$$\frac{dT_c(t)}{dt} = \frac{T_s(t) - T_c(t)}{R_1C_1} + \frac{Q_c(t)}{C_1}. \tag{B.4}$$

Appendix C. Open-circuit potential regression coefficients

See Table C for the electrode OCP regression coefficients.

Appendix D. Diffusion and reaction rate regression coefficients

See Table D for the diffusion/reaction rate regression coefficients.

Appendix E. Cell batch characteristics

Capacity and resistance scattering of the investigated lithium-ion cells, which were laser-welded to yield a 12s2p system, can be found in Table E.

Appendix F. Model parameter

All determined parameters for the investigated Sony/Murata US18650VTC5A lithium-ion cell can be found in Table F.

Table C
Coefficients of the anode/cathode OCP regressions.

	Anode	Cathode
p_1	64.59	−63606.43
p_2	0.53	396881.33
p_3	−95.32	−1087294.13
p_4	0.02	1718162.84
p_5	−0.23	−1728735.76
p_6	−0.04	1151449.10
p_7	−0.18	−509520.51
p_8	−1.04	145123.39
p_9	0.06	−24361.91
p_{10}	−64.64	1977.60
p_{11}	0.43	−107.92
p_{12}	0.14	38.59
p_{13}	−0.018	−6.15
p_{14}	−0.53	0.76
p_{15}	0.03	3.50

Table D
Coefficients of the reaction rate/diffusion coefficient regressions.

	Anode		Cathode	
	D_s^-	k^-	D_s^+	k^+
p_1	$-1.227 \cdot 10^{-14}$	$8.603 \cdot 10^{-6}$	$4.871 \cdot 10^{-15}$	$7.456 \cdot 10^{-6}$
p_2	$2.768 \cdot 10^{-14}$	$-9.880 \cdot 10^{-6}$	$-9.281 \cdot 10^{-15}$	$-1.964 \cdot 10^{-7}$
p_3	$-1.926 \cdot 10^{-14}$	$3.165 \cdot 10^{-6}$	$6.242 \cdot 10^{-15}$	$2.100 \cdot 10^{-7}$
p_4	$5.205 \cdot 10^{-15}$	–	$-8.020 \cdot 10^{-17}$	–

Table E
Capacity and DC resistances for all individual cells used for the system level design. μ = mean; σ = standard deviation; κ = coefficient of variation.

Cell ID	Capacity in Ah CCCV, 4.2–2.5 V, C/50 cut-off	DC-Resistance in mΩ 50 % SOC, 1C, 10s
1	2.529	18.31
2	2.508	17.89
3	2.522	17.72
4	2.545	17.72
5	2.543	17.81
6	2.539	17.84
7	2.547	17.89
8	2.591	17.53
9	2.505	17.72
10	2.576	17.18
11	2.537	17.59
12	2.540	17.70
13	2.533	17.65
14	2.564	17.39
15	2.513	17.77
16	2.513	17.44
17	2.543	17.92
18	2.543	17.82
19	2.538	17.87
20	2.552	17.94
21	2.513	17.83
22	2.542	17.66
23	2.543	17.77
24	2.542	17.91
μ	2.538	17.74
σ	0.020	0.217
κ	0.79%	1.22%

Table F
Determined model parameter for the electrochemical battery model of a commercially available Sony US18650VTC5A lithium-ion cell.

Description	Parameter	Value	Unit
Anode (−)			
Active electrode surface	A	1024[c]	cm^2
Electrode thickness	L	54.66[b]	µm
Active material mass fraction	ω_s	95[a]	%
Porosity	ϵ_e	27[a]	%
Volumetric active material fraction	ϵ_s	69.35[a]	%
Particle radius	R_s	7[a]	µm
Active material density	ρ_s	2.25[a]	g/cm^3
Specific active material capacity	q_s	343[a]	mA h/g
Max. active material lithium concentration	$c_{s,max}$	28.79×10^3[b]	mol/m^3
Open-circuit voltage	U	Eq. (11)[c]	V
Lithiation (0/100% SOC)	SP/EP	2.985×10^{-5} / 86.17[c]	%
Diffusion coefficient	D_s	Eq. (13)[c]	m^2/s
Reaction rate	k	Eq. (14)[c]	A $m^{2.5}/mol^{1.5}$
SEI resistance	R_f	4.4×10^{-3}[a]	Ω m^2
Cathode (+)			
Active electrode surface	A	1024[c]	cm^2
Electrode thickness	L	42.77[b]	µm
Active material mass fraction	ω_s	96[a]	%
Porosity	ϵ_e	13[a]	%
Volumetric active material fraction	ϵ_s	83.52[a]	%
Particle radius	R_s	2.5[a]	µm
Active material density	ρ_s	4.8[a]	g/cm^3
Specific active material capacity	q_s	168[a]	mA h/g
Max. active material lithium concentration	$c_{s,max}$	30.09×10^3[b]	mol/m^3
Open-circuit voltage	U	Eq. (12)[c]	V
Delithiation (0/100% SOC)	SP/EP	11.77 / 99.30[c]	%
Diffusion coefficient	D_s	Eq. (15)[c]	m^2/s
Reaction rate	k	Eq. (16)[c]	A $m^{2.5}/mol^{1.5}$
Electrolyte and separator			
Conductivity	κ	Eq. (8)[a]	S/m
Diffusion coefficient	D_e	Eq. (9)[a]	m^2/s
Activity	$\frac{d \ln f_{c/a}}{d \ln c_e}$	Eq. (10)[a]	–
Initial lithium concentration	$c_{e,0}$	1×10^3[a]	mol/m^3
Transport number	t_c^0	0.38[a]	–
Thickness	L^{sep}	8[a]	µm
Porosity	ϵ_e^{sep}	0.40[a]	–
Thermal parameter			
Activation energy of the anode reaction rate	E_k^-	36.08[c]	kJ/mol
Activation energy of the cathode reaction rate	E_k^+	56.04[c]	kJ/mol
Activation energy of the anode diffusion	E_D^-	22.51[c]	kJ/mol
Activation energy of the cathode diffusion	E_D^+	28.83[c]	kJ/mol
Activation energy of the electrolyte	E_e	17.12[a]	kJ/mol
Thermal capacity	C_1	590[c]	J/(kg K)
Radial heat transfer coefficient	h_1	0.23[c]	W/(m k)
Cell mass	m	47.7[b]	g

All experimental values are given without confidence intervals, but are subject to measurement-related scatter, which was not further investigated within this study.
[a]Literature.
[b]Calculated.
[c]Measured and/or fitted to measurements.

References

[1] D. Howell, S. Boyd, B. Cunningham, S. Gillard, L. Slezak, Enabling fast charging: A technology gap assessment. http://dx.doi.org/10.2172/1416167.

[2] European Technology and Innovation Platform, Batteries - Towards a competitive European industrial battery value chain for stationary applications and e-mobility: Draft proposal. URL https://ec.europa.eu/info/sites/default/files/research_and_innovation/funding/documents/ec_rtd_he-partnerships-european-industrial-battery-value-chain.pdf.

[3] P. Notten, J.O.h. Veld, J. van Beek, Boostcharging Li-ion batteries: A challenging new charging concept, J. Power Sources 145 (1) (2005) 89–94, http://dx.doi.org/10.1016/j.jpowsour.2004.12.038.

[4] D. Anseán, M. González, J.C. Viera, V.M. García, C. Blanco, M. Valledor, Fast charging technique for high power lithium iron phosphate batteries: A cycle life analysis, J. Power Sources 239 (2013) 9–15, http://dx.doi.org/10.1016/j.jpowsour.2013.03.044.

[5] P. Keil, A. Jossen, Charging protocols for lithium-ion batteries and their impact on cycle life—An experimental study with different 18650 high-power cells, J. Energy Storage 6 (2016) 125–141, http://dx.doi.org/10.1016/j.est.2016.02.005.

[6] M. Abdel Monem, K. Trad, N. Omar, O. Hegazy, B. Mantels, G. Mulder, P. van den Bossche, J. van Mierlo, Lithium-ion batteries: Evaluation study of different charging methodologies based on aging process, Appl. Energy 152 (2015) 143–155, http://dx.doi.org/10.1016/j.apenergy.2015.02.064.

[7] M. Abdel-Monem, K. Trad, N. Omar, O. Hegazy, P. van den Bossche, J. van Mierlo, Influence analysis of static and dynamic fast-charging current profiles on ageing performance of commercial lithium-ion batteries, Energy 120 (2017) 179–191, http://dx.doi.org/10.1016/j.energy.2016.12.110.

[8] J. Li, E. Murphy, J. Winnick, P.A. Kohl, The effects of pulse charging on cycling characteristics of commercial lithium-ion batteries, J. Power Sources 102 (1–2) (2001) 302–309, http://dx.doi.org/10.1016/S0378-7753(01)00820-5.

[9] N. Legrand, B. Knosp, P. Desprez, F. Lapicque, S. Raël, Physical characterization of the charging process of a Li-ion battery and prediction of Li plating by electrochemical modelling, J. Power Sources 245 (2014) 208–216, http://dx.doi.org/10.1016/j.jpowsour.2013.06.130.

[10] Z. Chu, X. Feng, L. Lu, J. Li, X. Han, M. Ouyang, Non-destructive fast charging algorithm of lithium-ion batteries based on the control-oriented electrochemical model, Appl. Energy 204 (2017) 1240–1250, http://dx.doi.org/10.1016/j.apenergy.2017.03.111.

[11] M. Song, S.-Y. Choe, Fast and safe charging method suppressing side reaction and lithium deposition reaction in lithium ion battery, J. Power Sources 436 (2019) 226835, http://dx.doi.org/10.1016/j.jpowsour.2019.226835.

[12] X. Lin, X. Hao, Z. Liu, W. Jia, Health conscious fast charging of Li-ion batteries via a single particle model with aging mechanisms, J. Power Sources 400 (2018) 305–316, http://dx.doi.org/10.1016/j.jpowsour.2018.08.030.

[13] X. Lin, Real-Time Prediction of Anode Potential in Li-ion Batteries Using Long Short-Term Neural Networks for Lithium Plating Prevention, J. Electrochem. Soc. 166 (10) (2019) A1893–A1904, http://dx.doi.org/10.1149/2.0621910jes.

[14] F. Ringbeck, M. Garbade, D.U. Sauer, Uncertainty-aware state estimation for electrochemical model-based fast charging control of lithium-ion batteries, J. Power Sources 470 (2020) 228221, http://dx.doi.org/10.1016/j.jpowsour.2020.228221.

[15] A. Tomaszewska, Z. Chu, X. Feng, S. O'Kane, X. Liu, J. Chen, C. Ji, E. Endler, R. Li, L. Liu, Y. Li, S. Zheng, S. Vetterlein, M. Gao, J. Du, M. Parkes, M. Ouyang, M. Marinescu, G. Offer, B. Wu, Lithium-ion battery fast charging: A review, ETransportation 1 (2019) 100011, http://dx.doi.org/10.1016/j.etran.2019.100011.

[16] N. Wassiliadis, J. Schneider, A. Frank, L. Wildfeuer, X. Lin, A. Jossen, M. Lienkamp, Review of fast charging strategies for lithium-ion battery systems and their applicability for battery electric vehicles, J. Energy Storage 44 (2021) 103306, http://dx.doi.org/10.1016/j.est.2021.103306.

[17] M. Doyle, T.F. Fuller, J. Newman, Modeling of Galvanostatic Charge and Discharge of the Lithium/Polymer/Insertion Cell, J. Electrochem. Soc. 140 (6) (1993) 1526–1533, http://dx.doi.org/10.1149/1.2221597.

[18] M. Ecker, S. Käbitz, I. Laresgoiti, D.U. Sauer, Parameterization of a Physico-Chemical Model of a Lithium-Ion Battery, J. Electrochem. Soc. 162 (9) (2015) A1849–A1857, http://dx.doi.org/10.1149/2.0541509jes.

[19] J. Schmalstieg, C. Rahe, M. Ecker, D.U. Sauer, Full Cell Parameterization of a High-Power Lithium-Ion Battery for a Physico-Chemical Model: Part I. Physical and Electrochemical Parameters, J. Electrochem. Soc. 165 (16) (2018) A3799–A3810, http://dx.doi.org/10.1149/2.0321816jes.

[20] C.-H. Chen, F. Brosa Planella, K. O'Regan, D. Gastol, W.D. Widanage, E. Kendrick, Development of Experimental Techniques for Parameterization of Multi-scale Lithium-ion Battery Models, J. Electrochem. Soc. 167 (8) (2020) 080534, http://dx.doi.org/10.1149/1945-7111/ab9050.

[21] J.C. Forman, S.J. Moura, J.L. Stein, H.K. Fathy, Genetic identification and fisher identifiability analysis of the Doyle–Fuller–Newman model from experimental cycling of a LiFePO4 cell, J. Power Sources 210 (2012) 263–275, http://dx.doi.org/10.1016/j.jpowsour.2012.03.009.

[22] E. Namor, D. Torregrossa, R. Cherkaoui, M. Paolone, Parameter identification of a lithium-ion cell single-particle model through non-invasive testing, J. Energy Storage 12 (2017) 138–148, http://dx.doi.org/10.1016/j.est.2017.04.008.

[23] N. Jin, D.L. Danilov, P.M. van den Hof, M. Donkers, Parameter estimation of an electrochemistry-based lithium-ion battery model using a two-step procedure and a parameter sensitivity analysis, Int. J. Energy Res. 42 (7) (2018) 2417–2430, http://dx.doi.org/10.1002/er.4022.

[24] S. Park, D. Kato, Z. Gima, R. Klein, S. Moura, Optimal Experimental Design for Parameterization of an Electrochemical Lithium-Ion Battery Model, J. Electrochem. Soc. 165 (7) (2018) A1309–A1323, http://dx.doi.org/10.1149/2.0421807jes.

[25] S.J. Moura, F.B. Argomedo, R. Klein, A. Mirtabatabaei, M. Krstic, Battery State Estimation for a Single Particle Model With Electrolyte Dynamics, IEEE Trans. Control Syst. Technol. 25 (2) (2017) 453–468, http://dx.doi.org/10.1109/TCST.2016.2571663.

[26] H.E. Perez, X. Hu, S. Dey, S.J. Moura, Optimal Charging of Li-ion Batteries With Coupled Electro-Thermal-Aging Dynamics, IEEE Trans. Veh. Technol. 66 (9) (2017) 7761–7770, http://dx.doi.org/10.1109/TVT.2017.2676044.

[27] K.W. Kim, H. Park, J.G. Lee, J. Kim, Y.-U. Kim, J.H. Ryu, J.J. Kim, S.M. Oh, Capacity variation of carbon-coated silicon monoxide negative electrode for lithium-ion batteries, Electrochim. Acta 103 (2013) 226–230, http://dx.doi.org/10.1016/j.electacta.2013.04.040.

[28] T. Amietszajew, E. McTurk, J. Fleming, R. Bhagat, Understanding the limits of rapid charging using instrumented commercial 18650 high-energy Li-ion cells, Electrochim. Acta 263 (2018) 346–352, http://dx.doi.org/10.1016/j.electacta.2018.01.076.

[29] C. Forgez, D. Vinh Do, G. Friedrich, M. Morcrette, C. Delacourt, Thermal modeling of a cylindrical LiFePO4/graphite lithium-ion battery, J. Power Sources 195 (9) (2010) 2961–2968, http://dx.doi.org/10.1016/j.jpowsour.2009.10.105.

[30] A. Nazari, S. Farhad, Heat generation in lithium-ion batteries with different nominal capacities and chemistries, Appl. Therm. Eng. 125 (2017) 1501–1517, http://dx.doi.org/10.1016/j.applthermaleng.2017.07.126.

[31] C. Li, N. Cui, C. Wang, C. Zhang, Simplified electrochemical lithium-ion battery model with variable solid-phase diffusion and parameter identification over wide temperature range, J. Power Sources 497 (2021) 229900, http://dx.doi.org/10.1016/j.jpowsour.2021.229900.

[32] L. Wildfeuer, N. Wassiliadis, A. Karger, F. Bauer, M. Lienkamp, Teardown analysis and characterization of a commercial lithium-ion battery for advanced algorithms in battery electric vehicles, J. Energy Storage 48 (2022) 103909, http://dx.doi.org/10.1016/j.est.2021.103909.

[33] Lain, Brandon, Kendrick, Design Strategies for High Power vs. High Energy Lithium Ion Cells, Batteries 5 (4) (2019) 64, http://dx.doi.org/10.3390/batteries5040064.

[34] J. Mao, W. Tiedemann, J. Newman, Simulation of Li-ion Cells by Dualfoil Model under Constant-Resistance Load, ECS Trans. 58 (48) (2014) 71–81, http://dx.doi.org/10.1149/05848.0071ecst.

[35] M. Ecker, T.K.D. Tran, P. Dechent, S. Käbitz, A. Warnecke, D.U. Sauer, Parameterization of a Physico-Chemical Model of a Lithium-Ion Battery, J. Electrochem. Soc. 162 (9) (2015) A1836–A1848, http://dx.doi.org/10.1149/2.0551509jes.

[36] P. Albertus, J. Christensen, J. Newman, Experiments on and Modeling of Positive Electrodes with Multiple Active Materials for Lithium-Ion Batteries, J. Electrochem. Soc. 156 (7) (2009) A606, http://dx.doi.org/10.1149/1.3129656.

[37] H. Lundgren, M. Behm, G. Lindbergh, Electrochemical Characterization and Temperature Dependency of Mass-Transport Properties of LiPF 6 in EC:DEC, J. Electrochem. Soc. 162 (3) (2015) A413–A420, http://dx.doi.org/10.1149/2.0641503jes.

[38] M. Lewerenz, G. Fuchs, L. Becker, D.U. Sauer, Irreversible calendar aging and quantification of the reversible capacity loss caused by anode overhang, J. Energy Storage 18 (2018) 149–159, http://dx.doi.org/10.1016/j.est.2018.04.029.

[39] L. Wild, Experimental investigation of model-based fast charging strategies for lithium-ion batteries.

[40] L.O. Valoen, J.N. Reimers, Transport Properties of LiPF6-Based Li-ion Battery Electrolytes, J. Electrochem. Soc. 152 (5) (2005) A882, http://dx.doi.org/10.1149/1.1872737.

[41] A. Barai, K. Uddin, M. Dubarry, L. Somerville, A. McGordon, P. Jennings, I. Bloom, A comparison of methodologies for the non-invasive characterisation of commercial Li-ion cells, Prog. Energy Combust. Sci. 72 (2019) 1–31, http://dx.doi.org/10.1016/j.pecs.2019.01.001.

[42] C. Birkenmaier, B. Bitzer, M. Harzheim, A. Hintennach, T. Schleid, Lithium Plating on Graphite Negative Electrodes: Innovative Qualitative and Quantitative Investigation Methods, J. Electrochem. Soc. 162 (14) (2015) A2646–A2650, http://dx.doi.org/10.1149/2.0451514jes.

[43] M. Safari, C. Delacourt, Modeling of a Commercial Graphite/LiFePO4 Cell, J. Electrochem. Soc. 158 (5) (2011) A562, http://dx.doi.org/10.1149/1.3567007.

[44] V. Murray, D.S. Hall, J.R. Dahn, A Guide to Full Coin Cell Making for Academic Researchers, J. Electrochem. Soc. 166 (2) (2019) A329–A333, http://dx.doi.org/10.1149/2.1171902jes.

[45] K. Levenberg, A method for the solution of certain non-linear problems in least squares, Q. Appl. Math. 2 (2) (1944) 164–168, http://dx.doi.org/10.1090/qam/10666.

[46] D.W. Marquardt, An Algorithm for Least-Squares Estimation of Nonlinear Parameters, J. Soc. Ind. Appl. Math. 11 (2) (1963) 431–441, http://dx.doi.org/10.1137/0111030.

[47] J.J. Moré, The Levenberg-Marquardt algorithm: Implementation and theory, in: G.A. Watson (Ed.), Numerical Analysis, in: Lecture Notes in Mathematics, vol. 630, Springer Berlin Heidelberg, Berlin, Heidelberg, 1978, pp. 105–116, http://dx.doi.org/10.1007/BFb0067700.

[48] P. Ramadass, B. Haran, P.M. Gomadam, R. White, B.N. Popov, Development of First Principles Capacity Fade Model for Li-ion Cells, J. Electrochem. Soc. 151 (2) (2004) A196, http://dx.doi.org/10.1149/1.1634273.

[49] X. Han, M. Ouyang, L. Lu, J. Li, Simplification of physics-based electrochemical model for lithium ion battery on electric vehicle. Part II: Pseudo-two-dimensional model simplification and state of charge estimation, J. Power Sources 278 (2015) 814–825, http://dx.doi.org/10.1016/j.jpowsour.2014.08.089.

[50] A. Mistry, D. Juarez-Robles, M. Stein, K. Smith, P.P. Mukherjee, Analysis of Long-Range Interaction in Lithium-Ion Battery Electrodes, J. Electrochem. Energy Convers. Storage 13 (3) (2016) http://dx.doi.org/10.1115/1.4035198.

[51] S.G. Marquis, V. Sulzer, R. Timms, C.P. Please, S.J. Chapman, An Asymptotic Derivation of a Single Particle Model with Electrolyte, J. Electrochem. Soc. 166 (15) (2019) A3693–A3706, http://dx.doi.org/10.1149/2.0341915jes.

[52] D.P. Abraham, S. Kawauchi, D.W. Dees, Modeling the impedance versus voltage characteristics of LiNi0.8Co0.15Al0.05O2, Electrochim. Acta 53 (5) (2008) 2121–2129, http://dx.doi.org/10.1016/j.electacta.2007.09.018.

[53] D.W. Dees, S. Kawauchi, D.P. Abraham, J. Prakash, Analysis of the Galvanostatic Intermittent Titration Technique (GITT) as applied to a lithium-ion porous electrode, J. Power Sources 189 (1) (2009) 263–268, http://dx.doi.org/10.1016/j.jpowsour.2008.09.045.

[54] R. Amin, D.B. Ravnsbæk, Y.-M. Chiang, Characterization of Electronic and Ionic Transport in Li 1-x Ni 0.8 Co 0.15 Al 0.05 O 2 (NCA), J. Electrochem. Soc. 162 (7) (2015) A1163–A1169, http://dx.doi.org/10.1149/2.0171507jes.

[55] J. Duan, C. Wu, Y. Cao, K. Du, Z. Peng, G. Hu, Enhanced electrochemical performance and thermal stability of LiNi0.80Co0.15Al0.05O2 via nano-sized LiMnPO4 coating, Electrochim. Acta 221 (2016) 14–22, http://dx.doi.org/10.1016/j.electacta.2016.10.158.

[56] G. Xia, L. Cao, G. Bi, A review on battery thermal management in electric vehicle application, J. Power Sources 367 (2017) 90–105, http://dx.doi.org/10.1016/j.jpowsour.2017.09.046.

[57] M.A. Cabañero, N. Boaretto, M. Röder, J. Müller, J. Kallo, A. Latz, Direct Determination of Diffusion Coefficients in Commercial Li-ion Batteries, J. Electrochem. Soc. 165 (5) (2018) A847–A855, http://dx.doi.org/10.1149/2.0301805jes.

[58] J. Dong, P. Xiao, D. Zhang, C. Chang, Enhanced rate performance and cycle stability of LiNi0.8Co0.15Al0.05O2 via Rb doping, J. Mater. Sci.: Mater. Electron. 29 (24) (2018) 21119–21129, http://dx.doi.org/10.1007/s10854-018-0260-1.

[59] S. Li, S. Pischinger, C. He, L. Liang, M. Stapelbroek, A comparative study of model-based capacity estimation algorithms in dual estimation frameworks for lithium-ion batteries under an accelerated aging test, Appl. Energy 212 (2018) 1522–1536, http://dx.doi.org/10.1016/j.apenergy.2018.01.008.

[60] S. Xia, F. Li, F. Chen, H. Guo, Preparation of FePO4 by liquid-phase method and modification on the surface of LiNi0.80Co0.15Al0.05O2 cathode material, J. Alloys Compd. 731 (2018) 428–436, http://dx.doi.org/10.1016/j.jallcom.2017.10.047.

[61] M. Morita, N. Nishimura, Y. Matsuda, Charge/discharge cycling behavior of pitch-based carbon fiber in organic electrolyte solutions, Electrochim. Acta 38 (13) (1993) 1721–1726, http://dx.doi.org/10.1016/0013-4686(93)85068-A.

[62] M.W. Verbrugge, B.J. Koch, Modeling Lithium Intercalation of Single–Fiber Carbon Microelectrodes, J. Electrochem. Soc. 143 (2) (1996) 600–608, http://dx.doi.org/10.1149/1.1836486.

[63] M.D. Levi, D. Aurbach, Diffusion Coefficients of Lithium Ions during Intercalation into Graphite Derived from the Simultaneous Measurements and Modeling of Electrochemical Impedance and Potentiostatic Intermittent Titration Characteristics of Thin Graphite Electrodes, J. Phys. Chem. B 101 (23) (1997) 4641–4647, http://dx.doi.org/10.1021/jp9701911.

[64] T. Piao, S.-M. Park, C.-H. Doh, S.-I. Moon, Intercalation of Lithium Ions into Graphite Electrodes Studied by AC Impedance Measurements, J. Electrochem. Soc. 146 (8) (1999) 2794–2798, http://dx.doi.org/10.1149/1.1392010.

[65] P. Yu, B.N. Popov, J.A. Ritter, R.E. White, Determination of the Lithium Ion Diffusion Coefficient in Graphite, J. Electrochem. Soc. 146 (1) (1999) 8–14, http://dx.doi.org/10.1149/1.1391556.

[66] A. Márquez, P.B. Balbuena, Molecular Dynamics Study of Graphite/Electrolyte Interfaces, J. Electrochem. Soc. 148 (6) (2001) A624, http://dx.doi.org/10.1149/1.1372216.

[67] H. Yang, H.J. Bang, J. Prakash, Evaluation of Electrochemical Interface Area and Lithium Diffusion Coefficient for a Composite Graphite Anode, J. Electrochem. Soc. 151 (8) (2004) A1247, http://dx.doi.org/10.1149/1.1763139.

[68] H.-j. Guo, X.-h. Li, X.-m. Zhang, H.-q. Wang, Z.-x. Wang, W.-j. Peng, Diffusion coefficient of lithium in artificial graphite, mesocarbon microbeads, and disordered carbon, New Carbon Mater. 22 (1) (2007) 7–10, http://dx.doi.org/10.1016/S1872-5805(07)60006-7.

[69] K. Eberman, P. Gomadam, G. Jain, E. Scott, Material and Design Options for Avoiding Lithium Plating during Charging, ECS Trans. 25 (35) (2009) 47–58, http://dx.doi.org/10.1149/1.3414003.

[70] K. Honkura, T. Horiba, Study of the deterioration mechanism of LiCoO2/graphite cells in charge/discharge cycles using the discharge curve analysis, J. Power Sources 264 (2014) 140–146, http://dx.doi.org/10.1016/j.jpowsour.2014.04.036.

[71] M. Mastali, M. Farkhondeh, S. Farhad, R.A. Fraser, M. Fowler, Electrochemical Modeling of Commercial LiFePO 4 and Graphite Electrodes: Kinetic and Transport Properties and Their Temperature Dependence, J. Electrochem. Soc. 163 (13) (2016) A2803–A2816, http://dx.doi.org/10.1149/2.1151613jes.

[72] M. Fleckenstein, S. Fischer, O. Bohlen, B. Bäker, Thermal Impedance Spectroscopy - A method for the thermal characterization of high power battery cells, J. Power Sources 223 (2013) 259–267, http://dx.doi.org/10.1016/j.jpowsour.2012.07.144.

[73] H. Maleki, S.A. Hallaj, J.R. Selman, R.B. Dinwiddie, H. Wang, Thermal Properties of Lithium–Ion Battery and Components, J. Electrochem. Soc. 146 (3) (1999) 947–954, http://dx.doi.org/10.1149/1.1391704.

[74] K.A. Murashko, J. Pyrhönen, J. Jokiniemi, Determination of the through-plane thermal conductivity and specific heat capacity of a Li-ion cylindrical cell, Int. J. Heat Mass Transf. 162 (2020) 120330, http://dx.doi.org/10.1016/j.ijheatmasstransfer.2020.120330.

[75] R.R. Richardson, P.T. Ireland, D.A. Howey, Battery internal temperature estimation by combined impedance and surface temperature measurement, J. Power Sources 265 (2014) 254–261, http://dx.doi.org/10.1016/j.jpowsour.2014.04.129.

[76] T.S. Bryden, B. Dimitrov, G. Hilton, C. Ponce de León, P. Bugryniec, S. Brown, D. Cumming, A. Cruden, Methodology to determine the heat capacity of lithium-ion cells, J. Power Sources 395 (2018) 369–378, http://dx.doi.org/10.1016/j.jpowsour.2018.05.084.

[77] M. Steinhardt, E.I. Gillich, A. Rheinfeld, L. Kraft, M. Spielbauer, O. Bohlen, A. Jossen, Low-effort determination of heat capacity and thermal conductivity for cylindrical 18650 and 21700 lithium-ion cells, J. Energy Storage 42 (2021) 103065, http://dx.doi.org/10.1016/j.est.2021.103065.

[78] M. Al-Zareer, A. Michalak, C. Da Silva, C.H. Amon, Predicting specific heat capacity and directional thermal conductivities of cylindrical lithium-ion batteries: A combined experimental and simulation framework, Appl. Therm. Eng. 182 (2021) 116075, http://dx.doi.org/10.1016/j.applthermaleng.2020.116075.

[79] P. Keil, K. Rumpf, A. Jossen, Thermal impedance spectroscopy for Li-ion batteries with an IR temperature sensor system, in: 2013 World Electric Vehicle Symposium and Exhibition (EVS27), IEEE, 2013, pp. 1–11, http://dx.doi.org/10.1109/EVS.2013.6914935.

[80] N. Wassiliadis, M. Ank, L. Wildfeuer, M.K. Kick, M. Lienkamp, Experimental investigation of the influence of electrical contact resistance on lithium-ion battery testing for fast-charge applications, Appl. Energy 295 (2021) 117064, http://dx.doi.org/10.1016/j.apenergy.2021.117064.

[81] N. Wassiliadis, M. Ank, L. Wildfeuer, M.K. Kick, M. Lienkamp, Experimental investigation of the influence of electric contact resistance of lithium-ion battery testing for fast-charge applications. http://dx.doi.org/10.14459/2021mp1611393.

[82] V. Ramadesigan, P.W.C. Northrop, S. De, S. Santhanagopalan, R.D. Braatz, V.R. Subramanian, Modeling and Simulation of Lithium-Ion Batteries from a Systems Engineering Perspective, J. Electrochem. Soc. 159 (3) (2012) R31–R45, http://dx.doi.org/10.1149/2.018203jes.

[83] E. Prada, D. Di Domenico, Y. Creff, J. Bernard, V. Sauvant-Moynot, F. Huet, Simplified Electrochemical and Thermal Model of LiFePO 4 -Graphite Li-ion Batteries for Fast Charge Applications, J. Electrochem. Soc. 159 (9) (2012) A1508–A1519, http://dx.doi.org/10.1149/2.064209jes.

[84] J. Marcicki, M. Canova, A.T. Conlisk, G. Rizzoni, Design and parametrization analysis of a reduced-order electrochemical model of graphite/LiFePO4 cells for SOC/SOH estimation, J. Power Sources 237 (2013) 310–324, http://dx.doi.org/10.1016/j.jpowsour.2012.12.120.

[85] C. Edouard, M. Petit, C. Forgez, J. Bernard, R. Revel, Parameter sensitivity analysis of a simplified electrochemical and thermal model for Li-ion batteries aging, J. Power Sources 325 (2016) 482–494, http://dx.doi.org/10.1016/j.jpowsour.2016.06.030.

[86] T. Gao, Y. Han, D. Fraggedakis, S. Das, T. Zhou, C.-N. Yeh, S. Xu, W.C. Chueh, J. Li, M.Z. Bazant, Interplay of Lithium Intercalation and Plating on a Single Graphite Particle, Joule 5 (2) (2021) 393–414, http://dx.doi.org/10.1016/j.joule.2020.12.020.

[87] V. Ramadesigan, K. Chen, N.A. Burns, V. Boovaragavan, R.D. Braatz, V.R. Subramanian, Parameter Estimation and Capacity Fade Analysis of Lithium-Ion Batteries Using Reformulated Models, J. Electrochem. Soc. 158 (9) (2011) A1048, http://dx.doi.org/10.1149/1.3609926.

[88] K. Uddin, S. Perera, W. Widanage, L. Somerville, J. Marco, Characterising Lithium-Ion Battery Degradation through the Identification and Tracking of Electrochemical Battery Model Parameters, Batteries 2 (2) (2016) 13, http://dx.doi.org/10.3390/batteries2020013.

[89] J. Sieg, J. Bandlow, T. Mitsch, D. Dragicevic, T. Materna, B. Spier, H. Witzenhausen, M. Ecker, D.U. Sauer, Fast charging of an electric vehicle lithium-ion battery at the limit of the lithium deposition process, J. Power Sources 427 (2019) 260–270, http://dx.doi.org/10.1016/j.jpowsour.2019.04.047.

[90] L.D. Couto, R. Romagnoli, S. Park, D. Zhang, S.J. Moura, M. Kinnaert, E. Garone, Faster and Healthier Charging of Lithium-Ion Batteries via Constrained Feedback Control, IEEE Trans. Control Syst. Technol. (2021) 1–12, http://dx.doi.org/10.1109/TCST.2021.3135149.

[91] G.L. Plett, Battery Management Systems, in: Artech House Power Engineering and Power Electronics, vol. 1, Artech House, Boston, 2015.

[92] D. Bernardi, E. Pawlikowski, J. Newman, A General Energy Balance for Battery Systems, J. Electrochem. Soc. 132 (1) (1985) 5–12, http://dx.doi.org/10.1149/1.2113792.

[93] V.V. Viswanathan, D. Choi, D. Wang, W. Xu, S. Towne, R.E. Williford, J.-G. Zhang, J. Liu, Z. Yang, Effect of entropy change of lithium intercalation in cathodes and anodes on Li-ion battery thermal management, J. Power Sources 195 (11) (2010) 3720–3729, http://dx.doi.org/10.1016/j.jpowsour.2009.11.103.

2.4 Model-based health-aware fast charging control of lithium-ion cells

The effectiveness of constant anode potential (CA) control strategies to improve the fast charging speed while avoiding the onset of lithium plating has commonly been investigated and experimentally quantified for high-energy-density cells. With the trend towards improved fast charging power, high-power density cells are brought to light, providing an optimized trade-off between energy and power density for various applications. However, the declining performance over charge throughput and time of high-power lithium-ion cells may also render fast charging a critical scenario for lithium plating, which should be countered by advanced model-based fast charging strategies aware of the SOH of the lithium-ion cell or pack. Beyond that, model-based charging current control strategies based on electrochemical models are challenging to put into practice due to their high complexity and computational requirements.

This section presents the empowerment and application of a model-based health-aware fast charging strategy mitigating the risk of lithium plating despite repetitive fast charging over the cycle life of the lithium-ion cells, as previously published by the author [58]. The characterized lithium-ion cell introduced in Section 2.2 and a parameterized electrochemical model of reduced order introduced in Section 2.3 have been used to derive a fast charging control strategy capable of real-time operation. In the first step, the model was discretized to keep the computational effort at a minimum while maintaining sufficient accuracy compared to high-fidelity resolutions based on a preliminary analysis of the model [200]. The optimized model is deployed within a robust control loop to allow for CA control to enhance the conventional CC control with a more sophisticated control strategy based on internal lithium-ion cell states and non-linear aging trigger conditions. The aging update, from now on referred to as SOH update, is a complex task due to the diagnostic effort to derive relevant parameters and transfer them to the complex electrochemical model parameter set, as highlighted in previous studies [201]. To provide practical guidance for linking the progressing age and change of cell parameters, commonly tracked down as a capacity decay ΔQ and an ohmic resistance increase ΔR by BMSs, to the electrochemical model at hand, a simple metric was developed to scale relevant model parameters with age. Prior to extensive cycle life testing, lithium plating pretests have been carried out, based on the results of a previous study [144], to provide evidence that aged lithium-ion cells can suffer under lithium plating even though the pristine cell may not. The resulting fast charging strategy dependent on the lithium-ion cell's SOC, temperature (T), and SOH was then deployed in extensive cycle life tests and regularly updated with the SOC, temperature, and SOH [202, 203]. All three quantities have been determined in a laboratory environment but can be easily exchanged with more sophisticated BMS functions as proposed in the author's previous publications [204–206]. The deployed control scheme is illustrated in Figure 2.4.

To enable laboratory testing and charging current control based on model outputs, a model deployment framework has been developed, empowering the electrochemical model of reduced order to communicate via a controlled area network (CAN) with the laboratory testing equipment [207], which has been used for all mentioned experiments in this work. The developed fast charging strategy was compared to fast charging with a simple CC control strategy to prove that the onset of non-linear aging can be avoided if model-based health-aware fast charging strategies are deployed. In the first early cycles, the silicon-doped graphite anode rapidly lost

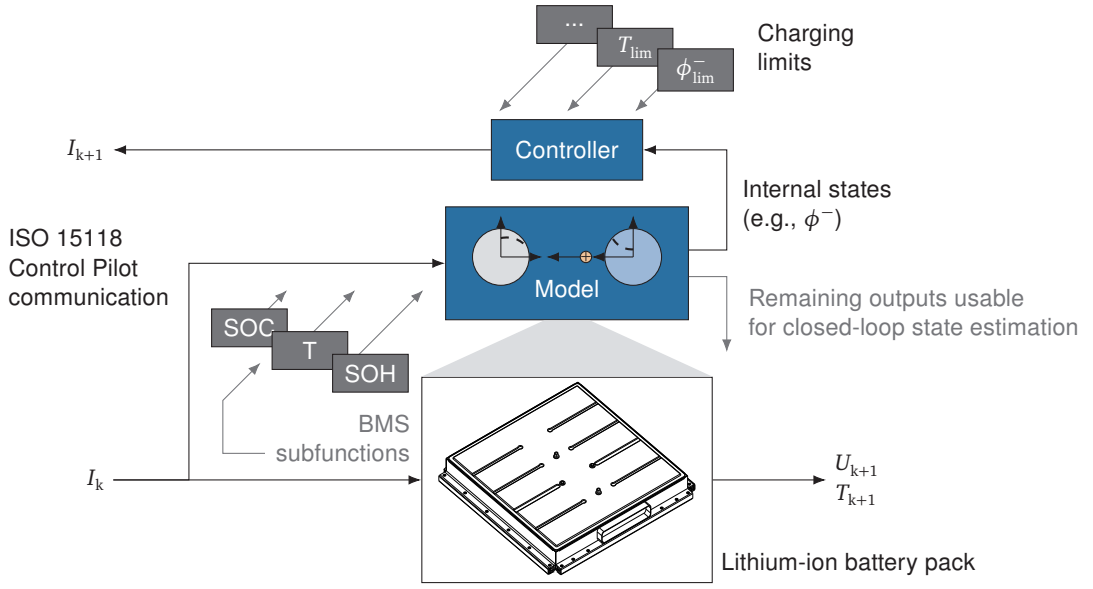

Figure 2.4: Fast charging control function for model-based health-aware fast charging control. The cell model is based on a downscaled P2D electrochemical model of reduced order, in the form of a SPM, deployed for battery internal state estimation and fed with relevant battery states of BMS subfunctions. Limits can be set to control the fast charging current, e.g., at the edge of lithium plating ($\phi > 0\,V$).

capacity [208, 209], which may originate from drastic mechanical deterioration of the graphite host structure due to the vast expansion of the silicon share at high charging currents and, therefore, strong inhomogeneity in the anode particle size. In a later stage of cycling, a sudden drop of capacity and rise of ohmic resistance could be observed for the CC reference fast charging cells at moderate ambient temperatures of $20\,°C$, leading to a rapid failure of the subjected cells. In contrast, the model-based health-aware fast charging followed a more moderate aging trend reaching a more than two-fold longer cycle life, even though DVA showed a similar electrode aging pattern compared to the CC fast charging strategy. Although a similar distinct onset of non-linear aging could not be observed in a comparable life cycle test at $0\,°C$ ambient temperature, the aging was decelerated to a comparable capacity fade rate and resistance rise as in the experiments at $20\,°C$ with model-based health-aware fast charging.

The results emphasize the need for physics-induced current derating by the BMS during fast charging events, which can be enabled by deploying electrochemical models. Beyond the use for fast-charging control algorithms in real-time, the developed model deployment framework for fast and efficient use of lithium-ion cell and pack models of different fidelity in CAN communication with laboratory environments has been published as an open source alongside the previous publication [210].

Author contribution: Nikolaos Wassiliadis carried out the conceptualization, methodology, investigation, software, validation, data curation, and writing of the original manuscript of this study. Johannes Kriegler supported this study with SEM and energy-dispersive X-ray analysis (EDX). Nikolaos Wassiliadis, Johannes Kriegler, Kareem Abo Gamra, and Markus Lienkamp reviewed and edited the manuscript. Markus Lienkamp provided the supervision and resources for this study.

Model-based health-aware fast charging to mitigate the risk of lithium plating and prolong the cycle life of lithium-ion batteries in electric vehicles

Nikolaos Wassiliadis, Johannes Kriegler, Kareem Abo Gamra, Markus Lienkamp

Journal of Power Sources 561, 2023.
Digital Object Identifier: 10.1016/j.jpowsour.2022.232586

Journal of Power Sources 561 (2023) 232586

Contents lists available at ScienceDirect

Journal of Power Sources

journal homepage: www.elsevier.com/locate/jpowsour

Model-based health-aware fast charging to mitigate the risk of lithium plating and prolong the cycle life of lithium-ion batteries in electric vehicles

Nikolaos Wassiliadis [a,*], Johannes Kriegler [b], Kareem Abo Gamra [a], Markus Lienkamp [a]

[a] Technical University of Munich (TUM), School of Engineering & Design, Institute of Automotive Technology, Germany
[b] Technical University of Munich (TUM), School of Engineering & Design, Institute for Machine Tools and Industrial Management, Germany

HIGHLIGHTS

- Investigation of the fast-charge capability of high-energy and high-power cells.
- Proposal of a model-based fast charging strategy adaptive to relevant battery states.
- Validation in an extensive aging study with a commercial lithium-ion cell type.
- Post-mortem investigation of the occurring aging mechanisms.

ARTICLE INFO

Dataset link: https://github.com/TUMFTM/EA_Battery_MDF

Keywords:
Battery electric vehicles
Fast charging
Lithium-ion battery
Lithium plating
Advanced battery management

ABSTRACT

The observed shift to a fully electrified transport sector with steadily increasing sales of battery electric vehicles has led to their wider use under demanding operation conditions, e.g., more frequent fast charging due to a higher degree of utilization with an increased share of operation under low ambient temperatures. These critical edge cases have to be precisely controlled by the battery management system to avoid accelerated battery aging and, in the worst case, safety-critical battery failure events. In this article, we present a model-based, health-aware fast charging strategy for current control of lithium-ion batteries to prevent the onset of non-linear aging and to prolong the cycle life. An electrochemical model of reduced order is used to avoid non-linear aging due to lithium plating. The model is regularly updated alongside the state-of-health of the battery to account for the rise of resistance. Extensive cycle life results reveal that the charging time can be significantly reduced while the cycle life can be prolonged compared to conventional charging. As the strategy is based on an electrochemical model of reduced order, inheriting the physics of lithium-ion batteries, the results can be easily transferred to other cell chemistries and/or formats.

1. Introduction

The growing demand for an enhanced all-electric range of battery electric vehicles (BEVs) comparable to conventional vehicles has led to technological advancements, dramatically improving the energy density of lithium-ion cells used in automotive lithium-ion battery packs [1]. However, an increased energy density decreases the power capability of lithium-ion cells, as the two electrode design principles are contradictory [2]. At the same time, the recharging of BEVs is targeted to reach time-parity with the refueling times of conventional vehicles. While the concept of both an ever-increasing all-electric range and high fast-charging capability, is generally to be questioned and should be rethought for the individual application [3], fast charging currently marks the most challenging scenario for state-of-the-art BEVs [4,5]. Moreover, industry and academia aspire to reach fast charging times of less than 15 min from 10–80% capacity. Unfortunately, this still remains elusive for commercial lithium-ion cell technology under a wide range of operating conditions.

Ideally, an optimal fast charging strategy should minimize the fast charging time while maintaining a long lithium-ion battery lifetime. During fast charging, the current must be precisely controlled at the physical limits to avoid any onset of abuse conditions which could cause non-linear aging or, in the worst case, a thermal runaway. Because of the variety of cell designs and materials used in automotive applications, determining a fast charging strategy that meets the aforementioned requirement is hugely time- and resource-consuming.

Over the last ten years, many studies have been carried out to identify and optimize fast charging strategies, as stated by a recent review in the field [6]. Most popularly, many different strategies were

* Corresponding author.
E-mail address: nikolaos.wassiliadis@tum.de (N. Wassiliadis).

https://doi.org/10.1016/j.jpowsour.2022.232586
Received 27 October 2022; Received in revised form 20 December 2022; Accepted 23 December 2022
Available online 6 February 2023

determined by extensive testing of numerous charging current sequences, revealing that by selecting an adequate charging sequence, the cycle life can be maintained while achieving shorter charging times. For example, many studies investigated boost- [7–9] or multi-stage charging current sequences [10,11], pulse charging sequences [12,13], or adjusted voltage control windows [14,15]. Keil et al. [16] applied a multitude of physically motivated charging sequences to commercial lithium-ion cells, concluding that a precise knowledge of the electrochemical behavior of the individual cell is required to find an optimal fast charging strategy. Schindler et al. [17] identified aging-minimal charging profiles by applying different charging sequences, using design of experiments to reduce the effort required to evaluate the different strategies. Recently, Mathieu et al. [18] investigated the root causes for the degradation of three different application-relevant materials, LFP, NMC, and NCA, in an aging study, emphasizing that each cell chemistry requires an adapted fast charging strategy. Model-based approaches were also investigated to pave the way for a fast upscale from electrode to cell level and transfer to other cell designs and electrode materials [19,20]. Besides data-driven methods [21–27], physics-enhanced equivalent circuit models (pECMs) [28–32], electrochemical models based on the popular pseudo-two dimensional model of Newman's group [33], and the reduced-order models (ROMs) thereof [34–42] with a cell-specific parameter set were also investigated.

In general, the aforementioned studies on model-based fast charging strategies either use offline optimizations, the result of which is then applied as a 1D or 2D current map in an experimental environment, or the model-based real-time strategy is only depending on some of the relevant battery states during operation, namely, the state of charge (SOC), the temperature (T), and the state of health (SOH). As a consequence, neither of the approaches tolerates broadly varying operation conditions during fast charging, which may lead to severe aging if boundary limits are exceeded. To date, there is still a need for intensive experimental validation of a real-time, model-based, and health-aware fast charging strategy adaptive to critical battery states [5]. Beyond that, the majority of the aforementioned studies emphasized the need for advanced fast charging strategies for high energy-dense lithium-ion cells, while one would more likely choose high power-dense lithium-ion cells to achieve short charging times, which are said to be less susceptible to lithium plating as the major aging mechanism [18]. We question whether the increasing growth of resistance due to raised cell core temperatures during fast charging may foster the onset of lithium plating at a later stage of age, even though lithium plating may not initially be a limitation for the lithium-ion cell.

1.1. Contributions

In this article, a model-based health-aware fast charging strategy is developed to mitigate the risk of non-linear aging during the operation of lithium-ion cells. Thereby, the shortest physically possible charging times from 10% to 80% SOC over a wide temperature range is targeted to allow for BEV operation. The parameter of the utilized model can be identified comprehensively from electrode to cell level, thus enabling a fast transfer to any lithium-ion cell design and chemistry. The developed strategy is deployed in real-time with a commercial lithium-ion cell at a moderate and a low ambient temperature of 20 °C and 0 °C, respectively. The model is continuously updated with the actual SOC, T, and SOH of the lithium-ion cell to reveal the strategy's impact on the cycle life. Furthermore, this study seeks to understand the barriers for applying a model-based fast charging strategy, supporting its transfer from theory and simulation to a real-world environment. The contributions of this study can be summarized as follows:

- **Development of a model-based health-aware fast charging strategy operating in real-time sensitive to the relevant states**
  An electrochemical ROM is utilized to derive a health-aware fast charging strategy, mitigating the risk for lithium plating and adapting to the actual lithium-ion cell states (SOC, T, SOH). This allows for the reduction of the charging time compared to the cell manufacturer's datasheet while enabling safe fast charging under varying operating conditions.
- **Application of the fast charging strategy from theory to a practical implementation in cell-level tests**
  The model and its implementation for a commercial SiC/NCA lithium-ion cell is outlined, a feedback control loop is developed, control parameters are identified, and cell tests are performed.
- **Extensive cycle life results and aging analysis**
  The developed fast charging strategy is deployed in extensive cycle life tests partly over 1500 cycles and compared to conventional constant current (CC) fast charging. Capacity and resistance tracking, differential voltage analysis (DVA), and *post-mortem* investigation of pristine and aged electrodes of the cycled lithium-ion cells via SEM and EDX are performed to evaluate the results.

1.2. Layout

Section 2 provides a basic understanding of the trigger conditions for non-linear aging of lithium-ion batteries from the literature. The deployed electrochemical model and derived fast charging strategy are presented in Section 3, including methods for successful ROM deployment. In Section 4, the experimental setup for the aging study is presented and the overall aging campaign is outlined. The results of the long-term aging study are presented and discussed from Section 5 to Section 7. The conclusions of this study are summarized in Section 8.

2. Fundamentals

In general, commercial automotive-grade lithium-ion cells use carbon-based intercalation anodes, predominantly made from natural and synthetic graphite due their cost-effectiveness and the comparably high specific energy enabled by the high specific capacity and the low electrochemical potential [43]. If the charging current is too high, lithium ions accumulate at the anode's surface, which leads to a drop of the potential below 0 V vs. Li/Li+, thermodynamically favoring the malicious side reaction of metallic lithium Li^0 deposition at the anode surface [44,45], well-known as *lithium plating* [46]. Despite the possibility of partly reversing this reaction by a subsequent discharge [47], deposits may further passivate against the electrolyte, form irreversible lithium deposits [26], and foster severe gassing [48], leading to accelerated capacity fade, resistance increase, and early non-linear failure of the lithium-ion cell [49]. Even though the charging current of some lithium-ion cells may be limited by maximum temperatures and thermal degradation mechanisms (such as electrolyte decomposition or gassing [50]) in the first early cycles, lithium plating can be the dominant aging mechanism at a later stage of the cycle life due to secondary solid electrolyte interphase (SEI) growth [51,52]. Therefore, thermal effects play an important role during repetitive fast charging. High thermal losses have to be countered by an active thermal management system, but the parasitic heat cannot be removed fast enough in practice. High temperatures foster SEI growth in the lithium-ion cell, consuming available lithium and consequently leading to capacity fade and resistance increase [53]. The accelerated SEI growth may in turn increase the likelihood of lithium plating because transport kinetics are reduced, which amplifies overpotentials [54,55]. In sum, the lithium plating and SEI growth mechanisms mainly depend on three operating parameters of the lithium-ion cell, as shown in Fig. 1, which must be controlled during fast charging:

- **State of charge (SOC)**
  The SOC of the anode directly affects the fast charge capability of the lithium-ion cell, as the anode potential is a function of the SOC. With increasing lithiation of the anode, the open-circuit

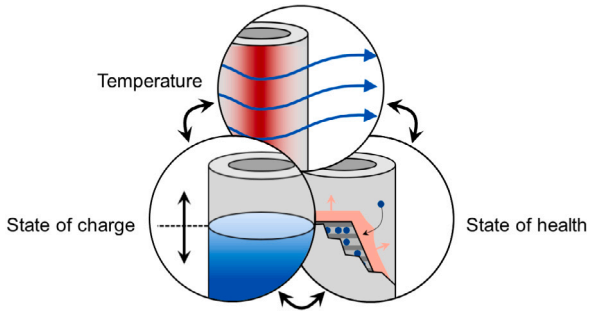

Fig. 1. Factors influencing the fast charging capability of graphite-based lithium-ion cells. All factors are complex by their nature, interdependent, and require thorough consideration if fast charging strategies are developed.

potential vs. Li/Li+ is steadily lowered, increasing the likelihood of falling below the critical threshold of 0 V vs. Li/Li+ during charging. Moreover, the impedance also increases due to the lowered diffusion at larger SOC [56,57], in turn increasing the overpotential and likelihood for undercutting the threshold potential. From a thermal perspective, the SOC directly exacerbates thermal aging conditions because the cell's heat rate also depends on the impedance, which is larger at low and high SOC.

- **Temperature (T)**
  The lithium-ion cell temperature influences the charging capability during operation. An elevated temperature decreases the anode impedance and the anode overpotential, reducing the risk of lithium plating while accelerating thermal-driven side reactions, which raises the SEI growth rate [58]. In addition, elevated temperatures reduce the lithium-ion cell's impedance and, following $P = R \cdot I^2$, the resulting power losses, which could be beneficial during fast charging [59,60]. However, critical thermal thresholds should be maintained to avoid intolerable high peak temperatures. On the other hand, lower temperatures are harmful from both a lithium plating and thermal management standpoint. The lowered kinetics within lithium-ion cells at low to subzero temperatures lead to increasing resistance, fostering overpotentials, and consequently lithium plating, as well as larger power losses, which lead to faster local self-heating without the ability to dissipate the heat quickly enough in actively thermally-managed environments.
- **State of health (SOH)**
  The SOH, as a function of the rising internal resistance R (SOH_R) and/or declining capacity Q (SOH_C), inhibits the fast charging capability of the cell or system over time. While previous studies pointed out that the fast charging capability depends on the different aging mechanisms and may equalize over time (mechanical fractures may enhance the anode surface and the intercalation kinetics, while SEI growth slows down intercalation kinetics) [27,61], other recent studies showed that an SOH-based current derating may prolong battery life [25,55,62,63]. The intrinsic SEI thickness growth during lithium-ion cell operation increases the anode overpotential, elevating the risk of lithium plating, which may provoke the onset of non-linear aging [51,54]. Furthermore, a more pronounced SEI increases the resistance over time, leading to higher power losses of the lithium-ion cells. As the lithium-ion cell ages, peak temperatures may rise and self-reinforce thermal side reactions during operation.

Following this argumentation, all three conditions have a major impact on the fast charge capability of the lithium-ion cell or system at multiple levels and are directly coupled to the two aging mechanisms, lithium plating and SEI growth, which makes it a tremendously complex problem to control during operation from a practical battery management perspective. An optimal fast charging strategy should respond to the changes of those parameters during operation to prolong the cycle life of the lithium-ion cells.

3. Development of the fast charging strategy

To take into account the aforementioned states of the lithium-ion cell or system during fast charging control and be able to adapt to different cell designs and materials, we first need to develop a capable model and empower it to run in a real-world experimental setup. Subsequently, a health-aware fast charging strategy is derived, i.e., controlling the current based on model states during the fast charging event regularly updated over lifetime.

3.1. Lithium-ion cell under study

All tests are performed with commercial weld-sealed 18650 lithium-ion cells from Sony/Murata with a nickel-rich NCA cathode, a silicon-doped graphite anode, and liquid electrolyte with unknown composition. The identified characteristic properties of the lithium-ion cell can be found in Table 1 and are partly derived from a previous teardown study of the cell by the authors [64]. The cells have a rated capacity of 2.5 Ah, which translates to a rated areal capacity of 2.4 mAh/cm^2. The gravimetric energy density is 191 Wh/kg.

The lithium-ion cell has been chosen as a representative candidate for fast-charged battery packs, as it provides a large charge power at a relatively large capacity compared to other commercial lithium-ion cells. NCA as the cathode material has been seen to be more robust against harsh charging conditions compared to its frequently used counterpart nickel-rich NMC [65]. This has led to extraordinary cycle life performance at high current rates [66]. Also, the rather large rated capacity while also achieving a high power capability is realized by adding silicon oxide (SiO_x) particles to the graphite anode (referred to as SiC), which has been increasingly added to pure graphite anodes in the past because it provides a high specific capacity in comparison to graphite (3579 mAh/g compared to 372 mAh/g) [67]. Therefore, it has the ability to compensate for negative effects on the cell's energy density of more power-oriented electrode designs. However, it also suffers under extreme mechanical stress during charging by a particle volume expansion of up to 400% [68], leading to severe aging if not properly controlled, which has to be countered by the operating voltage window [69].

3.2. Electrochemical model of reduced order

To mitigate the risk of critical aging mechanisms, such as the onset of lithium plating, the deployed model must be able to accurately predict the anode potential. The procedure to obtain such a type of model and validate it within the operating temperature range was presented in a previous study by the authors [70]. This model is based on the original developed reduced-order P2D model, well-known as the single particle model (SPM), provided as open source by Moura et al. [71] and Perez et al. [72]. For the sake of brevity, the reader is referred to the aforementioned publications for further details. Note that only the heat capacity and heat transfer coefficient have been changed to 986 $J K^{-1}$ and 0.0306 W/(mK), respectively, as an average of obtained literature values for cells of 18650 format.

3.3. Model deployment and discretization

The computationally complex lithium-ion cell model has to be simplified and discretized with a user-defined resolution so that it can predict the battery states in a specified time span without losing too much accuracy. Five quantities have to be defined before usage of the model, that is, the particle discretization (anode/cathode) in the radial direction and the layer discretization (anode/separator/cathode) in the

Table 1
Specifications of the commercial lithium-ion cell under study.

Property	Value	Unit
Manufacturer	Sony / Murata	–
Type	US18650VTC5A	–
Launch year	2017	–
Format	18650	–
Anode material	SiC	–
Cathode material	NCA	–
Rated capacity	2.5	Ah
Voltage bounds	2.5–4.2	V
Weight	47.1	g
Max. charge current (20 °C)	6.0	A
Max. discharge current (20 °C)	35.0	A

spatial direction. In this study, the radial dimension of the anode and cathode particles is referred to as one radial particle discretization Δ_r and the spatial dimension of the three layers is referred to as one spatial particle discretization Δ_x. The best compromise is hard to find, as the model behavior depends on many operating conditions which cannot be practically covered. To assess the trade-off between model complexity and accuracy, we performed an analysis of the achievable accuracy in terms of voltage for a 1C CC charge by calculating the root mean squared error (RMSE) against (1) a validation measurement and (2) a simulation with high fidelity, i.e., 30 finite elements in radial and spatial direction. The results of the simulations are shown in Appendix A. In this study and for the investigated lithium-ion cell, a good trade-off appeared at a radial particle discretization of 20 elements and a spatial discretization of 10 elements for the anode, separator, and cathode. The separator had been set to 5 elements only, as the effect on the error metric was only small, which is not illustrated for the sake of brevity.

Usually, the deployment of electrochemical models for advanced battery management is avoided due to the fact that electrochemical models inherit a great deal of computational complexity. For our given case, the major limitation in solving the partial differential equations (PDEs) of ROMs lies in numerical solutions and iterative methods to solve the posed problem, such as the use of finite element methods and the Runge–Kutta method [73], which is not deterministic and, consequently, not capable for real-time environments. During model operation, large computational threads, which did not lead to a solution in time, could be effectively managed by initializing the model iteratively with the measured states and only predicting the next time interval. Even if the previous attempt to solve the given problem did not lead to a solution, the hard termination of the calculation and new initialization of the model with its previous values helped to avoid any runtime issues. Thus, the given solution time was set to a small value (Δt =100 ms), reducing the impact of the system dynamics during a charge sequence. This could be a beneficial error handling approach in real-world applications, rebutting the long-standing argument that real-time application of electrochemical models inheriting PDEs and numerical solvers are impossible to realize in practice. With the rise of central control unit architectures in electrical systems of modern BEVs, the required high computational power may also be available in the future, as many computationally intensive control units are idle during a fast charging event (e.g., driving assistance systems).

3.4. Anode potential control

Previous studies demonstrated that inaccuracies may appear during the runtime of model-based fast charging strategies, emphasizing the need for an anode potential control above the threshold of 0 mV [40,62]. Therefore, we define the anode potential reserve ϕ^-_{limit} as the control input parameter. To derive an appropriate anode potential reserve, three major error sources appear in our approach, namely

- a model error ε_{ROM},
- a measurement error $\varepsilon_{\text{I/U}}$, and
- a controller error ε_{PID}.

The model error ε_{ROM} arises because the ROM is not able to perfectly match the reality and is further discretized to a level that inherits a certain degree of inaccuracy to find a good compromise with the computational complexity. This error component is difficult to practically quantify, as it is neither observable nor measurable. In our previous study [74], we performed a broad validation of the model and quantified the maximum absolute error under constant current charge sequences at the full cell level. Based on the results, a maximum allowable current I_{limit} is set to remain within the validation range with reasonable accuracy and the model error is set to the maximum absolute error occurring during the charge sequence from 10 to 80% SOC, e.g., 45 mV for 6C at 20 °C ambient temperature and likewise for 4C at 0 °C ambient temperature. The second error component, the measurement error $\varepsilon_{\text{I/U}}$, is mainly caused by inaccurate current measurements (commonly up to 50 mA in lab environments at cell level) which influences the SOC determination due to the deployed Ah-counter. To assess the error, we simulated the attained SOC for fast charging from 10% SOC under a CC measurement offset of 50 mA as the worst case. The current offset led to a capacity deviation of 45 mAh or 1.8 % SOC. By transferring the results to the anode potential control, an error of approximately 15 mV occurred compared to the reference, which is set as the measurement error $\varepsilon_{\text{I/U}}$ for the downstream deployment of the model. Pretests revealed that the anode potential controller overshoot ε_{PID} led to an error of approximately 5 mV during runtime. In total, the anode potential reserve is set to 70 mV as an appropriate limit to account for the inherited inaccuracies in this study. The overall closed-loop current control is illustrated in Fig. 2. Note that in more sophisticated environments with inaccurate initial conditions, further closed-loop control structures can be embedded to increase the accuracy of the model (e.g., SOC observer [75]).

3.5. Health awareness

A coupled current derating over time involving both the capacity decay and the internal resistance rise is of utmost importance to maintain cycle life during repetitive fast charging [25,55,62,63]. However, aging mechanisms are known to have complex origins [76,77], which are hard to track down in real-world applications. For example, fading electrolyte performance is a well-known issue during fast charging [78] but hard to quantify during the cycle life [79]. We seek a simplification to link the SOH, commonly determined online for the capacity and the internal resistance by the battery management system (BMS), to a physically motivated adjustment of the electrochemical model at hand. The model adjustments are then expected to lead to a more

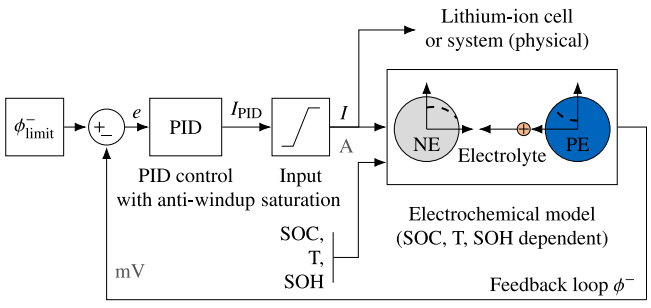

Fig. 2. Control loop structure of the health-aware fast charging strategy. PID controller parameters are set to P=0.05, I=0.05, and D=0.001 and adjusted over time to follow the changing system dynamics. The input current I is limited to I_{limit}, which is why an anti-windup control method is used to quickly follow the anode potential reserve signal.

conservative fast charging current control with increasing lithium-ion cell cycle life.

The capacity decay over time is considered by adjusting the cell capacity over time. To do so, we compute the capacity-related SOH, SOH_C, by evaluating the actual capacity Q of the lithium-ion cell relative to its initial capacity $Q_{initial}$ in a 1C constant current constant voltage (CCCV) discharge sequence according to

$$SOH_C = \min\left(\frac{Q_{1C,CCCV}}{Q_{initial}}, 1\right). \quad (1)$$

Here, we additionally ensure that the capacity is reduced over time by limiting the factor to an upper limit of 1. The degradation factor SOH_C is used to lower the initial capacity

$$Q = Q_{initial} \cdot SOH_C. \quad (2)$$

The adjusted capacity leads to a larger current density and an earlier reach of high SOC regions in the model. As the lithium-ion cell capacity is composed of the individual cell electrode capacities, we assume that the simplification of a likewise decreasing individual electrode capacity holds. It should be noted that this assumption may not be true in practice, but allows for the most practicable solution, as the online determination of accurate OCV curves is still being investigated by many researchers [80,81] and also the individual electrodes and their open-circuit potentials may change more drastically over time and different operating conditions than commonly expected [82,83].

The rise of resistance over time is linked to the SEI overpotential η_{SEI} of the model. Therefore, the pulse resistance $R_{\Delta t=10s}$ is computed by evaluating the voltage drop of a 1C pulse in the charge direction over 10 s according to

$$R_{\Delta t=10s} = \frac{U_{t=0} - U_{t=10s}}{I_{1C}}. \quad (3)$$

The pulse resistance is calculated at 20%, 50%, and 80% SOC. The maximum change relative to the initial value at the given SOC stage is then computed to a resistance-related SOH, SOH_R, as

$$SOH_R = \max\left(\frac{R_{\Delta t=10s}}{R_{initial}}, 1\right), \quad (4)$$

and it is also ensured that only a larger scaling is used even though the resistance may drop under specific conditions, as we do not want to yield faster charging times as initially expected. Subsequently, the degradation factor SOH_R is applied to the model by likewise increasing the SEI resistance R_{SEI} proportionally according to

$$R_{SEI} = R_{SEI,initial} \cdot SOH_R. \quad (5)$$

The gradual increase in the SEI resistance leads to an earlier control of the charging current over the cycle count of the lithium-ion cell. Note that both the change of capacity and impedance were computed in the RPT in this study (cf. Section 4.3) and can be substituted with an online SOH estimation algorithm [84,85] for more sophisticated applications.

3.6. Fast charging control strategy

Fig. 3 shows the resulting health-aware fast charging strategy at 20 °C ambient temperature. The lithium-ion cell is fast charged between 10% and 80% SOC, because it has been reported that low operating voltages (low lithiation stages of the SiC anode) may lead to severe aging due to rapid volume expansion [69] and should be avoided. Also, the used model reached large errors due to the strong hysteresis behavior of the cell, which may be also traced back to the different lithiation speeds of silicon and graphite at low SOC [67]. Furthermore, the charging current is initially limited to 15 A to account for the model validation boundary as discussed earlier and also to avoid excessive inhomogeneous heat generation in the lithium-ion cell. After approximately 40% SOC, the fast charging current of the pristine cell is controlled to the anode potential reserve limit, which

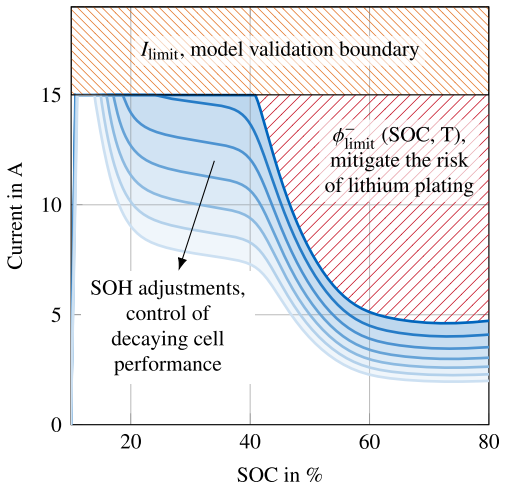

Fig. 3. Simulated fast charging current over time for the model-based health-aware fast charging at 20 °C ambient temperature.

results in a continuous current derating depending on the SOC and core temperature of the lithium-ion cell. Strictly speaking, we apply a constant current constant anode potential (CCCA) control with a real-time electrochemical model and regular SOH updates. The transition to anode potential control is reached at lower SOCs with progressive aging due to the regular model updates with the SOH (capacity and resistance) accounting for the decaying lithium-ion cell fast charging capability.

4. Experimental

In the following, the lithium-ion cell under study, the experimental test setup, and model deployment framework, as well as the test procedures used for the aging experiment are introduced.

4.1. Test setup

For the experiments, the lithium-ion cells were connected to an *XCTS50* battery cycler (BaSyTec GmbH, Germany) for cycling and connected to a *CTS* battery cycler (BaSyTec GmbH, Germany) for reference performance tests (RPTs). All tests were performed at controlled ambient temperatures within a *VC3-4100* thermal chamber (Weiss Technik GmbH, Germany) for 20 °C and a *KB400* thermal chamber (Binder GmbH, Germany) for 0 °C experiments. The experimental setup is illustrated in Appendix B.

As real-time control of the charging current is required and conventional battery cyclers usually do not provide an internal programming logic for state-dependent control of the charging current, we extended the setup with a microcontroller unit (MCU). The MCU directly communicates with the battery cycler via a controlled area network (CAN) and serves as a proxy for a battery management system (BMS). Prior to each fast charge sequence, the cycler provides the initial battery states to the MCU. During the fast charge sequence, the actual current I_k is also provided. An additional temperature sensor on the cell surface is used and connected to the MCU to enhance the temperature monitoring capabilities. All aforementioned quantities serve as model input to predict the anode potential ϕ_k. Subsequently, a PID controller adjusts the current for the next time step based on a predefined anode potential reserve ϕ^-_{limit}. The PID controller output is then limited to a predefined maximum charging current I_{max}. Also, the PID integrator is clamped for anti-windup control. The result is sent back to the battery cycler control unit. The overall procedure is repeated each 100 ms, which therefore limits the model execution and test bench communication time accordingly.

Table 2
Comparison of the parameter set used for fast charging current control of the investigated aging campaigns within the scope of this study.

Campaign #1: 20 °C ambient temperature				
	CCCA charging	CC charging		
CC		2.5 A	6 A	10 A
CV		4.2 V	4.2 V	4.2 V
I_{limit}	15 A			
ϕ^{-}_{limit}	70 mV			
SOH update	50 cyc.	50 cyc.	50 cyc.	50 cyc.
Until 60% SOH or 1500 cycles				
Campaign #2: 0 °C ambient temperature				
	CCCA charging	CC charging		
CC		1 A	2 A	8 A
CV		4.2 V	4.2 V	4.2 V
I_{limit}	10 A			
ϕ^{-}_{limit}	70 mV			
SOH update	50 cyc.	50 cyc.	50 cyc.	50 cyc.
Until 60% SOH or 1000 cycles				

4.2. Lithium plating pretests

Prior to the aging experiments, the lithium-ion cell under study was subjected to repeated charge current pulses to investigate the sensitivity to lithium deposition under different conditions, similar to a previous study in the literature [86]. After a charge current pulse excitation of rising amplitude, a relaxation sequence was applied to track down the mixed potential of the reintercalation reaction after the onset of lithium plating. A pristine and an arbitrarily aged Sony/Murata cell were subjected to rising current pulses between 0–75% SOC at 0 °C. In order to evaluate and compare the results, a high-energy reference lithium-ion cell INR18650-35E from Samsung SDI was similarly subjected to rising current pulse excitations; however, between a narrower charge window of 30–45% SOC, as lithium plating is expected to occur earlier.

4.3. Aging campaigns and test procedures

Three aging campaigns at 20 °C and 0 °C ambient temperature were performed, as summarized in Table 2. At each temperature level, health-aware fast charging strategies with anode potential reserve and SOH derating were applied to the lithium-ion cell under study and the lithium-ion cells were cycled until a remaining capacity of 60 % or a temperature-specific cycle limit. Likewise, conventional CC charging strategies with the manufacturer's recommended current, the manufacturer's maximum current, and a fast charging current reaching comparable charging times as the health-aware fast charging strategy were applied. Each test was performed with two individual cells of the same batch to hedge against misinterpretations due to cell manufacturing defects or unintended experimental coincidences during the cycle life test. The aging campaigns were carried out with the same test procedure except for the fast charge sequence. All lithium-ion cells were initially subjected to a RPT at 20 °C ambient temperature and subsequently cycled 50 times with the given test procedure at the given ambient temperature level of the aging campaign. The overall procedure is shown and elaborated in more detail in Appendix C.

4.3.1. Post-mortem cell investigation

Since non-invasive methods lack the ability to provide ground truth indications of the occuring aging mechanisms, we further assessed the aging mechanisms by subjecting selected cells to a *post-mortem* visual analysis. Therefore, the cells were discharged to 2.5 V. Subsequently, the cells were transferred to a glove-box (GS MEGA E-LINE, GS Glovebox, Germany) under argon atmosphere (H20 < 1 ppm, CO2 < 1 ppm) and the electrodes were harvested by a careful teardown of the lithium-ion cells similar to previous studies [64]. Camera images of the electrode strips were then taken and samples were cut out from the electrode areas formerly located at the edge and core position of the electrode coil. The samples were transferred to a dry room within an airtight container and placed into a SEM (IT-200, JEOL, Germany) for a qualitative assessment of the electrode surfaces. Additionally, selected samples were subjected to an elemental analysis via the EDX module of the SEM. The results were used to judge the aging mechanism by comparison to the electrode surfaces of a pristine cell.

5. Aging study

The lithium-ion cell under study was pretested for lithium plating sensitivity and cycled over 12 months in total partially achieving over 1500 cycles to compare the developed model-based health-aware fast charging strategy to the CC charging reference control with a special focus on the dilemma of charging speed versus cycle life.

5.1. Pretest to determine the sensitivity to lithium plating

Fig. 4 shows the results of a lithium plating current pulse pretest. As a reference, the voltage relaxation subsequent to an increasing current excitation of a high-energy lithium-ion cell is presented in Fig. 4(a)/(b). At a charging pulse of 2C over a narrow SOC range of only 30–45% SOC, the first voltage plateaus can be seen during relaxation, indicating the intercalation of reversible lithium deposits originating from previous lithium plating at the anode surface. In comparison, the pristine high-power lithium-ion cell does not show any indication of malicious lithium plating under harsh conditions, i.e., high current excitation and 0 °C ambient temperature, as shown in Fig. 4(c)/(d). However, if the high-power lithium-ion cell is aged down to 80% SOH_C, the voltage relaxation signal shows a voltage plateau at the beginning of the relaxation sequence, similar to that of the high-energy lithium-ion cell. Progressing age may, therefore, lead to the occurrence of lithium deposits at a later stage of operational service life, resulting in non-linear aging and a fast failure of the overall lithium-ion battery pack. As a consequence, fast charging algorithms must avoid any abuse over the complete lifetime of the lithium-ion cell if graphite-based anodes are deployed, independent of the cell design or cathode active material used.

5.2. Charging time comparison

Charging times slightly differ between the constant current constant anode potential (CCCA) controlled and the constant current (CC) controlled fast charging strategies. Starting from 10% SOC, the SOC increases faster with the CCCA fast charging strategy compared to the CC fast charging strategies until approximately 40% SOC as the adjusted CC limit lies above the CC limit of the reference strategies. The anode potential reserve limit leads to an initial CC control of the health-aware strategies because the high open-circuit potential of the anode at low SOC allows for high charging currents. After that inflection point, anode potential control is utilized and successively derates the charging current over SOC. It should be noted that the inflection point for the transition from the CC current limit to the anode potential control is reached earlier with decreasing temperature; however, in this study, the CC limit has been adjusted from 15 A to 10 A for the low ambient temperature scenario to account for lower model validity at lower ambient temperatures, resulting in a similar location of the inflection point.

Table 3 gives further comparison of the charging times of the health-aware fast charging strategy to the maximum charging current suggested by the cell manufacturer. Hereby, the strategy drastically reduces the charging time at partial charging to 80% SOC. The manufacturer conservatively limits the fast charging current, especially at low ambient temperature, increasing the charging time benefit of the health-aware fast charging strategy.

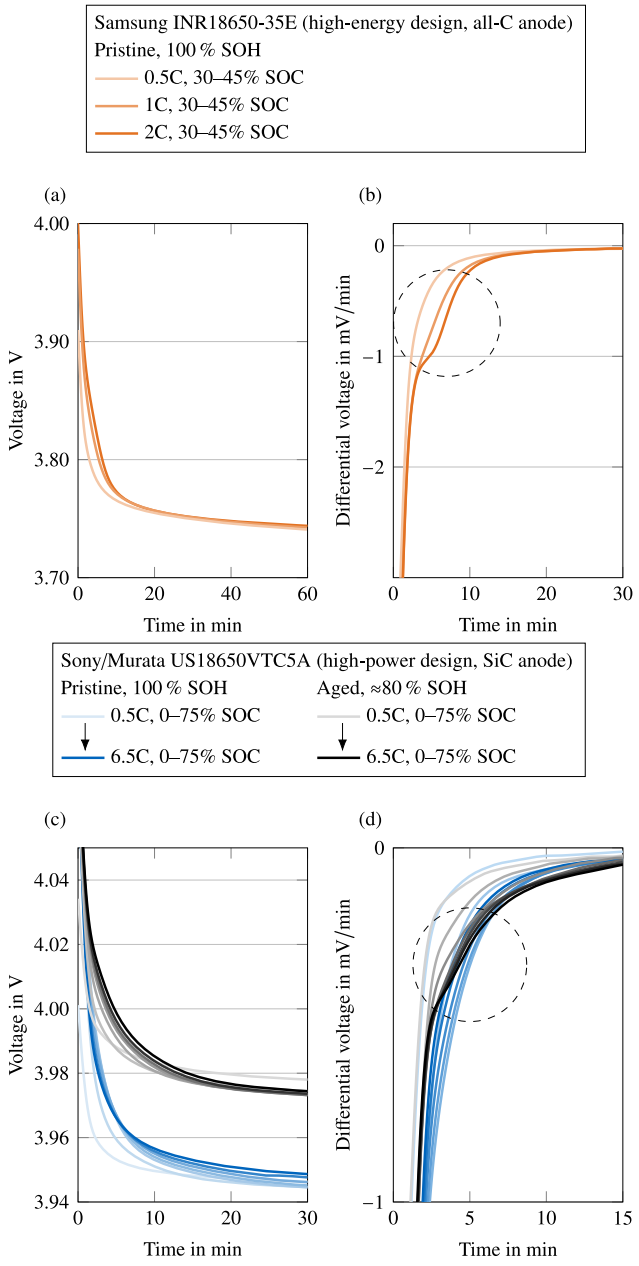

Fig. 4. Pretests for determination of the lithium deposition sensitivity. Charge current excitations are applied to different lithium-ion cells with a minimum subsequent relaxation period of 15 min at 0 °C ambient temperature. (a)/(b) a Samsung INR18650-35E 3.5 Ah as a high-energy reference, and (c)/(d) pristine Sony/Murata US18650VTC5 A compared to an aged Sony/Murata US18650VTC5 A with 80% SOH. Indications of prior lithium plating in the voltage relaxation signal are marked with dashed circles.

5.3. Cycle life

During operation, elevated ambient temperatures are commonly present during fast charging because the battery pack heats up during the prior discharge [87]. Besides moderate ambient temperatures, initial low ambient temperatures may also occur during a fast charging event, e.g., when starting BEVs from subzero temperatures or a rather low SOC with insufficient discharge time for enough thermal preconditioning of the lithium-ion cells. Commonly, the fast charging current is strictly limited in those scenarios, as the aging impact of larger currents

Table 3
Comparison of initial charging times to different SOCs (ΔSOC) of the health-aware fast charging and CC reference charging strategy with the maximum charging current taken from the manufacturer datasheet.

Temperature	ΔSOC	CCCA I_{lim}=10 A / Φ_{lim}=70 mV	CC 2 A datasheet limit
0 °C	10–50%	6.5 min. (–78%)	30.2 min.
	10–60%	9.7 min. (–74%)	37.7 min.
	10–70%	13.5 min. (–70%)	45.3 min.
	10–80%	17.4 min. (–67%)	52.8 min.
Temperature	ΔSOC	CCCA I_{lim}=15 A / Φ_{lim}=70 mV	CC 6 A datasheet limit
20 °C	10–50%	4.3 min. (–57%)	10.1 min.
	10–60%	6.7 min. (–47%)	12.6 min.
	10–70%	9.6 min. (–36%)	15.1 min.
	10–80%	12.6 min. (–28%)	17.6 min.

is not well understood. The results of the aging study at 20 °C and 0 °C are shown in Fig. 5.

With a closer look at the normalized capacity retention and resistance increase in Fig. 5(a)–(b), all strategies lead to a fast capacity and resistance decay. The observations can be explained by ongoing SEI formation due to its micro-cracking. SEI fracturing is a well-known issue with graphite-based lithium-ion cells [88,89], especially when larger shares of strongly expanding silicon particles are used to increase the energy density [90]. During cycling, the active material of the lithium-ion cell undergoes strong mechanical disturbances during intercalation of the lithium ions, particularly for the stage two phase of the graphite of the lithium-ion cell under study [91]. During this process, volume expansion leads to particle cracks, which expose fresh graphite to the electrolyte, subsequently leading to irreversible consumption of available lithium ions due to additional SEI growth. From a phenomenological perspective, the secondary SEI formation leads to a fast capacity fade due to the consumption of lithium inventory, but also a decrease in impedance due to the greater electrode surface. In particular, this can be seen for the cells cycled at low ambient temperature, where the internal resistance initially drops below the initial resistance, as the competition with the SEI thickness increase is assumed to be slower than the growth of secondary SEI at the exposed surface.

Beyond this first stage, the health-aware fast charging strategy follows a fast capacity decay in the following 200 cycles comparable to that of the CC fast charging strategy. A possible explanation is that the lithium-ion cells underwent high temperatures during cycling with both strategies, as the moderate ambient temperature allowed for large initial charging currents, resulting in high heat rates within the cell. Following this argument, an earlier deviation can be seen for cycling at lower ambient temperatures. This observation can be supported if the average (Fig. 5(c)) and peak (Fig. 5(d)) temperatures of the lithium-ion cells are analyzed. While the average temperature of the health-aware fast charging strategy is comparable to the average temperature of the 10 A CC reference in the first 200 cycles, the peak temperature reaches significantly lower values at 20 °C ambient temperature cycling. This can be contributed to the initially larger current of 15 A in the health-aware fast charging strategy leading to a faster heat rate at the beginning of the fast charging event, which allows for a more efficient charge sequence in the later course. Similar results are obtained at low ambient temperature. As different fast charging strategies are usually optimized to the energy efficiency in the literature, we hereby provide evidence that a fast charging strategy controlling the anode potential to a limit synchronously leads to a more efficient fast charging event due to the rapid heat-up of the lithium-ion cells.

Later in the progress, the capacity decay and impedance growth are decelerated for the health-aware fast charging strategy, as the continuous model update at every 50 cycles leads to an active derating of the charging current. This is further visible in the capacity decay rate

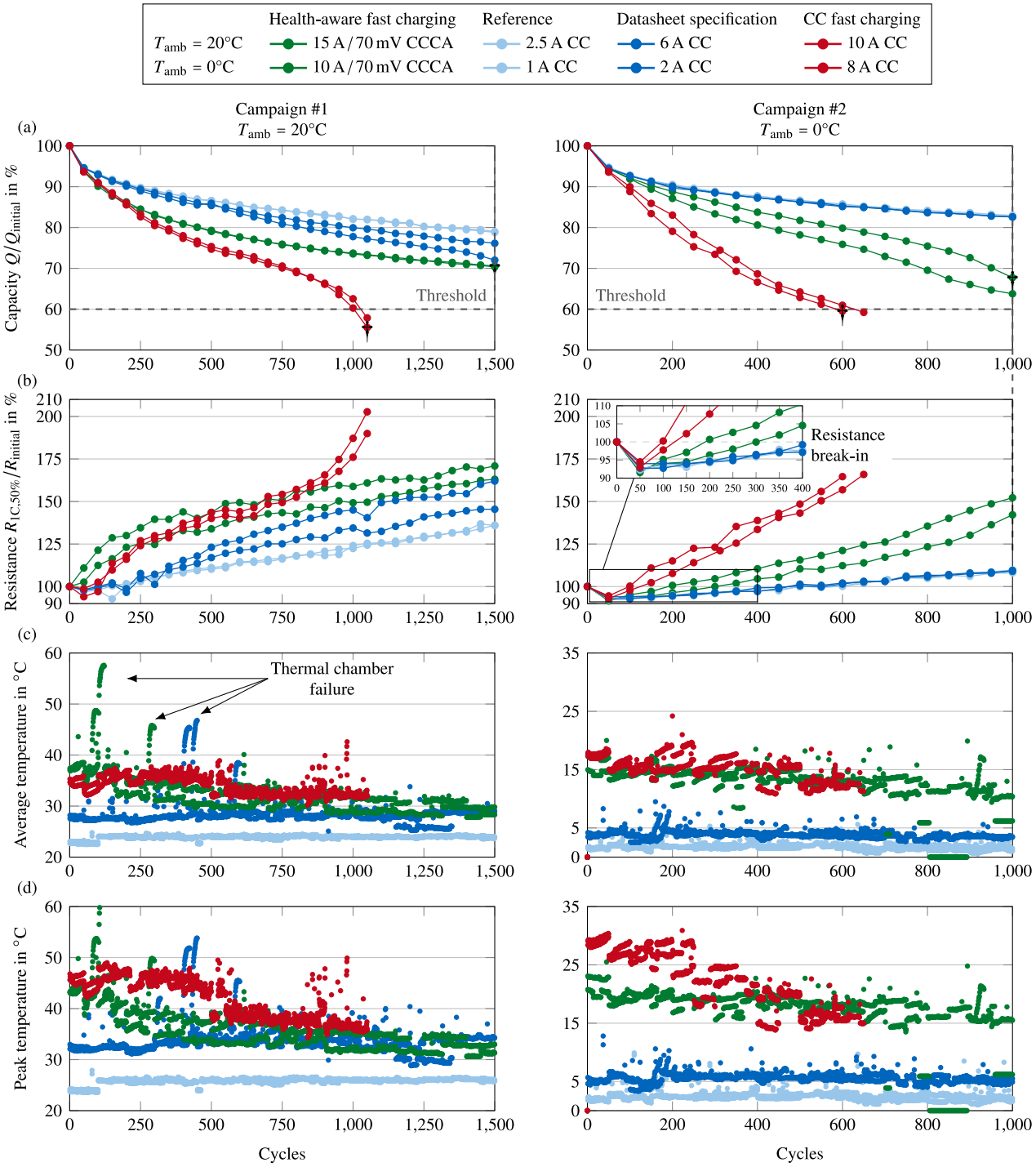

Fig. 5. Results of the aging campaigns for the fast charging strategies compared to manufacturer specifications at 20 °C and 0 °C ambient temperature. (a) Normalized capacity retention over cycles. (b) Pulse resistances at 50 % SOC over cycles. (c) Average cell temperatures and (d) peak cell temperatures during the fast charging sequence over cycles. Abnormal peaks in (c) and (d) are due to thermal chamber failures. Cells selected for post-mortem investigations are marked with †.

converging to the slow charging 2.5 A CC reference in the later course. Interestingly, the cells fast charged with the CC strategy reach a turning point at around 850 cycles at 20 °C ambient temperature, when the onset of nonlinear aging appeared and led to an early failure of these cells. The yielded cyclic aging rate of approximately 5% capacity loss over 50 cycles is constantly reached at 0 °C, which may indicate that a similar aging mechanism is contributing to the aging from the start. These results highlight the need for fast charging strategies adaptive to the SOH of the cells to prolong the cycle life, as fast charging capability is hampered over the operational life.

6. Differential voltage analysis

Differential voltage analysis (DVA) is a powerful tool to trace back the aging mechanism at cell level to the individual electrodes without the need for invasive techniques and *post-mortem* investigations during the runtime of the study. Hereby, the voltage signal U of a charge sequence with a low charging current (i.e., C/20) is differentiated from the charge throughput, following

$$DV = \frac{dU}{dQ} = \frac{dU}{dt} \cdot \frac{dt}{dQ} = \frac{dU}{dt} \cdot I^{-1}, \tag{6}$$

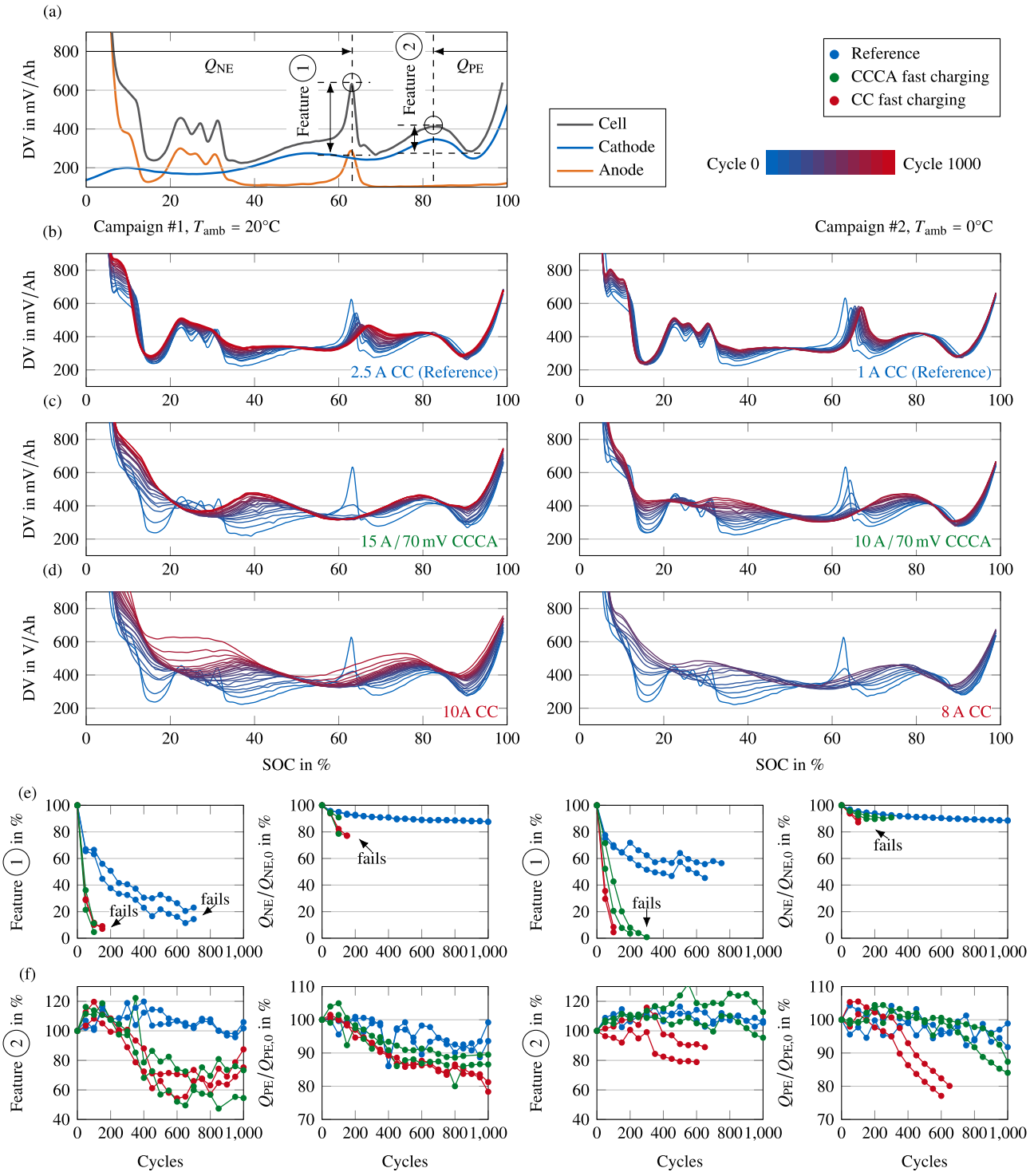

Fig. 6. Differential voltage analysis (DVA) of the fast charging strategies compared to the reference charging strategy at 20 °C ambient temperature (left) and 0 °C ambient temperature (right) for the first 1000 cycles. (a) Differential voltages (DVs) of a pristine cell including the differential electrode potentials to guide the reader's eye. DVs for (b) reference charging, (c) health-aware fast charging, and (d) CCCV fast charging. (e)–(f) Normalized feature evolutions to their initial value over cycles.

similar to the method presented by Bloom et al. [92,93] and Lewerenz et al. [94]. This reveals characteristic features in the voltage curve, which can be assigned to characteristic features of the individual electrodes, as illustrated in Fig. 6(a). With further analysis, decaying electrode capacities can be analytically evaluated.

Fig. 6 shows the DVAs of the CC reference, the CC fast charging, and the health-aware CCCA strategy of both aging campaigns for further analysis of the dominant aging mechanism. With respect to the individual open-circuit potentials of the electrodes in Fig. 6(a), individual features in the C/20 charge sequence can be attributed to either the anode (cf. ①) or the cathode (cf. ②). The height of these features has been reported as an indicator of inhomogeneous aging of the electrodes [94,95], which is why it is also used within this study normalized to a close minimum in the voltage trace (cf. arrows in Fig. 6(a)). Moreover, the change in the electrode capacities is evaluated by determining the normalized change in capacity with respect to the lithium-ion cell boundaries.

The differential voltages are illustrated in Fig. 6(b)–(d) and the evaluated features in Fig. 6(e)–(f). While feature ① slowly moves to higher SOC stages for the slow charging CC references and the remaining features showed almost no change over the cycle life, both fast charging strategies showed significant changes in the general slope. Feature ① completely vanished after 100 cycles (denoted by 'fails'), which has been also reported in previous studies, in which it has been seen as an indication of the occurring electrolyte decomposition due to cycling [96] and inhomogeneous aging [61,94]. This supports the previous observation of the initial fast capacity decay, originating from the expected strong volume expansion and micro-fractures due to the silicon content and high charging currents. This in turn leads to the lithium ions following different diffusion pathway lengths and resulting in a prominent manifestation of heterogeneity in the negative electrode. Another possible origin for the large detected inhomogeneity may lie in the cylindrical cell design. A steep thermal gradient within the cell may foster degradation and electrolyte decomposition in the cell core compared to the outer cell areas. The issue of the rapidly vanishing anode characteristics is discussed in the *post-mortem* analysis of the cells (cf. Section 7).

While the health-aware CCCA strategy seemed to be dominated by similar aging mechanisms as the CC fast charging strategy, the overall capacity decay was faster for the latter. A possible reason may be the combined fade of anode and cathode capacities until the onset of non-linear aging, which is generally larger for the CC fast charging strategy. Also, the severity of anode aging may be larger, which is unfortunately not trackable due to the vanishing feature ①. The fast non-linear capacity fade starting approximately from the 1000th cycle is also visible in the differential voltage signal. During this transition, the cathode capacity remained at a similar capacity fade rate, which is why the onset of anode degradation mechanisms can be considered as a highly likely origin even though it is not directly observable. However, although the presented health-aware fast charging strategy leads to a fast capacity decay in the first stage of cycle life, it can prevent the onset of non-linear aging at a later stage of cycle life, as it continuously adapts to the fast charging capability of the lithium-ion battery.

The observed generally faster degradation of the health-aware fast charging strategy in contrast to the 2.5 A CC charging sequence provided by the manufacturer can be explained by the larger power losses and therefore higher lithium-ion cell temperatures achieved during the fast charging event, as discussed previously and as can be seen in the observed cell temperatures in Fig. 5(c)–(d). However, over 2000 cycles with a controlled capacity fade rate could be achieved above 60% capacity retention at 20 °C, which corresponds to over 2000 fast charging events or over 5 years of daily fast charging.

7. Post-mortem analysis

For a more detailed analysis of the occurring aging mechanism and for tracing back the occurrence of lithium plating, a post-mortem teardown can precisely separate anode and cathode effects and provides deep insights into the electrode aging mechanisms. Two lithium-ion cells from each the cycle life experiment at 20 °C and 0 °C (all marked with † in Fig. 5) were compared to a pristine lithium-ion cell.

Fig. 7 shows a general overview of the individual electrodes. In direct comparison to the pristine cell shown in Fig. 7(a), both the CC and CCCA cycled cells cycled at 20 °C show severe aging of the electrodes. In particular, the anode suffered under large stress where a difference was already detected during the separator extraction from the anode layer. The graphite coating was partly detached and even peeled off down to the copper current collector along the center axis of the electrode, indicating strong active material delamination. A clear difference can be seen at this stage when the CC and the CCCA cell anodes are visually compared in Fig. 7(b) and (c), respectively. Note that the CCCA cell reached 50% more cycles compared to the CC cell. With further regard to the SEM images of the anode, differences between samples of the core and edge area of the cell can be observed. Depositions on the anode layer are seen mostly for the core area, which does not visually match the morphology of lithium plating reported by studies in this field, e.g., [97], and visualized in this study for a high-energy cell in Appendix D. However, as these deposits are mostly seen for the CC cell, it can be assigned either to the missing anode potential controlled strategy or the experienced high peak charging temperatures. The deposits are further investigated later by means of EDX. Beyond, graphite particle fractures can be seen for both strategies, which align to the observed fast capacity drop for all cells at the beginning of life. The strong heterogeneity of the cells, that is, (1) between the cell core and edge area and (2) between the individual particles due to the particle cracking, may explain the quick peak diminishing within the DVA of the anode voltage traces in Section 6.

A more significant appearance of the aforementioned deposition morphology and difference between the CC and CCCA cycled cells could be seen at 0 °C ambient temperature, where a more rapid cell failure also occurred. Fig. 7(d)–(e) show the CC cell in contrast to the CCCA cell. During teardown of the CC cell, a distinct gold electrode coloring was visible (cf. 45° angle image), which is usually seen as an indication of lithium plating in the literature [98,99]. SEM images show a strong deposition layer onto the graphite anode for both the edge and core areas of the CC cell. Similar to the results obtained at 20 °C, cathode aging could barely be identified from the SEM images, which aligns with the DVA results.

In order to further investigate the identified deposits onto the anode layer, an EDX analysis was performed in these areas. As the CC cycled lithium-ion cell at 0 °C showed the largest sensitivity to the deposition reaction, an electrode image with clear deposits and visible graphite particles has been captured, as seen in Fig. 8(a). The results revealed a congruent measurement of Al- and O-traces, as it can be seen in the yellow and purple colored traces in Fig. 8(b) and (c), respectively. This indicates that a ceramic coating (Al_2O_3) from the separator adhered to the graphite surface during manual peel-off. Separators are often coated with a ceramic layer to increase the thermal stability of the commonly used polyolefin-based structures, such as polyethylene [100,101]. However, the ceramic coatings suffer from limited mechanical adhesion [102]. No direct indications of lithium plating could be seen in the SEM images. Nevertheless, ceramic coating remnants occurred at significantly different degrees for the CC and CCCA cycled cells. Thus, it is hypothesized that irreversibly deposited lithium fractions origin from lithium plating may be present behind the ceramic coating of the separator, as reported in [103]. This indirect lithium plating indication would align with the observed locations onto the anode; that is, mostly in the core areas of the investigated lithium-ion cell. Metallic lithium deposition has been reported to occur in the core areas for small format cylindrical cells with low thermal capacity and large temperature heterogeneity [104], due to the rapid core temperature rise and a lowered resistance, leading to a higher core current exceeding the physical charge acceptance limits of the graphite anode. However, a direct evidence for this hypothesis could not be provided since the direct proof of lithium deposition is challenging to yield at these progressed aging states.

8. Conclusions

In this study, it was shown that a cycle life of over 1500 fast charging cycles from 10–80% SOC at a capacity retention of above 60% is possible to reach by applying a model-based health-aware fast charging strategy. This cycle count translates to over 5 years of daily fast charging. The real-time model-based approach mitigates the risk of non-linear aging during the cycle life. The developed fast charging strategy is based on an electrochemical model of reduced order sensitive to the three most critical states to control during fast charging, i.e., the SOC, T, and SOH, and mitigates the risk of lithium plating during operation. Special attention was given to investigate the steps

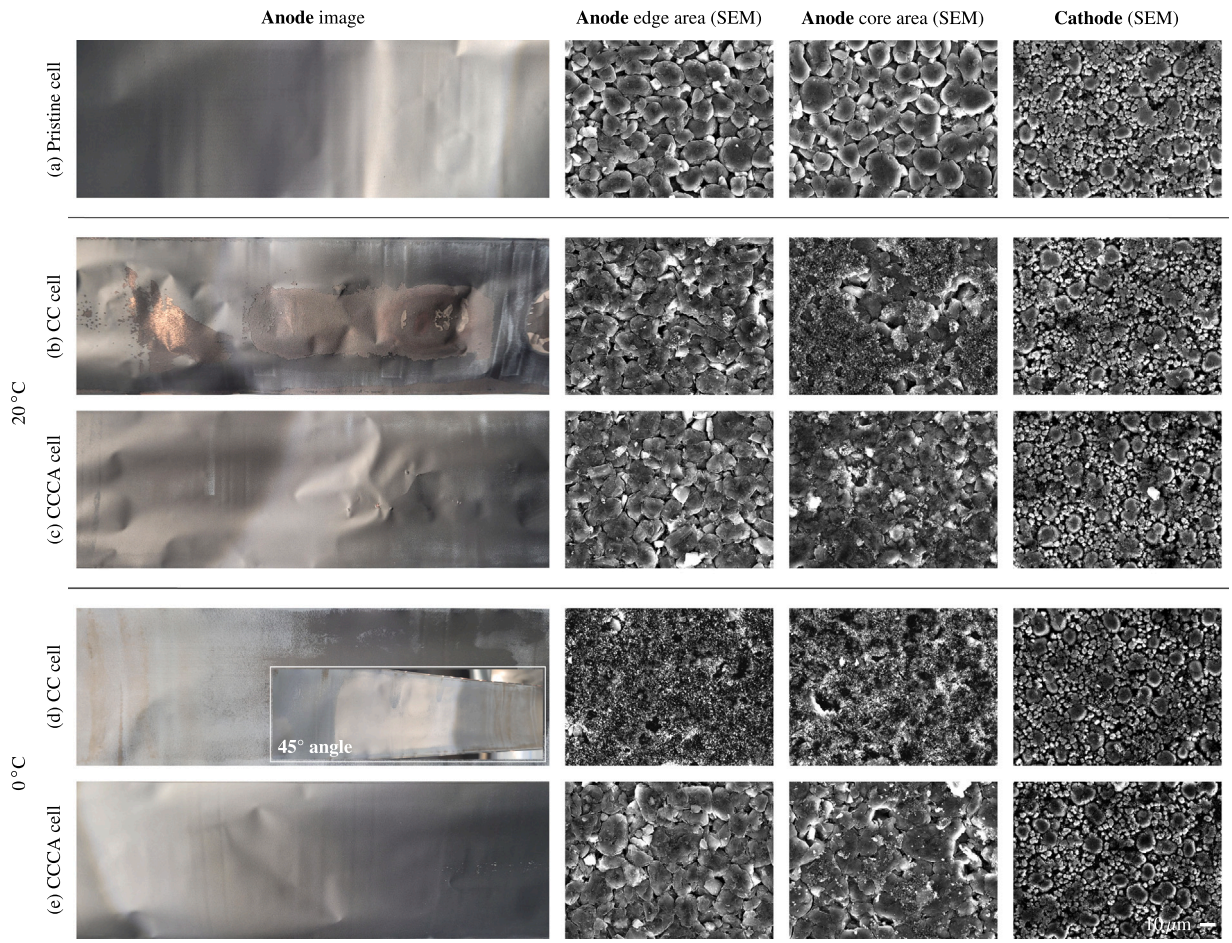

Fig. 7. Images of the electrode layers (macroscopic and SEM images). From top to bottom, (a) pristine cell, (b) CC, and (c) CCCA fast-charged cells at 20 °C ambient temperature, (d) CC and (e) CCCA fast-charged cells at 0 °C ambient temperature. Anode edge images are taken from samples obtained from the outer electrode regions; anode core images are also taken from samples obtained from the cell center.

required to transfer an electrochemical model of reduced order to a real-world implementation for health-aware fast charging strategies. Lithium plating may not be initially limiting the fast charging event for high-power cells, and the aging was traced back to particle cracking and thermal degradation. Furthermore, it was measured that the developed fast charging strategy is also more beneficial from a thermal management perspective compared to simply constant current fast charging. However, it was shown that lithium plating may occur in the later course of aging as the lithium-ion cell internal resistance and likewise the anode resistance increases due to high temperatures, which may swap the dominant aging effects.

The findings of this study can be summarized as follows:

- Fast charging generally leads to a faster degradation than slow charging for high-power cells. High current rates lead to elevated average temperatures and accelerated SEI growth. Further, high charge rates lead to inhomogeneous stress, particle cracking, and aging of the anode. As a consequence, fast charging events should be utilized only to a limited extent during operation to control the capacity fade rate.
- The investigated high-power lithium-ion cell is initially limited by thermal degradation without any indication of lithium plating at larger currents. At a later stage, accelerated thermal degradation can change the cell properties, which may lead to the onset of lithium plating and initiate non-linear aging. Model-based anode potential control strategies are therefore relevant to high-energy as well as high-power lithium-ion cells to prolong their cycle life if frequently fast charged. This is especially true at low ambient temperatures, as these strategies successfully preheat the lithium-ion cells and reduce the peak temperatures compared to CC strategies.
- Model-based fast charging enables physics-motivated derating of the fast charging current dependent to the three critical states of lithium-ion cells (SOC, T, SOH), which is a powerful tool for increasing the maximum achievable fast charge cycles during operation. The developed strategy may be particularly beneficial if use-case scenarios beyond the common warranty limits of 70–80% SOH are considered, as the likelihood of lithium plating amplifies. However, the deployed model in this study did not capture all observed effects (e.g., inhomogeneous aging, shifting of electrode balancing). Thus, extensions are needed to allow for further fine-tuning of the health-aware fast charging strategy.
- Lower ambient temperatures and/or aggressive cooling pose a critical edge case for fast-charged lithium-ion cells and systems, as an inhibited self-heating of the lithium-ion cells lead to a reduced fast charging capability. Advanced thermal preconditioning and optimized battery thermal management system (BTMS) engagement strategies should likewise be applied, if fast charging times of below 15 min are to be achieved.

The presented strategy can be deployed for any graphite-based cell of any format or cathode chemistry and can be further detailed or abstracted depending on the data availability and the intended lithium-ion cell application. Subsequent studies should improve the accuracy of the underlying model and current derating routine over age, e.g., by investigating the idea of an updated electrode balancing over age, as

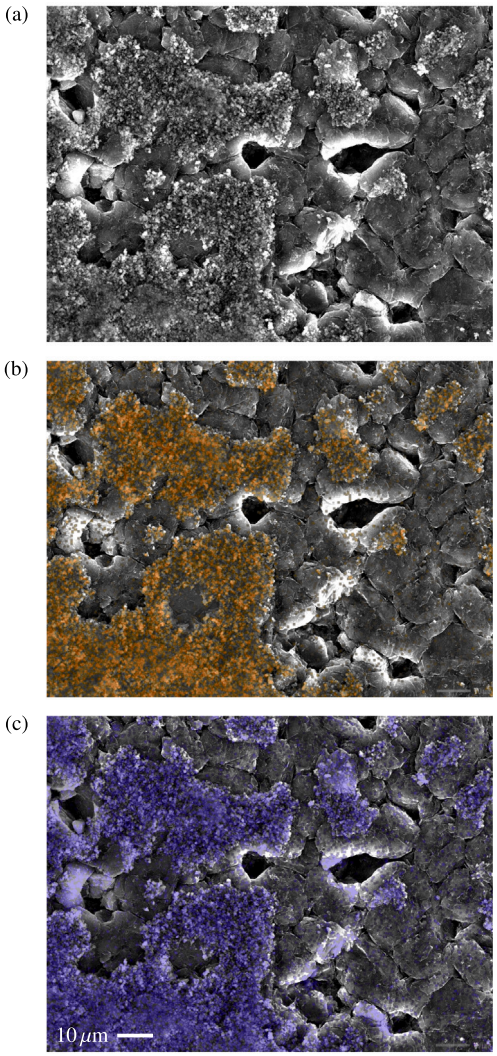

Fig. 8. Magnified SEM images containing various undefined structures with EDX overlay for Al–O traces of the CC cycled cell at 0 °C ambient temperature. (a) Pristine SEM image, SEM image overlayed with (b) Al-traces in yellow, and (c) O-traces in purple.

the impact of the electrode age on the model accuracy has not been within the scope of this study. Moreover, the physics of additional aging effects, such as particle cracking and fading electrolyte performance, should be added to the model to allow for control during fast charging. Additional experimental techniques beyond SEM/EDX could help to identify lithium plating and the remaining aging mechanisms during anode potential controlled fast charging as reported in recent studies [105–107].

CRediT authorship contribution statement

Nikolaos Wassiliadis: Conceptualization, Methodology, Software, Validation, Formal analysis, Investigation, Data curation, Writing – original draft, Writing – review & editing, Visualization, Project administration. **Johannes Kriegler:** Investigation, Resources, Writing – review & editing. **Kareem Abo Gamra:** Writing – review & editing. **Markus Lienkamp:** Writing – review & editing, Resources, Supervision.

Declaration of competing interest

The authors declare that they have no known competing financial interests or personal relationships that could have appeared to influence the work reported in this paper.

Data availability

The framework for real-time model deployment on micro controller units with CAN-capable test benches is provided as open source, accessible via GitHub: https://github.com/TUMFTM/EA_Battery_MDF.

Acknowledgments

We acknowledge the support of parts of this study by the German Federal Ministry for Economic Affairs and Climate Action (BMWK) within the project “ultraBatt” under grant number 01MV21015. The authors would like to thank Andreas Bach, Jan Veeh, Marcel Faika, Timm Kerscher, Lukas Wild, and Magdalena Frank for their contributions to this study during their master’s studies.

Appendix A. Model discretization

To determine a computationally efficient but also accurate model discretization, the voltage response of the model was compared to a 1C CC reference measurement and the reference simulation with a high-fidelity discretization. The model error over the varying discretization of the radial and spatial dimension is illustrated in Fig. A.

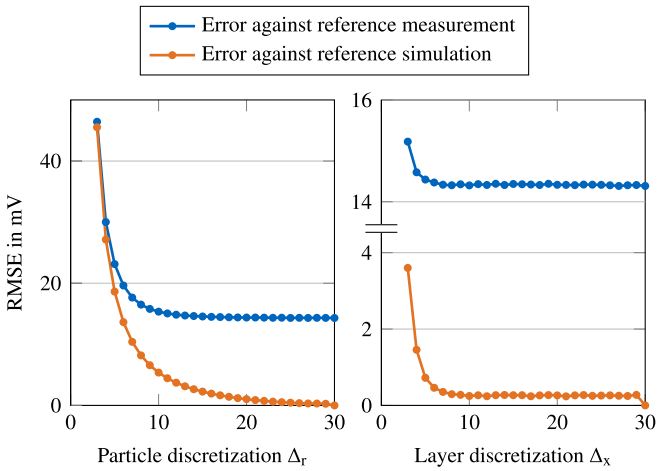

Fig. A. Model error for varying particle (radial direction, Δ_r), electrode layer (negative/positive), and separator layer discretizations (spatial direction, Δ_x). Here, the error is quantified as the root mean square error (RMSE) for a 1C CC charge sequence at 20 °C ambient temperature. Note that the illustrated spatial discretization Δ_x summarizes the spatial discretization of both electrodes and the separator for visualization purposes. The parameter were varied one at a time, i.e., the others were set to the default high-fidelity value of 30 elements.

Appendix B. Experimental setup

The overall experimental setup used for the aging tests presented in this study is illustrated in Fig. B. The cell is connected to a battery cycler and contained in a thermal chamber. Sensing of the testing equipment is extended with additional thermal sensors and all signals are fed into the model operating on a microcontroller unit (MCU). Here, the fast charging current is determined for the current cell state k and communicated to the battery cycler via controlled area network (CAN). The developed model deployment framework (MDF) is provided as open source along with this article (cf. Section ‘Data Availability’).

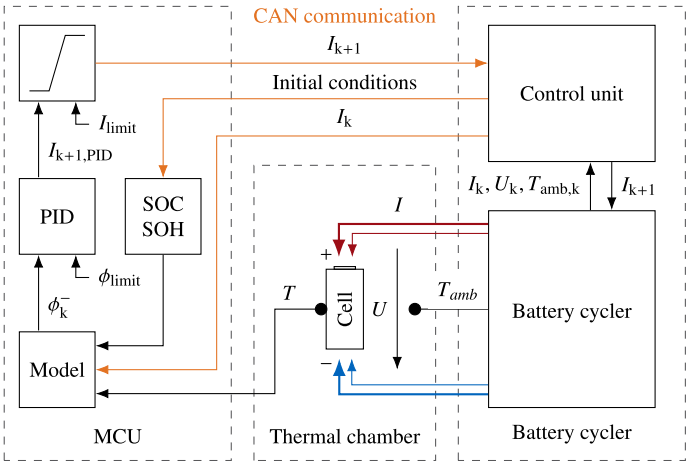

Fig. B. Experimental setup and framework for model-based fast charging control in real-time. The cell itself represents an electric vehicle (EV) battery pack, while the cycler represents the electric vehicle supply equipment (EVSE). The deployed microcontroller unit (MCU) serves as an advanced battery management system (ABMS), providing the maximum charging current I_{k+1} to the battery cycler dependent on the previous charging current (I_k), temperature (T_k), and initial conditions (SOC, SOH) of the lithium-ion cell. The model-based controlled fast charging current (I_{k+1}) hereby depends on all relevant impact factors (SOC, T, SOH).

Appendix C. Test procedures

Fig. C shows the aging procedure as well as the reference performance test (RPT). In the aging procedure, a 1/4 h relaxation sequence was performed to reach a relaxed state. Subsequently, the lithium-ion cells were discharged to 10 % SOC by coulomb counting and set to rest for 1 h to avoid any unintended thermal influence of the previous discharge on the following fast charging sequence. Then, either (1) a reference CC fast charge or, if the health-aware fast charging strategy was applied, (2) a model-based CCCA fast charge was performed to 80 %. Note that the model was initialized prior to the fast charge sequence and stopped after completion of the sequence. If the voltage limit of 4.2 V was reached earlier, a CV sequence was performed to 80% SOC. All strategies were followed by a 1C CCCV charge to 4.2 V and a cut-off current of 50 mA for direct comparison and recalibration point of the coulomb counter (SOC determination).

The RPT starts with a 3 h relaxation, followed by a repeated 1C CCCV capacity determination between the voltage bounds. The second capacity determination cycle was used to obliterate anode overhang effects during the handling of the cell between the two test positions with reference to an earlier study [108], which has been reported to interfere with the first capacity determination cycle. The sequence is followed by a C/20 charge sequence for DVA purposes and subsequently followed by 0.5C / 1C / 2C pulse resistance tests each at 20 / 50 / 80% SOC in declining order. The SOC levels are derived by charge titration based on the actual capacity determined earlier in the RPT.

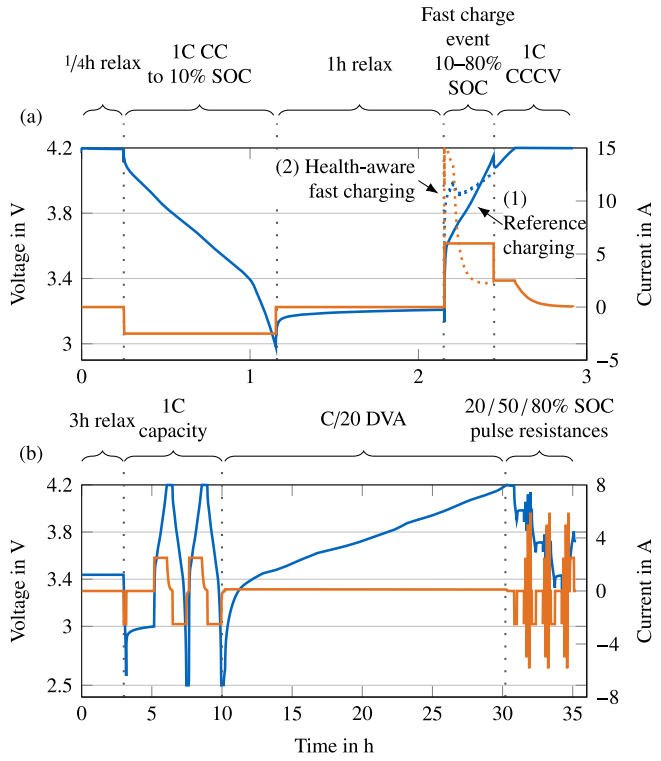

Fig. C. Aging and reference performance test (RPT) used in this aging study. (a) Cycling with varying fast charging strategies starting from 10% SOC and a thermally relaxed state to avoid any influence of the previous discharge. The final 1C CCCV sequence is performed to reset the test procedure to a well-defined 100% SOC to accurately perform the partial discharge of the following sequence. (b) Redundant 1C capacity discharge sequence, C/20 charge sequence for differential voltage analysis (DVA), and charge and discharge pulse resistance determination at 20%, 50%, and 80% SOC during the RPT.

Appendix D. Lithium plating reference

To yield a reference of the visual appearance of lithium plating, a high-energy lithium-ion cell (Samsung INR18650-35E) was charged under harsh conditions, provoking lithium plating. In detail, the lithium-ion cell underwent a CC charging sequences at 2 C (6.8 A) and discharging sequences at 1 C (3.4 A) repeated ten times at −10 °C ambient temperature. A rapid loss of capacity over cycles was observable although only ten charge/discharge repetitions were performed. The lithium-ion cell has been subsequently CC discharged to 2.5 V and transferred to a glove-box (GS MEGA E-LINE, GS Glovebox, Germany) under argon atmosphere (H20 < 1 ppm, CO2 < 1 ppm) for disassembly

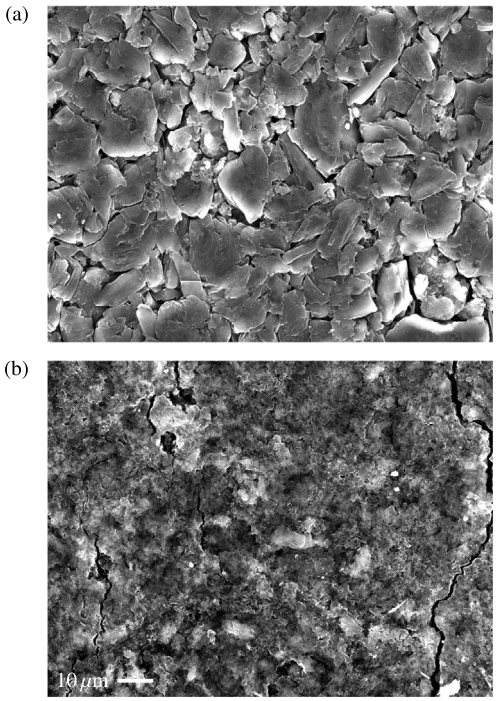

Fig. D. SEM images of (a) a pristine and (b) a 2 C fast-charged anode at −10 °C ambient temperature harvested from a high-energy lithium-ion cell (Samsung INR18650-35E).

of the cell, harvest of the anodes, and SEM imaging. As a reference, a pristine cell was likewise prepared. Both SEM images of the anode surface can be seen in Fig. D.

The graphite particles are clearly observable as a flake-like structure in the pristine cell (cf. Fig. D(a)), whereas these particles are not visible anymore in the fast-charged cell (cf. Fig. D(b)). A thick coating layer manifests itself onto the graphite particles, with clearly visible cracks across the coating layer. The observable coating thereby follows a structure reported by Ghanbari et al. [109], which allows for the hypothesis that the thick coating originates from lithium plating and secondary SEI formation. The coating was observed in a similar appearance for the overall anode layer; from the core to the edge of the jelly roll.

References

[1] H. Löbberding, S. Wessel, C. Offermanns, M. Kehrer, J. Rother, H. Heimes, A. Kampker, From cell to battery system in BEVs: Analysis of system packing efficiency and cell types, World Electr. Veh. J. 11 (4) (2020) 77, http://dx.doi.org/10.3390/wevj11040077.

[2] M. Singh, J. Kaiser, H. Hahn, Thick electrodes for high energy lithium ion batteries, J. Electrochem. Soc. 162 (7) (2015) A1196–A1201, http://dx.doi.org/10.1149/2.0401507jes.

[3] M.W. Verbrugge, C.W. Wampler, On the optimal sizing of batteries for electric vehicles and the influence of fast charge, J. Power Sources 384 (2018) 312–317, http://dx.doi.org/10.1016/j.jpowsour.2018.02.064.

[4] A. Tomaszewska, Z. Chu, X. Feng, S. O'Kane, X. Liu, J. Chen, C. Ji, E. Endler, R. Li, L. Liu, Y. Li, S. Zheng, S. Vetterlein, M. Gao, J. Du, M. Parkes, M. Ouyang, M. Marinescu, G. Offer, B. Wu, Lithium-ion battery fast charging: A review, ETransportation 1 (2019) 100011, http://dx.doi.org/10.1016/j.etran.2019.100011.

[5] E.J. Dufek, D.P. Abraham, I. Bloom, B.-R. Chen, P.R. Chinnam, A.M. Colclasure, K.L. Gering, M. Keyser, S. Kim, W. Mai, D.C. Robertson, M.-T.F. Rodrigues, K. Smith, T.R. Tanim, F.L. Usseglio-Viretta, P.J. Weddle, Developing extreme fast charge battery protocols – A review spanning materials to systems, J. Power Sources 526 (2022) 231129, http://dx.doi.org/10.1016/j.jpowsour.2022.231129.

[6] N. Wassiliadis, J. Schneider, A. Frank, L. Wildfeuer, X. Lin, A. Jossen, M. Lienkamp, Review of fast charging strategies for lithium-ion battery systems and their applicability for battery electric vehicles, J. Energy Storage 44 (2021) 103306, http://dx.doi.org/10.1016/j.est.2021.103306.

[7] P. Notten, J.O. h. Veld, J. van Beek, Boostcharging Li-ion batteries: A challenging new charging concept, J. Power Sources 145 (1) (2005) 89–94, http://dx.doi.org/10.1016/j.jpowsour.2004.12.038.

[8] S.S. Zhang, K. Xu, T.R. Jow, Study of the charging process of a LiCoO2-based Li-ion battery, J. Power Sources 160 (2) (2006) 1349–1354, http://dx.doi.org/10.1016/j.jpowsour.2006.02.087.

[9] D. Anseán, M. González, J.C. Viera, V.M. García, C. Blanco, M. Valledor, Fast charging technique for high power lithium iron phosphate batteries: A cycle life analysis, J. Power Sources 239 (2013) 9–15, http://dx.doi.org/10.1016/j.jpowsour.2013.03.044.

[10] M. Abdel Monem, K. Trad, N. Omar, O. Hegazy, B. Mantels, G. Mulder, P. van den Bossche, J. van Mierlo, Lithium-ion batteries: Evaluation study of different charging methodologies based on aging process, Appl. Energy 152 (2015) 143–155, http://dx.doi.org/10.1016/j.apenergy.2015.02.064.

[11] M. Abdel-Monem, K. Trad, N. Omar, O. Hegazy, P. van den Bossche, J. van Mierlo, Influence analysis of static and dynamic fast-charging current profiles on ageing performance of commercial lithium-ion batteries, Energy 120 (2017) 179–191, http://dx.doi.org/10.1016/j.energy.2016.12.110.

[12] J. Li, E. Murphy, J. Winnick, P.A. Kohl, The effects of pulse charging on cycling characteristics of commercial lithium-ion batteries, J. Power Sources 102 (1–2) (2001) 302–309, http://dx.doi.org/10.1016/S0378-7753(01)00820-5.

[13] L.-R. Chen, S.-L. Wu, D.-T. Shieh, T.-R. Chen, Sinusoidal-ripple-current charging strategy and optimal charging frequency study for Li-ion batteries, IEEE Trans. Ind. Electron. 60 (1) (2013) 88–97, http://dx.doi.org/10.1109/TIE.2012.2186106.

[14] M.H. Noh, P.X. Thivel, C. Lefrou, Y. Bultel, Fast-charging of lithium iron phosphate battery with ohmic-drop compensation method, J. Energy Storage 8 (2016) 160–167, http://dx.doi.org/10.1016/j.est.2016.10.005.

[15] A.S. Mussa, M. Klett, M. Behm, G. Lindbergh, R.W. Lindström, Fast-charging to a partial state of charge in lithium-ion batteries: A comparative ageing study, J. Energy Storage 13 (2017) 325–333, http://dx.doi.org/10.1016/j.est.2017.07.004.

[16] P. Keil, A. Jossen, Charging protocols for lithium-ion batteries and their impact on cycle life—An experimental study with different 18650 high-power cells, J. Energy Storage 6 (2016) 125–141, http://dx.doi.org/10.1016/j.est.2016.02.005.

[17] J. Schmalstieg, C. Rahe, M. Ecker, D.U. Sauer, Full cell parameterization of a high-power lithium-ion battery for a physico-chemical model: Part I, physical and electrochemical parameters, J. Electrochem. Soc. 165 (16) (2018) A3799–A3810, http://dx.doi.org/10.1149/2.0321816jes.

[18] R. Mathieu, O. Briat, P. Gyan, J.-M. Vinassa, Comparison of the impact of fast charging on the cycle life of three lithium-ion cells under several parameters of charge protocol and temperatures, Appl. Energy 283 (2021) 116344, http://dx.doi.org/10.1016/j.apenergy.2020.116344.

[19] S. Shi, J. Gao, Y. Liu, Y. Zhao, Q. Wu, W. Ju, C. Ouyang, R. Xiao, Multi-scale computation methods: Their applications in lithium-ion battery research and development, Chin. Phys. B 25 (1) (2016) 018212, http://dx.doi.org/10.1088/1674-1056/25/1/018212.

[20] G. Li, C.W. Monroe, Multiscale lithium-battery modeling from materials to cells, Annu. Rev. Chem. Biomol. Eng. 11 (2020) 277–310, http://dx.doi.org/10.1146/annurev-chembioeng-012120-083016.

[21] X. Lin, S. Wang, Y. Kim, A framework for charging strategy optimization using a physics-based battery model, J. Appl. Electrochem. 49 (8) (2019) 779–793, http://dx.doi.org/10.1007/s10800-019-01322-1.

[22] J. Hamar, C. Zoerr, S.V. Erhard, A. Jossen, Anode potential estimation in lithium-ion batteries using data-driven models for online applications, J. Electrochem. Soc. (2021) http://dx.doi.org/10.1149/1945-7111/abe721.

[23] F.B. Spingler, W. Wittmann, J. Sturm, B. Rieger, A. Jossen, Optimum fast charging of lithium-ion pouch cells based on local volume expansion criteria, J. Power Sources 393 (2018) 152–160, http://dx.doi.org/10.1016/j.jpowsour.2018.04.095.

[24] L. Hovestadt, K. Wildermann, A. Sahhary, R. Hanke-Rauschenbach, Investigation of temperature and pressure behaviour of constrained lithium ion cell under lithium plating conditions, J. Electrochem. Soc. (2020) http://dx.doi.org/10.1149/1945-7111/aba550.

[25] J. Sieg, J. Bandlow, T. Mitsch, D. Dragicevic, T. Materna, B. Spier, H. Witzenhausen, M. Ecker, D.U. Sauer, Fast charging of an electric vehicle lithium-ion battery at the limit of the lithium deposition process, J. Power Sources 427 (2019) 260–270, http://dx.doi.org/10.1016/j.jpowsour.2019.04.047.

[26] S.P. Rangarajan, Y. Barsukov, P.P. Mukherjee, Anode potential controlled charging prevents lithium plating, J. Mater. Chem. A 8 (26) (2020) 13077–13085, http://dx.doi.org/10.1039/d0ta04467a.

[27] B. Epding, B. Rumberg, M. Mense, H. Jahnke, A. Kwade, Aging–optimized fast charging of lithium ion cells based on three–electrode cell measurements, Energy Technol. 8 (10) (2020) 2000457, http://dx.doi.org/10.1002/ente.202000457.

[28] C. Zou, X. Hu, Z. Wei, X. Tang, Electrothermal dynamics-conscious lithium-ion battery cell-level charging management via state-monitored predictive control, Energy 141 (2017) 250–259, http://dx.doi.org/10.1016/j.energy.2017.09.048.

[29] J. Remmlinger, S. Tippmann, M. Buchholz, K. Dietmayer, Low-temperature charging of lithium-ion cells part II: Model reduction and application, J. Power Sources 254 (2014) 268–276, http://dx.doi.org/10.1016/j.jpowsour.2013.12.101.

[30] S. Tippmann, D. Walper, L. Balboa, B. Spier, W.G. Bessler, Low-temperature charging of lithium-ion cells part I: Electrochemical modeling and experimental investigation of degradation behavior, J. Power Sources 252 (2014) 305–316, http://dx.doi.org/10.1016/j.jpowsour.2013.12.022.

[31] W. Li, N. Sengupta, P. Dechent, D. Howey, A. Annaswamy, D.U. Sauer, One-shot battery degradation trajectory prediction with deep learning, J. Power Sources 506 (2021) 230024, http://dx.doi.org/10.1016/j.jpowsour.2021.230024.

[32] R. Drees, F. Lienesch, M. Kurrat, Fast charging lithium-ion battery formation based on simulations with an electrode equivalent circuit model, J. Energy Storage 36 (2021) 102345, http://dx.doi.org/10.1016/j.est.2021.102345.

[33] M. Doyle, T.F. Fuller, J. Newman, Modeling of galvanostatic charge and discharge of the lithium/polymer/insertion cell, J. Electrochem. Soc. 140 (6) (1993) 1526–1533, http://dx.doi.org/10.1149/1.2221597.

[34] R. Klein, N.A. Chaturvedi, J. Christensen, J. Ahmed, R. Findeisen, A. Kojic, Optimal charging strategies in lithium-ion battery, in: Proceedings of the 2011 American Control Conference, IEEE, 2011, pp. 382–387, http://dx.doi.org/10.1109/ACC.2011.5991497.

[35] M.F. Hasan, C.-F. Chen, C.E. Shaffer, P.P. Mukherjee, Analysis of the implications of rapid charging on lithium-ion battery performance, J. Electrochem. Soc. 162 (7) (2015) A1382–A1395, http://dx.doi.org/10.1149/2.0871507jes.

[36] S. Pramanik, S. Anwar, Electrochemical model based charge optimization for lithium-ion batteries, J. Power Sources 313 (2016) 164–177, http://dx.doi.org/10.1016/j.jpowsour.2016.01.096.

[37] C. Zou, X. Hu, Z. Wei, T. Wik, B. Egardt, Electrochemical estimation and control for lithium-ion battery health-aware fast charging, IEEE Trans. Ind. Electron. 65 (8) (2018) 6635–6645, http://dx.doi.org/10.1109/TIE.2017.2772154.

[38] M. Xu, R. Wang, P. Zhao, X. Wang, Fast charging optimization for lithium-ion batteries based on dynamic programming algorithm and electrochemical-thermal-capacity fade coupled model, J. Power Sources 438 (2019) 227015, http://dx.doi.org/10.1016/j.jpowsour.2019.227015.

[39] A. Adam, J. Wandt, E. Knobbe, G. Bauer, A. Kwade, Fast-charging of automotive lithium-ion cells: In-situ lithium-plating detection and comparison of different cell designs, J. Electrochem. Soc. 167 (13) (2020) 130503, http://dx.doi.org/10.1149/1945-7111/abb564.

[40] F. Ringbeck, M. Garbade, D.U. Sauer, Uncertainty-aware state estimation for electrochemical model-based fast charging control of lithium-ion batteries, J. Power Sources 470 (2020) 228221, http://dx.doi.org/10.1016/j.jpowsour.2020.228221.

[41] S. Kolluri, S.V. Aduru, M. Pathak, R.D. Braatz, V.R. Subramanian, Real-time Nonlinear Model Predictive Control (NMPC) strategies using physics-based models for advanced lithium-ion battery management system (BMS), J. Electrochem. Soc. 167 (6) (2020) 063505, http://dx.doi.org/10.1149/1945-7111/ab7bd7.

[42] H. Yang, J. Lee, Hyundai motor to replace battery systems in $900 MLN electric car recall, 2021.

[43] D. Andre, H. Hain, P. Lamp, F. Maglia, B. Stiaszny, Future high-energy density anode materials from an automotive application perspective, J. Mater. Chem. A 5 (33) (2017) 17174–17198, http://dx.doi.org/10.1039/C7TA03108D.

[44] N. Legrand, B. Knosp, P. Desprez, F. Lapicque, S. Raël, Physical characterization of the charging process of a Li-ion battery and prediction of Li plating by electrochemical modelling, J. Power Sources 245 (2014) 208–216, http://dx.doi.org/10.1016/j.jpowsour.2013.06.130.

[45] T. Waldmann, M. Wilka, M. Kasper, M. Fleischhammer, M. Wohlfahrt-Mehrens, Temperature dependent ageing mechanisms in lithium-ion batteries – A post-mortem study, J. Power Sources 262 (2014) 129–135, http://dx.doi.org/10.1016/j.jpowsour.2014.03.112.

[46] R.V. Bugga, M.C. Smart, Lithium plating behavior in lithium-ion cells, ECS Trans. 25 (36) (2010) 241–252, http://dx.doi.org/10.1149/1.3393860.

[47] C. von Lüders, J. Keil, M. Webersberger, A. Jossen, Modeling of lithium plating and lithium stripping in lithium-ion batteries, J. Power Sources 414 (2019) 41–47, http://dx.doi.org/10.1016/j.jpowsour.2018.12.084.

[48] B. Ng, P.T. Coman, E. Faegh, X. Peng, S.G. Karakalos, X. Jin, W.E. Mustain, R.E. White, Low-temperature lithium plating/corrosion hazard in lithium-ion batteries: Electrode rippling, variable states of charge, and thermal and nonthermal runaway, ACS Appl. Energy Mater. 3 (4) (2020) 3653–3664, http://dx.doi.org/10.1021/acsaem.0c00130.

[49] T.C. Bach, S.F. Schuster, E. Fleder, J. Müller, M.J. Brand, H. Lorrmann, A. Jossen, G. Sextl, Nonlinear aging of cylindrical lithium-ion cells linked to heterogeneous compression, J. Energy Storage 5 (2016) 212–223, http://dx.doi.org/10.1016/j.est.2016.01.003.

[50] E. Jo, J.-H. Park, J. Park, J. Hwang, K.Y. Chung, K.-W. Nam, S.M. Kim, W. Chang, Different thermal degradation mechanisms: Role of aluminum in Ni-rich layered cathode materials, Nano Energy 78 (2020) 105367, http://dx.doi.org/10.1016/j.nanoen.2020.105367.

[51] X.-G. Yang, Y. Leng, G. Zhang, S. Ge, C.-Y. Wang, Modeling of lithium plating induced aging of lithium-ion batteries: Transition from linear to nonlinear aging, J. Power Sources 360 (2017) 28–40, http://dx.doi.org/10.1016/j.jpowsour.2017.05.110.

[52] Y. Tian, C. Lin, H. Li, J. Du, R. Xiong, Detecting undesired lithium plating on anodes for lithium-ion batteries – A review on the in-situ methods, Appl. Energy 300 (2021) 117386, http://dx.doi.org/10.1016/j.apenergy.2021.117386.

[53] S.J. An, J. Li, C. Daniel, D. Mohanty, S. Nagpure, D.L. Wood, The state of understanding of the lithium-ion-battery graphite solid electrolyte interphase (SEI) and its relationship to formation cycling, Carbon 105 (2016) 52–76, http://dx.doi.org/10.1016/j.carbon.2016.04.008.

[54] M. Broussely, P. Biensan, F. Bonhomme, P. Blanchard, S. Herreyre, K. Nechev, R.J. Staniewicz, Main aging mechanisms in Li ion batteries, J. Power Sources 146 (1–2) (2005) 90–96, http://dx.doi.org/10.1016/j.jpowsour.2005.03.172.

[55] J. Keil, N. Paul, V. Baran, P. Keil, R. Gilles, A. Jossen, Linear and nonlinear aging of lithium-ion cells investigated by electrochemical analysis and in-situ neutron diffraction, J. Electrochem. Soc. 166 (16) (2019) A3908–A3917, http://dx.doi.org/10.1149/2.1271915jes.

[56] T. Piao, S.-M. Park, C.-H. Doh, S.-I. Moon, Intercalation of lithium ions into graphite electrodes studied by AC impedance measurements, J. Electrochem. Soc. 146 (8) (1999) 2794–2798, http://dx.doi.org/10.1149/1.1392010.

[57] M. Ecker, S. Käbitz, I. Laresgoiti, D.U. Sauer, Parameterization of a physico-chemical model of a lithium-ion battery, J. Electrochem. Soc. 162 (9) (2015) A1849–A1857, http://dx.doi.org/10.1149/2.0541509jes.

[58] V.A. Agubra, J.W. Fergus, The formation and stability of the solid electrolyte interface on the graphite anode, J. Power Sources 268 (2014) 153–162, http://dx.doi.org/10.1016/j.jpowsour.2014.06.024.

[59] X.-G. Yang, C.-Y. Wang, Understanding the trilemma of fast charging, energy density and cycle life of lithium-ion batteries, J. Power Sources 402 (2018) 489–498, http://dx.doi.org/10.1016/j.jpowsour.2018.09.069.

[60] J. Liu, Z. Chu, H. Li, D. Ren, Y. Zheng, L. Lu, X. Han, M. Ouyang, Lithium–plating–free fast charging of large–format lithium–ion batteries with reference electrodes, Int. J. Energy Res. 45 (5) (2021) 7918–7932, http://dx.doi.org/10.1002/er.6375.

[61] F. Grimsmann, T. Gerbert, F. Brauchle, A. Gruhle, J. Parisi, M. Knipper, Determining the maximum charging currents of lithium-ion cells for small charge quantities, J. Power Sources 365 (2017) 12–16, http://dx.doi.org/10.1016/j.jpowsour.2017.08.044.

[62] Z. Chu, X. Feng, L. Lu, J. Li, X. Han, M. Ouyang, Non-destructive fast charging algorithm of lithium-ion batteries based on the control-oriented electrochemical model, Appl. Energy 204 (2017) 1240–1250, http://dx.doi.org/10.1016/j.apenergy.2017.03.111.

[63] M. Schimpe, J.V. Barreras, B. Wu, G.J. Offer, Battery degradation-aware current derating: An effective method to prolong lifetime and ease thermal management, J. Electrochem. Soc. 168 (6) (2021) 060506, http://dx.doi.org/10.1149/1945-7111/ac0553.

[64] L. Wildfeuer, A. Karger, D. Ayguel, N. Wassiliadis, A. Jossen, M. Lienkamp, Experimental degradation study of a commercial lithium-ion battery, J. Power Sources http://dx.doi.org/10.1016/j.jpowsour.2022.232498.

[65] B. Wang, F. l. Zhang, X. a. Zhou, P. Wang, J. Wang, H. Ding, H. Dong, W. b. Liang, N. s. Zhang, S. y. Li, Which of the nickel-rich NCM and NCA is structurally superior as a cathode material for lithium-ion batteries? J. Mater. Chem. A 9 (23) (2021) 13540–13551, http://dx.doi.org/10.1039/d1ta01128f.

[66] L. Wildfeuer, N. Wassiliadis, A. Karger, F. Bauer, M. Lienkamp, Teardown analysis and characterization of a commercial lithium-ion battery for advanced algorithms in battery electric vehicles, J. Energy Storage 48 (2022) 103909, http://dx.doi.org/10.1016/j.est.2021.103909.

[67] X.-Y. Yao, M.G. Pecht, Tab design and failures in cylindrical Li-ion batteries, IEEE Access 7 (2019) 24082–24095, http://dx.doi.org/10.1109/ACCESS.2019.2899793.

[68] F. Dou, L. Shi, G. Chen, D. Zhang, Silicon/carbon composite anode materials for lithium-ion batteries, Electrochem. Energy Rev. 2 (1) (2019) 149–198, http://dx.doi.org/10.1007/s41918-018-00028-w.

[69] S. Bazlen, P. Heugel, O. von Kessel, W. Commerell, J. Tübke, Influence of charging protocols on the charging capability and aging of lithium-ion cells with silicon-containing anodes, J. Energy Storage 49 (2022) 104044, http://dx.doi.org/10.1016/j.est.2022.104044.

[70] N. Wassiliadis, M. Ank, A. Bach, M. Wanzel, A.-S. Zollner, K.A. Gamra, M. Lienkamp, A systematic approach for the parameter identification of electro-chemical battery models enabling health-aware fast charging control of battery electric vehicles, J. Energy Storage 56 (2022) 105951, http://dx.doi.org/10.1016/j.est.2022.105951.

[71] S.J. Moura, F.B. Argomedo, R. Klein, A. Mirtabatabaei, M. Krstic, Battery state estimation for a single particle model with electrolyte dynamics, IEEE Trans. Control Syst. Technol. 25 (2) (2017) 453–468, http://dx.doi.org/10.1109/TCST.2016.2571663.

[72] H.E. Perez, X. Hu, S. Dey, S.J. Moura, Optimal charging of Li-ion batteries with coupled electro-thermal-aging dynamics, IEEE Trans. Veh. Technol. 66 (9) (2017) 7761–7770, http://dx.doi.org/10.1109/TVT.2017.2676044.

[73] P. Bogacki, L.F. Shampine, A 3(2) pair of Runge - Kutta formulas, Appl. Math. Lett. 2 (4) (1989) 321–325, http://dx.doi.org/10.1016/0893-9659(89)90079-7.

[74] N. Wassiliadis, Electrochemical lithium-ion battery model and easy-to-apply parameterization procedures for fast-charge applications. URL https://github.com/TUMFTM/EA_Battery_SPMparameterization.

[75] J. Sturm, H. Ennifar, S.V. Erhard, A. Rheinfeld, S. Kosch, A. Jossen, State estimation of lithium-ion cells using a physicochemical model based extended Kalman filter, Appl. Energy 223 (2018) 103–123, http://dx.doi.org/10.1016/j.apenergy.2018.04.011.

[76] A. Barré, B. Deguilhem, S. Grolleau, M. Gérard, F. Suard, D. Riu, A review on lithium-ion battery ageing mechanisms and estimations for automotive applications, J. Power Sources 241 (2013) 680–689, http://dx.doi.org/10.1016/j.jpowsour.2013.05.040.

[77] C.R. Birkl, M.R. Roberts, E. McTurk, P.G. Bruce, D.A. Howey, Degradation diagnostics for lithium ion cells, J. Power Sources 341 (2017) 373–386, http://dx.doi.org/10.1016/j.jpowsour.2016.12.011.

[78] A.M. Colclasure, A.R. Dunlop, S.E. Trask, B.J. Polzin, A.N. Jansen, K. Smith, Requirements for enabling extreme fast charging of high energy density Li-ion cells while avoiding lithium plating, J. Electrochem. Soc. 166 (8) (2019) A1412–A1424, http://dx.doi.org/10.1149/2.0451908jes.

[79] N. Delpuech, N. Dupré, D. Mazouzi, J. Gaubicher, P. Moreau, J.S. Bridel, D. Guyomard, B. Lestriez, Correlation between irreversible capacity and electrolyte solvents degradation probed by NMR in si-based negative electrode of Li-ion cell, Electrochem. Commun. 33 (2013) 72–75, http://dx.doi.org/10.1016/j.elecom.2013.05.001.

[80] X. Chen, H. Lei, R. Xiong, W. Shen, R. Yang, A novel approach to reconstruct open circuit voltage for state of charge estimation of lithium ion batteries in electric vehicles, Appl. Energy 255 (2019) 113758, http://dx.doi.org/10.1016/j.apenergy.2019.113758.

[81] Y. Zheng, Y. Cui, X. Han, H. Dai, M. Ouyang, Lithium-ion battery capacity estimation based on open circuit voltage identification using the iteratively reweighted least squares at different aging levels, J. Energy Storage 44 (2021) 103487, http://dx.doi.org/10.1016/j.est.2021.103487.

[82] A. Farmann, D.U. Sauer, A study on the dependency of the open-circuit voltage on temperature and actual aging state of lithium-ion batteries, J. Power Sources 347 (2017) 1–13, http://dx.doi.org/10.1016/j.jpowsour.2017.01.098.

[83] T. Schöpfel, Simulative preliminary investigation on adaptive model- based fast charging strategies for lithium-ion batteries.

[84] N. Wassiliadis, J. Adermann, A. Frericks, M. Pak, C. Reiter, B. Lohmann, M. Lienkamp, Revisiting the dual extended Kalman filter for battery state-of-charge and state-of-health estimation: A use-case life cycle analysis, J. Energy Storage 19 (2018) 73–87, http://dx.doi.org/10.1016/j.est.2018.07.006.

[85] A. Karger, L. Wildfeuer, A. Maheshwari, N. Wassiliadis, M. Lienkamp, Novel method for the on-line estimation of low-frequency impedance of lithium-ion batteries, J. Energy Storage 32 (2020) 101818, http://dx.doi.org/10.1016/j.est.2020.101818.

[86] P.A. Schmidt, P. Schmitz, M.F. Zaeh, Laser beam welding of electrical contacts for the application in stationary energy storage devices, J. Laser Appl. 28 (2) (2016) 022423, http://dx.doi.org/10.2351/1.4943908.

[87] N. Wassiliadis, Model deployment framework (MDF) for real-time investigation and usage of battery models on CAN-capable test benches. URL https://github.com/TUMFTM/EA_Battery_MDF.

[88] R. Deshpande, M. Verbrugge, Y.-T. Cheng, J. Wang, P. Liu, Battery cycle life prediction with coupled chemical degradation and fatigue mechanics, J. Electrochem. Soc. 159 (10) (2012) A1730–A1738, http://dx.doi.org/10.1149/2.049210jes.

[89] R.D. Deshpande, D.M. Bernardi, Modeling solid-electrolyte interphase (SEI) fracture: Coupled mechanical/chemical degradation of the lithium ion battery, J. Electrochem. Soc. 164 (2) (2017) A461–A474, http://dx.doi.org/10.1149/2.0841702jes.

[90] B. Liang, Y. Liu, Y. Xu, Silicon-based materials as high capacity anodes for next generation lithium ion batteries, J. Power Sources 267 (2014) 469–490, http://dx.doi.org/10.1016/j.jpowsour.2014.05.096.

[91] S. Gantenbein, M. Schönleber, M. Weiss, E. Ivers-Tiffée, Capacity fade in lithium-ion batteries and cyclic aging over various state-of-charge ranges, Sustainability 11 (23) (2019) 6697, http://dx.doi.org/10.3390/su11236697.

[92] I. Bloom, A.N. Jansen, D.P. Abraham, J. Knuth, S.A. Jones, V.S. Battaglia, G.L. Henriksen, Differential voltage analyses of high-power, lithium-ion cells, J. Power Sources 139 (1–2) (2005) 295–303, http://dx.doi.org/10.1016/j.jpowsour.2004.07.021.

[93] I. Bloom, J. Christophersen, K. Gering, Differential voltage analyses of high-power lithium-ion cells, J. Power Sources 139 (1–2) (2005) 304–313, http://dx.doi.org/10.1016/j.jpowsour.2004.07.022.

[94] M. Lewerenz, A. Marongiu, A. Warnecke, D.U. Sauer, Differential voltage analysis as a tool for analyzing inhomogeneous aging: A case study for lifepo4|graphite cylindrical cells, J. Power Sources 368 (2017) 57–67, http://dx.doi.org/10.1016/j.jpowsour.2017.09.059.

[95] J. Sieg, M. Storch, J. Fath, A. Nuhic, J. Bandlow, B. Spier, D.U. Sauer, Local degradation and differential voltage analysis of aged lithium-ion pouch cells, J. Energy Storage 30 (2020) 101582, http://dx.doi.org/10.1016/j.est.2020.101582.

[96] I. Bloom, J.P. Christophersen, D.P. Abraham, K.L. Gering, Differential voltage analyses of high-power, lithium-ion cells, J. Power Sources 157 (1) (2006) 537–542, http://dx.doi.org/10.1016/j.jpowsour.2005.07.054.

[97] H. Honbo, K. Takei, Y. Ishii, T. Nishida, Electrochemical properties and Li deposition morphologies of surface modified graphite after grinding, J. Power Sources 189 (1) (2009) 337–343, http://dx.doi.org/10.1016/j.jpowsour.2008.08.048.

[98] X. Lin, X. Hao, Z. Liu, W. Jia, Health conscious fast charging of Li-ion batteries via a single particle model with aging mechanisms, J. Power Sources 400 (2018) 305–316, http://dx.doi.org/10.1016/j.jpowsour.2018.08.030.

[99] X. Lin, Real-time prediction of anode potential in Li-ion batteries using long short-term neural networks for lithium plating prevention, J. Electrochem. Soc. 166 (10) (2019) A1893–A1904, http://dx.doi.org/10.1149/2.0621910jes.

[100] L. Yu, Y. Jin, Y.S. Lin, Ceramic coated polypropylene separators for lithium-ion batteries with improved safety: Effects of high melting point organic binder, RSC Adv. 6 (46) (2016) 40002–40009, http://dx.doi.org/10.1039/C6RA04522G.

[101] C. Shi, J. Dai, X. Shen, L. Peng, C. Li, X. Wang, P. Zhang, J. Zhao, A high-temperature stable ceramic-coated separator prepared with polyimide binder/Al2O3 particles for lithium-ion batteries, J. Membr. Sci. 517 (2016) 91–99, http://dx.doi.org/10.1016/j.memsci.2016.06.035.

[102] A. Gogia, Y. Wang, A.K. Rai, R. Bhattacharya, G. Subramanyam, J. Kumar, Binder-free, thin-film ceramic-coated separators for improved safety of lithium-ion batteries, ACS Omega 6 (6) (2021) 4204–4211, http://dx.doi.org/10.1021/acsomega.0c05037?.

[103] A. Friesen, S. Hildebrand, F. Horsthemke, M. Börner, R. Klöpsch, P. Niehoff, F.M. Schappacher, M. Winter, Al2O3 coating on anode surface in lithium ion batteries: Impact on low temperature cycling and safety behavior, J. Power Sources 363 (2017) 70–77, http://dx.doi.org/10.1016/j.jpowsour.2017.07.062.

[104] H. Wang, Y. Zhu, S.C. Kim, A. Pei, Y. Li, D.T. Boyle, H. Wang, Z. Zhang, Y. Ye, W. Huang, Y. Liu, J. Xu, J. Li, F. Liu, Y. Cui, Underpotential lithium plating on graphite anodes caused by temperature heterogeneity, Proc. Natl. Acad. Sci. USA 117 (47) (2020) 29453–29461, http://dx.doi.org/10.1073/pnas.2009221117.

[105] P.P. Paul, V. Thampy, C. Cao, H.-G. Steinrück, T.R. Tanim, A.R. Dunlop, E.J. Dufek, S.E. Trask, A.N. Jansen, M.F. Toney, J. Nelson Weker, Quantification of heterogeneous, irreversible lithium plating in extreme fast charging of lithium-ion batteries, Energy Environ. Sci. 14 (9) (2021) 4979–4988, http://dx.doi.org/10.1039/D1EE01216A.

[106] N.R. Geise, R.M. Kasse, J. Nelson Weker, H.-G. Steinrück, M.F. Toney, Quantification of efficiency in lithium metal negative electrodes via operando X-ray diffraction, Chem. Mater. 33 (18) (2021) 7537–7545, http://dx.doi.org/10.1021/acs.chemmater.1c02585.

[107] W. Zhu, H. Demers, G. Girard, D. Clement, F. Zimin, A. Guerfi, M. Trudeau, A. Vijh, A. Paolella, Monitoring lithium metal plating/stripping in anode free//NMC811 battery by in-situ X-rays diffraction, J. Power Sources 546 (2022) 231941, http://dx.doi.org/10.1016/j.jpowsour.2022.231941.

[108] B. Epding, B. Rumberg, H. Jahnke, I. Stradtmann, A. Kwade, Investigation of significant capacity recovery effects due to long rest periods during high current cyclic aging tests in automotive lithium ion cells and their influence on lifetime, J. Energy Storage 22 (2019) 249–256, http://dx.doi.org/10.1016/j.est.2019.02.015.

[109] N. Ghanbari, T. Waldmann, M. Kasper, P. Axmann, M. Wohlfahrt-Mehrens, Detection of Li deposition by glow discharge optical emission spectroscopy in post-mortem analysis, ECS Electrochem. Lett. 4 (9) (2015) A100–A102, http://dx.doi.org/10.1149/2.0041509eel.

2.5 Impact of electrical contact resistances in fast-charged battery packs

Fast charging strategies for lithium-ion cells are commonly developed under controlled laboratory environments and later transferred to real-world applications (e.g., BEVs). During this transition, many additional pack-level aspects, such as the influence of balancing currents due to multiple lithium-ion cells connected in serial or parallel [211], varying thermal masses and thermal cell-to-cell effects [212], thermal management impact [213], or external electrical contacts and their resistance [214] need to be considered. As one supplement to this field of research, external electrical contacts have been investigated more thoroughly in this work.

Earlier work revealed that the electrical contact resistance (ECR) strongly differs between different experimental setups in laboratory environments and may lead to different thermal behavior of the lithium-ion cells under study [215, 216]. This issue is particularly interesting if high currents are applied in the future of ultra-fast-charged battery packs, as the high charging currents amplify the losses observable as parasitic heat (Joule heat) in the lithium-ion battery pack following a quadratic dependence on the charging current according to $P = I^2R$.

This section presents the results of a study investigating the impact of electrical contact resistance (ECR) on cell performance due to cell-to-cell joints, previously published by the author [217]. This study aims to quantify the thermal effects of fast charging current rates at battery module and pack level [217]. ECRs of different material combinations (e.g., Al-Cu) were compared based on a literature survey, revealing that industry-scale cell-to-cell joints, as shown in Figure 2.5, lie in a range of less than 1 mΩ as similar joining techniques are used. A simple loss model was used to show how the quadratic nature of the parasitic thermal impact at the cell tabs amplifies with larger current rates. To quantify the ECR present in lab-scale lithium-ion cell testing with reversible contacts and compare it to industry-scale contacts and real-world applications, ECR was measured with different contacting probes. Interestingly, simple one-pin contacts led to ECRs in a range of 22 mΩ far beyond the previously mentioned and targeted range of less than

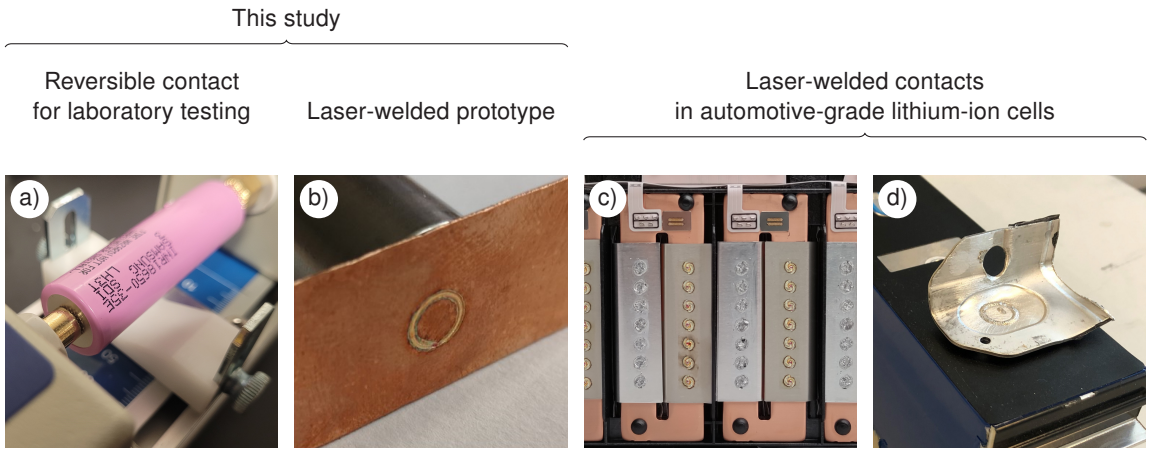

Figure 2.5: Visual comparison of lab-scale cell connections with cell connections present in industry-scale lithium-ion battery packs. (a) Typical reversible cell contact in laboratory environments, (b) laser-welded cell contact used to replicate industry-scale cell contacts, (c) cell contacts of a Volkswagen ID.3 1st edition (C/NMC) lithium-ion battery module, and (d) cell contacts of a Tesla Model 3 Standard Range+ (C/LFP) lithium-ion battery module. Images were collected from earlier work [217, 218].

1 mΩ. For a direct comparison, two different laboratory probes with varying contact resistances and a laser-welded benchmark were built and used to assess the temperature development of a cylindrical lithium-ion cell at both tabs and the cell center during a fast charge event. The laser-welded cell achieved lower cell center temperatures than the lab-scale cells, with more than 20 °C temperature differences of the cell center measurements at 5C. Moreover, the tab temperatures in both laboratory probes exceeded the core temperature at charging rates of 3C and larger. At the same time, the laser-welded cell reached the highest temperatures at the cell center up to 5C, with the tab temperatures never exceeding the cell center temperature. The lesser thermal impact was attributed to a faster thermal relaxation and lower peak temperatures of the laser-welded cells during long-term testing in contrast to the lab-scale cells. All measurements taken within this study were published as an open source [219].

The results reveal that fast-charged lithium-ion battery packs with low-resistance cell-to-cell joints, such as laser-welds, only suffer under low parasitic heat from the electrical connection even at high charging currents. Vice versa, lithium-ion cells tested in laboratory environments are strongly affected by parasitic heat from the cell tabs, which can be measured at the cell center. Therefore, the lithium-ion cell's thermal behavior in real-world applications can be expected to differ significantly from lab-scale cell-level tests if high currents are applied and no comparable ECR can be reached with reversible joints. Thus, the self-heating potential of lithium-ion cells under test may be overestimated compared to the real-world application. As elevated temperatures improve charge transfer and mass transport, the robustness against lithium plating may be overestimated, too. Beyond that and from a practical perspective, it was found that lithium-ion cell tests can be improved by simply scratching the contact pins on the lithium-ion cell tabs to remove the oxide layer and improve the electrical contact before long-term cell tests are carried out. This could be an advantageous method to keep the thermal interference of the ECR low even with simple contacting techniques in laboratory environments.

Author contribution: The general concept, methodology development, formal analysis, validation, investigation, and data curation was carried out by Nikolaos Wassiliadis except where noted otherwise. Manuel Ank supported the methodology development, formal analysis, validation, and investigation of the results in a preliminary study. Nikolaos Wassiliadis and Manuel Ank wrote the original manuscript. Leo Wildfeuer assisted in the formal analysis of the experimental data. Michael K. Kick provided the resources for the laser-welding of lithium-ion cells. Leo Wildfeuer, Michael Kick, and Markus Lienkamp reviewed and edited the original manuscript. Markus Lienkamp provided the supervision and resources.

Experimental investigation of the influence of electrical contact resistance on lithium-ion battery testing for fast-charge applications

Nikolaos Wassiliadis, Manuel Ank, Leo Wildfeuer, Michael K. Kick, Markus Lienkamp

Journal of Applied Energy 295, 2021
Digital Object Identifier: 10.1016/j.apenergy.2021.117064

Applied Energy 295 (2021) 117064

Contents lists available at ScienceDirect

Applied Energy

journal homepage: www.elsevier.com/locate/apenergy

Experimental investigation of the influence of electrical contact resistance on lithium-ion battery testing for fast-charge applications

Nikolaos Wassiliadis [a,*], Manuel Ank [a], Leo Wildfeuer [a], Michael K. Kick [b], Markus Lienkamp [a]

[a] Institute of Automotive Technology, Department of Mechanical Engineering, Technical University of Munich (TUM), Germany
[b] Institute for Machine Tools and Industrial Management, Department of Mechanical Engineering, Technical University of Munich (TUM), Germany

ARTICLE INFO

Keywords:
Electrical contact resistance
Thermal behavior
Lithium-ion battery
Fast charging
Battery testing

ABSTRACT

With the rising demand for electric vehicles with a fast-charging ability, high currents are applied to lithium-ion batteries to develop accurate battery models and intelligent fast-charging strategies. In order to achieve reliable results for automotive applications, single cell test conditions should be as close as possible to the conditions present in the battery pack of the battery electric vehicle. As cells are irreversibly connected in a battery pack, electrical contact resistance (ECR) is usually in the magnitude of <1 mΩ, and thus far lower than in reversible contacts during lab-testing. An interesting question arises as to whether this ECR has any unintended influence on the battery cell during testing. In this article, various experiments with high charge rates of up to 5 C are performed in order to assess the impact of the ECR of the measurement setup on the cells' behavior. Two different commercial contact probes with different ECRs are tested on a 18650 lithium-ion battery, and compared to a laser-welded cell as a benchmark. ECRs of the lab-testing setups are measured with a micro ohmmeter, and the temperature evolution of all cells studied is measured at both cell tabs and the cell mantle during cycling. The results show that high peak temperature differences due to parasitic joule heat at the lithium-ion battery tabs occur when applying full charge cycles from 0.5 C to 5 C. Repetitive cycling with a multistage fast-charging strategy indicates a correlation of ECR with peak temperatures and aging spread. As a consequence, high ECRs could negatively affect drawn conclusions of cycle life tests. They should therefore be taken into account and kept low in any examination of fast-charging strategies.

1. Introduction

The fast-charging of lithium-ion batteries (LIBs) has been identified as a key enabler of the world-wide adoption of battery electric vehicles (BEVs), tackling the concern of range anxiety of BEVs on long-distance trips [1–5]. The ability to charge a BEV in as short a time as it takes to refuel a combustion vehicle has therefore become the R&D goal of academia and industry. Charging times of approximately 15 minutes and lower involve charging at the physical limits of the LIB [6], posing the necessity for development and thorough experimental investigation of fast-charging strategies and accurate battery modeling for battery management system (BMS) prior to application. As such, intensive lab-testing is needed with conditions close to the conditions present in real-world applications, so as to be able to deduce reliable conclusions from the experimental observations.

Commonly in many energy applications, cells are connected in serial or parallel in battery modules, with non-detachable bonds between the cell tabs and bus bars/module current collectors. The resistance of those joints are usually far lower than internal resistances of the LIB itself. ECR is usually neglected during lab-testing, because it has no influence from an electrical viewpoint due to four-terminal sensing. However, ohmic resistances always lead to operational heat losses according to Ohm's law, in particular, if currents are large. With the upcoming large currents for fast charge applications, an interesting question arises as to whether the ECR of lab-testing is close to real world conditions and whether it has any unintended thermal influence on the measured cell behavior deteriorating experimental results.

1.1. Literature review

Many methods for the electrical and structural joining of individual cell tabs to module terminals currently exist and are used in various energy storage applications. Common materials in battery tab design are aluminum (Al) and nickel-coated copper (CuNi) for the positive and negative electrode, respectively, which have to be mounted to a cell can and module terminal material with high electrical conductivity [7]. Especially with cylindrical cells, a reliable solid-state

* Corresponding author.
E-mail address: nikolaos.wassiliadis@tum.de (N. Wassiliadis).

https://doi.org/10.1016/j.apenergy.2021.117064
Received 21 July 2020; Received in revised form 10 February 2021; Accepted 3 May 2021

Abbreviations

AC	Alternating current
BEV	Battery electric vehicle
BMS	Battery management system
CC	Constant current
CCCV	Constant current constant voltage
DC	Direct current
DUT	Device under test
ECR	Electrical contact resistance
EOL	End-of-life
HHS	Pressure film ~130 to 300 N/mm^2
HS	Pressure film ~50 to 130 N/mm^2
IECM	Interfacial electrically conductive material
LIB	Lithium-ion battery
LLLW	Pressure film ~0.2 to 0.6 N/mm^2
LLW	Pressure film ~0.5 to 2.5 N/mm^2
LW	Pressure film ~2.5 to 10 N/mm^2
MS	Pressure film ~10 to 50 N/mm^2
NCA	Nickel cobalt aluminum
NTC	Negative temperature coefficient
PCB	Printed circuit board
RPT	Reference performance test
SOC	State-of-charge
SOH	State-of-health

connection without a high temperature input into the cell is a difficult task and much effort is put into the correct tuning of process parameters or the finding of alternative non-heat-inducing techniques, such as mechanical clamping [8,9]. An overview of commonly used joining techniques and their accompanying ECRs is given in Table 1 and will be explained hereinafter. For further reference on joining techniques for battery module production, the reader is referred to the thorough reviews provided in the Refs. [10] and [11].

Resistance spot welding is based on the principle of applying high currents to the welding joint through a carrier substrate capable of high temperatures, inducing a high local heat gradient, and melting the surfaces of the connecting materials. The heat generated to fuse the targeted materials is focused on the welding spot, thereby inducing less heat into the battery cell core during manufacturing. However, due to a high likelihood of voids in welded nuggets, resistance spot welding is rather unsuitable for high-current applications such as fast-charging [10]. ECRs between 0.340 mΩ [12] and 0.167 mΩ [10] can be achieved, depending on the material.

Ultrasonic welding is a well-known technique for generating steady-state bonds between battery tabs and counter materials. Under a specific axial pressure, high-frequency lateral force is applied by a sonotrode in the range of typical 20 kHz [11], in order to generate heat at the welding spot by friction. Studies examining this technique achieved ECRs ranging from 0.169 mΩ [10] down to 0.005 mΩ [7].

Another important contacting technique is laser beam welding, in which high-energy laser-beams are directed at the contacting point to be welded and, due to local heating, are transformed into a materially bonded connection. This technique benefits from its energy- and time-efficiency, in reducing the thermal impact to battery cells during battery tab welding. ECRs as low as 0.130 mΩ [10] can be achieved.

As an alternative, mechanical clamping offers the potential of avoiding parasitic heat during the joining process. However, special attention must be paid in ensuring the correct adjustment of the applied force since mechanical deformations of LIBs, if occurring, can lead to a severe safety hazard. The authors Bolsinger et al. [9] provided an in-depth analysis of clamping batteries with varying force, indicating that ECRs of down to 38 mΩ can be achieved if copper is used as the counter material. Taheri et al. [16] investigated power losses due to ECRs in mechanical clamps, and emphasized the consequences on battery health and safety of parasitic tab heat during operation.

The literature overview proves that if materials are adequately prepared, ECRs below 1 mΩ and sometimes below 0.01 mΩ can be expected to be achieved in controlled series production processes of tab-to-busbar joints, by using state-of-the-art joining techniques. Besides earlier studies on resulting power losses, the question remains as to whether ECRs during lab-testing have any unintended influence on the achieved results, especially if fast-charging currents are applied.

1.2. Article contributions

The underlying study aims to clarify how far the ECRs of current lab-testing equipment differs from those of real-world automotive applications and, if differences are present, to quantify the impact on battery cell behavior during fast charging, it being the most challenging scenario. The main contributions can be summarized as follows:

1. **Comparison of the contact resistance of detachable and non-detachable automotive joints**
   An overview of ECR of state-of-the-art bonding methods is given, and contact resistances of two different state-of-the-art contacting pins are measured and compared. The difference between real-world non-detachable and detachable testing joints are highlighted.
2. **Impact on cell thermal behavior**
   Cell temperature evolution is measured during fast charging with two different state-of-the-art lab-testing contact pins with differences in ECR and compared to a laser-welded bond. The impact of ECR due to thermal conduction of power losses into the cell is shown to be relevant to the thermal behavior of the cell, especially under fast-charge-cycle testing.
3. **Impact on cycle life studies**
   The correlation of ECR and temperature evolution of cells under repetitive fast charge cycles are quantified by cycle life cell temperature histograms and cell capacity decay, indicating that contact resistance has an adverse impact on life-cycle studies .

1.3. Organization of the article

The remainder is structured as follows: Section 2 provides a theoretical background to contact resistance and its considerations in cell contacts for lab-testing. In Section 3, a detailed description of the battery cell under study, the experimental setup and testing procedures are given. The corresponding results are presented and discussed in Section 4. Based on the results, conclusions are drawn in Section 5. A brief summary of the implications of electrical contact resistance for battery cycle life tests involving fast-charging procedures is given in Section 6.

2. Theoretical background

In order to understand the origins of influences on the ECR in cell tests, the basics of metallic current-carrying contact partners must first be explained, as well as the projection to cell testing and the measurement principle.

Table 1
Literature review on ECRs of different material joints relevant to lithium-ion battery design.

Method	Author	Counter material	Tab material	Min. ECR in mΩ
Resistance spot welding	Brand et al. [10]	$CuZn_x$	$CuZn_x$	0.167
	Masomtob et al. [12]	CrNiMoTi	18 650 positive tab	0.170
		CrNiMoTi	18 650 negative tab	0.340
Ultrasonic welding	Brand et al. [10]	$CuZn_x$	$CuZn_x$	0.169
	Das et al. [7]	Cu	CuNi	0.005
		Al	CuNi	0.005
		Cu	Al	0.080
		Al	Al	0.065
	Shin and Leon [13]	Multilayer Cu	Cu	0.057
		Cu	Multilayer Cu	0.060
		Al	Multilayer Cu	0.072
		Multilayer Cu	Al	0.079
Laser beam welding	Brand et al. [10]	$CuZn_x$	$CuZn_x$	0.130
	Mehlmann et al. [14]	$CuSn_x$	Ni-plated steel	0.300
	Schmidt et al. [15]	Cu	Ni-plated steel	0.740
		Al	Ni-plated steel	0.740
		Ni-plated steel	Ni-plated steel	1.250
		Al	Al	0.250
		Cu	Cu	0.150
Mechanical clamping	Bolsinger et al. [9]	CrNiMoTi	CrNiMoTi	0.223
		Ni	CrNiMoTi	0.052
		$CuZn_x$	CrNiMoTi	0.050
		Al	CrNiMoTi	0.074
		Cu	CrNiMoTi	0.038
	Brand et al. [8]	Cu	Cu	0.018
		$CuZn_x$	$CuZn_x$	0.110
		Ni-plated steel	Ni-plated steel	0.186
		Al[a]	Al[a]	1.777

[a]Unpolished Al.

2.1. Fundamentals of electrical contact resistance

All surfaces of solid metals have a certain roughness on a microscopic scale [17,18]. Furthermore, it can be assumed that metallic surfaces in a natural atmosphere are completely or partially covered by thick impurity layers (a passivating film) [19]. In places with unevenness, mechanical contact occurs when two metals are pressed together under force. The load-bearing contact area A_{lb} describes only a fraction of the apparent contact interface with the area A_{app}, i.e. the surface on which a macroscopic contact occurs [18]. Depending on the contact pressure p, a deformation arises in ductile materials which deforms the highest microtips on the contact surface and thus increases the bearing contact surface A_{lb} [20,21]. During this process, the insulating tarnish films can tear open or be partially displaced into adjacent 'valleys' [18]. Due to these impurity layers on the metal surfaces, the electrically conductive area A_a is again smaller than the load-bearing area A_{lb} [20]. This effective contact area A_a describes the sum of all current-carrying contact areas (the so-called micro areas or a-spots), which are distributed unevenly on the apparent contact area A_{app} [18]. The following relationship applies, where the sum of the a-spots often results in less than 2 % of the apparent contact area [16,22]:

$$A_a < A_{lb} < A_{app} \tag{1}$$

Fig. 1 schematically illustrates the deformation of the rough surfaces of both metallic contact partners when applying a contact pressure p, including the possible current paths, the passivating films and the different contact surfaces [21,23].

The contact resistance R_c is composed of the sum of the two components constriction resistance R_{cr} and film resistance R_{fr} [18,23]. In addition, there is a negligible amount of resistance due to the disturbance of the periodicity of the crystal lattice in the metallic interfaces in the order of magnitude of $10^{-8}\,\Omega$ [18,19], leading to the following equation:

$$R_c = R_{cr} + R_{fr}, \quad \text{which is no longer permissible if } R_{fr} \gg R_{cr} \tag{2}$$

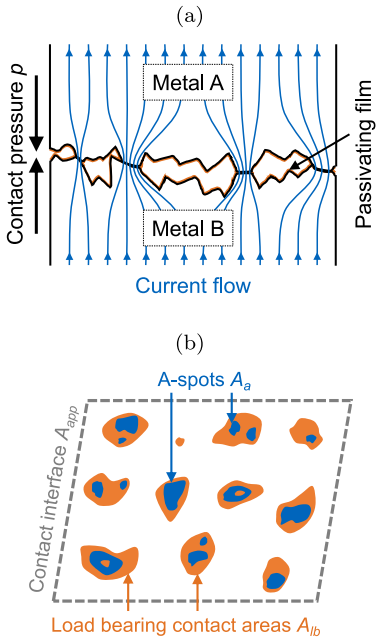

Fig. 1. Schematic representation of various aspects of contact resistance. Sectional view (a) laterally and (b) through the contact surface [21–23].

According to Holm [19] the possible points of contact can be classified with respect to the geometric shape of the surface:

1. **Metallic contact surfaces/a-spots** These areas only cause the constriction resistance R_{cr}, but not the film resistance R_{fr}.

2. **Quasimetallic contact surfaces** Such interfaces are covered with an adsorbed gas skin through which electrons can tunnel without loss.
3. **Semiconductive impurity layers** Electrons can no longer tunnel here, current flow only after mechanical destruction or electrical piercing.
4. **Mechanically bearing layers of another material** High resistance prevails here, up to the point of isolation.

The constriction resistance R_{cr} results from the constriction of the current paths in the micro-surfaces of the effective contact surface (Fig. 1(a)) and depends on the specific resistance of the material used, the surface irregularities and the number of effective contact surfaces [18]. The resistance component due to impurity films R_{fr} is caused by the reduced conductivity of the passivation layers on load-bearing contact surfaces which are not a-spots [21]. Corrosion-free precious metals such as gold, silver or platinum can be used to achieve low film resistance. In addition, the mechanical design of the contacts can ensure that the foreign layers of the contact pair are removed by friction.

The ECR of two compressed metals therefore depends on the contact pressure applied, the electrical properties of the metals and the surface microstructures. The following methods can be used to reduce the resistance [16,22]:

1. **Application of cohesive bonding** This can be achieved by brazing or welding the contact surfaces, for example.
2. **Use of interfacial electrically conductive materials (IECMs)** In such cases, contact lubricants or electrical grease can be applied, which can conform to the imperfect surface properties of the mating surfaces.
3. **Increase of the effective contact surface** A_a This can be achieved by increasing the contact pressure p or by reducing the surface roughness of the contact surfaces.

2.2. Considerations of electrical contact resistance in cell contacts for lab-testing

For battery contacts in test environments, not all of the points listed in Section 2.1 can be used to reduce the contact resistance: cohesive bonding is favorable but not suitable due to the necessary reversibility, while the use of IECM is conceivable, but leads to an increasing set-up effort for the use of cell holders in test environments, thereby counteracting the need for quick testing during multiple cell tests with different test devices. In the best and last case, the surface of the contacting element (e.g. a contact probe) is designed in such a way that it pierces any foreign layers on the contact partner, and at the same time provides sufficient effective contact surface A_a.

In addition, a large number of requirements are placed on the material contacting the cell. In the ideal case, the material has sufficient ductility and nevertheless avoids permanent deformations. Virtually wear-free material is advantageous for the service life of the contacts. In addition, the contact material must not corrode with the adjacent materials, otherwise the electrical contact may be lost [24]. The specific resistance of the contact metals, which represents the reciprocal of the electrical conductivity and is temperature-dependent, must also be taken into account [25].

For use in battery test scenarios, spring-loaded contact pins in receptacles with different diameters have been proven to reliably transmit the required currents. These components, which are designed for high cycle stability, are based on spring contact probe technology, which has been tried and tested for several decades and is used in printed circuit board (PCB) and chip tests. Usually such a contact probe consists of a plunger which moves in a cylinder or barrel, whereby a pre-stressed internal spring provides the desired contact pressure [26]. Theoretically, a large planar surface of the plunger tip would be ideal for the transmission of large currents. However, since in reality there are contamination particles on the contact surfaces, no reliable contact could be guaranteed. The other extreme would be a contacting mandrel, where the danger of sparking would increase. A compromise is to use a wafer shape on the pins, which penetrates any barrier layers on the surface to be contacted and also minimizes wear and possible marks on the device under test (DUT). Without penetration of these layers, no electrical connection is created. The contact forces are also of great importance: high forces counteract contamination, but lead to undesired increased wear. If the forces are too low, the contact tends to rebound elastically against the suspension during movements. The optimum contact pressure of a contact is therefore usually determined experimentally.

Coaxially designed high-current probes, well-known as Kelvin probes, combine the possibility of four-terminal sensing with low ECR through the use of separately spring-loaded single probes, intelligent material selection and wafer-shaped tip geometry. However, considerable differences exist in the ECRs of these contact pins. A high resistance can be disadvantageous in this application, since ohmic resistances convert electrical energy into thermal energy when a voltage drop occurs due to the present current. Each heat input into the battery cell to be tested has a parasitic influence on the cell temperature, and thus on the overall properties of the cell. The specified measurement conditions would no longer be given in the event of strong heat development at the poles – a measurement error can occur which is considerably more substantial with impedance measurements due to the AC characteristic and sensitivity than with DC techniques).

In the larger system environment (globally), the temperature differences are usually compensated by a climate chamber, but locally this can only be done by a low contact resistance at the contacting elements, since these directly border the cell poles and thus open up a short path of heat transfer to the inner cell chemistry.

Fig. 2 shows the theoretically resulting power loss P_{Loss} at different ECRs and applied currents I_{DC}. Furthermore, if a fictitious cell is used with a lumped 1D-thermal model according to

$$dT = \frac{dQ}{C} = \frac{P_{Loss}}{C} = \frac{R \cdot I^2}{m \cdot c}, \tag{3}$$

with the specific heat capacity $c = 900\ \mathrm{J/K}$ and the cell mass $m = 0.05\ \mathrm{kg}$, the resulting heat generation rate dT_{Cell} and C-rate emphasize the need for low ECRs if high currents are applied.

3. Experimental setup

Various tests with two different contacting probes and one laser-welded benchmark were carried out as part of this study, as illustrated in Fig. 3. In the following, the equipment used, the experimental setup and the procedures of the tests are described.

3.1. Battery cell under study

The investigation is carried out with a cylindrical cell of Sony US18650VTC5A type as a representative battery cell format with critical structure prone to parasitic thermal impact of disadvantageous ECRs. If parasitic heat is generated at the tabs of the 18 650 battery cell, short thermal heat conduction paths to the cell core lever undesired effects during testing. In general, the examined cell is capable of accepting higher charging currents due to its anode structure, which in turn is expected to accelerate the impact of repetitive fast charging: low cell-core temperatures could increase relative temperature differences between core and tab, increasing the transport of malicious parasitic heat, and leading to accelerated thermal aging of the battery cell. A summary of the cell specifications can be found in Table A.1.

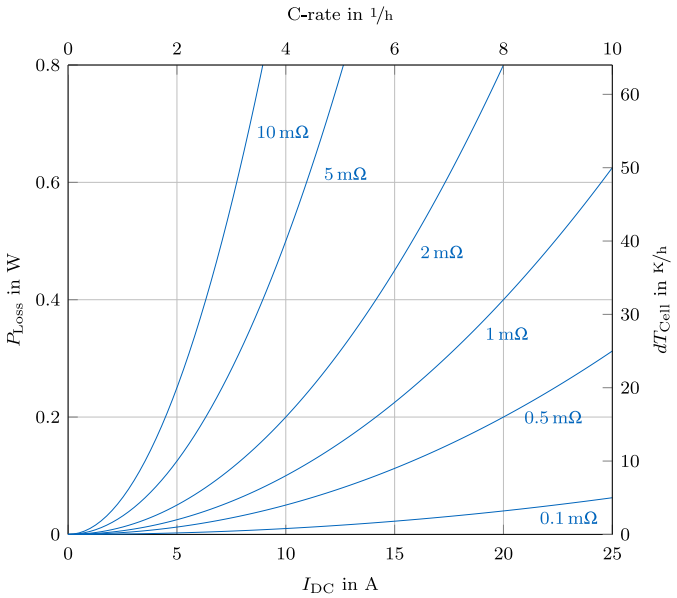

Fig. 2. Theoretical thermal impact of electrical contact resistance to lithium-ion batteries. Note that the illustrated C-rate and heat generation rate are related to a fictitious cell with 2.5 A h capacity, 0.05 kg thermal cell mass and 900 J/kg K heat capacity.

3.2. Preparation of benchmark laser-welded contacts

In order to compare the thermal impact of the probes versus a manufacturing process of series production, battery cells and cell connectors made of 0.3 mm thick and 20 mm wide copper sheets were contacted using laser beam welding. The frequency-doubled disk laser TruDisk 1020 and a programmable focusing optics PFO 20-2 were used to produce a circular weld seam geometry with a radius of 2.5 mm. The welding process was conducted with a laser power of 1000 W, a welding speed of 230 mm/s, and a spot diameter of 160 µm on the top surface.

3.3. Test setup and procedure

Prior to cell cycling, ECRs at the contact pins are measured with a Chauvin Arnoux 6250 micro ohmmeter with a resolution of 0.1 µΩ and a corresponding accuracy of 0.05 %. Two measurement paths are used, as illustrated in Fig. 4, to ensure reproducible measurements and ECRs are calculated by subtracting path B from path A. For the sake of simplicity, only one contact pin of each model is measured, since all structurally identical contact pins should be maintained in a similar range. The specifications of the contact probes can be retrieved from Table A.2.

Subsequently, all cells are connected to a Basytec XCTS battery cycler. Three NTC temperature sensors are positioned close to the contacts and at center of the cell mantle using heat transfer compound, to ensure correct thermal contact during measurement. All experiments

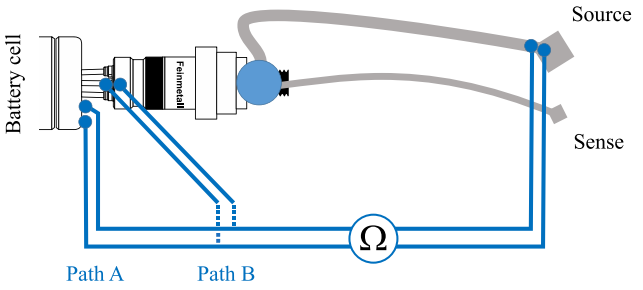

Fig. 4. Experimental setup with measurement paths associated with Table 2 to determine the ECRs of the contact pins with a micro ohmmeter. The decisive ECR values are determined by subtracting the measured readings of path B from those of path A.

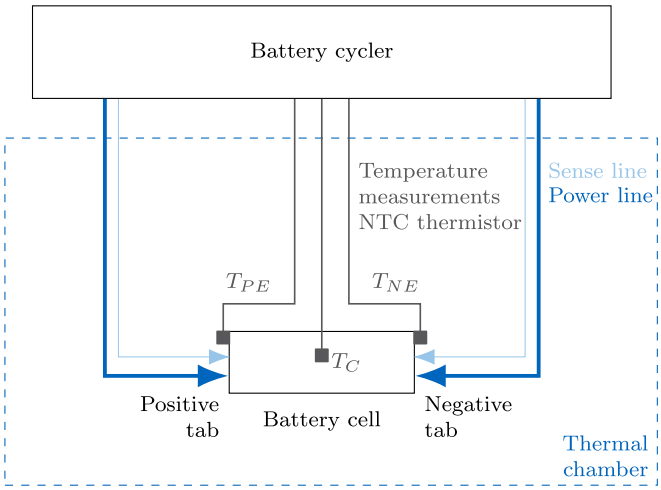

Fig. 5. Sketch of the experimental setup with three NTC temperature sensors used, connected to both cell tabs and the mantle with thermal-conducting compound. The overall setup is contained in a thermal chamber regulated to 25 °C.

are performed within a thermal chamber at 25 °C. The overall setup is illustrated in Fig. 5.

Three identical LIBs are measured synchronously, connected to the two different contact pins and laser-welded as a reference. To avoid an impact on the cells' behavior due to aging, all cells are first cycled with a constant current constant voltage (CCCV) charge to 4.15 V and a consecutive CCCV discharge to 2.5 V, reflecting the full operating range provided by the cell manufacturer. Subsequently, the cells are kept at rest for a period of 4 h to ensure an electrically and thermally relaxed state prior to fast charging. After the relaxation, the cells are charged at the target fast-charge rate, starting at 1 C increasing to 5 C. The test procedure is illustrated in Table B.1, with a 5 C charge rate taken by way of example.

(a) Probe 1: Full view and top view tip geometry

(b) Probe 2: Full view and top view tip geometry

(c) Laser-welded benchmark

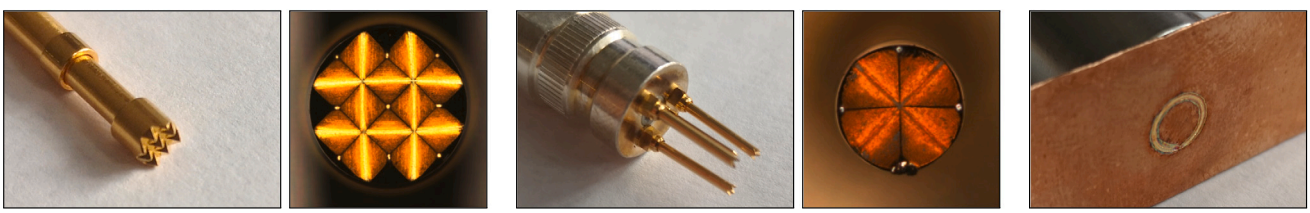

Fig. 3. Two different contact probes with their wafer-shaped tip geometry (a, b) and the laser-welded contact as a benchmark (c).

For the cycle life tests of Section 4.4, cells with the low, high ECR and laser-welded connection are each repetitively cycled with a multistage fast charge protocol in the charge direction and a 1 C CC discharge within the aforementioned voltage range. The multistage fast charge protocol starts with a 5 C charge phase until a voltage limit of 4.15 V is reached, then the charging rate is reduced by 2 C. If 1 C is reached, the cell is fully charged by a CCCV protocol. After 25 fast charge cycles, a reference performance test (RPT) with a capacity measurement is performed. The cells are cycled until 70% of the nominal capacity remains, which is defined as the batterys' end-of-life (EOL). The procedure is summarized in Table B.2. For each setup, two cells are synchronously cycled.

4. Results and discussion

The results of the experiments are presented hereinafter. The pressure distribution analysis will be addressed first, before the ECR measurements. The impact of the ECRs on the thermal and cycle life behavior will be discussed on the basis of further experiments.

4.1. Pressure distribution analysis of the two investigated contact probes

The pressure distribution between two components can be illustrated with Fujifilm's Prescale pressure film, where the surface pressure can be determined from the color depth. For low to medium pressure ranges, this is done by positioning a two-sheet type (two matching Prescale films, placed with the matt sides on top of each other) between the surfaces where the pressure is applied [27]. For medium to high pressure ranges, a mono-sheet type is used, which is inserted directly between the load surfaces [27].

The foil models for "ultra super low pressure" (LLLW), "super low pressure" (LLW), "low pressure" (LW), "medium pressure" (MS), "high pressure" (HS) and "super high pressure" (HHS) are used to visualize the pressure distribution at the two contact probes at pressure ranges from 0.2 to 300 N/mm^2 (specifications of the films can be taken from the product data sheet of the manufacturer [27]). When pressure is applied, the microcapsules in the film are destroyed, causing the color-developing layer to absorb the color-forming material, thereby generating a red coloration [27]. The test is carried out at nominal clamping length to represent the standard case, whereby the foils are each stressed for about 60 s. After exposure, the sheets are removed and the matching foils of the two-sheet type are separated again. The colored films are then visually inspected and scanned with high resolution.

The resulting pressure distributions of the experiment are shown in Fig. 6, with the geometric arrangement of the individual contact pins of Probe 2 clearly visible: the three concentrically arranged pins enclose the decentrally arranged sense pin. The tip geometry of the current-carrying contact pins is also apparent: due to the wafer shape, four tips per contact element contact the cell pole. This is particularly noticeable in the pressure distribution of the HS-film, as here only the points with high contact forces are colored red. The scattering of the pressure input increases with the use of more sensitive pressure measurement films — with the films of the type LLLW, LLW and LW 'smudging' the actual pressure points. The foils used to represent higher pressures act like a filter on these parasitic influences. From the pressure ranges investigated, it can be concluded that the maximum pressures present at individual contact points are between 50 and 130 N/mm^2 (the pressure range of the HS film). A pressure greater than 130 N/mm^2 does not have an effect, otherwise they would be visible in the HHS film.

The contact pressures for Probe 1 are mainly below 10 N/mm^2 (the pressure ranges of the films LLLW to LW), at higher pressures only a few force transfer points are visible. In the pressure distribution image of the HS-film only a single point of small size is observed. This is assigned to the eccentrically located sense pin and not to the screened current

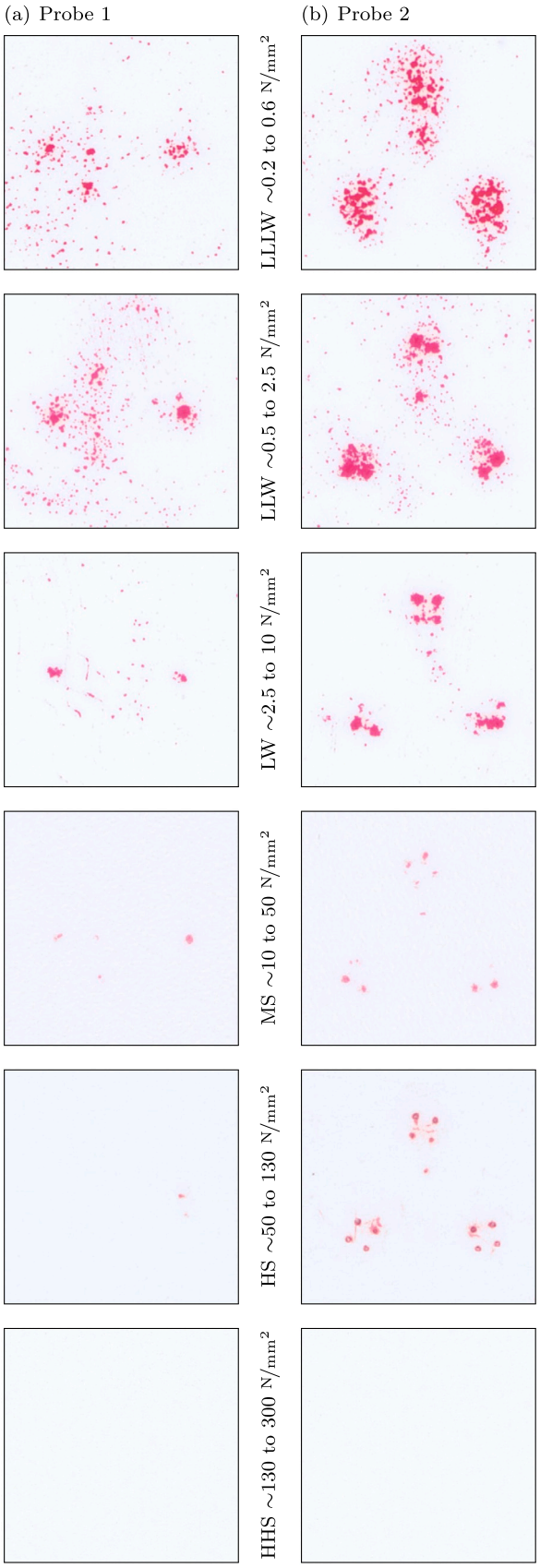

Fig. 6. Pressure distribution of the two investigated contact probes with pressure measurement films. Pressure sensitivity decreases from top to bottom, indicating a better electrical contact surface of (b) Probe 2 than (a) Probe 1. The images are matched with the Prescale film type and associated pressure range.

Table 2
Measured ECRs between the cell terminal and the source contact at the contact probe. Two different contact probes were tested (Feinmetall model F79606B230G300 as Probe 1 and Feinmetall model HC06B29010G as Probe 2). All measurement paths were repeatedly measured with a Chauvin Arnoux 6250 micro ohmmeter at approximately 25 °C and a time delay of 20 s to eliminate systematic measurement errors. All measured ECRs of Probe 2 were divided by three due to the presence of three electrical contacts in parallel per design.

Measurement configuration	Probe 1		Probe 2
	Clamped only	Clamped and twisted in mΩ	Clamped only
Measured ECRs	19.138	4.574	0.561
	15.139	4.288	0.573
	16.073	4.873	0.554
	18.769	5.136	0.545
	18.806	9.583	0.542
	19.336	5.441	0.555
	17.318	6.794	0.547
	18.072	4.601	0.567
	16.753	4.540	0.572
	16.141	5.180	0.545
	19.273	4.012	0.583
	18.005	4.872	0.563
	25.657	4.737	0.535
	26.521	4.522	0.546
	16.006	5.702	0.540
	17.274	4.923	0.614
	22.649	4.167	0.517
	24.550	3.969	0.532
	22.625	3.901	0.519
	26.148	3.985	0.524
Mean value	19.713	4.990	0.552
Standard deviation	3.647	1.284	0.023
Coefficient of variation	0.185	0.257	0.042

contact pin. The source contact element causes several contacting paths of lower contact pressures.

When comparing the pressure distributions of the two contact probes, it becomes apparent that Probe 2 has a significantly higher contact area at higher contact pressure. This results in a lower contact resistance of the press contact. Probe 1 has a considerably smaller contact area available for current transfer, and the screened tip geometry is also less pronounced in the distribution image. Due to the higher contact pressures and the superior tip geometry of Probe 2, even stronger contamination and thicker barrier layers on the cell poles are successfully penetrated. It was demonstrated that a pressure distribution analysis of contact pairs can already provide initial indications of the anticipated performance of the respective joint.

4.2. Electrical contact resistance measurements

The results of the resistance measurement on the two contact pins are shown in Table 2. Both contacting probes were measured after the battery cell was clamped, with Probe 2 making a scratching movement on the surface during clamping due to its angled design that pierces any impurity layers, as illustrated in Fig. 7. Here, the angle of the external current-carrying contact pins of 2.5° each causes a scratching motion of 0.044 mm on the cell surface per millimeter of spring deflection. Probe 1, on the other hand, is arranged orthogonally to the cell pole surface and therefore does not automatically scratch any foreign layers during the clamping process. In order to simulate the scratch effect with Probe 1, a further procedure was carried out in addition to measuring the basic clamping process: after clamping, the battery cell was rotated manually around the cell center axis so that the surface of the cell pole is scratched by the Probe 1 pressing on it, also illustrated in Fig. 7.

In addition to the measured values, Table 2 shows the mean values, standard deviations and the coefficient of variation of each measurement configuration. It becomes clear that Probe 2 is of two magnitudes

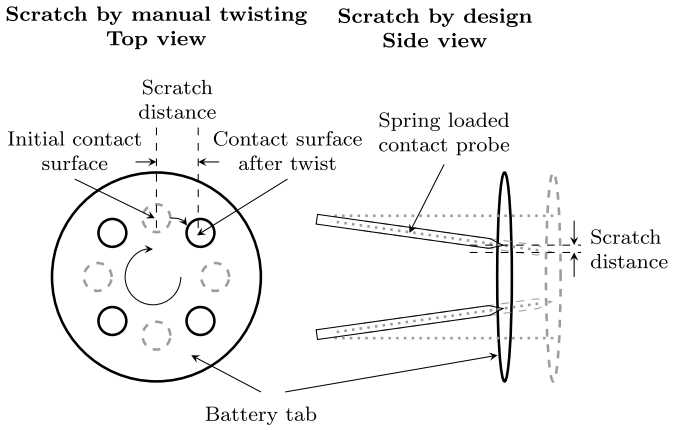

Fig. 7. Principle of decreasing ECR by manually twisting the non-angled contact probe (left) or scratching the battery tab surface per angled design (right).

less and, according to Fig. 1, has a significantly lower ECR than Probe 1. ECRs achieve values around 0.552 mΩ. The variation between the individual measurements is also lowest with Probe 2, with reliability increasing if multiple cell tests are performed. The contact resistance of Probe 1 can be significantly reduced by axially twisting the battery cell after the clamping process, but it is still one magnitude higher than with Probe 2. In addition, the coefficient of variation is highest in this measurement configuration, since the individual values of the measurements sometimes deviate greatly due to the manual rotation of the cell.

The available data demonstrates that there are major differences in the ECR of contact probes for battery tests resulting from the probe design. An angled design leads to a reproducible penetration of foreign layers with low variation, whereas a contact probe with multiple current-carrying contacts further reduces the existing resistance by parallel connection. The achieved low ECRs are close to irreversible ECRs of state-of-the-art manufacturing processes, as introduced in Section 1.1. Manual piercing of the impurity layers by twisting the cell leads to an improvement of the contact quality, although it causes unintended high variation between the measurements leading to unreliable connections. The order of magnitude of the ECRs in the case of multiple current-carrying contacts is unmatched by single current-carrying contacts. If a reproducible low ECR is required when contacting batteries for high current applications, contact probes similar in design to Probe 2 are recommended.

4.3. Impact on cell thermal behavior under different charge rates up to 5 C

Fig. 8 shows the measured temperature evolution of all three NTC thermal sensors for charge rates from 0.5 C to 5 C of the investigated LIB. For each charge rate, measurements were performed with bad/high and good/low ECRs by varying the contact probes of the cell holder (Section 3). In addition, the temperature development of a laser-welded connection to the cell with a similar thermal sensor arrangement is presented as a benchmark.

It is apparent that higher charging rates result in higher temperatures at all sensors. For example, at a charge rate of 0.5 C, maximum temperatures of up to 21.5 °C are observed, while temperatures of up to 31.3 °C are reached at 2 C, and even of above 60 °C at 5 C. A higher heat input at a higher current flow is to be expected due to the fundamental relationship $P = R \cdot I^2$, whereby higher power losses occur when a higher charging current is applied. Furthermore, the instantaneous rise in temperatures after the start of the current load is visible. The time of the temperature maxima matches the end of the charging period. A non-instantaneous drop in temperature is attributable to the response

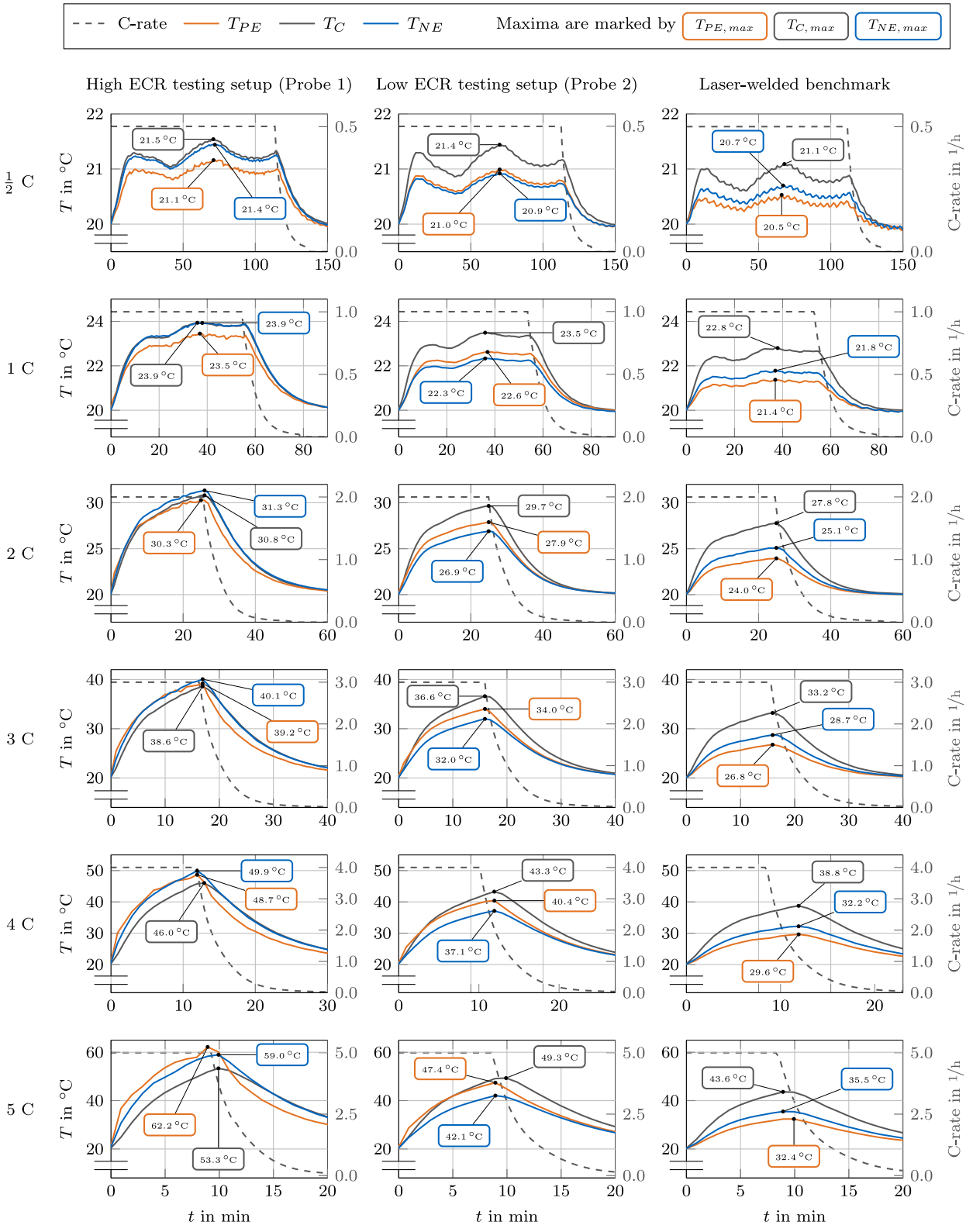

Fig. 8. Measured temperature evolution of all three NTC thermal sensors and applied C-rate for different charge rates as well as high and low ECRs at the left and the center, respectively, starting at 25 °C ambient temperature. Laser-welded benchmark temperature evolution with similar thermal sensor setup at the right.

time of the sensors used, but mainly due to the generated and available heat output.

The temperature evolutions of the positive and negative tabs of the cell (T_{PE} and T_{NE}) for all three setups (high and low ECR testing setup as well as the laser-welded benchmark) show a comparable progression on a roughly similar scale. However, an inconsistent behavior is apparent in the low ECR testing setup (use of Probe 2): the temperature curve of the positive tab is constantly higher than that of the negative tab — unlike in the other two setups. This may be caused by various effects, which are, however, not of importance in this work, since the decisive

characteristic curve for assessing the influence of contact resistance is the temperature development of the cell mantle surface T_C, which most closely reflects the value of the cell core temperature.

Minor outliers, such as the overshoot of the positive temperature measurement at 5 C of the high ECR testing setup (use of Probe 1), are due to the particular measurement arrangement and the local system characteristics. They do not alter the general picture of the developments.

Looking at the temperature development at the cell mantle surface T_C, there is a distinct tendency when comparing the three setups: in the high ECR testing setup (use of Probe 1), comparatively high temperature maxima are measured on the cell mantle surface, which are significantly reduced in the low ECR testing setup (use of Probe 2). The development is in line with expectations: at lower ECRs, the maximum temperature of the cell mantle surface approaches the temperature evolution of the laser-welded benchmark. This confirms that the ECR has a definite influence on the temperature development of the cell in lab-testing scenarios. The lower the present ECR, the lower the occurring temperatures and maxima.

The graphs of the three setups at the same C-rates are remarkably similar in shape, which suggests that the series of measurements was performed properly. Furthermore, a strong correlation between the graphs of the cell mantle surface and those of the positive and negative tabs is evident, which suggests a well-defined thermal coupling of the surveyed cell regions.

In conclusion, a significant influence on the temperature at the cell mantle can be determined with a worst-case temperature difference of approximately 25 K compared to laser-welded cells, which are usually deployed in automotive applications. Whether the measurements with a higher ECR show a higher temperature of the cell core compared to the measurements with a lower ECR can neither be excluded nor proven by this experiment. However, due to the perceptible differences in cell mantle temperature at varying ECRs across the different charging rates, it is likely that there is a substantial deviation in cell core temperature.

4.4. Impact on cell behavior over cycle life

To substantiate the aforementioned observations and translate them to applications, the results of repetitive fast charging with the multistage CC charging protocol described in Table B.2 are shown in Fig. 9. Fig. 9(a) shows that the multistage fast-charging protocol yields 80 % SOC in approximately 10 minutes, as expected by experimental design. For the further analysis hereinafter, the temperature behavior of the LIBs is investigated in the next paragraph and supported subsequently by aging behavior analysis.

Within Fig. 9(b), measured peak temperatures at the cell mantle are shown during the fast charge period over the cycle life. As studied before, cell mantle temperatures are increased with increased ECR. Differences of around 5 °C are present between the worst contact and the laser-welded benchmark, leading to the conclusion that tab temperatures may be worse, as has been observed previously. Surprisingly, the low ECR contact probes do not lead to significantly decreased cell mantle temperatures. This may have multiple reasons. Since this phenomenon is observed only for the lower ECR contact probe in contrast to the laser-welded contacts, the contamination of the low ECR contact probe with thermal conductive compound originating from the prior setup may be possible, even though a thorough cleaning in ultrasonic baths was performed prior to testing. In turn, as observed earlier during single cycling, parasitic heat may not be clearly detectable at the cell's mantle, because charging times may be too short to allow for sufficient heat transfer from the cell's core to the mantle sensor setup. The latter may be visible if aging paths are investigated. In Fig. 9(c), the normalized distribution p of the cell mantle temperature is illustrated for the individual contacts/contact types for further analysis of the thermal development during fast charging. At first glance, a strong peak at ambient temperatures of the laser-welded setup is visible, originating from a faster thermal relaxation than the contact probes, as LIBs cool down earlier because of lower cell temperatures during fast charging. This interpretation is supported by the secondary peaks observed at high temperatures, where peaks in temperature distribution correlate with the ECR of the deployed setups. Based on the observations, significantly slower aging may be expected for the lower ECR setups, i.e. the low ECR and laser-welded setup, due to lower rest time at high temperatures and lower overall peak temperatures.

Fig. 9(d)–(f) further extends the analysis with the cell performance in terms of capacity decay over the cycle life. For a common understanding of the used quantities, we refer to the definition of SOH according to

$$\mathrm{SOH} = \frac{C}{C_N}, \tag{4}$$

where C denotes the actual cell capacity and C_N denotes the normalized cell capacity, determined at the initial capacity characterization cycle. For further analysis of the aging spread between the two cells used in each setup, we define

$$\Delta\mathrm{SOH} = \frac{|\mathrm{SOH} - \varnothing\mathrm{SOH}|}{\varnothing\mathrm{SOH}}, \tag{5}$$

where we normalize the SOH difference of one cell to the SOH average of both cells.

Interestingly, if the first 100 equivalent full cycles (500 A h) are analyzed in Fig. 9(d) in the first place, capacity decay slows down for the laser-welded benchmark and is accelerated for the low and high ECR setups. No clear aging trend differentiation can be deduced from the low and high ECR setup. However, the accelerated aging behavior of the two ECR setups compared to the laser-welded cell confirms a correlation between temperature conditioning times and aging speed of Fig. 9(c). Conversely, aging speed increases with the low ECR contact probe compared to the high ECR contact probe, despite slightly higher peak mantle temperatures. Here, no clear conclusion can be drawn which would support prior observations.

If aging results are analyzed in a neighborhood close to the EOL at around 70 %, as depicted in Fig. 9(e), the trend of reduced aging of the laser-welded cells, and accelerated aging of the low and high ECR cells can be further pursued. The lab testing probes fail earlier than the laser-welded probes, with exception to the cell 2 high ECR probe. Apparently, aging paths of the laser-welded cells do not differ significantly in contrast to the high variations in low and high ECR cells, which should be further analyzed.

Accordingly, Fig. 9(f) presents the aging spread between the two cells used in each setup in percent to the mean value of each cell pair over the cycle life. With increasing ECR, the aging spread also increases with increasing cycle life of the cells under study. In particular, if 0.5 % are taken as a threshold, the earliest divergence occurs within the high ECR setup. At two-fold greater charge throughput, the low ECR setup follows. The most stable aging behavior can be observed for the laser-welded setup. Consequently, the results support the hypothesis that ECR affects the battery cycle life and lead to the conclusion that the aging path correlate with ECRs of the investigated setups. However, only two cells in each setup were used, which should be further elaborated within future studies.

5. Conclusions

Based on the aforementioned results, variations in temperature and cycle-life impact of different electrical contact resistance (ECR) setups are present even at the low capacity cell level and currents investigated within this study, from which we can conclude that the ECR setup should be strongly considered in model-validation procedures and cycle-life studies if fast-charging strategies are investigated. If ECR is neglected, differences in peak temperatures and aging paths can be expected. This effect is expected to be reinforced if lithium-ion batteries with larger capacities are used, as it is common in the development of

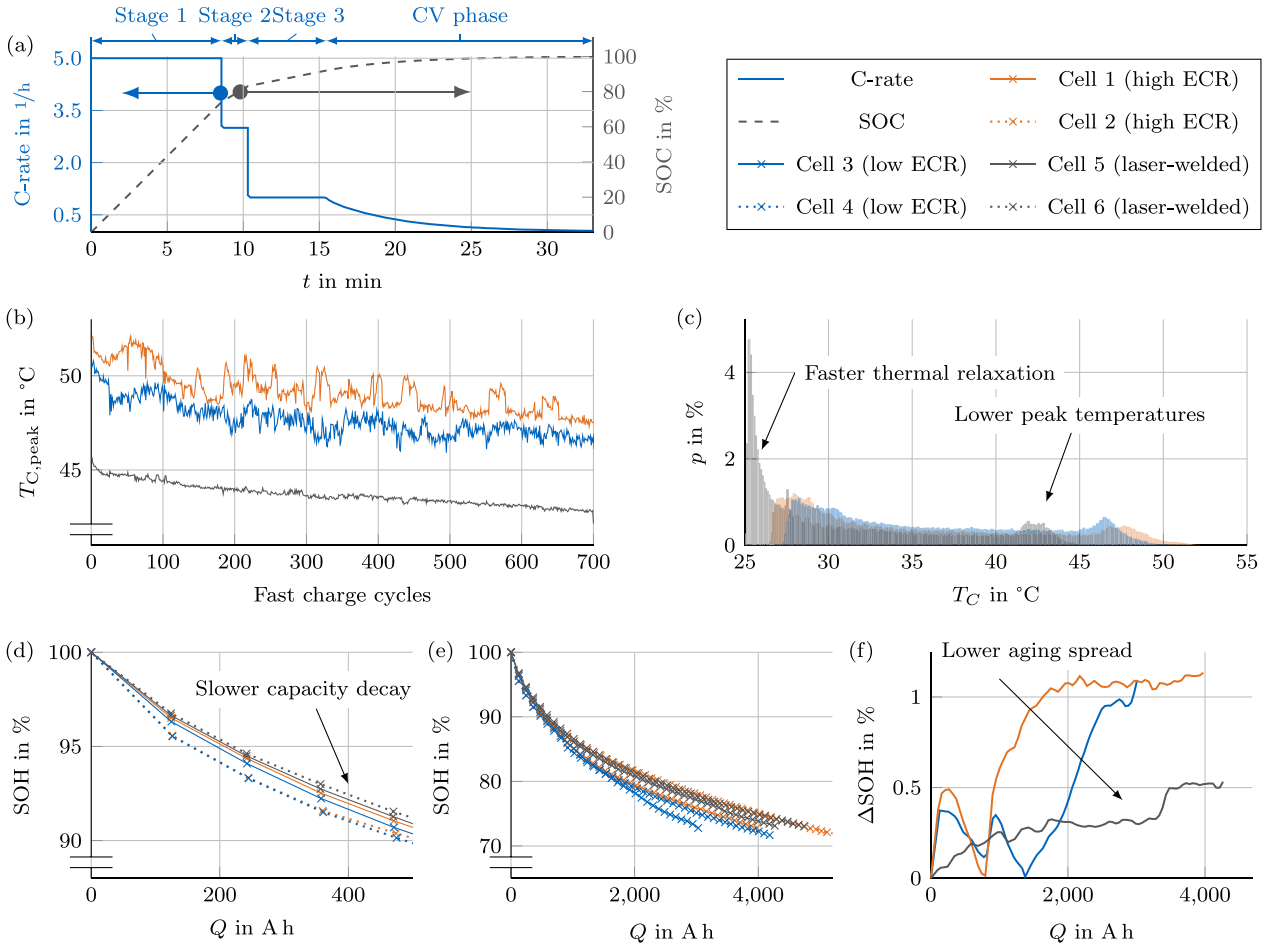

Fig. 9. Overview of the behavior of the cells under study during repetitive multistage CC fast charging. (a) Single fast charge cycle illustrating the applied CC stages and SOC over time, (b) peak cell mantle temperatures during charge phases over the first 700 fast charge cycles, (c) normalized distribution p of the cell mantle temperature during fast charge, (d) SOH over the first 500 A h and (e) overall SOH and (f) SOH deviation over charge throughput.

current automotive battery packs and increases the absolute current at a given C-rate. Measured cell temperatures may be superimposed by parasitic heat of an artificial nature, and do not represent the conditions present in real-world applications, leading to an overestimation of short-term battery thermal behavior if battery models are validated accordingly. If the battery thermal behavior on module or pack level is of special interest, the battery parasitic heat may be overestimated. With regard to the long-term cell behavior in cycle life studies, the resulting peak temperatures in the cell core may aggravate electrolyte decomposition and interfere with temperature-driven cell reactions, which in turn further deteriorate aging studies with projections to real-world laser-welded applications. If cycle life studies with short thermal relaxation phases between the cycling are performed, the ECR setup should be as low as possible to avoid accelerated aging due to increased average cell temperatures by parasitic heat generated at the cell tabs. This may further reduce aging spread and avoid an overly conservative estimate of the cycle life of a given battery cell under excessive fast charging. If mean values of the cell pairs are taken and the results are extrapolated from the undertaken study, real-world cells may have a longer cycle life than commonly expected from lab-testing results.

6. Summary and recommendations

The main goal of this study was to evaluate the impact of different ECRs during battery testing with fast charge protocols and compare them to state-of-the-art automotive joining techniques. Two different setups with varying ECRs to the battery tab were examined. ECRs were quantified in both setups with a difference of up to two magnitudes. Only the angled scratch contact achieved ECRs below 1 mΩ close to non-detachable bonds of state-of-the-art manufacturing processes. In a cell study, both tab and cell mantle temperatures were measured during CCCV charging up to 5 C, and compared to a laser-welded cell with a similar temperature measurement setup. Peak temperatures at the tabs in the high ECR setup exceeded the temperatures of the low ECR setup with approximately 15 K difference present at 5 C charging, and approximately 25 K difference compared to the laser-welded cell. In a second study with repetitive fast-charging cycles, different aging paths evolved for the cells under study, and aging spread increased with increasing ECR.

For the investigation of fast-charging strategies, ECRs during lab-testing should be considered and reduced to the actual ECR in series production, so as to reduce the parasitic heat generated at the tabs, to avoid malicious thermal influence on the battery cells under study, and to secure reliable conclusions for real-world applications. In particular, the contacting techniques and the expected ECR during testing should be considered and mentioned, if fast charging is investigated, to avoid misinterpretations in terms of overestimation of the cell's thermal behavior or underestimation of the achievable battery cycle life in automotive applications.

The findings should be further confirmed by simulations or additional experimental studies with other cell formats to provide further insights into the thermal heat conductive paths of the parasitic heat generated due to ECRs in lab-testing setups.

CRediT authorship contribution statement

Nikolaos Wassiliadis: First author, Conceptualization, Methodology, Formal analysis, Validation, Investigation, Data Curation, Writing - Original Draft, Visualization. **Manuel Ank:** Methodology, Formal analysis, Validation, Investigation, Data Curation, Writing - Original Draft, Visualization. **Leo Wildfeuer:** Formal analysis, Writing - Review & Editing. **Michael K. Kick:** Resources, Writing - Review & Editing. **Markus Lienkamp:** Writing - Review & Editing, Resources, Supervision.

Declaration of competing interest

The authors declare that they have no known competing financial interests or personal relationships that could have appeared to influence the work reported in this paper.

Data availability

Raw measurement datasets related to this article can be found via https://doi.org/10.14459/2021mp1611393, provided by mediaTUM.

Acknowledgments

We would like to thank the Bavarian Research Foundation, Germany for financially supporting this contribution within the project 'Nutzerorientierte Elektromobilität' under the project grant AZ-1203-16 and the Federal Ministry for Economic Affairs and Energy, Germany (BMWi) within the project 'ReVISEDBatt' under the project grant 03ETE004B. Moreover, we thank Kratzer Automation AG for supporting the underlying study with material, Sophie Ziegler for supporting the measurements and Florian Biechl as well as the staff from our laboratory for their helpful advice.

Appendix A. Specifications

Table A.1
Cell specifications of the device under test taken from the data sheet of the cell manufacturer, except where noted otherwise.

Attribute	Specification
Manufacturer	Sony
Cell type	VTC5A
Cell top	Flat
Cathode chemistry	NCA
Anode chemistry	Si-doped Graphite
Rated capacity	2.5 A h
Nominal voltage	3.6 V
Energy density	196 $^{Wh}/_{kg}$ [28]
Recommended charge rate	6 A CCCV
Cell mass	47.9 g

Table A.2
Contact probe specifications taken from the data sheets of the corresponding manufacturer. Probe 1 is a common contact pin, while Probe 2 is a concentric scratch contact probe with multiple current-carrying contacts.

Attribute	Probe 1	Probe 2
Manufacturer	Feinmetall	Feinmetall
Model	F79606B230G300	HC06B29010G
Rated current (max.)	10 A	50 A
Number of sense pins	1	1
Number of source pins	1	3
Design	straight	angled
Operating temperature	−20 °C to +80 °C	−40 °C to +200 °C
Tip geometry	wafer shaped	wafer shaped

Table B.1
Extract of the measurement procedure for a 5 C charge test after a complete discharge followed by a relaxation period.

#	Command	Parameter	Skip criterion	Comment
1	Start	–	–	–
2	Charge	$I = 0.5$ C $U = 4.2$ V	$I < 1/20$ C	*Initial condition*
3	Discharge	$I = -1$ C $U = 2.5$ V	$I > -1/20$ C	*Capacity test*
4	Pause	–	$t > 4$ h	–
5	Charge	$I = 5$ C $U = 4.2$ V	$I < 1/20$ C	*Fast charge*
6	End	–	–	–

Appendix B. Testing procedures

The excerpts from the test and measurement procedures used are shown in Tables B.1 and B.2, specifying the current and voltage parameters applied and the respective skip criterion to the next step. The measurement procedures for the charge rates from 0.5 C to 4 C are structured analogously to the 5 C sequence in Table B.1.

Table B.2
Extract of the measurement procedure for the repetitive fast charge cycling with a 5 C multistage fast charging protocol.

#	Command	Parameter	Skip criterion	Comment
1	Cycle 1 start	–	–	–
2	Pause	–	$t > 15$ min	–
3	Charge	$I = 1$ C $U = 4.15$ V	$I < 100$ mA	–
4	Pause	–	$t > 15$ min	–
5	Discharge	$I = -1$ C $U = 2.5$ V	$I > -100$ mA	*RPT*
6	Pause	–	$t > 15$ min	–
7	Cycle 2 start	–	–	–
8	Charge	$I = 5$ C	$U > 4.15$ V	*Stage 1*
9	Charge	$I = 3$ C	$U > 4.15$ V	*Stage 2*
10	Charge	$I = 1$ C $U = 4.15$ V	$I < 100$ mA	*Stage 3*
11	Pause	–	$t > 5$ min	–
12	Discharge	$I = -1$ C	$U < 2.5$ V	–
13	Pause	–	$t > 5$ min	–
14	Cycle 2 end	–	–	–
15	Cycle 1 end	–	–	–

References

[1] Michelbacher C, Ahmed S, Bloom I, Burnham A, Carlson B, Dias F, Dufek EJ, Jansen AN, Keyser M, Markel A, Meintz A, Mohanpurkar M, Pesaran A, Scoffield D, Shirk M, Stephens T, Tanim T, Vijayagopal R, Zhang J. Enabling fast charging – Introduction and overview. J Power Sources 2017;367:214–5. http://dx.doi.org/10.1016/j.jpowsour.2017.08.008.

[2] Ahmed S, Bloom I, Jansen AN, Tanim T, Dufek EJ, Pesaran A, Burnham A, Carlson RB, Dias F, Hardy K, Keyser M, Kreuzer C, Markel A, Meintz A, Michelbacher C, Mohanpurkar M, Nelson PA, Robertson DC, Scoffield D, Shirk M, Stephens T, Vijayagopal R, Zhang J. Enabling fast charging – A battery technology gap assessment. J Power Sources 2017;367:250–62. http://dx.doi.org/10.1016/j.jpowsour.2017.06.055.

[3] Keyser M, Pesaran A, Li Q, Santhanagopalan S, Smith K, Wood E, Ahmed S, Bloom I, Dufek E, Shirk M, Meintz A, Kreuzer C, Michelbacher C, Burnham A, Stephens T, Francfort J, Carlson B, Zhang J, Vijayagopal R, Hardy K, Dias F, Mohanpurkar M, Scoffield D, Jansen AN, Tanim T, Markel A. Enabling fast charging – Battery thermal considerations. J Power Sources 2017;367:228–36. http://dx.doi.org/10.1016/j.jpowsour.2017.07.009.

[4] Meintz A, Zhang J, Vijayagopal R, Kreutzer C, Ahmed S, Bloom I, Burnham A, Carlson RB, Dias F, Dufek EJ, Francfort J, Hardy K, Jansen AN, Keyser M, Markel A, Michelbacher C, Mohanpurkar M, Pesaran A, Scoffield D, Shirk M, Stephens T, Tanim T. Enabling fast charging – Vehicle considerations. J Power Sources 2017;367:216–27. http://dx.doi.org/10.1016/j.jpowsour.2017.07.093.

[5] Burnham A, Dufek EJ, Stephens T, Francfort J, Michelbacher C, Carlson RB, Zhang J, Vijayagopal R, Dias F, Mohanpurkar M, Scoffield D, Hardy K, Shirk M, Hovsapian R, Ahmed S, Bloom I, Jansen AN, Keyser M, Kreuzer C, Markel A, Meintz A, Pesaran A, Tanim TR. Enabling fast charging – Infrastructure and economic considerations. J Power Sources 2017;367:237–49. http://dx.doi.org/10.1016/j.jpowsour.2017.06.079{#}.

[6] Liu Y, Zhu Y, Cui Y. Challenges and opportunities towards fast-charging battery materials. Nat Energy 2019;4(7):540–50. http://dx.doi.org/10.1038/s41560-019-0405-3.

[7] Das, Barai, Masters, Williams. Comparison of tab-to-busbar ultrasonic joints for electric vehicle li-ion battery applications. World Electr Veh J 2019;10(3):55. http://dx.doi.org/10.3390/wevj10030055.

[8] Brand MJ, Berg P, Kolp EI, Bach T, Schmidt P, Jossen A. Detachable electrical connection of battery cells by press contacts. J Energy Storage 2016;8:69–77. http://dx.doi.org/10.1016/j.est.2016.09.011.

[9] Bolsinger C, Zorn M, Birke KP. Electrical contact resistance measurements of clamped battery cell connectors for cylindrical 18650 battery cells. J Energy Storage 2017;12:29–36. http://dx.doi.org/10.1016/j.est.2017.04.001.

[10] Brand MJ, Schmidt PA, Zaeh MF, Jossen A. Welding techniques for battery cells and resulting electrical contact resistances. J Energy Storage 2015;1:7–14. http://dx.doi.org/10.1016/j.est.2015.04.001.

[11] Das A, Li D, Williams D, Greenwood D. Joining technologies for automotive battery systems manufacturing. World Electr Veh J 2018;9(2):22. http://dx.doi.org/10.3390/wevj9020022.

[12] Masomtob M, Sukondhasingha R, Becker J, Sauer DU. Parametric study of spot welding between li-ion battery cells and sheet metal connectors. Eng J 2017;21(7):457–73. http://dx.doi.org/10.4186/ej.2017.21.7.457.

[13] Shin H-S, de Leon M. Mechanical performance and electrical resistance of ultrasonic welded multiple Cu-Al layers. J Mater Process Technol 2017;241:141–53. http://dx.doi.org/10.1016/j.jmatprotec.2016.11.004.

[14] Mehlmann B. Spatially modulated laser beam micro welding of CuSn6 and Nickel-plated DC04 steel for battery applications. J Laser Micro/Nanoeng 2014;9(3):276–81. http://dx.doi.org/10.2961/jlmn.2014.03.0019.

[15] Schmidt PA, Schmitz P, Zaeh MF. Laser beam welding of electrical contacts for the application in stationary energy storage devices. J Laser Appl 2016;28(2):022423. http://dx.doi.org/10.2351/1.4943908.

[16] Taheri P, Hsieh S, Bahrami M. Investigating electrical contact resistance losses in lithium-ion battery assemblies for hybrid and electric vehicles. J Power Sources 2011;196(15):6525–33. http://dx.doi.org/10.1016/j.jpowsour.2011.03.056.

[17] Timsit S. Electrical contact resistance: properties of stationary interfaces. In: Electrical contacts - 1998. Proceedings of the forty-fourth IEEE holm conference on electrical contacts (Cat. No.98CB36238). 1998, p. 1–19. http://dx.doi.org/10.1109/HOLM.1998.722422.

[18] Slade P. Electrical contacts: Principles and applications. 2nd ed.. Boca Raton, FL: CRC Press; 2017, http://dx.doi.org/10.1201/b15640.

[19] Holm R. Electric contacts. Theory and application. Berlin/Heidelberg, DE: Springer; 1967, http://dx.doi.org/10.1007/978-3-662-06688-1.

[20] Johnson K. Contact mechanics. Cambridge, UK: Cambridge University Press; 1985, http://dx.doi.org/10.1017/CBO9781139171731.

[21] Brand MJ, Berg P, Kolp EI, Bach T, Schmidt P, Jossen A. Detachable electrical connection of battery cells by press contacts. J Energy Storage 2016;8:69–77. http://dx.doi.org/10.1016/j.est.2016.09.011.

[22] Taheri P, Hsieh S, Bahrami M. Effects of electrical contact resistance on external energy losses in lithium-ion battery packs for hybrid and electric vehicles. In: ASME 2011 5th international conference on energy sustainability, ES 2011. 2011, p. 1–10. http://dx.doi.org/10.1115/ES2011-54660.

[23] Brand M. Lithium-ion battery cells and systems under dynamic electric loads. Utz Verlag GmbH; 2018.

[24] Holdings E. Battery compartment and device - Design considerations. Tech. rep., St. Louis, MO: Energizer Holdings, Inc.; 2013.

[25] Meaden G. Electrical resistance of metals. The international cryogenics monograph series, Springer; 1965, http://dx.doi.org/10.1007/978-1-4899-5717-7.

[26] Feinmetall GmbH, Contact probes for radio frequency and kelvin - measurement and fine pitch applications. Herrenberg, DE; 2019, Contact probe catalogue, Version 1.0.

[27] Pressure measurement film. Prescale. Products Guide, Herrenberg, DE: Fujifilm Corporation; 2017, IB-0807E5.

[28] Lain, Brandon, Kendrick. Design strategies for high power vs. High energy lithium ion cells. Batteries 2019;5(4):64. http://dx.doi.org/10.3390/batteries5040064.

3 Discussion

The presented contributions to the approach of successfully applying model-based health-aware fast charging control to lithium-ion cells or packs starting with unknown properties of a commercial cell bear benefits and drawbacks, which need to be further analyzed and reflected to allow for reasonable interpretation and inform future research in the field. The proposed method and key findings of the preceding chapter are critically discussed in the context of the theoretical and practical implications that arose, and recommendations for extensions are made building upon the results published in earlier work. Further, aspects of the method's applicability for real-world applications are critically discussed.

3.1 Reflection of the proposed method

The developed method is tangent to an intensively researched field, where no consensus exists, and which still needs to be explored in many respects. Therefore, the presented approach highlights one singular solution that has advantages and disadvantages compared to other approaches, which is critically reflected in the subsequent sections.

3.1.1 Cell teardown and electrode characterization

The step-by-step approach to teardown and characterize commercial lithium-ion cells proposed in Section 2.2 marks the first step in the overall procedure and is at the same time one of the most important ones, as errors may propagate throughout the method. The teardown procedure could be improved based on the experiences gained during the downstream process. The individual steps for improvement are emphasized hereafter.

Harvested electrode stamps were used directly to build the two-electrode half cells without any cleaning of unintended artificial material contamination. It is apparent that residuals of the original electrolyte system (e.g., conductive salts such as $LiPF_6$ [187]) are still present in the freshly built half cells due to the prior formation and cycling of the lithium-ion cell. Typically, those electrolyte residues are washed out with a carbonate solvent of, e.g., ethylene carbonate (EC) or dimethyl carbonate (DMC) (e.g., 1:7 (EC:DMC) [45]) with subsequent drying (e.g., $70\,°C$ for $12\,h$ [45] or $120\,°C$ for $6\,h$ [188]) to improve the performance of the built half cells, as, e.g., unintended conductive salt concentrations change the performance of lithium-ion cells [220]. However, in this work, a reliable coulombic efficiency during the formation and the low-rate cycling could be achieved without any electrode washing, similar to other studies investigating the electrochemical performance of *post-mortem* lithium-ion cells [221]. It is assumed that the impact of the residuals, most probably by a change to larger conductive salt concentrations of the

electrolyte, has a low impact on low current rate tests such as GITT, pOCV, and EIS procedures, as carried out. This would also align with the general expectations of the manifestation of electrolyte overpotentials at larger C-rates [167]. A downstream analysis could be made by comparing the half-cell performance of washed and unwashed electrodes, which could provide ground-truth data on the hypothesis made.

In addition, the half-cell preparation relied on a new electrolyte composition, most probably differing from the original one. The reason for the use of a new electrolyte system lies in the contamination of the original electrolyte with metal particles during the lithium-ion cell teardown, as the original electrolyte can only be harvested if sufficiently enough residual is available at the bottom of the cell packaging (here, at the bottom of the cell can). Small metal particles originating from the can-opening process have been observed during the reported tear-down study, which could lead to altered cell properties and internal short-circuits if reused in the crafted two-electrode half cells, as reported by other studies [222]. However, similar to the previously mentioned issue, no significant deterioration of the added artificial electrolyte could be seen during the low-rate characterization procedure in this work. If more dynamic tests with higher C-rates are to be completed, the original electrolyte system should be harvested, analyzed, and a similar composition used.

To conclude, the electrolyte system plays an important role in defining the electrochemical behavior of the half-cells, either due to residuals of the original electrolyte or due to different electrolyte properties compared to the original electrolyte in the built half-cells. Moreover, no distinct adverse impact on the low-rate characterization was observed in this work.

3.1.2 Electrochemical model parameter identification

Section 2.3 proposed a new approach to the systematic parameter identification of electrochemical models and achieved low errors at high charge rates and elevated temperatures, mainly present during a fast-charging event. However, despite the thorough parameter identification, error sources are inevitable during modeling and parameter identification and must be considered if the procedure is transferred to other cell types or applications.

An electrolyte model extension of the SPM has been used to account for the electrolyte overpotential at high current rates and increase its fidelity, as reported in the literature [194]. However, the electrolyte parameters were taken exclusively from the literature as a comprehensive electrolyte characterization was not possible due to the difficult electrolyte extraction process during the cell teardown, as discussed in Section 3.1.1. In later work, the electrolyte parameters and their dependence on the temperature have been seen to critically interfere with the model validation at subzero ambient temperatures [198], stressing that the model fidelity requires a more in-depth electrolyte characterization for the individual lithium-ion cell under investigation.

The electrochemical submodel's parameter identification has been performed using regressions instead of numeric tables, which are commonly linearized between the grid points, e.g., in prior studies in the literature [223]. The polynomial regressions used in this work (e.g., for the cathode OCP, electrode diffusion coefficients, and reaction rates) offer the benefit of a more accurate extrapolation behavior due to their non-linear nature and less computational demand as the information is stored in a single analytical equation. This may be beneficial if either fewer measurement data points are gathered, which has been seen to be resource- and time-intensive,

or the lithium-ion cell is operated beyond the parameterized supporting points of the model. Beside the use of simple polynomials of n-th order, a hyperbolic regression has been adopted for the anode OCP, which provides a high modeling fidelity of the non-linear anode OCP and maps the modeling-critical stage transitions well, but may lead to downstream computational issues during deployment as $tanh(\cdot)$ is difficult to solve on automotive hardware. If this issue arises in specific applications, similar analytical polynomials of n-th order can be employed as a substitute; however, coming at the expense of fidelity.

In the downstream process, the dynamic cell behavior regressions (diffusion coefficients and reaction rates) were scaled to fit the thermal dynamic cell behavior at different ambient conditions. The scaling was performed linearly by multiplying a scaling factor to each regression. The reason for this lays in the improved performance of the optimization routine, which is accelerated in terms of computational time with linear correlations. However, the approach triggers an unevenly scaled parameter set with temperature over SOC, as the scaling factor has different weights on different absolute values of the respective curve. For example, low diffusion coefficients of the anode in high SOC neighborhoods may be less stretched with a constant scaling factor than high diffusion coefficients in low SOC neighborhoods. The linear scaling approach, therefore, may introduce an unintentional error of non-physical nature. However, it is justified here by the low computational effort of the optimization problem and a practical application of the overall approach.

In sum, it can be concluded that knowledge of the electrolyte properties can further improve the identification of the electrochemical parameters, as this was not considered in this work, but is considered crucial for the general validity of the model from a retrospective. Beyond, numerical methods to identify cell parameters based on previously identified electrode parameters pose an unintended error, which may deteriorate the method's success if transferred to other use-cases.

3.1.3 Thermal model parameter identification

Beyond the electrical submodel, the thermal submodel likewise relied on experimental methods incorporating significant uncertainty. The resulting errors may propagate to the results in downstream deployment of the model and need to be accounted for if thermal parameters are identified.

The applied method from Section 2.3 resulted in a specific heat capacity C_1 of $590\,\mathrm{J/(kgK)}$ and a thermal resistance R_1 of $4.26\,\mathrm{K/(W)}$ or heat transfer coefficient h_c of $0.23\,\mathrm{W/(mK)}$. Both parameters significantly differ from the values from the literature ($C_1 > 800\,\mathrm{J/(kgK)}$ [224, 225] and $R_1 > 30\,\mathrm{K/(W)}$ [225–227]). Possible error sources of the method were identified:

- **Inaccurate current, voltage, and temperature measurements**
  Experimentally determined thermal model parameters rely on current, voltage, and temperature measurements. All sensors are subject to noise, offsets, and drifts, which may interfere with the identified parameters. In laboratory settings at the cell level, voltage measurements are relatively accurate (with the setup discussed for this study, 0.03 %), while current measurements suffer under more considerable deterioration (with the setup discussed for this study, 0.8 %) due to the measurement principle at high current rates. Likewise, temperature sensors differ and drift over time. Moreover, the thermal contact between the lithium-ion

cell and the temperature sensor may vary due to the manual process of applying a temperature sensor with thermal compound onto the cell surface.

- **Thermal impact of the electrical contact resistance**
  At high current rates, it was found that poor electrical contact resistance may induce parasitic heat [219], which can be measured at the cell surface in experimental laboratory settings. These differences may interfere with the yielded temperature response of the lithium-ion cell.

- **Varying calculation definitions (e.g., heat generation $\dot{Q}$)**
  The heat generation $\dot{Q}$ during the pulse current excitation is calculated from the difference between the lithium-ion cell OCV U_{OCV} and the measured terminal voltage U. The cell OCV U_{OCV} may be inaccurately determined if relaxation times are too short prior to the experiment. The cell terminal voltage U oscillates in the charge and discharge sequence with different current excitations, which requires averaging the heat generation. This can be improved by applying sinusoidal current excitations in which the heat rate predominantly originates from ohmic losses, as reported by Steinhardt et al. [225], which allows for direct calculation from the measurement signals (current, voltage).

- **Thermal impact of the low airflow of the convective thermal chamber**
  The convection of thermal chambers controlling the ambient temperature may interfere with the experimental setup, i.e., having a cooling effect on the lithium-ion cell under study. Therefore, the assumption of free convection may not be valid and lead to different results.

The inaccuracies have been noted to deteriorate the results in this study ($551-708$ J/(kgK) for C_1, $2.95-4.26$ W/K for R_1, [197]). Interestingly, measurements with and without thermal compound triggered only 1 K of temperature difference. Despite the large spread in the results, all investigated setups did not yield values close to those reported in the literature.

It can be concluded that additional, more accurate determination methods for the thermal parameters, e.g., calorimetry for the thermal capacity, need to be applied to identify reference values for the thermal parameter of the specific lithium-ion cell under study and to further elaborate on the results. The apparent difference in the heat capacity and heat transfer coefficient, however, may be more relevant to lithium-ion cells with less self-heating capability, e.g., large format or actively-cooled lithium-ion cells, as the thermal model parameters have been seen to be less sensitive for anode potential control limits since the lithium-ion cell quickly heats up to elevated temperatures with less sensitivity on the thermal-dependent electrical properties. The precision in thermal parameter determination should therefore be stressed if the method is transferred to other lithium-ion cell types with less self-heating capability.

3.1.4 Degree of model fidelity

This work uses a P2D-based electrochemical model of reduced order, the SPM, to derive a health-aware fast charging strategy. P2D-based electrochemical models may be more accurate from a theoretical standpoint due to their incorporation of physical laws. Still, they may lose their accuracy due to simplification (i.e., downscale from pack to cell level), model-order reduction

(i.e., downscale of computational complexity with similar modeling objectives) to improve computational efficiency, and complex parameter identification. All pathways may be critical for practical applications and will be discussed in the following.

The introduced model simplification by downscaling the multi-model approach of modeling each individual lithium-ion cell in a battery pack to a single lithium-ion cell model drastically improves the computational efficiency. Conversely, many critical pack-level effects (as discussed below in Section 3.1.7) with impact on the model fidelity and accuracy become unobservable. This approach is justified in this work, as only a single lithium-ion cell has been studied without any deterioration of system effects on the results. If the method is to be scaled, pack-level effects need to be considered. This can be done efficiently by identifying the most vulnerable lithium-ion cells in the system, that is, the lithium-ion cells with the lowest and highest charging capability, e.g., in cold and hot spots.

Beyond the downscale to a single model, the model-order reduction from a full-scale P2D electrochemical model to an SPM leads to model fidelity and accuracy losses. The general principle lies in assuming a constant electrolyte concentration and reaction current across the thickness of the electrode. Following this assumption, a great compromise is given by likewise reducing the computational complexity if only one single spherical particle is simulated and also only a single partial differential equations (PDEs) is solved for each electrode. Following the computational complexity of solving the PDEs in the electrode particle, the PDEs are discretized using a finite difference method [194]. Here, a lower resolution of the particle, i.e., lesser nodes throughout the particle for which the concentration needs to be calculated, triggers a lower solution accuracy. Within this work, we benchmarked lower resolutions against the loss of accuracy compared to a high-fidelity model to account for this issue. A comparison of the achieved accuracy with a high-fidelity reference simulation and the computational effort, expressed as floating point operations, is given in Figure 3.1 for different discretizations. However, the results are specific to the underlying investigation and cannot rigorously be transferred to other investigations without repeated assessment.

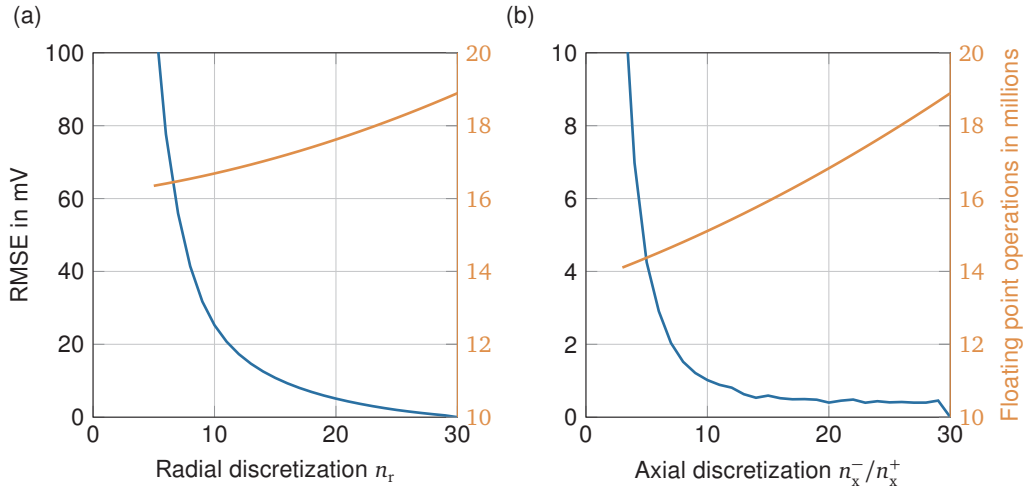

Figure 3.1: Comparison of the achieved cell voltage accuracy against a high-fidelity reference simulation ($n_r = n_x = 30$) during a 5 C charge sequence and the computational effort to yield the results expressed as required floating point operations [200]. Note that discretization parameters are varied once at a time for (a) the radial discretization n_r of both electrodes and (b) the axial discretization of both electrodes n_x^-/n_x^+.

Beyond the model-order reduction, a large set of required parameters remains, which needs to be identified before any application of the model. As outlined in the preceding sections, some of the parameters are hard to obtain (e.g., electrolyte parameters) due to their microscale, and if identified, they suffer from measurement-induced inaccuracies. These adverse factors were seen to contradict and outweigh the inherited theoretical accuracy of the electrochemical modeling approach. It is to be questioned, whether first-principle electrochemical models meet the expectations of their promising high theoretical modeling accuracy if parameters are prone to large uncertainties, or if other more simplified modeling approaches could lead to similar results due to their improved parameter identification precision.

Finally, from a practical perspective, no clear superiority of electrochemical models compared to more simplified approaches (e.g., pECM or data-based approaches) can be seen for fast charging control due to its accuracy vulnerability during the required model-order reduction and laborious parameter identification. Other modeling approaches, such as anode pECM or characteristic maps based on half-cell measurements, may have an enhanced accuracy due to their inherited simplicity of identifying the relevant parameters, even though they may have a more crude theoretical model fidelity. This could be advantageous for practical applications if the required methods for accurate parameter identification or the laboratory resources for electrode characterization are lacking. As these methods were not directly compared to each other, a clear recommendation in favor or against an individual method cannot be made based on this work.

3.1.5 Model updates over the cycle life and current derating

A critical step in the overall approach was taken by identifying and linking common SOH quantities present in automotive applications to the electrochemical-thermal model within this study, which enables a health-aware current derating over cycle life by regular model updates to the actual SOH of the investigated lithium-ion cells. In earlier contributions, the capacity decay SOH_C and resistance rise SOH_R were calculated based on the maximum change relative to a 1 C charge pulse at 20, 50, and 80 % SOC determined during regular check-up intervals in the laboratory. These were linked to the electrode scaling (cell capacity Q) and SEI resistance increase (SEI overpotential η_{SEI}). Many study-specific definitions, simplifications, and assumptions were made within this step, which is critically discussed and highlighted in the sections below.

Both SOH quantities usually vary in their specific definition throughout the field of research. For example, the capacity decay can be calculated between different voltage bounds (cycling windows), starting from varying initial conditions (charge cut-off current or voltage), and terminating at different cut-off criteria (discharge cut-off current or voltage). Likewise, the resistance rise may be identified at different initial conditions (relaxation time period, temperature), in different directions (discharge or charge) at varying C-rates and time periods, and at varying SOCs. Variations in these definitions may lead to different results if used in a downstream relative calculation of the SOH.

Following this approach, a further simplification was made by linking both SOH quantities to the electrochemical-thermal model. In theory, many other model parameters are subjected to aging processes and must be regularly updated. For example, capacity decay is known to originate from a changing electrode balancing, which changes along the individual aging modes of the cathode and anode over age [228], or the resistance rise is known to originate also from

changing electrode properties affecting the diffusion and reaction rates of all components [229]. All aspects above have been neglected based on the assumption that the measurements needed for the parameter update are practically unavailable in typical applications and less relevant, justifying the more straightforward approach. However, this may further deteriorate the overall validity of the model over age and, therefore, may impact the accuracy of the model-based fast charging strategy, which is worth further investigation beyond the underlying study.

3.1.6 Transferability to other materials or formats

One important feature, which has not been assessed in the earlier contributions listed in this thesis, is the flexibility to easily transfer the method to other lithium-ion cells of different materials or formats. In general, all three steps could be repeated, if necessary:

- the cell teardown and electrode characterization (Section 2.2),
- the model parameter identification at electrode and cell level (Section 2.3),
- and the electrochemical model deployment within a control strategy (Section 2.4).

To account for the transferability aspect of the proposed method, both a change in material or format and their impact on the individual steps of the method are discussed in the following, as depicted in Figure 3.2.

It has become common practice to vary the active cathode materials to account for performance, price, or sustainability targets in R&D. Most prominently, LFP has been frequently deployed due to the absence of cobalt as a rare and expensive raw material for cost-effective vehicle segments, while NCA or NMC have been used for mid- to high-performance vehicle segments due to their enhanced specific energy density, as introduced in Section 1.1.2. The most drastic change may lie in a complete change of the material systems, that is, a change in anode and cathode material, design, or production process parameters without changing the cell format. While the singular change in cathode material may only lead to a characterization and model parameter identification for the cathode-relevant properties, a complete characterization and model parameter identification must be performed if the anode and cathode material is changed. In both cases, geometrical properties can be maintained as the cell design or format does not change.

Regarding the cell format, a global trend is currently seen to increase the size of cylindrical cells (from 18650 to 4680) as well as prismatic and pouch cells (beyond $70\,\mathrm{A\,h}$) to keep the inactive material share low and improve the energy density of the lithium-ion battery pack. A larger format, for instance, comes with a change in electrode size, which impacts the capacity and impedance occupied in the deployed model. The model parameters must adapt to these changes by, theoretically, adjusting the electrode surface in the electrical submodel if the same material is used in a carefully crafted model for a smaller cell format. A complete electrode characterization and parameter identification can be skipped in this case, except for the thermal submodel parameters (e.g., specific heat capacity and heat transfer), which are highly dependent on the cell format.

Ultimately, a proof-of-concept for a transfer of the method to other graphite-based lithium-ion cells has been out of scope, so reliable conclusions cannot be drawn at this point. Investigation

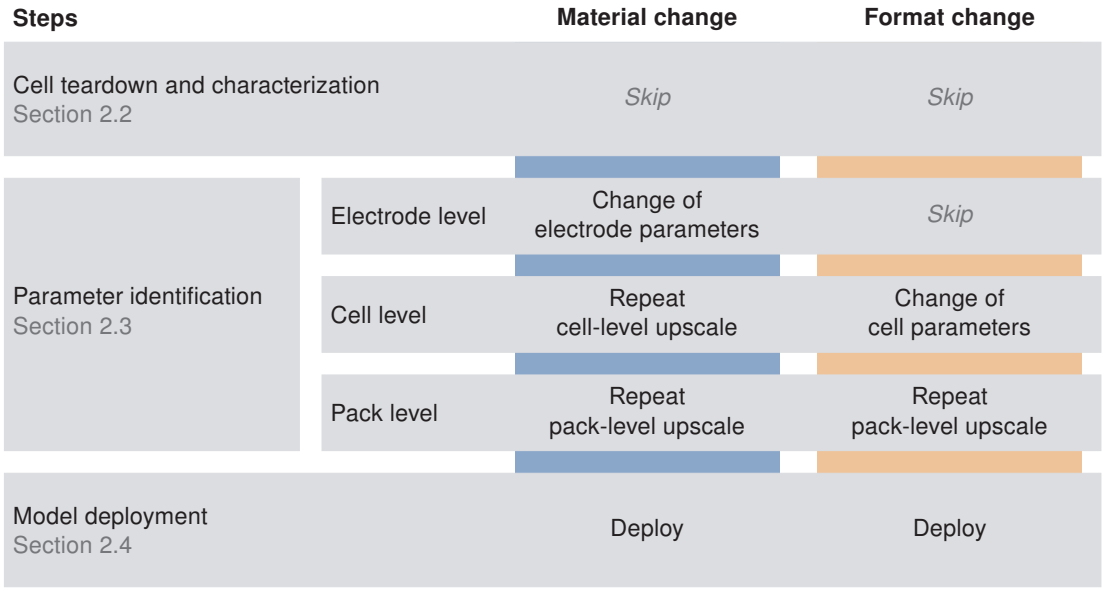

Figure 3.2: Transferability of the developed method within this work. Impact of a change in electrode material or cell format on the individual steps taken to determine the health-aware fast charging control strategy within this work.

of the method's transfer capability to other materials or formats following the arguments in this discussion is, however, necessary to evaluate the limitations of the presented method.

3.1.7 Additional effects during the upscale to pack level

Similar to the limitations arising with model simplification and generalization from electrode particle to cell level, similar restrictions occur if scaled to pack level. In Section 2.4, the derived model has been scaled to 12s2p level. It is apparent, however, that despite the proposed simple model extension with ECR, a lumped scaling to a multitude of lithium-ion cells leads to further inhomogeneity in the modeled system due to the presence of

- inhomogenous balancing currents between parallel-connected lithium-ion cells,
- disbalance due to delayed balancing of serial-connected lithium-ion cells,
- thermal cell-to-cell interactions, or
- thermal management cooling gradients throughout the pack,

which will be even more dominant if the model is scaled to larger architectures.

Prior studies observed diminishing effects while scaling cell level results to the pack level. Tanim et al. [230] observed a significantly faster capacity fade at the pack level compared to cell-level tests, which has been traced back to cell-to-cell interactions using ICA. Yang et al. [231] proposed an anode potential control for six individual lithium-ion cells connected in parallel with a symmetrical busbar tab orientation. They showed that the lithium-ion cell closest to the busbars suffered under the highest charging current due to current distribution. They also highlighted the necessity to manifest a system perspective in designing anode potential control algorithms at the pack level. Symmetrical busbar tab orientation is, however, rarely found in automotive practice due to packaging reasons in constaint volumina. Thermal cell-to-cell effects may, therefore, be more critical since the temperature is, in general, not controlled at each individual lithium-ion cell

in automotive practice, thermal gradients may evolve rapidly in a non-homogeneously cooled lithium-ion battery pack due to the rapid heat-up during a fast-charging event, and waste heat may be more challenging to remove from the overall system, as observed by Sieg et al. [189] with a 96s1p pack architecture.

To sum up, the upscale to pack level inherits several uncertainties beyond the considered one in this work, which must be accounted for if model-based health-aware fast charging strategies are to be applied at the pack level. Investigations at this scale are time- and resource-intensive but imperative to ensure a good cycle life and safety during frequent fast charging.

3.2 Projection to battery electric vehicle applications

One of the most important aspects in engineering science is the relevance of developed approaches to real-world environments. Limitations which arose in the preceding sections are discussed in the context of BEV applications in the following section.

3.2.1 Impact of current derating on the charging time

During the proposed health-aware fast charging control strategy, the current is constantly reduced with aging according to the predicted physical limits of the lithium-ion cell. This leads to two opposite effects on the charging time. On the one hand, the decreasing capacity shortens the fast charge time because less capacity or energy needs to be charged between similar SOC limits. On the other hand, increasing SEI resistance leads to an earlier reach of anode potential limits during CA control and increases the charge time. Capacity and resistance do not age proportionally [185], so this effect can lengthen, shorten or even cancel out over the lifetime.

To discuss the impact of derating on the fast charging time for different cycling conditions, the lithium-ion cell model parameterized in earlier work (Section 2.3) is used to show the impact of different aging stages under conventional cycling on the fast charging time. Therefore, theoretical aging scenarios must be defined as lithium-ion cells are always subject to individual aging processes depending on their material, format, and use. As such, different aging trends reported in aging studies with close-to-real-world cycling conditions (dynamic discharge, large DOD) are chosen, and their resistance rise is assumed to originate entirely from the anode and is aligned to the capacity decay to yield a generalized aging behavior. As discussed earlier (Section 3.1.5), this may not be true in practice, as various aging mechanisms are known to occur synchronously. Still, it is a justified worst-case assumption since a more precise splitting of the individual aging mechanisms is hard to obtain in practice.

In a previous study of the author, an automotive-grade pouch C/NMC 78 Ah lithium-ion cell (LGX E78) from a Volkswagen ID.3 1st edition was discharged with a real-world highway cycle and charged with a 100 kW-peak fast charging sequence downscaled to cell level between $100\,\%$ and $28\,\%$ SOC and $20\,°$C ambient temperature. Using this experiment relatively close to automotive operating conditions, polynomial regressions are employed to correlate the capacity fade with the resistance rise, formally $\mathrm{SOH_R} = f(\mathrm{SOH_C})$. The aging correlation regression then follows

$$\mathrm{SOH_R} = 4.678 \cdot \mathrm{SOH_C^2} - 9.578 \cdot \mathrm{SOH_C} + 5.913 \tag{3.1}$$

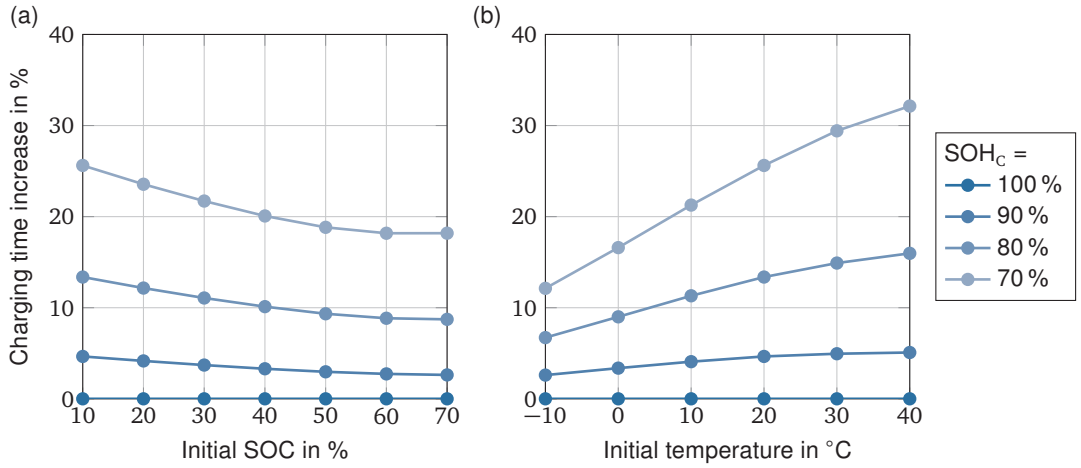

Figure 3.3: Charging time increase until 80 % SOC with a CCCA fast charging strategy if fast charging events are derated based on the capacity decay and resistance rise. Charging time increases at (a) 20 °C temperature with different initial SOCs and (b) starting from 10 % initial SOC with different initial temperatures. Capacity decay and resistance rise is captured in regressions generalized from a reported aging trend in the literature, as stated in Equation 3.1. Any aging impact of the fast charging events is neglected.

with a goodness of fit of $R^2 = 89.2\%$ and is used for model parameter adjustments following the current derating principle proposed in Section 2.4.

If the model is now parameterized with the defined aging scenario by updating the SOH according to the regressions stated earlier and CA fast charging is taking place, the charging time differs from the initial fast charge with a pristine lithium-ion cell with progressing age. Figure 3.3 shows the relative change of this simulation study. Even though capacity continuously fades, resistance rises and dominates the current derating. Figure 3.3(a) shows the relative change in time to the initial fast charge if the initial SOC is varied and the temperature is kept at 20 °C. Here, the resistance rise leads to a predominant increase in charging time at low initial SOCs because the inflection point for CA control is reached earlier, resulting in a less self-heating rate of the cell, and leads to a more significant impact on the charging time than at higher initial SOCs. A similar mechanism can be seen in Figure 3.3(b), which shows the relative change in time to the initial fast charge if the initial temperature is varied at an initial SOC of 10 %. Lower temperatures profit from the raised resistance due to an elevated self-heating rate.

In conclusion, the theoretical model showcases how a rising anode resistance limits the fast charging capability over the lifetime of the lithium-ion battery pack and electric vehicle. Even though a capacity decay shortens the charging time, the resistance increase leads to a prolonged fast charging time over age. If this scenario is projected in the simplest way to a mass-series electric vehicle, for example, a Volkswagen ID.3 1st edition with a fast charging time of 33 min [232], this would result in an increase in the charging time of up to 32 % until the manufacturer warranty is reached at a remaining capacity of 70 %. To this end, to mitigate the risk of lithium plating and, consequently, nonlinear aging in a later stage of life, fast charging requires an active current derating by a health-aware fast charging strategy at the cost of additional charging time.

3.2.2 Physical limitations due to predefined initial conditions

Even though advanced fast charging control depicts a promising lever to shorten the charging time while remaining within a safe operating window during operation, the physical limits of lithium-ion cells cannot be overcome. Particularly during fast charging at low initial temperatures, which is expected to become more relevant in the future [143], lithium-ion cell kinetics is inhibited, leading to high overpotentials ultimately followed by large temperature spreads and a higher risk of lithium deposition. Besides low temperatures, a mid-level starting SOC drastically inhibits the fast charging capability as the lithium-ion cell is not capable of self-heating fast enough due to the reduced charging current capability with rising SOC. Both effects and their impact on charging time are quantified in Figure 3.4 for the lithium-ion cell investigated within this work. Model-based control algorithms for current control cannot overcome these physical barriers.

Prior work has shown that preheating the lithium-ion battery pack prior to a fast charging event can significantly shorten the charging time of a Tesla Model 3 (LFP version) compared to an arbitrary fast charging stop without any preconditioning [232]. This is usually done in the automotive industry by raising the coolant circuit temperature with waste heat from other powertrain components and, therefore, relying on a sufficiently large time frame before any fast charging due to the thermal inertia (large thermal capacity) of the thermal management system. For the Tesla Model 3 (LFP version), preheating starts at approximately $60\,\mathrm{min}$ before the fast charging event, and the targeted temperature of $40\,^{\circ}\mathrm{C}$ is reached after about $30\,\mathrm{min}$ [232]. The raised temperature then leads to accelerated calendar aging, which is accepted and traded with the benefit of improved fast charging speed. Unfortunately, preheating by a thermal management system is only possible once the user has manually entered a fast charging event, which is usually performed on long-distance trips, but rarely accomplished in short- to mid-distance trips in, e.g., urban environments.

Many studies have already investigated different techniques to increase the speed of preheating a lithium-ion battery pack before a fast-charging event. While experimental studies with lithium-ion cells modified with a Ni-heating foil embedded into the cell showed extraordinary cycle life with fast charging times under $10\,\mathrm{min}$ [27–29], techniques without the need for cell modifications

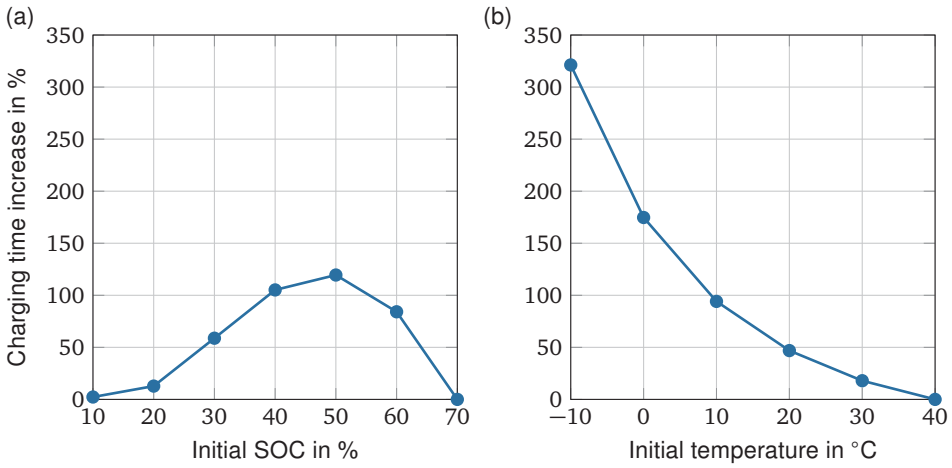

Figure 3.4: Charging time increase until $80\,\%$ SOC with a CCCA fast charging strategy due to variations in initial temperature and SOC at (a) $-10\,^{\circ}\mathrm{C}$ initial temperature and (b) $50\,\%$ starting SOC relative to the shortest respective charging time [233].

have been proposed. Here, internal heating techniques have been proposed using the thermal losses of applied current pulse [234], but also alternating current techniques generated by an external power device [235]. A recent numerical study reviewed the time-saving potential of different preheating methods in the literature, showing that a time-saving potential between 20 % to 72 % with heat rates of $3\,\mathrm{K/min}$ to $60\,\mathrm{K/min}$, respectively, compared to anode potential-controlled fast charging without any preheating in the extreme scenario of $50\,\%$ SOC and $-10\,^{\circ}\mathrm{C}$ initial lithium-ion cell temperature [233]. The time-saving potential of advanced preheating is high. It may become more critical with the broader use of BEVs in harsher use-case environments, rendering additional measures to a positive cost-benefit ratio.

Consequently, the presented model-based fast charging strategy controlling the current during a fast charging event should always be complemented with fast preheating control strategies to raise the temperature to an optimum and further reduce the charging time if sluggish lithium-ion cell kinetics restrict the charging time. As many situations require a fast preheating of the lithium-ion battery pack, preheating should be further advanced with more powerful devices and combined with fast charging stop prediction and scheduling algorithms based on the predicted charging behavior of the individual user.

4 Conclusions, recommendations, and future work

This work proposed a framework to empower coupled electrochemical-thermal models to control the fast charging current at the edge of the physical limitations of lithium-ion cells. The required steps from a lithium-ion cell with unknown properties to a fast charging current control strategy operating in real-time depending on the three most relevant states, i.e., SOC, temperature, and SOH of the lithium-ion cell have been presented.

4.1 Key findings and conclusions

Following the results of this work, key conclusions can be drawn from the initially identified problems and research objectives in Section 1.5. Answers to the posed questions are given in the following.

(1) *What are the remaining challenges in fast charging control?*

To answer this question, a novel clustering of existing methods of the state of the art was applied, and the various studies were categorized into heuristic and model-based approaches. Whilst the first is more straight-forward but requires vast resources (i.e., aging experiments to assess the effectiveness of the best fast charging strategy) due to their exhaustive nature, the latter provides a more flexible and sustainable approach as these methods inherit the physical relations of lithium-ion cells and are, therefore, transferable to different lithium-ion cell types and formats. With this, electrochemical models offer the largest potential and depth of detail but also the largest complexity. The identified key challenges for this particular field were identified to improve the precision of these models incorporating the physical limits of the lithium-ion cell (e.g., lithium plating) and accurately projecting these limits to the application level to allow for current control by the BMS. This includes trading off the required fidelity of the model with the required accuracy for fast charging current control. These models must be able to run robustly in real-world environments and need to be experimentally validated with proof-of-concept studies, which is seen to be rarely realized in scientific practice. A major barrier still is the need for applicable model parameter identification techniques. While model-based fast charging strategies are often used to prevent the occurrence of lithium plating depending on the cell's SOC and temperature, studies incorporating the SOH are rarely found in the literature.

(2) *How can commercial lithium-ion cells be characterized to identify essential parameters for electrochemical modeling?*

A step-by-step procedure has been proposed to tear down commercial lithium-ion cells and gather the most important measurements to determine the individual electrode behavior for electrochemical modeling, i.e., separating the anode from the cathode behavior. The electrode-individual properties for electrochemical modeling can be identified with the individual electrode layers at hand. Beyond constant properties, half cells have been built to gather descriptive measurements for downstream parameter identification of dynamic parameters affected by the conditions of the lithium-ion cell. The results pave the way for accurate parameter identification of electrochemical models without electrode ambiguities deteriorating the validity of the crafted model.

(3) *How can electrochemical models be systematically parameterized for fast charging control?*

To conclusively answer this question, this work proposed a new approach to systematically identifying the parameters relevant for electrochemical models of reduced order, i.e., a single particle model (SPM). The uniqueness of this approach lies in the efficient balancing of the empirically identified parameters at electrode level and the numerically identified parameters at the cell level, thus trading off the need for resource-intensive and precise laboratory techniques with more vague but practical optimization problems while maintaining sufficient accuracy of the developed model. The step-wise parameter identification approach carefully excludes interdependencies of the individual parameters, e.g., by using isothermal environments to exclude thermal effects. In a broad validation campaign up to 6C, between $-10\,^{\circ}$C and $50\,^{\circ}$C ambient temperature, and up to 12s2p module architecture, the accuracy has been proven, e.g., by showing a root mean square error (RMSE) less than $29\,$mV at $20\,^{\circ}$C. At the same time, remaining inaccuracies have been revealed, e.g., due to the difficult quantification of the diffusion of discharged cells (low SOC range) and inaccurate electrolyte and thermal parameter set (subzero temperature). Finally, a health-aware fast charging strategy has been proposed, mapping the capacity drop and resistance rise to the model-based fast charging control strategy over cycle life.

(4) *How to deploy electrochemical models for health-aware fast charging control and which aging mechanism do occur?*

The crafted electrochemical model of reduced order has been transferred to a laboratory environment by performing extensive aging tests. Prior to deployment, the model was discretized to balance the accuracy with the computational effort optimally. The individual error terms were identified and considered to determine a defensive anode potential limit, defined as anode potential reserve. As conventional cycling equipment in scientific laboratory environments does not allow dynamic charging currents, a CAN-based communication between the commonly used cycling equipment and a microcontroller unit has been developed and published as open source [218], referred to as model deployment framework. Intensive cycle life tests and comparisons between CC and CA charging were performed, highlighting that model-based health-aware fast charging strategies can prolong the cycle life, especially at low ambient

temperatures. *Post-mortem* analysis of the electrode indicated the occurrence of ceramic coating remnants onto the graphite anode surface, which prevented a clear visual lithium plating evidence via SEM. However, indirect detection methods by capacity and resistance tracking indicated the onset of non-linear aging for the affected cells. In conclusion, aging mechanisms during frequent fast charging can lead to the onset of nonlinear aging if conventional charging principles are deployed. In contrast, model-based health-aware fast charging algorithms regularly updated with the SOH enable a prolonged cycle life due to the mitigation of non-linear aging due to the adaptive current to the SOC, temperature, and SOH.

(5) *How do electrical contacts in lithium-ion battery packs influence lithium-ion cell performance during fast charging?*

As one crucial but often disregarded pack-level effect, the impact of ECR on lithium-ion cell performance has been identified and studied under large charging currents up to 5C in laboratory and real-world setups. Besides studies investigating the impact of ECR on the homogeneity at the pack level, this work assessed the thermal impact of losses occurring in the cell to busbar contact. It was shown that laboratory setups with reversible cell contacts suffer under approximately ten-fold larger ECRs than real-world laser-welded contacts. This significant difference has been experimentally investigated. Large peak temperature variations of approximately $10\,\mathrm{K}$ could be observed, tracked down to significant cell tab temperature variations due to the parasitic thermal impact of high ECRs. The results were correlated to an entirely different thermal behavior of the lithium-ion cells cycled in laboratory setups compared to the lithium-ion cells cycled with laser-welded joints. This may lead to an overestimation of the cycle life under repetitive high charging currents, as in fast charging studies, and the underestimation of the occurrence of lithium plating at elevated ambient temperatures due to slower self-heating of the lithium-ion cells during a fast charging event.

4.2 Recommendations for industrial applications

Scientific research is usually carried out to provide the first steps into new fields, including the inherited risks of the involved open-ended ideas. This often comes at the expense of the recognition that these ideas cannot be directly implemented in commercial applications. Even though the goal was to pave the way for enhanced technological readiness of the proposed solution, the developed solution is not plug-and-play applicable to commercial products and needs to be tailored to the individual application.

Despite the intensive effort to achieve a more precise replica of the lithium-ion cell under study by the proposed systematic and hybrid (experimental and numerical) parameter identification procedure building upon recent studies in the field, this work revealed once more the difficulties in the parameter identification of electrochemical models. If the method is intended to be transferred to practical applications, the precision of the model parameters found with the proposed method needs additional cross-validation with other methods to avoid using wrongly set parameters and ensure safe, fast charging control. This is especially the case if the method is applied to other lithium-ion cells of different form and material, which has not been investigated in this work. From

the author's point of view, the use of electrochemical models is still far away from real-world BMS applications due to its inherited inaccuracy of parameter identification.

Precise control of the fast charging current also requires accurate knowledge of the remaining battery states, e.g., the SOC, which has been out of scope within this work. To unfold the overall potential of model-based fast charging control, the presented algorithm must be embedded in a multi-scale functional environment, including the precise estimation of all upstream lithium-ion cell states and system interdependencies [58], which should be tested comprehensively to hedge against error propagation and critical situations during fast charging control.

The practical implementation of the model used in this study showed that the computational effort could be controlled without any severe drawbacks in a real-time environment, however, running in an artificial laboratory environment. Resources for computational-intensive tasks are sparse in automotive environments, which usually raises the argument that advanced algorithms based on such models may be impractical in commercial applications. With the upraise of centralized electronic control devices in the automotive field [236], which are capable of processing a large amount of data to handle the complexity of autonomous driving functions, this may be manageable in the future, as many autonomous driving functions are not relevant during a fast charging event. Additionally, cloud-based allocation of the required resources could enable advanced fast charging algorithms with increasing calculation effort, as already pursued for other resource-intensive estimation tasks [237]. Moreover, if all attempts fail to yield a numerical solution, a defensive current control based on implemented static current maps should be used as a fallback solution.

Beyond any further use of the framework, the developed method needs additional validation with more redundant and distinctive lithium-ion cells (form and material) under test, in-depth *post-mortem* investigation and comparison of the cycled lithium-ion cells at various aging stages.

4.3 Peek into future work

Even though model-based fast charging control strategies can improve the fast-charging capability of commercial lithium-ion cells due to their health awareness, many hurdles still require additional research activities in various fields. Following the results and discussion of this work, recommendations for future work are seen in the following topics.

- Improvement of the methods to accurately determine dynamic electrochemical model parameters (e.g., electrolyte properties, diffusion and reaction kinetics, thermal behavior) to extend the accuracy over a wide operational range, especially at low ambient temperatures.
- Transfer of the proposed systematic parameter identification approach to other lithium-ion cell formats and cathode materials to verify the general validity of the approach.
- Inclusion of additional aging-inducing phenomena and their effects (e.g., mechanical expansion and particle cracking, electrolyte depletion) to the model and

implementation of additional current control limits to the fast charging control framework.

- Design of model-based preheating strategies to bridge the gap between inhibited charging and self-heating capability of lithium-ion cells at low temperatures. These strategies should take into account the properties of the thermal management system to optimize the operation strategy of the vehicle prior to a fast charging event.
- Application of the model-based health-aware fast charging control strategy at the battery pack level to explore the as yet unknown effects of multiple connected lithium-ion cells in series and parallel and the thermal management system cooling flux on the aging under frequent fast charging.

Apart from the remaining challenges in optimizing the method and practical implementation, fast charging will always be limited by the physical limits of lithium-ion cells. It must be questioned whether simply increasing the range of BEVs by increasing the energy density of lithium-ion battery packs will lead to the optimal solution for the next-generation mobility, or whether power density will have to take precedence as additional range will be less important at a certain point than charging speed.

List of Figures

List of Tables

Bibliography

[1] F. Orsi, M. Muratori, M. Rocco, E. Colombo and G. Rizzoni, „A multi-dimensional well-to-wheels analysis of passenger vehicles in different regions: Primary energy consumption, CO2 emissions, and economic cost," *Applied Energy*, vol. 169, pp. 197–209, 2016, DOI: 10.1016/j.apenergy.2016.02.039.

[2] R. Sacchi, C. Bauer, B. Cox and C. Mutel, „When, where and how can the electrification of passenger cars reduce greenhouse gas emissions?," *Renewable and Sustainable Energy Reviews*, vol. 162, p. 112475, 2022, DOI: 10.1016/j.rser.2022.112475.

[3] M. Grosso et al., „How will vehicle automation and electrification affect the automotive maintenance, repair sector?," *Transportation research interdisciplinary perspectives*, vol. 12, None, 2021, DOI: 10.1016/j.trip.2021.100495.

[4] H. Campello-Vicente, R. Peral-Orts, N. Campillo-Davo and E. Velasco-Sanchez, „The effect of electric vehicles on urban noise maps," *Applied Acoustics*, vol. 116, pp. 59–64, 2017, DOI: 10.1016/j.apacoust.2016.09.018.

[5] S. Englberger et al., „Electric vehicle multi-use: Optimizing multiple value streams using mobile storage systems in a vehicle-to-grid context," *Applied Energy*, vol. 304, p. 117862, 2021, DOI: 10.1016/j.apenergy.2021.117862.

[6] H. Löbberding et al., „From Cell to Battery System in BEVs: Analysis of System Packing Efficiency and Cell Types," *World Electric Vehicle Journal*, vol. 11, no. 4, p. 77, 2020, DOI: 10.3390/wevj11040077.

[7] C. Reiter, N. Wassiliadis, L. Wildfeuer, T. Wurster and M. Lienkamp, „Range Extension of Electric Vehicles through Improved Battery Capacity Utilization: Potentials, Risks and Strategies," in *2018 21st International Conference on Intelligent Transportation Systems (ITSC)*, Maui, HI, 2018, pp. 321–326, ISBN: 978-1-7281-0321-1. DOI: 10.1109/ITSC.2018.8569455.

[8] M. W. Verbrugge and C. W. Wampler, „On the optimal sizing of batteries for electric vehicles and the influence of fast charge," *Journal of Power Sources*, vol. 384, pp. 312–317, 2018, DOI: 10.1016/j.jpowsour.2018.02.064.

[9] A. Burnham et al., „Enabling fast charging – Infrastructure and economic considerations," *Journal of Power Sources*, vol. 367, pp. 237–249, 2017, DOI: 10.1016/j.jpowsour.2017.06.079.

[10] R. Wolbertus and R. van den Hoed, „Electric Vehicle Fast Charging Needs in Cities and along Corridors," *World Electric Vehicle Journal*, vol. 10, no. 2, p. 45, 2019, DOI: 10.3390/wevj10020045.

[11] B. Nykvist and O. Olsson, „The feasibility of heavy battery electric trucks," *Joule*, vol. 5, no. 4, pp. 901–913, 2021, DOI: 10.1016/j.joule.2021.03.007.

[12] A. Masias, J. Marcicki and W. A. Paxton, „Opportunities and Challenges of Lithium Ion Batteries in Automotive Applications," *ACS Energy Letters*, vol. 6, no. 2, pp. 621–630, 2021, DOI: 10.1021/acsenergylett.0c02584.

[13] T. Gnann et al., „Fast charging infrastructure for electric vehicles: Today's situation and future needs," *Transportation Research Part D: Transport and Environment*, vol. 62, pp. 314–329, 2018, DOI: 10.1016/j.trd.2018.03.004.

[14] D. Howell, S. Boyd, B. Cunningham, S. Gillard and L. Slezak, „Enabling fast charging: A Technology Gap Assessment," 2017, DOI: 10.2172/1416167.

[15] EUCAR, „Battery requirements for future automotive applications," 2019. Available: https://www.eucar.be/battery-requirements-for-future-automotive-applications/ [visited on 04/08/2022].

[16] P. Morrissey, P. Weldon and M. O'Mahony, „Future standard and fast charging infrastructure planning: An analysis of electric vehicle charging behaviour," *Energy Policy*, vol. 89, pp. 257–270, 2016, DOI: 10.1016/j.enpol.2015.12.001.

[17] C. R. Birkl, M. R. Roberts, E. McTurk, P. G. Bruce and D. A. Howey, „Degradation diagnostics for lithium ion cells," *Journal of Power Sources*, vol. 341, pp. 373–386, 2017, DOI: 10.1016/j.jpowsour.2016.12.011.

[18] T. Junior, „Study on the charging behavior of electric vehicles," Bachelor's thesis, Institute of Automotive Technology, Technical University of Munich, 2022.

[19] N. Wassiliadis and M. Lienkamp, „A concept for assessing the impact of enhanced fast charging availability on battery operation and design," *Advanced Automotive Battery Conference (AABC) Europe, Strasbourg, France*, 2019.

[20] S. Ahmed et al., „Enabling fast charging – A battery technology gap assessment," *Journal of Power Sources*, vol. 367, pp. 250–262, 2017, DOI: 10.1016/j.jpowsour.2017.06.055.

[21] Y. Liu, Y. Zhu and Y. Cui, „Challenges and opportunities towards fast-charging battery materials," *Nature Energy*, vol. 4, no. 7, pp. 540–550, 2019, DOI: 10.1038/s41560-019-0405-3.

[22] J. B. Habedank, J. Kriegler and M. F. Zaeh, „Enhanced Fast Charging and Reduced Lithium-Plating by Laser-Structured Anodes for Lithium-Ion Batteries," *Journal of The Electrochemical Society*, vol. 166, no. 16, A3940–A3949, 2019, DOI: 10.1149/2.1241915jes.

[23] L. Hille et al., „Laser structuring of graphite anodes and NMC cathodes – Proportionate influence on electrode characteristics and cell performance," *Electrochimica Acta*, vol. 392, p. 139002, 2021, DOI: 10.1016/j.electacta.2021.139002.

[24] J. Kriegler et al., „Enhanced performance and lifetime of lithium-ion batteries by laser structuring of graphite anodes," *Applied Energy*, vol. 303, p. 117693, 2021, DOI: 10.1016/j.apenergy.2021.117693.

[25] E. R. Logan and J. R. Dahn, „Electrolyte Design for Fast-Charging Li-Ion Batteries," *Trends in Chemistry*, vol. 2, no. 4, pp. 354–366, 2020, DOI: 10.1016/j.trechm.2020.01.011.

[26] A. Tomaszewska et al., „Lithium-ion battery fast charging: A review," *eTransportation*, vol. 1, p. 100011, 2019, DOI: 10.1016/j.etran.2019.100011.

[27] X.-G. Yang, G. Zhang, S. Ge and C.-Y. Wang, „Fast charging of lithium-ion batteries at all temperatures," *Proceedings of the National Academy of Sciences of the United States of America*, vol. 115, no. 28, pp. 7266–7271, 2018, DOI: 10.1073/pnas.1807115115.

[28] X.-G. Yang and C.-Y. Wang, „Understanding the trilemma of fast charging, energy density and cycle life of lithium-ion batteries," *Journal of Power Sources*, vol. 402, pp. 489–498, 2018, DOI: 10.1016/j.jpowsour.2018.09.069.

[29] X.-G. Yang et al., „Asymmetric Temperature Modulation for Extreme Fast Charging of Lithium-Ion Batteries," *Joule*, 2019, DOI: 10.1016/j.joule.2019.09.021.

[30] M. Keyser et al., „Enabling fast charging – Battery thermal considerations," *Journal of Power Sources*, vol. 367, pp. 228–236, 2017, DOI: 10.1016/j.jpowsour.2017.07.009.

[31] A. Meintz et al., „Enabling fast charging – Vehicle considerations," *Journal of Power Sources*, vol. 367, pp. 216–227, 2017, DOI: 10.1016/j.jpowsour.2017.07.093.

[32] A. König et al., „An Overview of Parameter and Cost for Battery Electric Vehicles," *World Electric Vehicle Journal*, vol. 12, no. 1, p. 21, 2021, DOI: 10.3390/wevj12010021.

[33] Nic Lutsey and Michael Nicholas, „Update on electric vehicle costs in the United States through 2030," 2019, DOI: 10.13140/RG.2.2.25390.56646.

[34] V. Freyermuth and A. Rousseau, „Long Term Impact of Vehicle Electrification on Vehicle Weight and Cost Breakdown," in *SAE Technical Paper Series*, 2017, DOI: 10.4271/2017-01-1174.

[35] M. Winter, J. O. Besenhard, M. E. Spahr and P. Novák, „Insertion Electrode Materials for Rechargeable Lithium Batteries," *Advanced Materials*, vol. 10, no. 10, pp. 725–763, 1998, DOI: 10.1002/(SICI)1521-4095(199807)10:10<725::AID-ADMA725>3.0.CO;2-Z.

[36] A. Jossen, „Fundamentals of battery dynamics," *Journal of Power Sources*, vol. 154, no. 2, pp. 530–538, 2006, DOI: 10.1016/j.jpowsour.2005.10.041.

[37] L. Wildfeuer, N. Wassiliadis, A. Karger, F. Bauer and M. Lienkamp, „Teardown analysis and characterization of a commercial lithium-ion battery for advanced algorithms in battery electric vehicles," *Journal of Energy Storage*, vol. 48, p. 103909, 2022, DOI: 10.1016/j.est.2021.103909.

[38] N. Wassiliadis et al., „A systematic approach for the parameter identification of electrochemical battery models enabling health-aware fast charging control of battery electric vehicles," *Journal of Energy Storage*, vol. 56, p. 105951, 2022, DOI: 10.1016/j.est.2022.105951.

[39] D. Bernardi, E. Pawlikowski and J. Newman, „A General Energy Balance for Battery Systems," *Journal of The Electrochemical Society*, vol. 132, no. 1, pp. 5–12, 1985, DOI: 10.1149/1.2113792.

[40] P. Keil, „Aging of Lithium-Ion Batteries in Electric Vehicles," Dissertation, Technische Universität München, München, 2017.

[41] W. Waag, C. Fleischer and D. U. Sauer, „Critical review of the methods for monitoring of lithium-ion batteries in electric and hybrid vehicles," *Journal of Power Sources*, vol. 258, pp. 321–339, 2014, DOI: 10.1016/j.jpowsour.2014.02.064.

[42] S. Chae, S.-H. Choi, N. Kim, J. Sung and J. Cho, „Integration of Graphite and Silicon Anodes for the Commercialization of High-Energy Lithium-Ion Batteries," *Angewandte Chemie (International ed. in English)*, vol. 59, no. 1, pp. 110–135, 2020, DOI: 10.1002/anie.201902085.

[43] H. Buqa, D. Goers, M. Holzapfel, M. E. Spahr and P. Novák, „High Rate Capability of Graphite Negative Electrodes for Lithium-Ion Batteries," *Journal of The Electrochemical Society*, vol. 152, no. 2, A474, 2005, DOI: 10.1149/1.1851055.

[44] S. L. Glazier, J. Li, A. J. Louli, J. P. Allen and J. R. Dahn, „An Analysis of Artificial and Natural Graphite in Lithium Ion Pouch Cells Using Ultra-High Precision Coulometry, Isothermal Microcalorimetry, Gas Evolution, Long Term Cycling and Pressure Measurements," *Journal of The Electrochemical Society*, vol. 164, no. 14, A3545–A3555, 2017, DOI: 10.1149/2.0421714jes.

[45] F. J. Günter and N. Wassiliadis, „State of the Art of Lithium-Ion Pouch Cells in Automotive Applications: Cell Teardown and Characterization," *Journal of The Electrochemical Society*, vol. 169, 2022, DOI: 10.1149/1945-7111/ac4e11.

[46] G. E. Blomgren, „The Development and Future of Lithium Ion Batteries," *Journal of The Electrochemical Society*, vol. 164, no. 1, A5019–A5025, 2017, DOI: 10.1149/2.0251701jes.

[47] S. Albrecht et al., „Electrochemical and thermal behavior of aluminum- and magnesium-doped spherical lithium nickel cobalt mixed oxides $Li_{1-x}(Ni_{1-y-z}Co_yM_z)O_2$ (M = Al, Mg)," *Journal of Power Sources*, vol. 119-121, pp. 178–183, 2003, DOI: 10.1016/S0378-7753(03)00175-7.

[48] S. Watanabe, M. Kinoshita, T. Hosokawa, K. Morigaki and K. Nakura, „Capacity fading of $LiAl_yNi_{1-x-y}Co_xO_2$ cathode for lithium-ion batteries during accelerated calendar and cycle life tests (effect of depth of discharge in charge–discharge cycling on the suppression of the micro-crack generation of $LiAl_yNi_{1-x-y}Co_xO_2$ particle)," *Journal of Power Sources*, vol. 260, pp. 50–56, 2014, DOI: 10.1016/j.jpowsour.2014.02.103.

[49] H.-H. Ryu et al., „A highly stabilized Ni-rich NCA cathode for high-energy lithium-ion batteries," *Materials Today*, vol. 36, pp. 73–82, 2020, DOI: 10.1016/j.mattod.2020.01.019.

[50] W. Li, S. Lee and A. Manthiram, „High-Nickel NMA: A Cobalt-Free Alternative to NMC and NCA Cathodes for Lithium-Ion Batteries," *Advanced Materials*, vol. 32, no. 33, e2002718, 2020, DOI: 10.1002/adma.202002718.

[51] M. Li, J. Lu, Z. Chen and K. Amine, „30 Years of Lithium-Ion Batteries," *Advanced Materials*, e1800561, 2018, DOI: 10.1002/adma.201800561.

[52] B. Wang et al., „Which of the nickel-rich NCM and NCA is structurally superior as a cathode material for lithium-ion batteries?," *Journal of Materials Chemistry A*, vol. 9, no. 23, pp. 13540–13551, 2021, DOI: 10.1039/d1ta01128f.

[53] J. A. Gilbert, I. A. Shkrob and D. P. Abraham, „Transition Metal Dissolution, Ion Migration, Electrocatalytic Reduction and Capacity Loss in Lithium-Ion Full Cells," *Journal of The Electrochemical Society*, vol. 164, no. 2, A389–A399, 2017, DOI: 10.1149/2.1111702jes.

[54] A. K. Padhi, K. S. Nanjundaswamy and J. B. Goodenough, „Phospho–olivines as Positive–Electrode Materials for Rechargeable Lithium Batteries," *Journal of The Electrochemical Society*, vol. 144, no. 4, pp. 1188–1194, 1997, DOI: 10.1149/1.1837571.

[55] H.-H. Ryu, H. H. Sun, S.-T. Myung, C. S. Yoon and Y.-K. Sun, „Reducing cobalt from lithium-ion batteries for the electric vehicle era," *Energy & Environmental Science*, vol. 14, no. 2, pp. 844–852, 2021, DOI: 10.1039/D0EE03581E.

[57] N. Wassiliadis et al., „Review of fast charging strategies for lithium-ion battery systems and their applicability for battery electric vehicles," *Journal of Energy Storage*, vol. 44, p. 103306, 2021, DOI: 10.1016/j.est.2021.103306.

[58] N. Wassiliadis, J. Kriegler, K. A. Gamra and M. Lienkamp, „Model-based health-aware fast charging to mitigate the risk of lithium plating and prolong the cycle life of lithium-ion batteries in electric vehicles," *Journal of Power Sources*, vol. 561, p. 232586, 2023, DOI: 10.1016/j.jpowsour.2022.232586.

[59] N. Wassiliadis et al., „Quantifying the state of the art of electric powertrains in battery electric vehicles: Range, efficiency, and lifetime from component to system level of the Volkswagen ID.3," 2022, DOI: 10.14459/2022mp1656314.

[60] N. Wassiliadis et al., „Electric powertrain data of a Volkswagen ID.3 during real-world driving situations," 2022, DOI: 10.14459/2022mp1656314.

[61] A. Basic, „Measurement and analysis of fast charging processes of battery electric vehicles," Bachelor's Thesis, Institute of Automotive Technology, Technical University of Munich, 2021.

[62] M. Broussely et al., „Main aging mechanisms in Li ion batteries," *Journal of Power Sources*, vol. 146, no. 1-2, pp. 90–96, 2005, DOI: 10.1016/j.jpowsour.2005.03.172.

[63] X. Ma et al., „Editors' Choice—Hindering Rollover Failure of Li[$Ni_{0.5}Mn_{0.3}Co_{0.2}$]O_2/Graphite Pouch Cells during Long-Term Cycling," *Journal of The Electrochemical Society*, vol. 166, no. 4, A711–A724, 2019, DOI: 10.1149/2.0801904jes.

[64] P. Fermín-Cueto et al., „Identification and machine learning prediction of knee-point and knee-onset in capacity degradation curves of lithium-ion cells," *Energy and AI*, vol. 1, p. 100006, 2020, DOI: 10.1016/j.egyai.2020.100006.

[65] P. M. Attia et al., „Review—"Knees" in Lithium-Ion Battery Aging Trajectories," *Journal of The Electrochemical Society*, vol. 169, no. 6, p. 060517, 2022, DOI: 10.1149/1945-7111/ac6d13.

[66] S. F. Schuster et al., „Nonlinear aging characteristics of lithium-ion cells under different operational conditions," *Journal of Energy Storage*, vol. 1, pp. 44–53, 2015, DOI: 10.1016/j.est.2015.05.003.

[67] T. C. Bach et al., „Nonlinear aging of cylindrical lithium-ion cells linked to heterogeneous compression," *Journal of Energy Storage*, vol. 5, pp. 212–223, 2016, DOI: 10.1016/j.est.2016.01.003.

[68] X.-G. Yang, Y. Leng, G. Zhang, S. Ge and C.-Y. Wang, „Modeling of lithium plating induced aging of lithium-ion batteries: Transition from linear to nonlinear aging," *Journal of Power Sources*, vol. 360, pp. 28–40, 2017, DOI: 10.1016/j.jpowsour.2017.05.110.

[69] J. Keil et al., „Linear and Nonlinear Aging of Lithium-Ion Cells Investigated by Electrochemical Analysis and In-Situ Neutron Diffraction," *Journal of The Electrochemical Society*, vol. 166, no. 16, A3908–A3917, 2019, DOI: 10.1149/2.1271915jes.

[70] J. Keil and A. Jossen, „Electrochemical Modeling of Linear and Nonlinear Aging of Lithium-Ion Cells," *Journal of The Electrochemical Society*, vol. 167, no. 11, p. 110535, 2020, DOI: 10.1149/1945-7111/aba44f.

[71] F. Steinsberger, „Investigation of the influence of fast charging processes on aging of lithium ion batteries," Bachelor's Thesis, Institute of Automotive Technology, Technical University of Munich, 2019.

[72] T. R. Jow, S. A. Delp, J. L. Allen, J.-P. Jones and M. C. Smart, „Factors Limiting Li + Charge Transfer Kinetics in Li-Ion Batteries," *Journal of The Electrochemical Society*, vol. 165, no. 2, A361–A367, 2018, DOI: 10.1149/2.1221802jes.

[73] C. Mao, R. E. Ruther, J. Li, Z. Du and I. Belharouak, „Identifying the limiting electrode in lithium ion batteries for extreme fast charging," *Electrochemistry Communications*, vol. 97, pp. 37–41, 2018, DOI: 10.1016/j.elecom.2018.10.007.

[74] S. Schindler, M. Bauer, H. Cheetamun and M. A. Danzer, „Fast charging of lithium-ion cells: Identification of aging-minimal current profiles using a design of experiment approach and a mechanistic degradation analysis," *Journal of Energy Storage*, vol. 19, pp. 364–378, 2018, DOI: 10.1016/j.est.2018.08.002.

[75] T. Waldmann, B.-I. Hogg and M. Wohlfahrt-Mehrens, „Li plating as unwanted side reaction in commercial Li-ion cells – A review," *Journal of Power Sources*, vol. 384, pp. 107–124, 2018, DOI: 10.1016/j.jpowsour.2018.02.063.

[76] Y. Gao, X. Zhang, C. Zhu and B. Guo, „Global Parameter Sensitivity Analysis of Electrochemical Model for Lithium-Ion Batteries Considering Aging," *IEEE/ASME Transactions on Mechatronics*, vol. 26, no. 3, pp. 1283–1294, 2021, DOI: 10.1109/TMECH.2021.3067923.

[77] A. Raj, M.-T. F. Rodrigues and D. P. Abraham, „Rate-Dependent Aging Resulting from Fast Charging of Li-Ion Cells," *Journal of The Electrochemical Society*, vol. 167, no. 12, p. 120517, 2020, DOI: 10.1149/1945-7111/abace9.

[78] D. Liu et al., „On the stress characteristics of graphite anode in commercial pouch lithium-ion battery," *Journal of Power Sources*, vol. 232, pp. 29–33, 2013, DOI: 10.1016/j.jpowsour.2012.12.110.

[79] K. Takahashi and V. Srinivasan, „Examination of Graphite Particle Cracking as a Failure Mode in Lithium-Ion Batteries: A Model-Experimental Study," *Journal of The Electrochemical Society*, vol. 162, no. 4, A635–A645, 2015, DOI: 10.1149/2.0281504jes.

[80] B. Stiaszny, J. C. Ziegler, E. E. KrauSS, J. P. Schmidt and E. Ivers-Tiffée, „Electrochemical characterization and post-mortem analysis of aged $LiMn_2O_4$–$Li(Ni_{0.5}Mn_{0.3}Co_{0.2})O_2$/graphite lithium ion batteries. Part I: Cycle aging," *Journal of Power Sources*, vol. 251, pp. 439–450, 2014, DOI: 10.1016/j.jpowsour.2013.11.080.

[81] K. Zhao, M. Pharr, J. J. Vlassak and Z. Suo, „Fracture of electrodes in lithium-ion batteries caused by fast charging," *Journal of Applied Physics*, vol. 108, no. 7, p. 073517, 2010, DOI: 10.1063/1.3492617.

[82] M. Ashuri, Q. He and L. L. Shaw, „Silicon as a potential anode material for Li-ion batteries: where size, geometry and structure matter," *Nanoscale*, vol. 8, no. 1, pp. 74–103, 2016, DOI: 10.1039/c5nr05116a.

[83] F. Dou, L. Shi, G. Chen and D. Zhang, „Silicon/Carbon Composite Anode Materials for Lithium-Ion Batteries," *Electrochemical Energy Reviews*, vol. 2, no. 1, pp. 149–198, 2019, DOI: 10.1007/s41918-018-00028-w.

[84] T. Sun et al., „Modeling the inhomogeneous lithium plating in lithium-ion batteries induced by non-uniform temperature distribution," *Electrochimica Acta*, vol. 425, p. 140701, 2022, DOI: 10.1016/j.electacta.2022.140701.

[85] D. Aurbach, „A short review of failure mechanisms of lithium metal and lithiated graphite anodes in liquid electrolyte solutions," *Solid State Ionics*, vol. 148, no. 3-4, pp. 405–416, 2002, DOI: 10.1016/S0167-2738(02)00080-2.

[86] X. Ma et al., „A study of highly conductive ester co-solvents in $Li[Ni_{0.5}Mn_{0.3}Co_{0.2}]O_2$/Graphite pouch cells," *Electrochimica Acta*, vol. 270, pp. 215–223, 2018, DOI: 10.1016/j.electacta.2018.03.006.

[87] Q. Q. Liu, D. J. Xiong, R. Petibon, C. Y. Du and J. R. Dahn, „Gas Evolution during Unwanted Lithium Plating in Li-Ion Cells with EC-Based or EC-Free Electrolytes," *Journal of The Electrochemical Society*, vol. 163, no. 14, A3010–A3015, 2016, DOI: 10.1149/2.0711614jes.

[88] M. Lewerenz et al., „New method evaluating currents keeping the voltage constant for fast and highly resolved measurement of Arrhenius relation and capacity fade," *Journal of Power Sources*, vol. 353, pp. 144–151, 2017, DOI: 10.1016/j.jpowsour.2017.03.136.

[89] J. Sieg et al., „Fast-charging capability of lithium-ion cells: Influence of electrode aging and electrolyte consumption," *Applied Energy*, vol. 305, p. 117747, 2022, DOI: 10.1016/j.apenergy.2021.117747.

[90] A. M. Colclasure et al., „Requirements for Enabling Extreme Fast Charging of High Energy Density Li-Ion Cells while Avoiding Lithium Plating," *Journal of The Electrochemical Society*, vol. 166, no. 8, A1412–A1424, 2019, DOI: 10.1149/2.0451908jes.

[91] T. Gao et al., „Interplay of Lithium Intercalation and Plating on a Single Graphite Particle," *Joule*, vol. 5, no. 2, pp. 393–414, 2021, DOI: 10.1016/j.joule.2020.12.020.

[92] Z. Li, J. Huang, B. Yann Liaw, V. Metzler and J. Zhang, „A review of lithium deposition in lithium-ion and lithium metal secondary batteries," *Journal of Power Sources*, vol. 254, pp. 168–182, 2014, DOI: 10.1016/j.jpowsour.2013.12.099.

[93] N. Legrand, B. Knosp, P. Desprez, F. Lapicque and S. Raël, „Physical characterization of the charging process of a Li-ion battery and prediction of Li plating by electrochemical modelling," *Journal of Power Sources*, vol. 245, pp. 208–216, 2014, DOI: 10.1016/j.jpowsour.2013.06.130.

[94] M. Ecker, P. Shafiei Sabet and D. U. Sauer, „Influence of operational condition on lithium plating for commercial lithium-ion batteries – Electrochemical experiments and post-mortem-analysis," *Applied Energy*, vol. 206, pp. 934–946, 2017, DOI: 10.1016/j.apenergy.2017.08.034.

[95] M. W. Verbrugge and B. J. Koch, „The effect of large negative potentials and overcharge on the electrochemical performance of lithiated carbon," *Journal of Electroanalytical Chemistry*, vol. 436, no. 1-2, pp. 1–7, 1997, DOI: 10.1016/S0022-0728(97)00031-4.

[96] C. Uhlmann, J. Illig, M. Ender, R. Schuster and E. Ivers-Tiffée, „In situ detection of lithium metal plating on graphite in experimental cells," *Journal of Power Sources*, vol. 279, pp. 428–438, 2015, DOI: 10.1016/j.jpowsour.2015.01.046.

[97] I. A. Shkrob, M.-T. F. Rodrigues, D. W. Dees and D. P. Abraham, „Fast Charging of Li-Ion Cells: Part II. Nonlinear Contributions to Cell and Electrode Polarization," *Journal of The Electrochemical Society*, vol. 166, no. 14, A3305–A3313, 2019, DOI: 10.1149/2.0561914jes.

[98] J. Sturm et al., „Modeling and simulation of inhomogeneities in a 18650 nickel-rich, silicon-graphite lithium-ion cell during fast charging," *Journal of Power Sources*, vol. 412, pp. 204–223, 2019, DOI: 10.1016/j.jpowsour.2018.11.043.

[99] D. Ren et al., „Investigation of Lithium Plating-Stripping Process in Li-Ion Batteries at Low Temperature Using an Electrochemical Model," *Journal of The Electrochemical Society*, vol. 165, no. 10, A2167–A2178, 2018, DOI: 10.1149/2.0661810jes.

[100] C. von Lüders, J. Keil, M. Webersberger and A. Jossen, „Modeling of lithium plating and lithium stripping in lithium-ion batteries," *Journal of Power Sources*, vol. 414, pp. 41–47, 2019, DOI: 10.1016/j.jpowsour.2018.12.084.

[101] X. Lin, K. Khosravinia, X. Hu, J. Li and W. Lu, „Lithium Plating Mechanism, Detection, and Mitigation in Lithium-Ion Batteries," *Progress in Energy and Combustion Science*, vol. 87, p. 100953, 2021, DOI: 10.1016/j.pecs.2021.100953.

[102] T. Piao, S.-M. Park, C.-H. Doh and S.-I. Moon, „Intercalation of Lithium Ions into Graphite Electrodes Studied by AC Impedance Measurements," *Journal of The Electrochemical Society*, vol. 146, no. 8, pp. 2794–2798, 1999, DOI: 10.1149/1.1392010.

[103] M. Ecker, S. Käbitz, I. Laresgoiti and D. U. Sauer, „Parameterization of a Physico-Chemical Model of a Lithium-Ion Battery," *Journal of The Electrochemical Society*, vol. 162, no. 9, A1849–A1857, 2015, DOI: 10.1149/2.0541509jes.

[104] J. Schmalstieg, C. Rahe, M. Ecker and D. U. Sauer, „Full Cell Parameterization of a High-Power Lithium-Ion Battery for a Physico-Chemical Model: Part I. Physical and Electrochemical Parameters," *Journal of The Electrochemical Society*, vol. 165, no. 16, A3799–A3810, 2018, DOI: 10.1149/2.0321816jes.

[105] P. Kuntz et al., „Identification of Degradation Mechanisms by Post-Mortem Analysis for High Power and High Energy Commercial Li-Ion Cells after Electric Vehicle Aging," *Batteries*, vol. 7, no. 3, p. 48, 2021, DOI: 10.3390/batteries7030048.

[106] H. Rahimi-Eichi, U. Ojha, F. Baronti and M.-Y. Chow, „Battery Management System: An Overview of Its Application in the Smart Grid and Electric Vehicles," *IEEE Industrial Electronics Magazine*, vol. 7, no. 2, pp. 4–16, 2013, DOI: 10.1109/MIE.2013.2250351.

[107] P. Rosner, „Study of a method for the development of lithium-ion battery fast charge protocols," Master's thesis, Institute of Automotive Technology, Technical University of Munich, 2020.

[108] J. Steiger, D. Kramer and R. Mönig, „Microscopic observations of the formation, growth and shrinkage of lithium moss during electrodeposition and dissolution," *Electrochimica Acta*, vol. 136, pp. 529–536, 2014, DOI: 10.1016/j.electacta.2014.05.120.

[109] J. C. Burns, D. A. Stevens and J. R. Dahn, „In-Situ Detection of Lithium Plating Using High Precision Coulometry," *Journal of The Electrochemical Society*, vol. 162, no. 6, A959–A964, 2015, DOI: 10.1149/2.0621506jes.

[110] X. Lin, X. Hao, Z. Liu and W. Jia, „Health conscious fast charging of Li-ion batteries via a single particle model with aging mechanisms," *Journal of Power Sources*, vol. 400, pp. 305–316, 2018, DOI: 10.1016/j.jpowsour.2018.08.030.

[111] Y. Wu and N. Liu, „Visualizing Battery Reactions and Processes by Using In Situ and In Operando Microscopies," *Chem*, vol. 4, no. 3, pp. 438–465, 2018, DOI: 10.1016/j.chempr.2017.12.022.

[112] J.-H. Cheng et al., „Visualization of Lithium Plating and Stripping via in Operando Transmission X-ray Microscopy," *The Journal of Physical Chemistry C*, vol. 121, no. 14, pp. 7761–7766, 2017, DOI: 10.1021/acs.jpcc.7b01414.

[113] N. Ghanbari, T. Waldmann, M. Kasper, P. Axmann and M. Wohlfahrt-Mehrens, „Detection of Li Deposition by Glow Discharge Optical Emission Spectroscopy in Post-Mortem Analysis," *ECS Electrochemistry Letters*, vol. 4, no. 9, A100–A102, 2015, DOI: 10.1149/2.0041509eel.

[114] N. Ghanbari, T. Waldmann, M. Kasper, P. Axmann and M. Wohlfahrt-Mehrens, „Inhomogeneous Degradation of Graphite Anodes in Li-Ion Cells: A Postmortem Study Using Glow Discharge Optical Emission Spectroscopy (GD-OES)," *The Journal of Physical Chemistry C*, vol. 120, no. 39, pp. 22225–22234, 2016, DOI: 10.1021/acs.jpcc.6b07117.

[115] R. Bhattacharyya et al., „In situ NMR observation of the formation of metallic lithium microstructures in lithium batteries," *Nature materials*, vol. 9, no. 6, pp. 504–510, 2010, DOI: 10.1038/nmat2764.

[116] J. Wandt, P. Jakes, J. Granwehr, R.-A. Eichel and H. A. Gasteiger, „Quantitative and time-resolved detection of lithium plating on graphite anodes in lithium ion batteries," *Materials Today*, vol. 21, no. 3, pp. 231–240, 2018, DOI: 10.1016/j.mattod.2017.11.001.

[117] M. A. Cabañero, M. Hagen and E. Quiroga-González, „In-operando Raman study of lithium plating on graphite electrodes of lithium ion batteries," *Electrochimica Acta*, vol. 374, p. 137487, 2021, DOI: 10.1016/j.electacta.2020.137487.

[118] V. Zinth et al., „Lithium plating in lithium-ion batteries at sub-ambient temperatures investigated by in situ neutron diffraction," *Journal of Power Sources*, vol. 271, pp. 152–159, 2014, DOI: 10.1016/j.jpowsour.2014.07.168.

[119] T. Waldmann, M. Kasper and M. Wohlfahrt-Mehrens, „Optimization of Charging Strategy by Prevention of Lithium Deposition on Anodes in high-energy Lithium-ion Batteries – Electrochemical Experiments," *Electrochimica Acta*, vol. 178, pp. 525–532, 2015, DOI: 10.1016/j.electacta.2015.08.056.

[120] T. Waldmann et al., „Interplay of Operational Parameters on Lithium Deposition in Lithium-Ion Cells: Systematic Measurements with Reconstructed 3-Electrode Pouch Full Cells," *Journal of The Electrochemical Society*, vol. 163, no. 7, A1232–A1238, 2016, DOI: 10.1149/2.0591607jes.

[121] S. P. Rangarajan, Y. Barsukov and P. P. Mukherjee, „In operando signature and quantification of lithium plating," *Journal of Materials Chemistry A*, vol. 7, no. 36, pp. 20683–20695, 2019, DOI: 10.1039/C9TA07314K.

[122] B. Bitzer and A. Gruhle, „A new method for detecting lithium plating by measuring the cell thickness," *Journal of Power Sources*, vol. 262, pp. 297–302, 2014, DOI: 10.1016/j.jpowsour.2014.03.142.

[123] C. R. Birkl, E. McTurk, M. R. Roberts, P. G. Bruce and D. A. Howey, „A Parametric Open Circuit Voltage Model for Lithium Ion Batteries," *Journal of The Electrochemical Society*, vol. 162, no. 12, A2271–A2280, 2015, DOI: 10.1149/2.0331512jes.

[124] A. Zülke, Y. Li, P. Keil and H. Hoster, „Communication—Why High-Precision Coulometry and Lithium Plating Studies on Commercial Lithium-Ion Cells Require Thermal Baths," *Journal of The Electrochemical Society*, vol. 166, no. 13, A2921–A2923, 2019, DOI: 10.1149/2.0841913jes.

[125] M. Ouyang et al., „Low temperature aging mechanism identification and lithium deposition in a large format lithium iron phosphate battery for different charge profiles," *Journal of Power Sources*, vol. 286, pp. 309–320, 2015, DOI: 10.1016/j.jpowsour.2015.03.178.

[126] D. Anseán et al., „Operando lithium plating quantification and early detection of a commercial $LiFePO_4$ cell cycled under dynamic driving schedule," *Journal of Power Sources*, vol. 356, pp. 36–46, 2017, DOI: 10.1016/j.jpowsour.2017.04.072.

[127] M. C. Smart et al., „Performance characteristics of lithium ion cells at low temperatures," *IEEE Aerospace and Electronic Systems Magazine*, vol. 17, no. 12, pp. 16–20, 2002, DOI: 10.1109/MAES.2002.1145732.

[128] J. Fan and S. Tan, „Studies on Charging Lithium-Ion Cells at Low Temperatures," *Journal of The Electrochemical Society*, vol. 153, no. 6, A1081, 2006, DOI: 10.1149/1.2190029.

[129] R. V. Bugga and M. C. Smart, „Lithium Plating Behavior in Lithium-Ion Cells," *ECS Transactions*, vol. 25, no. 36, pp. 241–252, 2010, DOI: 10.1149/1.3393860.

[130] M. Petzl and M. A. Danzer, „Nondestructive detection, characterization, and quantification of lithium plating in commercial lithium-ion batteries," *Journal of Power Sources*, vol. 254, pp. 80–87, 2014, DOI: 10.1016/j.jpowsour.2013.12.060.

[131] R. Bednorz and T. Gewald, „Investigation of the Effects of Charging Processes on Lithium-Ion Cells with SiC Anodes at Low Temperatures," *Batteries*, vol. 6, no. 2, p. 34, 2020, DOI: 10.3390/batteries6020034.

[132] S. Schindler, M. Bauer, M. Petzl and M. A. Danzer, „Voltage relaxation and impedance spectroscopy as in-operando methods for the detection of lithium plating on graphitic anodes in commercial lithium-ion cells," *Journal of Power Sources*, vol. 304, pp. 170–180, 2016, DOI: 10.1016/j.jpowsour.2015.11.044.

[133] L. J. Krause, L. D. Jensen and J. R. Dahn, „Measurement of Parasitic Reactions in Li Ion Cells by Electrochemical Calorimetry," *Journal of The Electrochemical Society*, vol. 159, no. 7, A937–A943, 2012, DOI: 10.1149/2.021207jes.

[134] L. E. Downie et al., „In Situ Detection of Lithium Plating on Graphite Electrodes by Electrochemical Calorimetry," *Journal of The Electrochemical Society*, vol. 160, no. 4, A588–A594, 2013, DOI: 10.1149/2.049304jes.

[135] M. Koseoglou et al., „Lithium plating detection using dynamic electrochemical impedance spectroscopy in lithium-ion batteries," *Journal of Power Sources*, vol. 512, p. 230508, 2021, DOI: 10.1016/j.jpowsour.2021.230508.

[136] Y. Li et al., „Errors in the reference electrode measurements in real lithium-ion batteries," *Journal of Power Sources*, vol. 481, p. 228933, 2021, DOI: 10.1016/j.jpowsour.2020.228933.

[137] B. Rieger et al., „Multi-directional laser scanning as innovative method to detect local cell damage during fast charging of lithium-ion cells," *Journal of Energy Storage*, vol. 8, pp. 1–5, 2016, DOI: 10.1016/j.est.2016.09.002.

[138] J. Sturm, F. B. Spingler, B. Rieger, A. Rheinfeld and A. Jossen, „Non-Destructive Detection of Local Aging in Lithium-Ion Pouch Cells by Multi-Directional Laser Scanning," *Journal of The Electrochemical Society*, vol. 164, no. 7, A1342–A1351, 2017, DOI: 10.1149/2.0161707jes.

[139] F. B. Spingler, W. Wittmann, J. Sturm, B. Rieger and A. Jossen, „Optimum fast charging of lithium-ion pouch cells based on local volume expansion criteria," *Journal of Power Sources*, vol. 393, pp. 152–160, 2018, DOI: 10.1016/j.jpowsour.2018.04.095.

[140] I. Bloom et al., „Differential voltage analyses of high-power, lithium-ion cells," *Journal of Power Sources*, vol. 139, no. 1-2, pp. 295–303, 2005, DOI: 10.1016/j.jpowsour.2004.07.021.

[141] I. Bloom, J. Christophersen and K. Gering, „Differential voltage analyses of high-power lithium-ion cells," *Journal of Power Sources*, vol. 139, no. 1-2, pp. 304–313, 2005, DOI: 10.1016/j.jpowsour.2004.07.022.

[142] I. Bloom, J. P. Christophersen, D. P. Abraham and K. L. Gering, „Differential voltage analyses of high-power, lithium-ion cells," *Journal of Power Sources*, vol. 157, no. 1, pp. 537–542, 2006, DOI: 10.1016/j.jpowsour.2005.07.054.

[143] Y. Motoaki, W. Yi and S. Salisbury, „Empirical analysis of electric vehicle fast charging under cold temperatures," *Energy Policy*, vol. 122, pp. 162–168, 2018, DOI: 10.1016/j.enpol.2018.07.036.

[144] J. Veeh, „Investigation of the Li-plating behavior of lithium-ion batteries and parameterization of an electrochemical battery model," Master's Thesis, Institute of Automotive Technology, Technical University of Munich, 2022.

[145] Q. Liu et al., „Understanding undesirable anode lithium plating issues in lithium-ion batteries," *RSC Advances*, vol. 6, no. 91, pp. 88683–88700, 2016, DOI: 10.1039/c6ra19482f.

[146] I. D. Campbell, M. Marzook, M. Marinescu and G. J. Offer, „How Observable Is Lithium Plating? Differential Voltage Analysis to Identify and Quantify Lithium Plating Following Fast Charging of Cold Lithium-Ion Batteries," *Journal of The Electrochemical Society*, vol. 166, no. 4, A725–A739, 2019, DOI: 10.1149/2.0821904jes.

[147] L. Hovestadt, K. Wildermann, A. Sahhary and R. Hanke-Rauschenbach, „Investigation of Temperature and Pressure Behaviour of Constrained Lithium Ion Cell under Lithium Plating Conditions," *Journal of The Electrochemical Society*, 2020, DOI: 10.1149/1945-7111/aba550.

[148] N. Harting, N. Wolff and U. Krewer, „Identification of Lithium Plating in Lithium-Ion Batteries using Nonlinear Frequency Response Analysis (NFRA)," *Electrochimica Acta*, vol. 281, pp. 378–385, 2018, DOI: 10.1016/j.electacta.2018.05.139.

[149] G. Li and C. W. Monroe, „Multiscale Lithium-Battery Modeling from Materials to Cells," *Annual review of chemical and biomolecular engineering*, vol. 11, pp. 277–310, 2020, DOI: 10.1146/annurev-chembioeng-012120-083016.

[150] M. Doyle, T. F. Fuller and J. Newman, „Modeling of Galvanostatic Charge and Discharge of the Lithium/Polymer/Insertion Cell," *Journal of The Electrochemical Society*, vol. 140, no. 6, pp. 1526–1533, 1993, DOI: 10.1149/1.2221597.

[151] C. M. Doyle, „Design and Simulation of Lithium Rechargeable Batteries," Dissertation, Lawrence Berkeley National Laboratory, University of California, Berkeley, California, 1995.

[152] G. L. Plett, *Battery management systems*, (Artech House power engineering and power electronics). vol. 1, Boston, Artech House, 2015, ISBN: 978-1-63081-023-8.

[153] J. Sturm et al., „State estimation of lithium-ion cells using a physicochemical model based extended Kalman filter," *Applied Energy*, vol. 223, pp. 103–123, 2018, DOI: 10.1016/j.apenergy.2018.04.011.

[154] Y. Gao, K. Liu, C. Zhu, X. Zhang and D. Zhang, „Co-Estimation of State-of-Charge and State-of- Health for Lithium-Ion Batteries Using an Enhanced Electrochemical Model," *IEEE Transactions on Industrial Electronics*, vol. 69, no. 3, pp. 2684–2696, 2022, DOI: 10.1109/TIE.2021.3066946.

[155] P. Ramadass, B. Haran, P. M. Gomadam, R. White and B. N. Popov, „Development of First Principles Capacity Fade Model for Li-Ion Cells," *Journal of The Electrochemical Society*, vol. 151, no. 2, A196, 2004, DOI: 10.1149/1.1634273.

[156] A. Lamorgese, R. Mauri and B. Tellini, „Electrochemical-thermal P2D aging model of a $LiCoO_2$/graphite cell: Capacity fade simulations," *Journal of Energy Storage*, vol. 20, pp. 289–297, 2018, DOI: 10.1016/j.est.2018.08.011.

[157] M. Xu, Z. Zhang, X. Wang, L. Jia and L. Yang, „Two-dimensional electrochemical–thermal coupled modeling of cylindrical $LiFePO_4$ batteries," *Journal of Power Sources*, vol. 256, pp. 233–243, 2014, DOI: 10.1016/j.jpowsour.2014.01.070.

[158] K. H. Kwon, C. B. Shin, T. H. Kang and C.-S. Kim, „A two-dimensional modeling of a lithium-polymer battery," *Journal of Power Sources*, vol. 163, no. 1, pp. 151–157, 2006, DOI: 10.1016/j.jpowsour.2006.03.012.

[159] A. Frank, J. Sturm, M. Steinhardt, A. Rheinfeld and A. Jossen, „Impact of Current Collector Design and Cooling Topology on Fast Charging of Cylindrical Lithium-Ion Batteries," *ECS Advances*, 2022, DOI: 10.1149/2754-2734/ac97e0.

[160] A. Tourani, P. White and P. Ivey, „A multi scale multi-dimensional thermo electrochemical modelling of high capacity lithium-ion cells," *Journal of Power Sources*, vol. 255, pp. 360–367, 2014, DOI: 10.1016/j.jpowsour.2014.01.030.

[161] A. Samba et al., „Development of an Advanced Two-Dimensional Thermal Model for Large size Lithium-ion Pouch Cells," *Electrochimica Acta*, vol. 117, pp. 246–254, 2014, DOI: 10.1016/j.electacta.2013.11.113.

[162] A. Jokar, B. Rajabloo, M. Désilets and M. Lacroix, „Review of simplified Pseudo-two-Dimensional models of lithium-ion batteries," *Journal of Power Sources*, vol. 327, pp. 44–55, 2016, DOI: 10.1016/j.jpowsour.2016.07.036.

[163] A. Fotouhi, D. J. Auger, K. Propp, S. Longo and M. Wild, „A review on electric vehicle battery modelling: From Lithium-ion toward Lithium–Sulphur," *Renewable and Sustainable Energy Reviews*, vol. 56, pp. 1008–1021, 2016, DOI: 10.1016/j.rser.2015.12.009.

[164] Y. Wang et al., „A comprehensive review of battery modeling and state estimation approaches for advanced battery management systems," *Renewable and Sustainable Energy Reviews*, vol. 131, p. 110015, 2020, DOI: 10.1016/j.rser.2020.110015.

[165] F. Ringbeck, M. Garbade and D. U. Sauer, „Uncertainty-aware state estimation for electrochemical model-based fast charging control of lithium-ion batteries," *Journal of Power Sources*, vol. 470, p. 228221, 2020, DOI: 10.1016/j.jpowsour.2020.228221.

[166] G. Ning and B. N. Popov, „Cycle Life Modeling of Lithium-Ion Batteries," *Journal of The Electrochemical Society*, vol. 151, no. 10, A1584, 2004, DOI: 10.1149/1.1787631.

[167] S. Santhanagopalan, Q. Guo, P. Ramadass and R. E. White, „Review of models for predicting the cycling performance of lithium ion batteries," *Journal of Power Sources*, vol. 156, no. 2, pp. 620–628, 2006, DOI: 10.1016/j.jpowsour.2005.05.070.

[168] M. Guo, G. Sikha and R. E. White, „Single-Particle Model for a Lithium-Ion Cell: Thermal Behavior," *Journal of The Electrochemical Society*, vol. 158, no. 2, A122, 2011, DOI: 10.1149/1.3521314.

[169] T. R. Tanim, C. D. Rahn and C.-Y. Wang, „A Temperature Dependent, Single Particle, Lithium Ion Cell Model Including Electrolyte Diffusion," *Journal of Dynamic Systems, Measurement, and Control*, vol. 137, no. 1, 2015, DOI: 10.1115/1.4028154.

[170] J. Li, N. Lotfi, R. G. Landers and J. Park, „A Single Particle Model for Lithium-Ion Batteries with Electrolyte and Stress-Enhanced Diffusion Physics," *Journal of The Electrochemical Society*, vol. 164, no. 4, A874–A883, 2017, DOI: 10.1149/2.1541704jes.

[171] M.-T. von Srbik, M. Marinescu, R. F. Martinez-Botas and G. J. Offer, „A physically meaningful equivalent circuit network model of a lithium-ion battery accounting for local electrochemical and thermal behaviour, variable double layer capacitance and degradation," *Journal of Power Sources*, vol. 325, pp. 171–184, 2016, DOI: 10.1016/j.jpowsour.2016.05.051.

[172] Y. Merla, B. Wu, V. Yufit, R. F. Martinez-Botas and G. J. Offer, „An easy-to-parameterise physics-informed battery model and its application towards lithium-ion battery cell design, diagnosis, and degradation," *Journal of Power Sources*, vol. 384, pp. 66–79, 2018, DOI: 10.1016/j.jpowsour.2018.02.065.

[173] Y. Li et al., „A physics-based distributed-parameter equivalent circuit model for lithium-ion batteries," *Electrochimica Acta*, vol. 299, pp. 451–469, 2019, DOI: 10.1016/j.electacta.2018.12.167.

[174] Z. Geng, S. Wang, M. J. Lacey, D. Brandell and T. Thiringer, „Bridging physics-based and equivalent circuit models for lithium-ion batteries," *Electrochimica Acta*, vol. 372, p. 137829, 2021, DOI: 10.1016/j.electacta.2021.137829.

[175] R. Drees, F. Lienesch and M. Kurrat, „Fast charging lithium-ion battery formation based on simulations with an electrode equivalent circuit model," *Journal of Energy Storage*, vol. 36, p. 102345, 2021, DOI: 10.1016/j.est.2021.102345.

[176] R. Drees, F. Lienesch and M. Kurrat, „Durable Fast Charging of Lithium-Ion Batteries Based on Simulations with an Electrode Equivalent Circuit Model," *Batteries*, vol. 8, no. 4, p. 30, 2022, DOI: 10.3390/batteries8040030.

[177] T. Zhao et al., „A study on half–cell equivalent circuit model of lithium–ion battery based on reference electrode," *International Journal of Energy Research*, vol. 45, no. 3, pp. 4155–4169, 2021, DOI: 10.1002/er.6081.

[178] C. Zhang et al., „Real-time estimation of negative electrode potential and state of charge of lithium-ion battery based on a half-cell-level equivalent circuit model," *Journal of Energy Storage*, vol. 51, p. 104362, 2022, DOI: 10.1016/j.est.2022.104362.

[179] X. Lin, „Real-Time Prediction of Anode Potential in Li-Ion Batteries Using Long Short-Term Neural Networks for Lithium Plating Prevention," *Journal of The Electrochemical Society*, vol. 166, no. 10, A1893–A1904, 2019, DOI: 10.1149/2.0621910jes.

[180] J. Hamar, C. Zoerr, S. V. Erhard and A. Jossen, „Anode Potential Estimation in Lithium-Ion Batteries Using Data-Driven Models for Online Applications," *Journal of The Electrochemical Society*, 2021, DOI: 10.1149/1945-7111/abe721.

[181] W. Li et al., „Physics-informed neural networks for electrode-level state estimation in lithium-ion batteries," *Journal of Power Sources*, vol. 506, p. 230034, 2021, DOI: 10.1016/j.jpowsour.2021.230034.

[182] A. M. Baum, „Identification and evaluation of fast charging protocols for lithium-ion batteries," Master's thesis, Institute of Automotive Technology, Technical University of Munich, 2019.

[183] M. Ecker et al., „Parameterization of a Physico-Chemical Model of a Lithium-Ion Battery," *Journal of The Electrochemical Society*, vol. 162, no. 9, A1836–A1848, 2015, DOI: 10.1149/2.0551509jes.

[184] J. Schmalstieg and D. U. Sauer, „Full Cell Parameterization of a High-Power Lithium-Ion Battery for a Physico-Chemical Model: Part II. Thermal Parameters and Validation," *Journal of The Electrochemical Society*, vol. 165, no. 16, A3811–A3819, 2018, DOI: 10.1149/2.0331816jes.

[185] L. Wildfeuer et al., „Experimental degradation study of a commercial lithium-ion battery," *Journal of Power Sources*, vol. 560, p. 232498, 2023, DOI: 10.1016/j.jpowsour.2022.232498.

[186] J. Illig, „Physically based Impedance Modelling of Lithium-ion Cells," Dissertation, Karlsruher Institut für Technologie, Karlsruhe, 2014.

[187] T. Waldmann et al., „Review—Post-Mortem Analysis of Aged Lithium-Ion Batteries: Disassembly Methodology and Physico-Chemical Analysis Techniques," *Journal of The Electrochemical Society*, vol. 163, no. 10, A2149–A2164, 2016, DOI: 10.1149/2.1211609jes.

[188] S. Schindler, „Diskrete elektrochemische Modellierung und experimentelle Identifikation von Lithium-Ionen-Zellen basierend auf Halbzellpotentialen," Dissertation, Universität Bayreuth, Bayreuth, 2018.

[189] J. Sieg et al., „Fast charging of an electric vehicle lithium-ion battery at the limit of the lithium deposition process," *Journal of Power Sources*, vol. 427, pp. 260–270, 2019, DOI: 10.1016/j.jpowsour.2019.04.047.

[190] H. Jaffal, „Evaluation of impedance measurements for evaluation of the fast-charging capability of lithium-ion batteries," Term Thesis, Institute of Automotive Technology, Technical University of Munich, 2021.

[191] J. C. Forman, S. J. Moura, J. L. Stein and H. K. Fathy, „Genetic identification and fisher identifiability analysis of the Doyle–Fuller–Newman model from experimental cycling of a LiFePO4 cell," *Journal of Power Sources*, vol. 210, pp. 263–275, 2012, DOI: 10.1016/j.jpowsour.2012.03.009.

[192] C.-H. Chen et al., „Development of Experimental Techniques for Parameterization of Multi-scale Lithium-ion Battery Models," *Journal of The Electrochemical Society*, vol. 167, no. 8, p. 080534, 2020, DOI: 10.1149/1945-7111/ab9050.

[193] E. Namor, D. Torregrossa, R. Cherkaoui and M. Paolone, „Parameter identification of a lithium-ion cell single-particle model through non-invasive testing," *Journal of Energy Storage*, vol. 12, pp. 138–148, 2017, DOI: 10.1016/j.est.2017.04.008.

[194] S. J. Moura, F. B. Argomedo, R. Klein, A. Mirtabatabaei and M. Krstic, „Battery State Estimation for a Single Particle Model With Electrolyte Dynamics," *IEEE Transactions on Control Systems Technology*, vol. 25, no. 2, pp. 453–468, 2017, DOI: 10.1109/TCST.2016.2571663.

[195] H. E. Perez, X. Hu, S. Dey and S. J. Moura, „Optimal Charging of Li-Ion Batteries With Coupled Electro-Thermal-Aging Dynamics," *IEEE Transactions on Vehicular Technology*, vol. 66, no. 9, pp. 7761–7770, 2017, DOI: 10.1109/TVT.2017.2676044.

[196] M. Wanzel, „Modeling and parameterization of a battery model for lithium-ion battery fast charging," Master's thesis, Institute of Automotive Technology, Technical University of Munich, 2020.

[197] A.-S. Zollner, „Experimental parameterization and validation of a thermal lithium-ion battery model," Term Thesis, Institute of Automotive Technology, Technical University of Munich, 2021.

[198] J. Weiss, „Extension of the validity of a lithium-ion battery model for fast charging to larger temperature ranges," Term Thesis, Institute of Automotive Technology, Technical University of Munich, 2020.

[199] N. Wassiliadis, „Electrochemical lithium-ion battery model and easy-to-apply parameterization procedures for fast-charge applications," 2022. Available: https://github.com/TUMFTM/EA_Battery_SPMparameterization.

[200] T. Kerscher, „Implementation and computing time evaluation of a battery model for deployment in fast charging applications," Term thesis, Institute of Automotive Technology, Technical University of Munich, 2020.

[201] T. Schöpfel, „Simulative preliminary investigation on adaptive model- based fast charging strategies for lithium-ion batteries," Term Thesis, Institute of Automotive Technology, Technical University of Munich, 2021.

[202] L. Wild, „Experimental investigation of model-based fast charging strategies for lithium-ion batteries," Term Thesis, Institute of Automotive Technology, Technical University of Munich, 2021.

[203] M. Frank, „Experimental investigation of the influence of varying cell states on fast charging strategies for lithium-ion batteries," Term Thesis, Institute of Automotive Technology, Technical University of Munich, 2022.

[204] N. Wassiliadis et al., „Revisiting the dual extended Kalman filter for battery state-of-charge and state-of-health estimation: A use-case life cycle analysis," *Journal of Energy Storage*, vol. 19, pp. 73–87, 2018, DOI: 10.1016/j.est.2018.07.006.

[205] N. Wassiliadis, T. Herrmann, L. Wildfeuer, C. Reiter and M. Lienkamp, „Comparative Study of State-Of-Charge Estimation with Recurrent Neural Networks," in *2019 IEEE Transportation Electrification Conference and Expo (ITEC)*, Detroit, MI, USA, 2019, pp. 1–6, ISBN: 978-1-5386-9310-0. DOI: 10.1109/ITEC.2019.8790597.

[206] A. Karger, L. Wildfeuer, A. Maheshwari, N. Wassiliadis and M. Lienkamp, „Novel method for the on-line estimation of low-frequency impedance of lithium-ion batteries," *Journal of Energy Storage*, vol. 32, p. 101818, 2020, DOI: 10.1016/j.est.2020.101818.

[207] A. Wiedemann, „Development and construction of a test bench for the investigation of model-based fast charging strategies for lithium-ion batteries," Master's Thesis, Institute of Automotive Technology, Technical University of Munich, 2019.

[208] A. Bach, „Investigation of model-based fast charging strategies used for lithium-ion batteries," Master's thesis, Institute of Automotive Technology, Technical University of Munich, 2021.

[209] M. Faika, „Evaluation of a model-based fast charging strategy for lithium-ion batteries," Master's thesis, Institute of Automotive Technology, Technical University of Munich, 2022.

[210] N. Wassiliadis et al., „Quantifying the state of the art of electric powertrains in battery electric vehicles: Range, efficiency, and lifetime from component to system level of the Volkswagen ID.3," *eTransportation*, p. 100167, 2022, DOI: 10.1016/j.etran.2022.100167.

[211] C. Reiter et al., „A Holistic Approach for Simulation and Evaluation of Electrical and Thermal Loads in Lithium-Ion Battery Systems," in *2019 Fourteenth International Conference on Ecological Vehicles and Renewable Energies (EVER)*, Monte-Carlo, Monaco, 2019, pp. 1–17, ISBN: 978-1-7281-3703-2. DOI: 10.1109/EVER.2019.8813640.

[212] X. Tang et al., „A fast estimation algorithm for lithium-ion battery state of health," *Journal of Power Sources*, vol. 396, pp. 453–458, 2018, DOI: 10.1016/j.jpowsour.2018.06.036.

[213] C. Reiter, N. Wassiliadis and M. Lienkamp, „Design of Thermal Management Systems for Battery Electric Vehicles," in *2019 Fourteenth International Conference on Ecological Vehicles and Renewable Energies (EVER)*, Monte-Carlo, Monaco, 2019, pp. 1–10, ISBN: 978-1-7281-3703-2. DOI: 10.1109/EVER.2019.8813671.

[214] L. Wildfeuer, N. Wassiliadis, C. Reiter, M. Baumann and M. Lienkamp, „Experimental Characterization of Li-Ion Battery Resistance at the Cell, Module and Pack Level," in *2019 Fourteenth International Conference on Ecological Vehicles and Renewable Energies (EVER)*, Monte-Carlo, Monaco, 2019, pp. 1–12, ISBN: 978-1-7281-3703-2. DOI: 10.1109/EVER.2019.8813578.

[215] M. Ank, „Design of lithium-ion cell holders to improve the quality of battery models," Master's thesis, Institute of Automotive Technology, Technical University of Munich, 2019.

[216] S. Ziegler, „Experimental pre-study of the effect of contact resistance on high current measurements," Bachelor's Thesis, Institute of Automotive Technology, Technical University of Munich, 2019.

[217] N. Wassiliadis, M. Ank, L. Wildfeuer, M. K. Kick and M. Lienkamp, „Experimental investigation of the influence of electric contact resistance of lithium-ion battery testing for fast-charge applications," 2021, DOI: 10.14459/2021mp1611393.

[218] N. Wassiliadis, „Model deployment framework (MDF) for real-time investigation and usage of battery models on CAN-capable test benches," 2022. Available: https://github.com/TUMFTM/EA_Battery_MDF.

[219] N. Wassiliadis, M. Ank, L. Wildfeuer, M. K. Kick and M. Lienkamp, „Experimental investigation of the influence of electrical contact resistance on lithium-ion battery testing for fast-charge applications," *Applied Energy*, vol. 295, p. 117064, 2021, DOI: 10.1016/j.apenergy.2021.117064.

[220] L. O. Valøen and J. N. Reimers, „Transport Properties of LiPF6-Based Li-Ion Battery Electrolytes," *Journal of The Electrochemical Society*, vol. 152, no. 5, A882, 2005, DOI: 10.1149/1.1872737.

[221] M. Kassem and C. Delacourt, „Postmortem analysis of calendar-aged graphite/$LiFePO_4$ cells," *Journal of Power Sources*, vol. 235, pp. 159–171, 2013, DOI: 10.1016/j.jpowsour.2013.01.147.

[222] N. Williard, B. Sood, M. Osterman and M. Pecht, „Disassembly methodology for conducting failure analysis on lithium–ion batteries," *Journal of Materials Science: Materials in Electronics*, vol. 22, no. 10, pp. 1616–1630, 2011, DOI: 10.1007/s10854-011-0452-4.

[223] L. Li et al., „Lithium-ion battery cathode and anode potential observer based on reduced-order electrochemical single particle model," *Journal of Energy Storage*, vol. 44, p. 103324, 2021, DOI: 10.1016/j.est.2021.103324.

[224] T. S. Bryden et al., „Methodology to determine the heat capacity of lithium-ion cells," *Journal of Power Sources*, vol. 395, pp. 369–378, 2018, DOI: 10.1016/j.jpowsour.2018.05.084.

[225] M. Steinhardt et al., „Low-effort determination of heat capacity and thermal conductivity for cylindrical 18650 and 21700 lithium-ion cells," *Journal of Energy Storage*, vol. 42, p. 103065, 2021, DOI: 10.1016/j.est.2021.103065.

[226] H. Maleki, S. A. Hallaj, J. R. Selman, R. B. Dinwiddie and H. Wang, „Thermal Properties of Lithium–Ion Battery and Components," *Journal of The Electrochemical Society*, vol. 146, no. 3, pp. 947–954, 1999, DOI: 10.1149/1.1391704.

[227] P. Keil, K. Rumpf and A. Jossen, „Thermal impedance spectroscopy for Li-ion batteries with an IR temperature sensor system," in *2013 World Electric Vehicle Symposium and Exhibition (EVS27)*, Barcelona, Spain, 2013, pp. 1–11, ISBN: 978-1-4799-3832-2. DOI: 10.1109/EVS.2013.6914935.

[228] J. Schmitt, M. Schindler and A. Jossen, „Change in the half-cell open-circuit potential curves of silicon–graphite and nickel-rich lithium nickel manganese cobalt oxide during cycle aging," *Journal of Power Sources*, vol. 506, p. 230240, 2021, DOI: 10.1016/j.jpowsour.2021.230240.

[229] G. K. Prasad and C. D. Rahn, „Model based identification of aging parameters in lithium ion batteries," *Journal of Power Sources*, vol. 232, pp. 79–85, 2013, DOI: 10.1016/j.jpowsour.2013.01.041.

[230] T. R. Tanim, M. G. Shirk, R. L. Bewley, E. J. Dufek and B. Y. Liaw, „Fast charge implications: Pack and cell analysis and comparison," *Journal of Power Sources*, vol. 381, pp. 56–65, 2018, DOI: 10.1016/j.jpowsour.2018.01.091.

[231] S. Yang et al., „Minimum lithium plating overpotential control based charging strategy for parallel battery module prevents side reactions," *Journal of Power Sources*, vol. 494, p. 229772, 2021, DOI: 10.1016/j.jpowsour.2021.229772.

[232] N. Wassiliadis, K. Abo Gamra, F. Schmid, M. Zähringer and M. Lienkamp, „Fast charging strategy comparison of battery electric vehicles and the benefit of advanced fast charging algorithms," *Advanced Automotive Battery Conference (AABC) Europe, Mainz, Germany*, 2022.

[233] K. Abo Gamra, N. Wassiliadis and M. Lienkamp, „The impact of battery electric vehicle initial conditions on ultra-fast charging events," in *35th International Electric Vehicle Symposium and Exhibition (EVS35)*, Oslo, Norway, 2022.

[234] Z. G. Qu, Z. Y. Jiang and Q. Wang, „Experimental study on pulse self–heating of lithium–ion battery at low temperature," *International Journal of Heat and Mass Transfer*, vol. 135, pp. 696–705, 2019, DOI: 10.1016/j.ijheatmasstransfer.2019.02.020.

[235] H. Ruan et al., „A rapid low-temperature internal heating strategy with optimal frequency based on constant polarization voltage for lithium-ion batteries," *Applied Energy*, vol. 177, pp. 771–782, 2016, DOI: 10.1016/j.apenergy.2016.05.151.

[236] S. Sommer et al., „RACE: A Centralized Platform Computer Based Architecture for Automotive Applications," in *2013 IEEE International Electric Vehicle Conference (IEVC)*, Santa Clara, CA, USA, 2013, pp. 1–6, ISBN: 978-1-4799-1451-7. DOI: 10.1109/IEVC.2013.6681152.

[237] W. Li et al., „Parameter sensitivity analysis of electrochemical model-based battery management systems for lithium-ion batteries," *Applied Energy*, vol. 269, p. 115104, 2020, DOI: 10.1016/j.apenergy.2020.115104.

Prior Publications

During the development of this dissertation, publications and student theses were written in which partial aspects of this work were presented.

Journals; Scopus/Web of Science listed (peer-reviewed)

[37] L. Wildfeuer, N. Wassiliadis, A. Karger, F. Bauer and M. Lienkamp, „Teardown analysis and characterization of a commercial lithium-ion battery for advanced algorithms in battery electric vehicles," *Journal of Energy Storage*, vol. 48, p. 103909, 2022, DOI: 10.1016/j.est.2021.103909.

[45] F. J. Günter and N. Wassiliadis, „State of the Art of Lithium-Ion Pouch Cells in Automotive Applications: Cell Teardown and Characterization," *Journal of The Electrochemical Society*, vol. 169, 2022, DOI: 10.1149/1945-7111/ac4e11.

[57] N. Wassiliadis, J. Schneider, A. Frank, L. Wildfeuer, X. Lin, A. Jossen and M. Lienkamp, „Review of fast charging strategies for lithium-ion battery systems and their applicability for battery electric vehicles," *Journal of Energy Storage*, vol. 44, p. 103306, 2021, DOI: 10.1016/j.est.2021.103306.

[58] N. Wassiliadis, J. Kriegler, K. A. Gamra and M. Lienkamp, „Model-based health-aware fast charging to mitigate the risk of lithium plating and prolong the cycle life of lithium-ion batteries in electric vehicles," *Journal of Power Sources*, vol. 561, p. 232586, 2023, DOI: 10.1016/j.jpowsour.2022.232586.

[185] L. Wildfeuer, A. Karger, D. Aygül, N. Wassiliadis, A. Jossen and M. Lienkamp, „Experimental degradation study of a commercial lithium-ion battery," *Journal of Power Sources*, vol. 560, p. 232498, 2023, DOI: 10.1016/j.jpowsour.2022.232498.

[204] N. Wassiliadis, J. Adermann, A. Frericks, M. Pak, C. Reiter, B. Lohmann and M. Lienkamp, „Revisiting the dual extended Kalman filter for battery state-of-charge and state-of-health estimation: A use-case life cycle analysis," *Journal of Energy Storage*, vol. 19, pp. 73–87, 2018, DOI: 10.1016/j.est.2018.07.006.

[206] A. Karger, L. Wildfeuer, A. Maheshwari, N. Wassiliadis and M. Lienkamp, „Novel method for the on-line estimation of low-frequency impedance of lithium-ion batteries," *Journal of Energy Storage*, vol. 32, p. 101818, 2020, DOI: 10.1016/j.est.2020.101818.

[210] N. Wassiliadis, M. Steinsträter, M. Schreiber, P. Rosner, L. Nicoletti, F. Schmid, M. Ank, O. Teichert, L. Wildfeuer, J. Schneider, A. Koch, A. König, A. Glatz, J. Gandlgruber, T. Kröger, X. Lin and M. Lienkamp, „Quantifying the state of the art of electric powertrains in battery electric vehicles: Range, efficiency, and lifetime from component to system level of the Volkswagen ID.3," *eTransportation*, p. 100167, 2022, DOI: 10.1016/j.etran.2022.100167.

[219] N. Wassiliadis, M. Ank, L. Wildfeuer, M. K. Kick and M. Lienkamp, „Experimental investigation of the influence of electrical contact resistance on lithium-ion battery testing for fast-charge applications," *Applied Energy*, vol. 295, p. 117064, 2021, DOI: 10.1016/j.apenergy.2021.117064.

Conferences, Periodicals; Scopus/Web of Science listed (peer-reviewed)

[7] C. Reiter, N. Wassiliadis, L. Wildfeuer, T. Wurster and M. Lienkamp, „Range Extension of Electric Vehicles through Improved Battery Capacity Utilization: Potentials, Risks and Strategies," in *2018 21st International Conference on Intelligent Transportation Systems (ITSC)*, Maui, HI, 2018, pp. 321–326, ISBN: 978-1-7281-0321-1. DOI: 10.1109/ITSC.2018.8569455.

[205] N. Wassiliadis, T. Herrmann, L. Wildfeuer, C. Reiter and M. Lienkamp, „Comparative Study of State-Of-Charge Estimation with Recurrent Neural Networks," in *2019 IEEE Transportation Electrification Conference and Expo (ITEC)*, Detroit, MI, USA, 2019, pp. 1–6, ISBN: 978-1-5386-9310-0. DOI: 10.1109/ITEC.2019.8790597.

[211] C. Reiter, L. Wildfeuer, N. Wassiliadis, T. Krahl, J. Dirnecker and M. Lienkamp, „A Holistic Approach for Simulation and Evaluation of Electrical and Thermal Loads in Lithium-Ion Battery Systems," in *2019 Fourteenth International Conference on Ecological Vehicles and Renewable Energies (EVER)*, Monte-Carlo, Monaco, 2019, pp. 1–17, ISBN: 978-1-7281-3703-2. DOI: 10.1109/EVER.2019.8813640.

[213] C. Reiter, N. Wassiliadis and M. Lienkamp, „Design of Thermal Management Systems for Battery Electric Vehicles," in *2019 Fourteenth International Conference on Ecological Vehicles and Renewable Energies (EVER)*, Monte-Carlo, Monaco, 2019, pp. 1–10, ISBN: 978-1-7281-3703-2. DOI: 10.1109/EVER.2019.8813671.

[214] L. Wildfeuer, N. Wassiliadis, C. Reiter, M. Baumann and M. Lienkamp, „Experimental Characterization of Li-Ion Battery Resistance at the Cell, Module and Pack Level," in *2019 Fourteenth International Conference on Ecological Vehicles and Renewable Energies (EVER)*, Monte-Carlo, Monaco, 2019, pp. 1–12, ISBN: 978-1-7281-3703-2. DOI: 10.1109/EVER.2019.8813578.

Patents

No patents have been filed at the time of writing.

Journals, Conferences, Periodicals, Reports, Conference Proceedings and Poster, etc.; not Scopus/Web of Science listed

[19] N. Wassiliadis and M. Lienkamp, „A concept for assessing the impact of enhanced fast charging availability on battery operation and design," *Advanced Automotive Battery Conference (AABC) Europe, Strasbourg, France*, 2019.

[232] N. Wassiliadis, K. Abo Gamra, F. Schmid, M. Zähringer and M. Lienkamp, „Fast charging strategy comparison of battery electric vehicles and the benefit of advanced fast charging algorithms," *Advanced Automotive Battery Conference (AABC) Europe, Mainz, Germany*, 2022.

[233] K. Abo Gamra, N. Wassiliadis and M. Lienkamp, „The impact of battery electric vehicle initial conditions on ultra-fast charging events," in *35th International Electric Vehicle Symposium and Exhibition (EVS35)*, Oslo, Norway, 2022.

Thesis-relevant open-source software and data

[59] N. Wassiliadis, M. Steinsträter, M. Schreiber, P. Rosner, L. Nicoletti, F. Schmid, M. Ank, O. Teichert, L. Wildfeuer, J. Schneider, A. Koch, A. König, A. Glatz, J. Gandlgruber, T. Kröger, X. Lin and M. Lienkamp, „Quantifying the state of the art of electric powertrains in battery electric vehicles: Range, efficiency, and lifetime from component to system level of the Volkswagen ID.3," 2022, DOI: 10.14459/2022mp1656314.

[60] N. Wassiliadis, M. Steinsträter, M. Schreiber, P. Rosner, L. Nicoletti, F. Schmid, M. Ank, O. Teichert, L. Wildfeuer, J. Schneider, A. Koch, A. König, A. Glatz, J. Gandlgruber, T. Kröger, X. Lin and M. Lienkamp, „Electric powertrain data of a Volkswagen ID.3 during real-world driving situations," 2022, DOI: 10.14459/2022mp1656314.

[199] N. Wassiliadis, „Electrochemical lithium-ion battery model and easy-to-apply parameterization procedures for fast-charge applications," 2022. Available: https://github.com/TUMFTM/EA_Battery_SPMparameterization.

[217] N. Wassiliadis, M. Ank, L. Wildfeuer, M. K. Kick and M. Lienkamp, „Experimental investigation of the influence of electric contact resistance of lithium-ion battery testing for fast-charge applications," 2021, DOI: 10.14459/2021mp1611393.

[218] N. Wassiliadis, „Model deployment framework (MDF) for real-time investigation and usage of battery models on CAN-capable test benches," 2022. Available: https://github.com/TUMFTM/EA_Battery_MDF.

Supervised Students' Theses

The following student theses were written within the framework of the dissertation under the supervision of the author in terms of content, technical and scientific support as well as under relevant guidance of the author. In the following, the bachelor, semester and master theses relevant and related to this dissertation are listed. Many thanks to the authors of these theses for their extensive support within the framework of this research project.

[18] T. Junior, „Study on the charging behavior of electric vehicles," Bachelor's thesis, Institute of Automotive Technology, Technical University of Munich, 2022.

[61] A. Basic, „Measurement and analysis of fast charging processes of battery electric vehicles," Bachelor's Thesis, Institute of Automotive Technology, Technical University of Munich, 2021.

[71] F. Steinsberger, „Investigation of the influence of fast charging processes on aging of lithium ion batteries," Bachelor's Thesis, Institute of Automotive Technology, Technical University of Munich, 2019.

[107] P. Rosner, „Study of a method for the development of lithium-ion battery fast charge protocols," Master's thesis, Institute of Automotive Technology, Technical University of Munich, 2020.

[144] J. Veeh, „Investigation of the Li-plating behavior of lithium-ion batteries and parameterization of an electrochemical battery model," Master's Thesis, Institute of Automotive Technology, Technical University of Munich, 2022.

[182] A. M. Baum, „Identification and evaluation of fast charging protocols for lithium-ion batteries," Master's thesis, Institute of Automotive Technology, Technical University of Munich, 2019.

[190] H. Jaffal, „Evaluation of impedance measurements for evaluation of the fast-charging capability of lithium-ion batteries," Term Thesis, Institute of Automotive Technology, Technical University of Munich, 2021.

[196] M. Wanzel, „Modeling and parameterization of a battery model for lithium-ion battery fast charging," Master's thesis, Institute of Automotive Technology, Technical University of Munich, 2020.

[197] A.-S. Zollner, „Experimental parameterization and validation of a thermal lithium-ion battery model," Term Thesis, Institute of Automotive Technology, Technical University of Munich, 2021.

[198] J. Weiss, „Extension of the validity of a lithium-ion battery model for fast charging to larger temperature ranges," Term Thesis, Institute of Automotive Technology, Technical University of Munich, 2020.

[200] T. Kerscher, „Implementation and computing time evaluation of a battery model for deployment in fast charging applications," Term thesis, Institute of Automotive Technology, Technical University of Munich, 2020.

[201] T. Schöpfel, „Simulative preliminary investigation on adaptive model- based fast charging strategies for lithium-ion batteries," Term Thesis, Institute of Automotive Technology, Technical University of Munich, 2021.

[202] L. Wild, „Experimental investigation of model-based fast charging strategies for lithium-ion batteries," Term Thesis, Institute of Automotive Technology, Technical University of Munich, 2021.

[203] M. Frank, „Experimental investigation of the influence of varying cell states on fast charging strategies for lithium-ion batteries," Term Thesis, Institute of Automotive Technology, Technical University of Munich, 2022.

[207] A. Wiedemann, „Development and construction of a test bench for the investigation of model-based fast charging strategies for lithium-ion batteries," Master's Thesis, Institute of Automotive Technology, Technical University of Munich, 2019.

[208] A. Bach, „Investigation of model-based fast charging strategies used for lithium-ion batteries," Master's thesis, Institute of Automotive Technology, Technical University of Munich, 2021.

[209] M. Faika, „Evaluation of a model-based fast charging strategy for lithium-ion batteries," Master's thesis, Institute of Automotive Technology, Technical University of Munich, 2022.

[215] M. Ank, „Design of lithium-ion cell holders to improve the quality of battery models," Master's thesis, Institute of Automotive Technology, Technical University of Munich, 2019.

[216] S. Ziegler, „Experimental pre-study of the effect of contact resistance on high current measurements," Bachelor's Thesis, Institute of Automotive Technology, Technical University of Munich, 2019.